SYNTHESES AND REACTIVITY OF TRANSITION METAL COMPLEXES OF MACROCYCLES CONTAINING SULFUR AND NITROGEN LIGATING ATOMS

by

SAVITRI CHANDRASEKHAR

M.Sc., University of Bombay, 1980

A DISSERTATION SUBMITTED IN PARTIAL FULFILLMENT

OF THE REQUIREMENTS FOR THE DEGREE OF

DOCTOR OF PHILOSOPHY

in the Department

of

Chemistry

ACCEPTED
FACULTY OF GRADUATE STUDIES

DEAN

DATE 1991-05-13

We accept this dissertation as conforming
to the required standard

Dr. A. McAuley

Dr. P. R. West

Dr. D. J. Berg

Dr. C. D. Scarfe

Dr. P. M. Boorman

Supervisor: Professor A. McAuley.

ABSTRACT

The ligands of the ten-membered series, [10]-aneS_3, [10]-aneS_2N, [10]-aneSN_2 and the macrobicyclic ligand - 1,4-bis(1-aza-4,8-dithia-4-cyclodecyl)ethane, and their transition metal complexes were successfully synthesised. Chromium (III) complexes of the homoleptic hexaaza ligands [18]-aneN_6 and [20]-aneN_6 were synthesised, structurally characterised and their spectral properties studied.

Bis complexes of Ni(II) with [10]-aneS_3, [10]-aneS_2N and [10]-aneSN_2 were octahedral as is evident from their crystal structures. The esr spectra of the corresponding Ni(III) complexes are characteristic of a low spin d^7 ion in a compressed octahedral coordination in the complex based on [10]-aneS_2N and an elongated octahedral coordination in the complexes based on [10]-aneSN_2 and [10]-aneS_3. The spectral and electrochemical properties of the various Ni(II) complexes are compared with each other. The redox reactivity of the Ni(II) complex based on [10]-aneS_3 was studied.

The synthesis of a macrobicyclic ligand is described. The Ni(II)complex of the macrobicyclic ligand is a distorted octahedron and the esr spectrum of the Ni(III) complex is characteristic of a low spin d^7 ion in a compressed geometry. The covalency parameter K, and the energy separation between the low spin ground state and the first excited high spin

state were determined from the esr and the electronic spectra of the Ni(III) complex.

Two isomers for the Pd(II) bis complexes of [10]-aneS_2N were obtained and characterised by X-ray methods and nmr spectroscopy. Evidence for the formation of a high spin Pd(II) octahedral species has been provided for the first time. Oxidation of the Pd(II) complex is metal centered and the esr spectra of the Pd(III) complexes are characteristic of a low spin d^7 PdS_4N_2 core.

Fe(II), Fe(III), Co(II), Co(III), Ni(II) and Pd(II) bis complexes of the ligand [10]-aneS_3 were synthesised and characterised by elemental analysis, nmr and esr spectroscopies, where appropriate, and their spectral and electrochemical properties studied. The crystal structures of Fe(II), Co(II) and Ni(II) bis complexes of [10]-aneS_3 were octahedral with three S atoms from each of the thioether ligands coordinated to the central metal ion. The esr spectra of the Fe(III) bis complexes of [9]-aneS_3 and [10]-aneS_3 were characteristic of a low spin d^5 complex ion. The ligand field distortion parameters were obtained from the electronic and esr spectra and the energies of the Jahn-Teller splitting were estimated.

The Co(II, bis complex of [10]-aneS_3 is low spin. The half-wave potentials due to the $[Co([10]\text{-ane}S_3)_2]^{3+/2+}$ and $[Co([10]\text{-ane}S_3)_2]^{2+/+}$ couples were obtained by cyclic voltammetry. The electron self exchange rate constant for the

$[Co([10]\text{-}aneS_3)_2]^{3+/2+}$ and the $[Co([9]\text{-}aneS_3)_2]^{3+/2+}$ couples were determined by the ^{59}Co nmr line broadening technique for the first time. The self exchange rate constant for the $[Fe([10]\text{-}aneS_3)_2]^{3+/2+}$ couple was determined by the ^{1}H nmr line broadening technique.

The crystal structure of the Pd(II) bis complex of [10]-$aneS_3$ is essentially square planar with significant interactions from the axial S atoms. This complex is fluxional as is evidenced in the variable temperature nmr spectra.

Examiners:

Dr. A. McAuley

Dr. P. R. West

Dr. D. J. Berg

Dr. C. D. Scarfe

Dr. P. M. Boorman

TABLE OF CONTENTS

LIST OF TABLES

LIST OF FIGURES

LIST OF SCHEMES

LIST OF IMPORTANT COMPOUNDS.

22	[9]-aneN_3	1,4,7-triazacyclononane.
23	[10]-aneS_3	1,4,7-trithiacyclodecane.
24	[10]-aneS_2N	8-aza-1,5-dithiacyclodecane.
25	[10]-aneSN_2	4,8-diaza-1-thiacyclodecane.
26	Macrobicyclic ligand	1,4-bis(1-aza-4,8-dithia-4-cyclodecyl)ethane.
27	[18]-aneN_6	1,4,7,10,13,16-hexaazacyclo-octadecane.
28	[20]-aneN_6	1,4,7,11,14,17-hexaazacycloeicosane.
62	[10]-aneN_3	1,4,7-triazacyclodecane.
63	[18]-aneS_4N_2	7,16-diaza-1,4,10,13-tetrathia cyclooctadecane.
64	[9]-aneS_3	1,4,7-trithiacyclononane.
65	[9]-aneS_2N	7-aza-1,4-dithiacyclononane.
84	[9]-aneSN_2	4,7-diaza-1-thiacyclononane.
85	Open-chain	3-thiapentane-1,5-diamine.

ACKNOWLEDGEMENT

I take this opportunity to thank Prof. A. McAuley for his guidance, support, freedom and constant encouragement throughout the course of this work. The help extended by my colleagues Dr. D. G. Fortier, Dr. S. Subramanian, Dr. T. W. Whitcombe, Mr. C. Xu, Ms. B. Cameron, Ms. B. Chak and Mr. K. Coulter is gratefully acknowledged. I would like to thank Dr. C. J. MacDonald and Dr. Henry Zhang for their kind encouragement during their visits. I would also like to thank all the members of the faculty for useful discussions. The ready assistance rendered by Ms. K. Beveridge, Ms. C. G. Greenwood and other technical and non-technical staff of the Department of Chemistry is sincerely acknowledged.

I am grateful to Mrs. and Mr. Kambo and their family for their moral support and cooperation during the entire course of this work. The constant encouragement and moral support given by all the members of my family, especially my husband who also showed immense patience, is greatly appreciated.

Dedicated to my

parents-in-law and my parents.

CHAPTER 1

Introduction

1.1. Historical development of donor-acceptor compounds:

Perhaps the first encounter with a coordination compound or complex ion was that of Libavius who noted in 1597 the formation of the deep blue ion now known to be $Cu(NH_3)_4^{2+}$.[1] The formation can be represented by the following reaction,

$$[Cu(H_2O)_4]^{2+} + 4NH_3 \longrightarrow [Cu(NH_3)_4]^{2+} + 4H_2O. \quad \text{--- 1.1}$$

Tassert in 1798, observed the formation of what is now known as $Co(NH_3)_6^{3+}$, in solution. The complexes were known by their discoverers' names: Zeise's salt -- $\{KPt(C_2H_2)Cl_3.H_2O\}$, Magnus's salt -- $\{[Pt(NH_3)_4]^{2+}[PtCl_4]^{2-}\}$, Peyrone's salt -- {*cis*-$Pt(NH_3)_2Cl_2$}, and many others.[2] The systematic exploration of coordination chemistry began with the chemist O.W. Gibbs, who in 1856, prepared a series of Co(III) ammines, *e.g.*, $[Co(NH_3)_6]^{3+}$, $[Co(NH_3)_5H_2O]^{3+}$, etc.. The bonding theory of the time suggested that the geometry around a metal atom was governed by its oxidation state so that chains of ammonia molecules were required in order to increase the number of bonds to the metal.

In 1893, Alfred Werner established the structural basis for modern coordination chemistry. He suggested the octahedral geometry that is now accepted for nearly all six-coordinated complexes, pointing out that either anions or neutral molecules could occupy coordination sites at the corners of the octahedron and that ammonia and water were completely equivalent in their functions.[3]

S.M. Jørgensen (1837 - 1914) conducted extensive studies

on the syntheses of such "complex" compounds and observed that the metal halides and other salts could give compounds with neutral molecules and that many of these compounds could be formed in aqueous solutions.

The stereochemical studies of Werner were later followed by Lewis' theory of bonding in terms of electron pairs (1916) and in 1927 N.V. Sidgwick showed that a chemical bond required a shared pair of electrons.[4] This led to the idea that a neutral molecule with an electron pair (Lewis base) could donate these electrons to a metal ion or other electron acceptor (Lewis acid). It was also during the 1920s that magnetic studies of the transition metals began to provide direct evidence for electron structure in their ions. In the 1930s, Linus Pauling proposed the valence-bond theory of bonding in transition metal complexes. According to this theory, each ligand was viewed as a two-electron donor with a sigma bond to the metal ion.[5] Around the same time ionic bonding in complexes was suggested by Langmuir and the basic idea of the crystal field theory, namely, that the metal ion in the complexes is subjected to an electric field originating from the ligands, was proposed by Becquerel (1929). In the same year the quantum mechanical theory of ionic bonding, *viz.*, the crystal field theory was formulated by Bethe.[6]

The first application of the crystal field theory to transition metal complexes was made in 1932 by Penny and Schlapp,[7] and by Van Vleck,[8] who used the theory to calculate

magnetic susceptibilities.

Both the valence-bond picture and that of the crystal field can be considered as specializations of the molecular-orbital method due to Mulliken.[9] Indeed, the most comprehensive approach to these compounds is now called the ligand field theory, which is really nothing more than a hybridization of the ideas of Bethe and Van Vleck with those of Mulliken. The use of crystal field theory in the study of transition metal complexes was then discussed by Orgel[10] and Tanabe and Sugano.[11] Significant contributions to the theory and, particularly, to its applications were made by Ballhausen,[12] Griffith,[13] Cotton[14] and many others. These chemists have been responsible in large measure for the subsequent development and application of the ligand field theory.

In the early 1950s the increased use of infrared and uv-visible spectra were helpful in describing the bonding in coordination compounds. New techniques such as NMR and EPR have increased our knowledge of structural and magnetochemical aspects. Later, other spectroscopic techniques like Mössbauer spectra for certain elements (which helped establish coordination symmetry, formal charge and electron delocalization) and photoelectron spectroscopy were developed. Many electrochemical techniques, such as, cyclic voltammetry were also introduced together with computerized X-ray diffraction methods for detailed structural analysis.

The most convenient way of classifying transition metal complexes structurally is by their coordination numbers, the number of electron-donor atoms or donor pairs bonded to a given metal atom. Under varying conditions, transition metal atoms can be isolated with coordination numbers up to 12.

1.2. Classification of ligands:

Ligands can be classified structurally, by the number of connections they make to the central atom. When only one atom is bonded to the central metal ion, the ligand is said to be *unidentate* [*e.g.*, the ligands in $Co(NH_3)_6^{3+}$, $AlCl_4^-$, $Fe(CN)_6^{3-}$]. When a ligand becomes attached by two atoms it is *bidentate*, and similarly for *tridentate*, generally multidentate.

Bidentate ligands when bound entirely to one atom are termed *chelate*, as in **1**, **2**, and **3** :

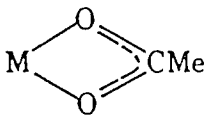

1

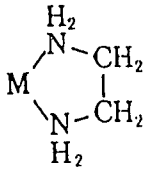

2

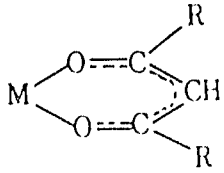

3

Terpyridine **4** and acylhydrazones of salicylaldehyde **5** are examples of chelating tridentate ligands as shown below:

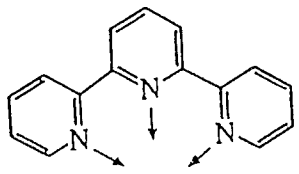

4

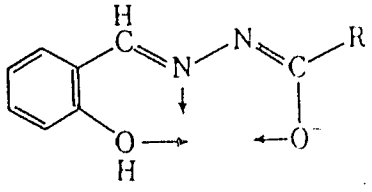

5

Ligands of the type $X(-Y)_3$, where X is N, P, or As, the Y groups are R_2N, R_2P, R_2As, RS, or RSe and the connecting chains (-) are $(CH_2)_2$, $(CH_2)_3$ or -phenylene, are called *tripod* ligands. Tripod ligands are used to form trigonal-bipyramidal complexes **6**, although square pyramidal complexes can also be formed **7**. If the polydentate ligand is cyclic in nature, a *macrocyclic* ligand results. This is defined as a cyclic compound with nine or more members and containing three or more ligating atoms.[15]

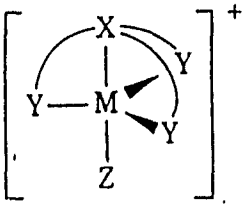

6

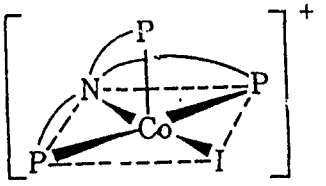

7

Cryptates[16] are yet another type of a multidentate ligand and are macrobicyclic (*e.g.*, **8**).

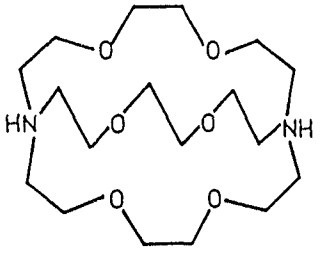

8

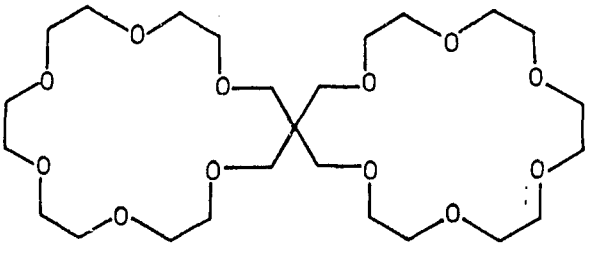

9

Binucleating ligands, **9**, **10**, and **11**, allow for incorporation of two metal atoms into their structure.[16,17]

Encapsulating ligands[18] are a type of ligand which are synthesized around the metal ion as a result of which the

metal ion cannot be released readily (*e.g.*, **12**). Such ligands can also enforce unusual coordination geometries.

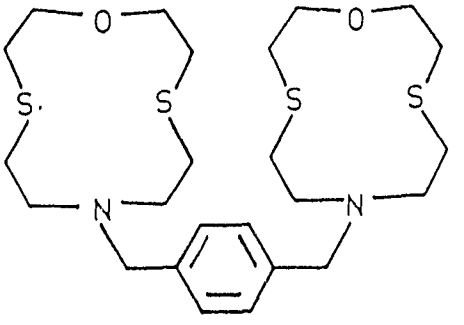

10

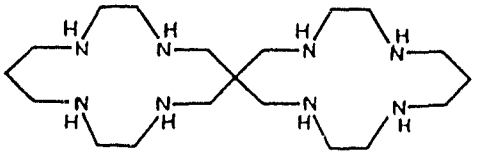

11

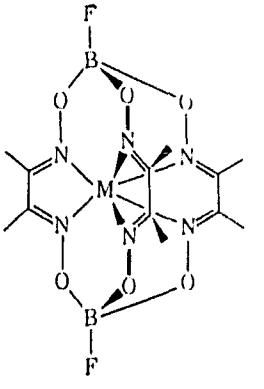

12

Complexation can thus be treated as an acid-base reaction wherein the donor atoms with the lone pair of electrons can be considered as Lewis bases and the metal ions that can accept the electrons can be viewed as Lewis acids. According to Ahrland, *et al*[19] the electron acceptors (metal ions) can be classified (Table 1.1.) based on relative base peferences and stabilities of complexes formed by closely related ligands with a wide range of metal ions.

Table 1.1. Classification of metal ions.

Class *a* behaviour	: H, the alkali and alkaline earth metals, the elements Sc → Cr, Al → Cl, Zn → Br, In, Sn, Sb, and I, the lanthanides and actinides.
Class *b* behaviour	: Rh, Pd, Ag, Ir, Pt, Au, Hg
Borderline behaviour	: the elements Mn → Cu, Tl → Po, Mo, Te, Ru, W, Re, Os, Cd

Metal ion-ligand interactions can also be explained based on Pearson's concept of hard and soft acids and bases.[20] Thus a hard acid will prefer to combine with a hard base and a soft acid will prefer to combine with a soft base.

1.3. Complexes of macrocyclic ligands:

The understanding of the metal-ion chemistry of macrocyclic ligands has important implications in a range of chemical and biochemical areas. The fact that macrocyclic ligand complexes are involved in a number of fundamental biological systems has long been recognized. The importance of such complexes, to the mechanism of photosynthesis for example, or to the transport of oxygen in mammalian and other respiratory systems, has provided a motivation for investigation of the metal-ion chemistry in these macrocyclic

systems. The porphyrin ring **13** of the iron-containing haem proteins and the related chlorin **14** complexes of magnesium in chlorophyll, together with the corrin ring **15** of the vitamin B_{12} have been studied for many years. Only one category of synthetic macrocyclic ligand *viz.* phthalocyanine **16** was known prior to 1960.

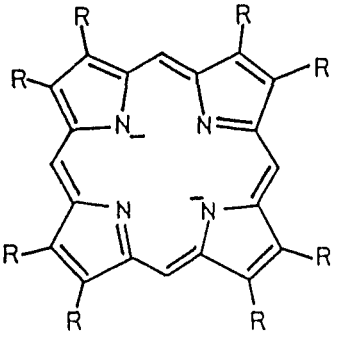

13

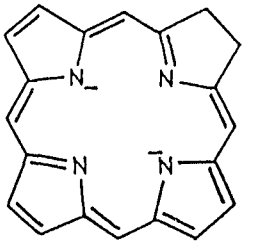

14

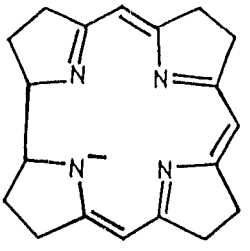

15

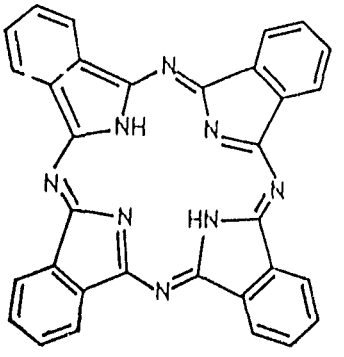

16

Since then a large number of synthetic macrocycles have been prepared. The possibility of using synthetic macrocyclic complexes as models for the biological systems has provided an impetus for much of this research. Apart from the biological implications, the chemistry of macrocyclic ligands is of

relevance to a number of other areas. Many of the developments impinge on topics such as metal-ion catalysis, organic synthesis, metal-ion discrimination and analytical methods, as well as on a number of potential industrial, medical and other applications.[15,16] However, with the natural macrocycles described above, metal-donor interactions are complicated because of an extensive π system. The ligands are powerful chromophores, so that d-d spectra are not readily observable in their complexes. Redox interactions are complicated by electron transfers that may involve the metal ion, the ligand, or both. Use of synthetic saturated macrocyclic ligands provides the opportunity to understand the special properties of their metal complexes resulting from the cyclic nature of the ligand. Macrocycles with N donors have been studied extensively for reasons cited above.[21,22]

1.4. The chelate and macrocyclic effects:

The term "chelate effect" refers to the enhanced stability of the complex system containing chelate rings when compared to the stability of a system that is as similar as possible but contains no chelate rings. For example,

$$[Ni(H_2O)_6]^{2+} + 6NH_3 \rightleftharpoons [Ni(NH_3)_6]^{2+} + 6H_2O \quad (\log \beta = 8.61) \quad --1.2$$

$$[Ni(H_2O)_6]^{2+} + 3en \rightleftharpoons [Ni(en)_3]^{2+} + 6H_2O \quad (\log \beta = 18.28) \quad --1.3$$

The thermodynamic contribution to the chelate effect in these Ni complexes are shown in Table 1.2.[23] Although the enthalpies make a slight favourable contribution the main source of the

chelate effect is due to the entropy factor.

Table 1.2.

Thermodynamic contributions to the chelate effect in complexes of ethylene diamine with Ni(II)[a]

Unidentate complexes:	$[Ni(NH_3)_2(H_2O)_4]^{2+}$	$[Ni(NH_3)_4(H_2O)_2]^{2+}$	$[Ni(NH_3)_6]^{2+}$
ΔG	-6.93	-11.08	-12.39
ΔH	-7.80	-15.60	-24.00
ΔS	-3.00	-15.00	-39.00
Chelate Analog:	$[Ni(en)(H_2O)_4]^{2+}$	$[Ni(en)_2(H_2O)_2]^{2+}$	$[Ni(en)_3]^{2+}$
ΔG	-10.03	-18.47	-24.16
ΔH	-9.00	-18.30	-28.00
ΔS	4.00	3.00	-10.00
ΔG^{*}[b]	-3.10	-7.40	-11.77
ΔH^{*}[b]	-1.20	-2.70	-4.00
ΔS^{*}[b]	7.00	18.00	29.00
$7.9n$[c]	7.90	15.80	23.70

[a]All data from ref. 23; ΔG and ΔH in kcal mol^{-1}; ΔS in cal deg^{-1} mol^{-1}.

[b]The thermodynamic manifestation of the chelate effect, such that $\Delta G^{*} = \Delta G(\text{en complex}) - \Delta G(NH_3 \text{ complex})$.

[c]The value of $7.9n$, where n is the number of chelate rings in the complex should be compared with ΔS^{*}.

1.4.1. Origins of entropy contribution in the chelate effect:

The main cause of the large entropy increase is the number of unbound molecules. Although $6NH_3$ displace $6H_2O$, (eq. 1.2) making no net change in the number of independent molecules, it takes only 3 ethylenediamine (en) molecules to displace $6H_2O$, (eq. 1.3). The model of Schwarzenbach[24] considers the chelate effect to arise because, once one donor atom of a chelating ligand has been attached to a metal ion, the second donor atom is constrained to move in a greatly reduced volume as compared to the situation for the unidentate system.

The chelate effect is largely due to an increase in translational entropy. The entropy contributions to the chelate effect are expected to be 7.9 $cal.deg^{-1}.mol^{-1}$ per chelate ring and are found as expected (Table 1.2.).[23]

1.4.2. Macrocyclic effect:

In the macrocyclic effect, the stability of the complex of the macrocyclic ligand is compared with that of its open-chain analog. The number of particles in both equilibria is the same so that no translational entropy effects are expected, which is an important difference between the macrocyclic and chelate effects.

The term "macrocyclic effect" was introduced by Cabbiness and Margerum[25] to account for the greater thermodynamic stability of complexes containing macrocyclic ligands of

similar structure. A representative comparison would be between the following pair :

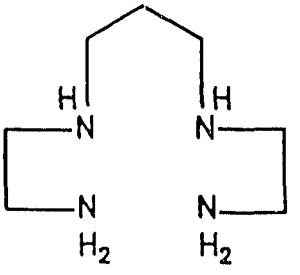

17

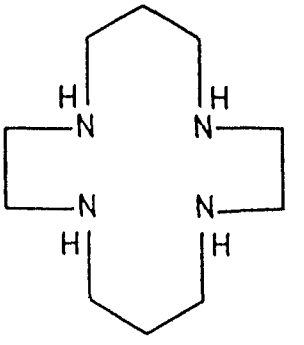

18

The thermodynamic parameters of the Zn(II) complexes of the ligands **17** and **18** are listed in Table 1.3. The overall macrocyclic effect is both enthalpic and entropic in nature.

Table 1.3. Thermodynamic properties of ZnII[**17**] and ZnII[**18**].

Ligands	**17**	**18**
log *K*	11.25	15.34
$-\Delta H°$ (kcal mol^{-1})	10.61	14.79
$\Delta S°$ (cal deg^{-1} mol^{-1})	15.89	20.51

Busch and co-workers[26] used the term "multiple juxtapositional fixedness" to account for the enhanced stability of macrocyclic complexes in terms of their inertness towards substitution, even in the presence of strong acids. A macrocyclic ligand cannot dissociate from a metal ion by a replacement process similar to that which occurs for non-

cyclic ligands since the structure of the ring does not provide an "end" at which the successive, stepwise removal process can be initiated. Thus the increased stability of macrocyclic complexes compared with similar non-macrocyclic complexes must be explained by consideration of both thermodynamic and kinetic effects.

1.4.3. Thermodynamics of the macrocyclic effect:

Whether the macrocyclic effect is a result of enthalpic stabilization, or entropic stabilization, or a combination of these, depends on several factors. In making comparisons a good match between the size of the metal ion and the macrocyclic cavity is necessary. Table 1.4.[23] shows the thermodynamic contributions to the macrocyclic effect in Cu(II) and Ni(II) complexes of tetraazamacrocycles:[21]

Table 1.4.
Thermodynamic contributions to the macrocyclic effect in complexes of tetraazamacrocycles[a]

		Cu(II)	Ni(II)
log K_1:	cyclam	26.5	~19.4
	2,3,2-tet	23.2	15.9
	log K (MAC)	3.3	~3.5
ΔH:	cyclam	-32.4	-24.1
	2,3,2-tet	-27.7	-18.6
	ΔH (MAC)	-4.7	-5.5
ΔS:	cyclam	13.0	~8.0
	2,3,2-tet	13.0	10.0
	ΔS (MAC)	0.0	~-2.0

[a]Units: ΔH, kcal mol^{-1}, ΔS, cal deg^{-1} mol^{-1}; the thermodynamic contributions to the macrocyclic effect are K (MAC), ΔH (MAC), and ΔS (MAC).

The evidence suggests then, that if there is not a serious mismatch between the size of the metal ion and the macrocyclic cavity, there will always be a substantial contribution from enthalpy to the macrocyclic effect, with entropy contributing sometimes, but usually to a lesser extent. Strain energy effects are larger if there is a mismatch between the size of the metal ion and the macrocyclic cavity and this leads to unfavourable entropic contribution to the macrocyclic effect. The origins of the macrocyclic effect may be attributed to the relative importance of the following contributing factors:

(a) preorganization of the ligand,

(b) desolvation of the donor atoms in the confined space of the macrocyclic cavity,

(c) intrinsic basicity effects, and

(d) dipole-dipole repulsion in the cavity of the ligand.

'Preorienting' and 'multiple juxtapositional fixedness' have been grouped under preorganization of the ligand. In the simplest case, preorganization of the ligand, involves the ligand already being in the proper conformation for complex formation.

A major contribution to the macrocyclic effect arises because of the large energy required to take the open-chain analog from its minimum energy linear conformer to that required for complexation, which is not necessary in the pre-strained macrocycle. A photoelectron spectroscopic study of

crown ethers and N- donor macrocycles and their open-chain analogs has indicated a greater ease of removal of electrons from the dipoles on the donor atoms of the macrocycle than of the open-chain compounds.[27] All these factors namely, preorganization, solvation and dipole-dipole repulsion lead to a high-energy state for the macrocycle, which is relieved on complex formation.

The greater basicity of the donor atoms along the series NH_3, NH_2R, NHR_2, NR_3, (R = alkyl group), and, as ethylene bridges are added, makes a substantial contribution to the macrocyclic effect. The basicity of the secondary amines in the cyclic ring is enhanced as a result of the electron donating property of the methylene chains bridging the donor atoms. If the donor atoms in the cyclic ring are made tertiary as in tetramethyl- cyclam the stability of its Ni(II) complex decreases, ($\log K_f$ for $Ni[cyclam]^{2+}$ is 20 and for $Ni[tetramethylcyclam]^{2+}$ is 8.6) due to the frontal strain effects.[23] The important aspect of the macrocyclic structure is that macrocycles are sterically efficient and allow for exercising of the greater basicity of the donor atoms without paying the steric penalities that are incurred in open-chain ligands when the addition of N-alkyl groups is used to change donor atoms from primary to secondary. In summary, the macrocyclic effect is predominantly an enthalpy effect.

1.5. Synthesis of macrocyclic ligands:

Synthesis of macrocyclic ligands can be achieved *via* the template methods or the non-template method.

1.5.1. Template method:

The term "template method" reflects the controlling influence of the metal ion in a particular synthesis. It can be kinetic or thermodynamic.

In the template method, the organic substrates are reacted to form the macrocycle in the presence of a suitable metal ion to yield the metal complex directly. For example, one of the early synthetic macrocyclic ligands was synthesised when Curtis[28] attempted to recrystallize $[Ni(II)(en)_3]^{2+}$, **19**, from acetone but, instead, obtained the Ni(II) macrocyclic complexes, **20** and **21**.

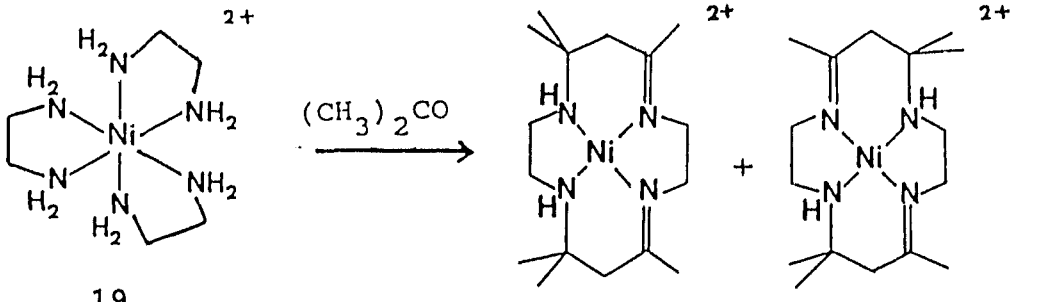

19 20 21 --- 1.4

The complex was stable to acid hydrolysis and stable Ni(III) species could be obtained. These unusual properties exhibited by the macrocyclic ligands paved the way for a systematic study of this class of ligands and their complexes with alkali, alkaline earth and transition metal ions. Without the

presence of the metal ion in these reactions, the macrocycles are produced in insignificant yields or are not formed at all. Thus the metal ion plays an important role in directing the steric course of condensation reactions. Lindoy and Busch[29] have discussed this role in terms of coordination template effects. A kinetic template effect (1.5) is said to be operative if the directive influence of the metal ion controls the steric course of a sequence of stepwise reactions. If the metal ion preferentially coordinates with one of the components thereby perturbing an existing equilibrium in the organic system, then a thermodynamic template effect is said to be operative.

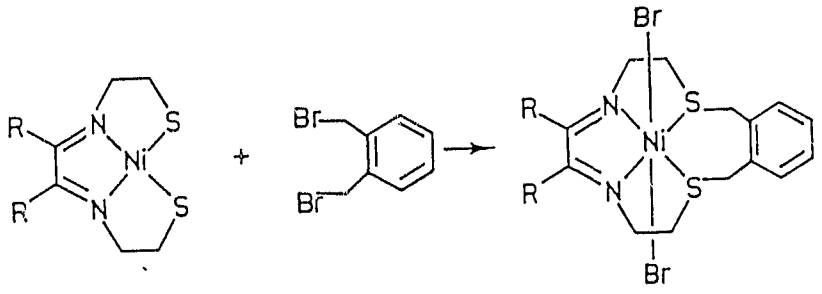

-- 1.5

However, the template method of synthesis of macrocyclic ligands is metal-ion and substrate specific and not a general one.

1.5.2. Non-template method:

In the non-template method, the macrocyclic ligands are synthesised and characterised before complexation with any metal ion. Changes in the macrocyclic ligand upon complexation may be detected if the physical properties of the

ligand can be compared with those of the complex. A normal priority in both direct and template procedures is to maximize yields of the required product by choosing strategies which inhibit competing linear polymerization and other reactions.

A typical direct synthetic procedure involves the reaction in equimolar concentrations, of two reagents incorporating the required fragments for the target macrocycle such that 1:1 condensation occurs. Under high-dilution conditions cyclization is favoured by enhancing the prospect of the 'half condensed' moiety reacting with itself 'head-to-tail' rather than undergoing an intermolecular condensation with another molecule in the reaction solution.

a) Cyclization performed at high dilution:

Preparation of a 14-membered N_4-donor macrocycle serves as a good example for the direct synthetic procedure at high dilution.[30]

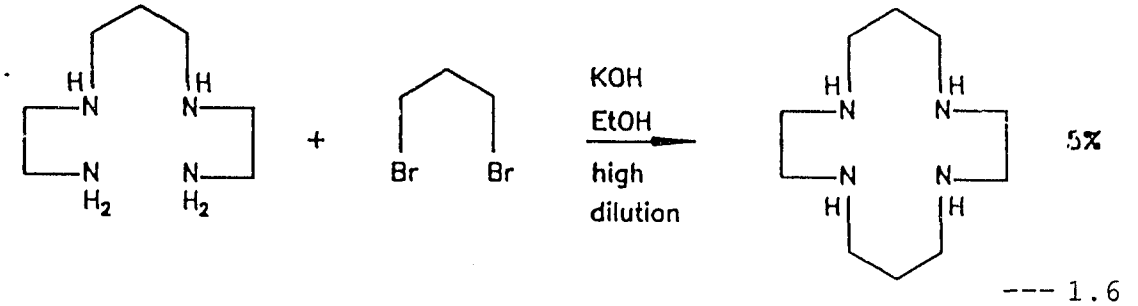

--- 1.6

b) Cyclization at moderate to low dilutions:

A series of N-tosylated (tosyl = p-toluene sulfonyl; Ts) macrocycles may be prepared by direct means starting from pre-

tosylated reactants (Richman and Atkins, 1974).[31] Reasonable yields (better than 50%) of such cyclic tosylated products are obtained although such reactions are performed at moderate dilutions. The tosyl groups reduce the number of conformational degrees of freedom in the reactants. It is this reduction which is thought to facilitate cyclization relative to polymerization for these systems. An example of this reaction type is given below:

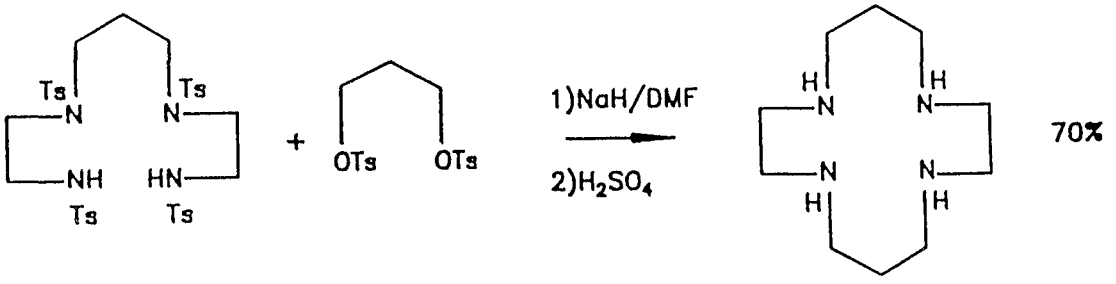

--- 1.7

Cyclizations taking advantage of the dilution principle (DP) usually start with open chained adduct compounds bearing two or more functional groups, and, as a rule, only one of the possible oligomers, the monomeric cyclization product, is the desired main product. The preference of the monomer formation is not simply based on the use of a large solvent volume and/or addition of highly diluted reagents. Contrarily, in "dilution principle reactions" not the total amount of the solvent volume is decisive, but, instead the establishment of a stationary concentration of the adducts in the reaction flask that is as low as necessary, to steer the cyclization

reaction in such a way that ideally the same amount of the starting material is flowing into the reaction flask per unit time as is reacted to yield the optimum of the target cyclization product.[32]

1.5.3. Synthesis of macrocycles containing C-S and C-N bonds:

According to the type of the attacking nucleophile (S, O, N, and C), cyclization can lead to the formation of C-S, C-O or C-N bonds.

a) Synthesis of macrocycles containing C-S bonds:

C-S bonds can be formed using sulfide ions generated from $Na_2S.9H_2O$ or from thioacetamide. C-S bonds can also be formed from metal thiolates or from free thiols which form thiolates in basic solutions *in situ*. Typical examples[32,33] using each of these methods are shown below:

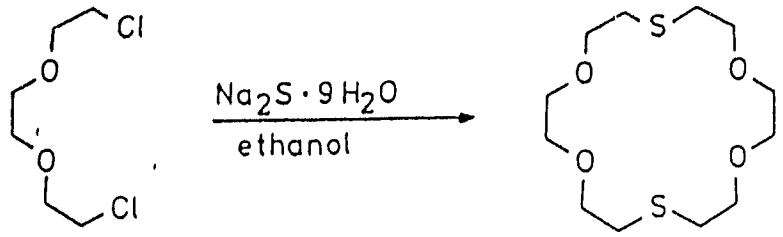

-- 1.8

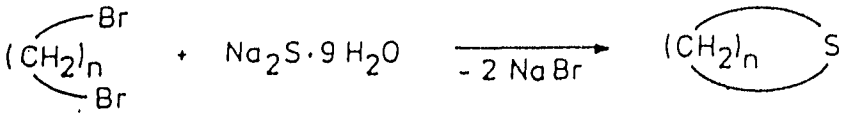

-- 1.9

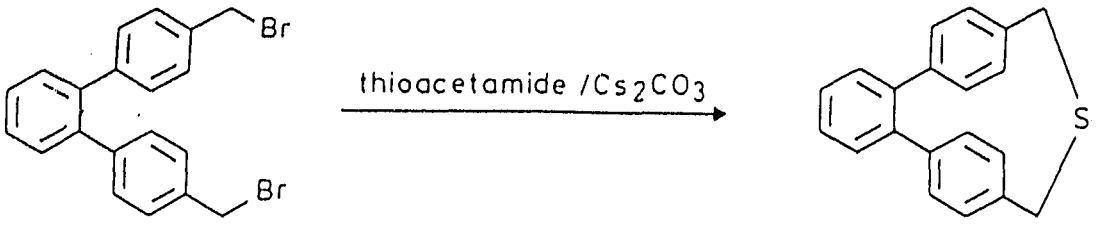

-- 1.10

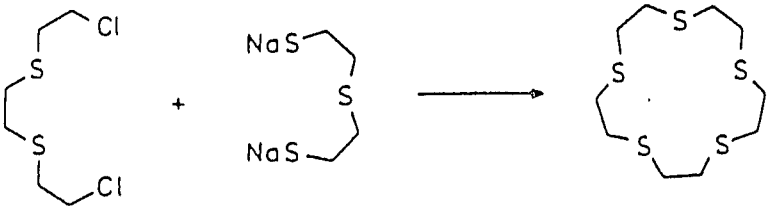

-- 1.11

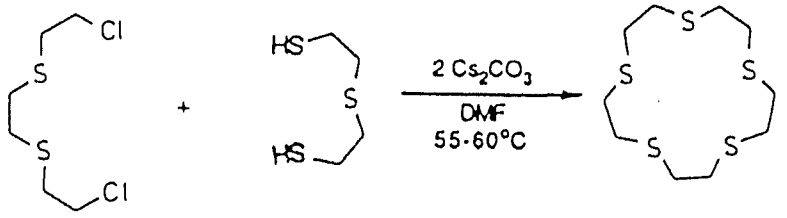

-- 1.12

b) Synthesis of macrocycles using C-N bond formation:

Synthesis of macrocycles using C-N bond formation can be exemplified by the formation of a 20-membered ring containing four N donor atoms as shown below:

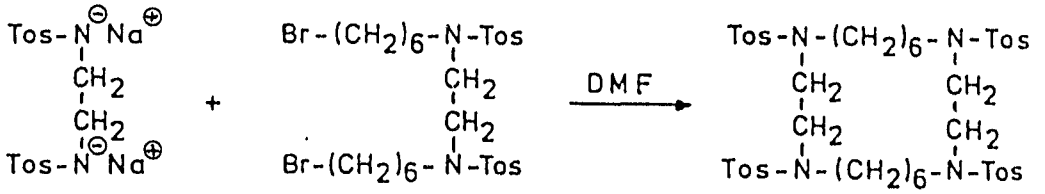

--- 1.13

1.5.4. The cesium effect:

The principle in the syntheses of various 'thia-crown' macrocycles is S_N2 substitution by thiolate on a suitably activated carbon atom. It has been found by Buter and Kellogg[34] that the use of cesium thiolates showed substantial improvement in the yield of the macrocyclization step, relative to the use of Na or K thiolates. This has been attributed by these authors to what is known as 'the cesium effect'. Thiols were found to be deprotonated readily by Cs_2CO_3 in DMF to form cesium thiolates which are reasonably soluble in DMF. An example of the synthesis of a 'thia-crown' macrocycle is given below:

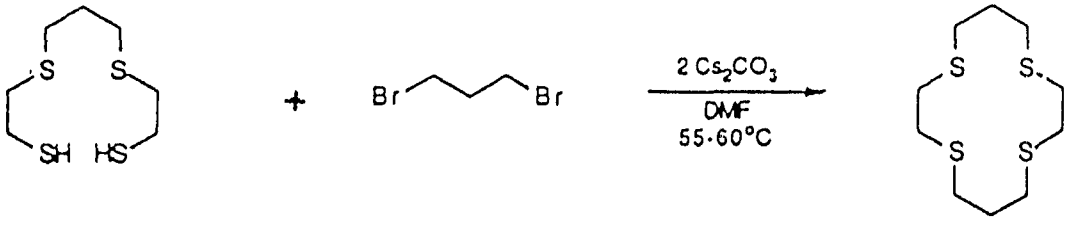

--- 1.14

As a working model it is assumed that cyclization occurs in two steps as illustrated below:

$Cs^{\oplus}.S^{\ominus}(chain)_aS^{\ominus}Cs^{\oplus} + Br(chain)_bBr \rightarrow Cs^{\oplus}.S^{\ominus}(chain)_aS(chain)_bB-$

$+ CsBr$

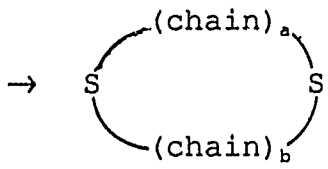

$+ CsBr$

--- 1.15

The cesium ion is large (ionic diameter, 3.3 Å) and it has a low charge/surface area ratio (0.03 $Z/Å^2$) compared to smaller cations such as Na^+. Cesium is the most polarizable of the alkali metal cations (2.9 $Å^3$ for Cs^+, 1.1 $Å^3$ for K^+, 0.3 $Å^3$ for Na^+) and with the exception of thallium (4.3 $Å^3$), the most polarizable of the common monovalent cations. As a result the cesium ion is not as well solvated as smaller ions in DMF. In short, the hydrolysis is based on the idea that the thiolate anion is a better nucleophile because it encapsulates the cesium ion leaving a highly reactive naked anion. The S_N2 reaction leading to intermolecular cyclization is thought to occur on the "surface" of the highly polarizable cesium ion.

1.5.5. Purification of the macrocyclic ligands:

The macrocyclic ligands may be purified by column chromatography or by recrystallization from mixed solvents. Another method of purifying them is to first convert them into their hydrochloride or hydrobromide salts, purify the salts by recrystallization and then regenerate the ligand as and when

required. For example, [9]-aneN_3, **22**, ligand is converted to the [9]-aneN_3.3HCl salt, recrystallized and then the ligand can be regenerated by continuously extracting the aqueous salt solution (made basic, pH ~ 12 with conc. NaOH) with $CHCl_3$.

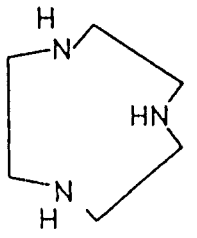

22

A different approach to purifying macrocycles is to form their metal complexes, usually with Ni^{2+} or Cu^{2+}. The metal-ion complexes can be purified either by column chromatography using a weak cation exchange (Sephadex) column, C-25, or by recrystallization methods. The purified complex is then demetallated (decomplexed) to yield the pure, free ligand. Demetallation may be induced by addition of a strongly competing ligand to a solution of the macrocyclic complex, *e.g.*, the cyanide ion or ethylenediaminetetraacetate. In some cases, for example, when sulfide or hydroxide ion is used as the scavenging ligand, the metal may be removed as an insoluble precipitate (the metal sulfide or hydroxide) leaving the metal-free macrocycle in the supernatant liquid.

1.6. Characterisation studies:

The free ligands are usually characterised by spectroscopic methods which include IR, NMR and mass

spectroscopy. The transition metal complexes are characterised by their elemental analysis, IR spectra and NMR spectra (if the complexes are diamagnetic). Several other physical methods are also used in the characterisation studies. These include,

1. x-ray crystal structure determination
2. electronic absorption spectra
3. electron paramagnetic resonance
4. cyclic voltammetry.

1.7. Redox reactions:

Redox reactions involve two species that vary in oxidation state. Many metal ions can be stabilized in a variety of oxidation states [*e.g.*, Ni(I) to Ni(III), Cu(I) to Cu(III) or Cr(-II) to Cr(IV)].[20,35] The role of transition metal ions in life processes depends on their ability to participate selectively in electron transfer reactions in complexes. A number of natural macrocyclic complexes are central to *in vivo* redox behaviour.[36] Many of the synthetic macrocyclic complexes serve as models for natural cyclic systems and hence the redox chemistry of macrocyclic ligand complexes has received much attention. Copper and iron containing proteins dominate in the electron transfer role, with the polypeptide or protein component appearing to tune the metal centre to the required redox role. Since the discovery of the Ni(III) and Ni(I) in methanogenic bacteria

there have been extensive investigations on the redox chemistry of nickel.[37] For different macrocyclic systems the variation of the E° values for the oxidants provides a wide range of driving force for the reactants, (Fig. 1.1.).[38]

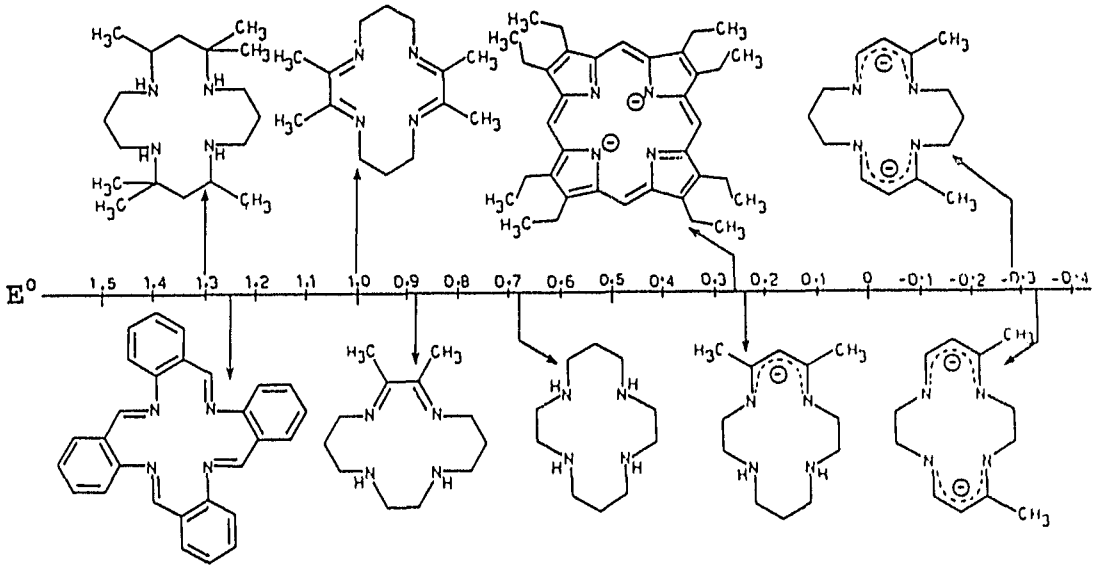

Fig. 1.1. E^0 values for some Ni macrocyclic systems.

In addition, the inertness of many macrocyclic systems makes them attractive for electrochemical studies since the redox changes are less likely to be influenced by competing equilibria involving ligand dissociation as compared to the non-cyclic systems. Macrocyclic ligand systems tend to provide a well-defined environment for the metal ion which, in the case of the more rigid ligands, will not vary greatly from reactant to product. There is an interest in obtaining stable, water-soluble, redox reagents based on inexpensive

materials for use in such devices as photochemical cells and redox storage batteries. Macrocyclic systems appear to be candidates for such applications.

The study of redox reactions comprises understanding the mechanisms of electron transfer in these systems. There are two principal mechanisms by which electron transfer occurs: outer sphere and inner sphere.

1.7.1. Outer-sphere reactions:

In outer sphere reactions transfer of an electron from reductant to oxidant takes place with no disruption of the primary coordination spheres of the reagents, for example,

$$Fe(phen)_3^{2+} + Ru(phen)_3^{3+} \rightleftharpoons Fe(phen)_3^{3+} + Ru(phen)_3^{2+} \quad -- \ 1.16$$

In this case, the o-phenanthroline (phen) complexes of the metal ions are substitution inert on the time scale of the redox step. Where the electron transfer takes place between forms of the same metal ion in two oxidation states, the process is frequently described as self-exchange. For example,

$$Fe(H_2O)_6^{3+} + Fe^*(H_2O)_6^{2+} \rightleftharpoons Fe^*(H_2O)_6^{3+} + Fe(H_2O)_6^{2+} \quad -- \ 1.17$$

$$Mn^*O_4^- + MnO_4^{2-} \rightleftharpoons Mn^*O_4^{2-} + MnO_4^- \quad --- \ 1.18$$

In equation (1.18) the rate of transfer between MnO_4^- and MnO_4^{2-} studied by isotopic exchange is several orders of magnitude greater than the exchange of oxygen between MnO_4^- and solvent water.[39,40]

1.7.2. Inner-sphere reactions:

The principal feature of the inner-sphere process is that the oxidant and reductant share a ligand in their coordination spheres, the electron being "transferred" across the bridging group. An example of this process is given below:

$$Co(NH_3)_5Cl^{2+} + Cr^{2+} \rightleftharpoons Co(NH_3)_5ClCr^{4+}$$

$$Co(NH_3)_5ClCr^{4+} \rightarrow CrCl^{2+} + Co(NH_3)_5^{2+}$$

$$Co(NH_3)_5^{2+} + 5H^+ \rightleftharpoons Co^{2+}\ 5NH_4^+ \quad -- \quad k = 6 \times 10^5\ M^{-1}s^{-1}; \quad -- \quad 1.19$$

Both Cr(III) and Co(III) complexes are substitution inert, so that at no time is the chloride ion free in solution.

1.8. Mechanism of outer-sphere reactions:

Kinetic investigations of outer sphere electron transfer reactions involve the experimental determination of the rate of a reaction and determining the self-exchange rate constants.

The experimental determination of a reaction rate involves the initiation of the reaction and the monitoring of the time-dependent changes in the concentration of the reactants and/or products.

(a) Methods of initiation:

The choice of the method by which the reaction may be initiated is governed by the velocity of the reaction, which may be expected in terms of the half-life ($t_{1/2}$) or the relaxation time (τ) :

$$k = 0.693/t_{1/2} = 1/\tau\ , \qquad --- \quad 1.20$$

Depending on the half-life of a reaction, the experimental techniques may be classified into three groups:

(i) Static methods, ($t_{1/2}$ > 1 min.):

Static methods involve initiating the reaction by simply mixing the reactants together in a vessel in prearranged concentrations and conditions.

(ii) flow methods, (1 min > $t_{1/2}$ > 10^{-3} s):

For reactions with half-life as short as 0.001 s, flow methods may be used. In a flow system solutions of reactants can be mixed efficiently within a millisecond in a specially designed mixing chamber. The mixed reaction solution may then be treated in several ways and the course of the reaction followed by one of a variety of monitoring techniques.

In the stopped flow method,[39] the solution is abruptly stopped after mixing, and observation made using a detector at a point close to the mixer. The monitoring device must respond quickly to the rapid changes of concentration of species that occur in the stopped solution. The most commonly employed spectroscopic monitoring technique is the use of the ultraviolet and visible regions of the electromagnetic spectrum. Through the use of the spectroscopic stopped-flow methods, second-order rate constants of up to 10^7 $M^{-1}s^{-1}$ for redox reactions have been measured.

(iii) Relaxation methods, ($t_{1/2} < 10^{-3}$ s):

In the relaxation methods, a system at chemical equilibrium is perturbed by one of the several means and the adjustment of the system to a new equilibrium position is then monitored. The three most common methods of producing changes in the equilibrium of a chemical system are the temperature, the pressure jump and the electric field jump. A drawback of this method is that the system must be in equilibrium with K ~10^3 or less.

(b) The methods of monitoring the progress of a reaction:

The choice of a monitoring technique is dictated by the nature of the reaction, but in principle any property of the reactants or products that is related to their concentrations can be used. Spectroscopic methods such as uv-visible, i.r., EPR, proven methods like pH changes, ion specific electrodes, conductivity, and polarographic methods, are most commonly used, with the suitability of each depending on the sensitivity and response time for a particular reaction system.[40] Other methods like fluorescence quenching, polarimetric methods and isotopic exchange methods can also be used to monitor the progress of a reaction.

(i) Spectroscopic methods:

Almost all regions of the electromagnetic spectrum have been used in one kinetic study or another to follow the

progress of a chemical reaction. The use of the uv-visible region has been discussed in ref. 39. NMR and EPR methods will be discussed below:

(ii) NMR line broadening:

The determination of the rates for exchange processes by nmr broadening experiments has played an important role in the understanding of complex-ion reactions, a few of which are discussed below:

1) Exchange rate of methyl protons between two different chemical environments, for example,

$$Pt[P(OEt)_3]_4 + P(OEt)_3 \rightleftharpoons Pt[P(OEt)_3]_4 + P(OEt)_3. \quad -- \ 1.21$$

2) Exchange of multidentate ligands between the free and the complexed states. In these experiments, the broadening of the line is studied as a function of temperature and, depending on the rates of exchange, the spectra are divided into the slow-exchange region, the intermediate exchange region and the fast exchange region. These aspects have been discussed in ref. 39.

One of the important uses of nmr line broadening is in transition metal chemistry, where the nuclei examined can exist in two environments, one of which is close to a paramagnetic ion. The exchange of solvent between metal coordinated (paramagnetic) and free (bulk) solvent has been studied using this method. The subject of nuclear magnetic relaxation in electron transfer reactions has been rigorously

treated by Swift and Connick[41] and later by Johnston and Grant.[42] The effect of exchange of solvent between metal coordinated and free (bulk) solvent on the linewidth and resonance position of the diamagnetic D signal can be expressed as

$$\pi(W_A^E - W_A^\circ) = \frac{1}{T_2} - \frac{1}{T_{2A}} = \frac{P_M}{\tau_M}\left[\frac{\frac{1}{T_{2M}^2} + \frac{1}{\tau_M T_{2M}} + \Delta_{\omega M}^2}{\left(\frac{1}{T_{2M}} + \frac{1}{\tau_M}\right)^2 + \Delta_{\omega M}^2}\right] \quad \text{--- 1.22}$$

where, T_{2A}, T_2 are the transverse relaxation times for bulk solvent nuclei alone, and with solute (concentration [M]) respectively; T_{2M} is the relaxation time in the environment of the metal; τ_M is the average residence time of the solvent molecule in the metal coordination sphere; P_M is the mole fraction of the solvent that is coordinated to the metal; Δw_M is the chemical shift between the two environments and the subscripts A and M refer to the bulk and coordinated solvent respectively. Depending on the relative rates of chemical exchange and that of the relaxation mechanisms three regions can be identified in the plot of $(1/P_M)(1/T_2 - 1/T_{2A})$ *vs* T^{-1}, (Fig. 1.2.).

(a) If $\Delta w_M^2 >> T_{2M}^{-2}$, τ_M^{-2},

or $T_{2M}^{-2} >> \Delta w_{M-2}$, τ_M^{-2},

then from 1.20, $1/T_2 - 1/T_{2A} = P_M/\tau_M$. --- 1.23

This is the slow exchange region (II in Fig. 1.2.) and is most useful in obtaining kinetic data since the relaxation is

controlled by ligand exchange between bulk and coordinated ligand. A semi-log plot of $1/P_M(1/T_2 - 1/T_{2A})$ *vs* $1/T$, should give an Arrhenius type plot from which k_1 at any temperature can be directly determined. For example, in Fig. 1.2., at T = 25° C, $1/T = 3.36 \times 10^{-3}$, and $k_1 = 3 \times 10^3\ s^{-1}$. The above

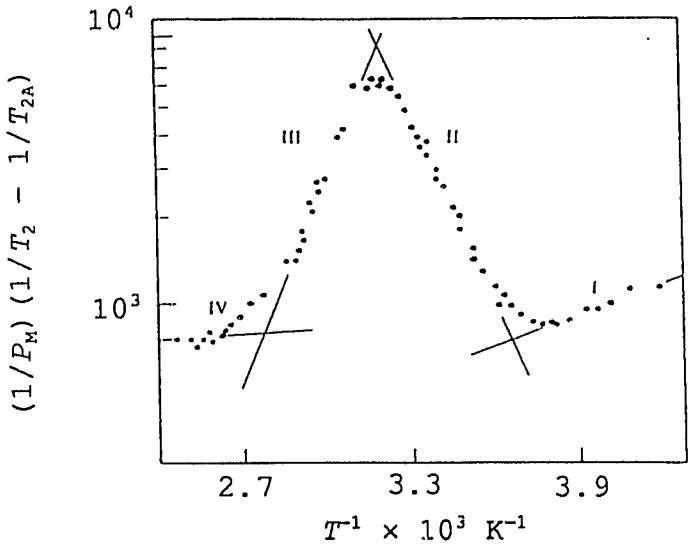

Fig. 1.2. Temperature dependence of $(1/P_M)(1/T_2 - 1/T_{2A})$ for protons in CH_3CN solutions of $Ni(CH_3CN)_6^{2+}$ at 56.4 MHz.

example deals with the study of solvent exchange. This method can be applied to the study of exchange between free ligand and ligand coordinated to a metal ion. It can also be used to determine directly the self-exchange rate in electron transfer reactions. For e.g. Smolenaers et al[43] have determined the self-exchange rate constant of the reaction 1.24 using ^1H nmr.

$$Ru(NH_3)_6^{2+} + Ru^*(NH_3)_6^{3+} == Ru(NH_3)_6^{3+} + Ru^*(NH_3)_6^{2+} \quad --1.24$$

Beattie et al[44] have also investigated the electron exchange reaction 1.25 using ^{13}C nmr.

$$Ru(en)_3^{2+} + Ru^*(en)_3^{3+} == Ru(en)_3^{3+} + Ru^*(en)_3^{2+} \quad -- 1.25$$

From equations 1.20 and 1.21, in the slow-exchange region

$$\pi(W_A^E - W_A^0) = (1/T_2 - 1/T_{2A}) = P_M/\tau_M, \quad \text{or,}$$

$$\pi(W_{DP} - W_D) = [Ru(III)]/\tau_M = k_{11}[Ru(III)]. \quad --- 1.26$$

where, W_D = full width at half maximum of the diamagnetic signal.

W_{DP} = fullwidth at half maximum in the presence of the paramagnetic species.

k_{11} = self-exchange rate constant.

[Ru(III)] = concentration of the paramagnetic species.

From a plot of W_{DP} *vs* [Ru(III)], (Fig. 1.3.), k_{11} can be determined.

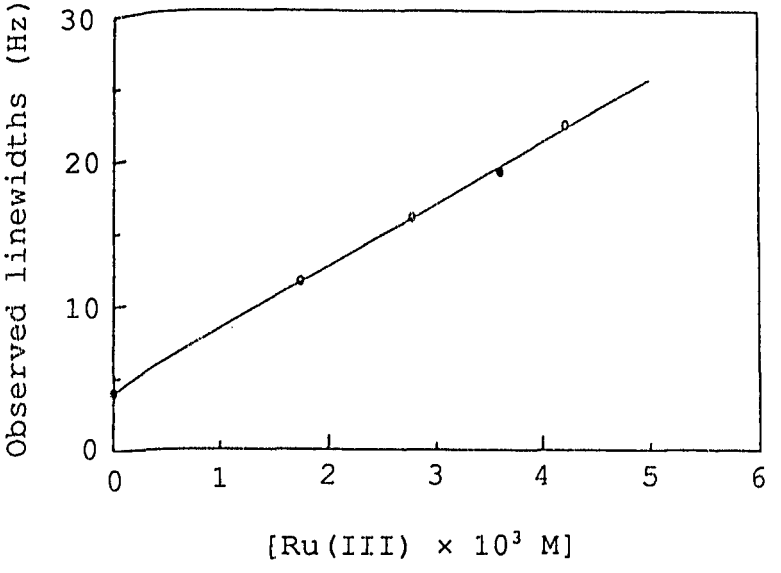

Fig. 1.3. Ru(II) linewidth dependence on [Ru(III)].

(iii) EPR line broadening:

This technique has been used for the study of the interaction of ligands with square planar complexes at the axial positions. Examples include the reaction of $VO(acac)_2$, (acac = acetyl acetonate) with pyridine and pyridine derivatives, and solvent exchange at the axial position of $VO(DMF)_5^{2+}$.[45]

EPR line broadening can be used for the study of electron transfer reactions by following the paramagnetic linewidth as a function of the concentration of the diamagnetic species and using equation 1.26 to determine directly the self-exchange rate constant. It can also be determined by monitoring the growth of the hyperfine splitting in the esr signal. This method has been used to measure the self-exchange rate for Ni(III)/Ni(II) $cyclam^{3+/2+}$.[46]

1.8.2. Marcus cross correlation:

One of the objects of studying the outer-sphere electron transfer reactions is to measure the self exchange rate constants for the redox couple. In section **1.8.1.** direct methods to determine the self exchange rate constant have been discussed. The self exchange rate constants can be calculated indirectly using the Marcus cross correlation equation,[47,48] given by:

$$k_{12} = (k_{11}k_{22}K_{12}f)^{1/2}, \quad \text{--- 1.27}$$

where, k_{12} is the rate of the cross reaction, *e.g.*,

$Fe(phen)_3^{2+} + Ru(phen)_3^{3+} \rightleftharpoons Fe(phen)_3^{3+} + Ru(phen)_3^{2+}$ - 1.28,

k_{11} and k_{22} are the self-exchange rates of the two components, *e.g.*,

$Fe(phen)_3^{3+} + Fe^*(phen)_3^{2+} \rightleftharpoons Fe(phen)_3^{2+} + Fe^*(phen)_3^{3+}$ - 1.29

$Ru(phen)_3^{2+} + Ru^*(phen)_3^{3+} \rightleftharpoons Ru(phen)_3^{3+} + Ru^*(phen)_3^{2+}$ - 1.30,

K_{12} is the equilibrium constant of the reaction 1.28, and the factor *f*, related to the collision frequency Z, is defined by,

$$\log f = (\log K_{12})^2\{(4 \log k_{11}k_{22}/Z^2)\}^{-1} \quad \text{--- 1.31,}$$

where $Z \sim 10^{11}\ M^{-1}s^{-1}$.

1.9. Objectives and achievements of the present investigations:

One of the objectives of the present investigations was to study the ligating abilities of homoleptic and heteroleptic macrocyclic ligands containing N and S donor atoms. The other aim was to synthesise novel macrocyclic ligands and their transition metal complexes that would serve as one electron outer sphere reagents in electron transfer reactions. One of the requirements of an outer-sphere electron transfer reagent is that the ligand imposes identical geometry on both oxidation states concerned, so that the electron transfer is accompanied by a minimum reorganization. In addition the ligand should effectively block all the coordination sites of the metal centre so that there will be no inner-sphere electron transfer paths. The bis complexes of the ligand [9]-aneN_3, **22**, are well suited for the study of outer-sphere

constants for the $\{Ni([9]\text{-}aneN_3)_2\}^{3+/2+}$ couples have been studied.[49] However, in the bis metal complexes, the nine-membered ring is not large enough for the axial donor atom to reach over and occupy the apical position. In other words, the nine-membered ring "perches". This prompted the present investigations of the ten-membered ring systems.

The ten-membered ligands, **23**, **24**, **25**, were successfully synthesised. In addition a novel macrobicyclic ligand, **26**, was also synthesised.

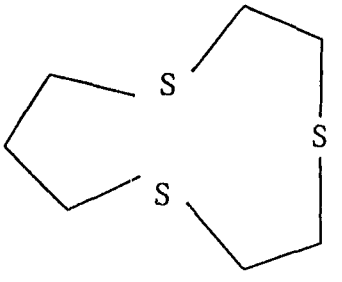

23

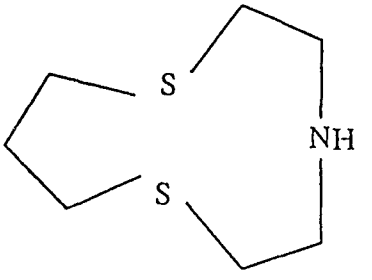

24

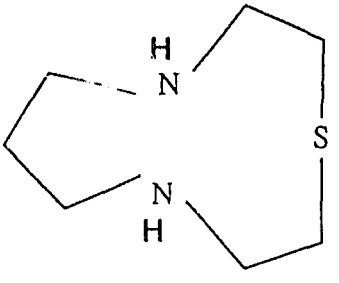

25

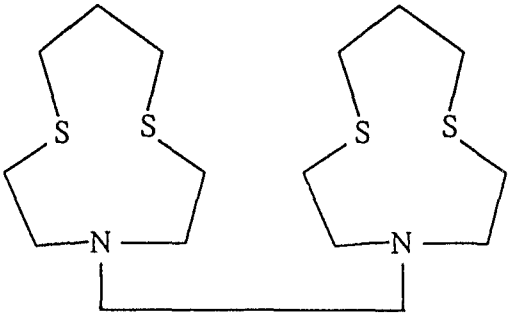

26

In Chapter 3, the syntheses of the transition metal complexes of hexaazamacrocyclic ligands are discusssed. Crystal structures of the chromium(III) complexes of [18]-aneN_6, **27**, and [20]-aneN_6, **28**, are compared. UV-visible and ESR spectroscopic studies have been carried out. The electrochemical properties have been studied using cyclic voltammetry.

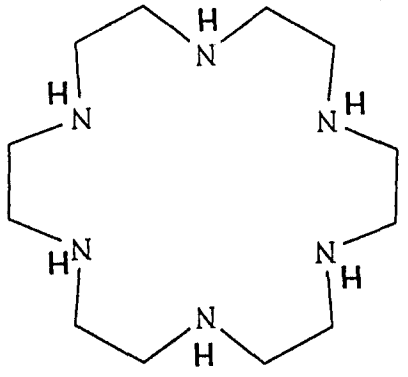

27

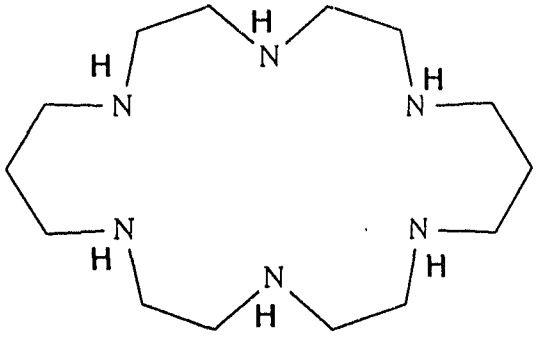

28

The syntheses of the ligand [10]-aneS_2NH, **24**, and its Ni and Pd complexes are discussed in Chapter 4. ^{1}H and ^{13}C nmr spectroscopy, and X-ray crystallography, have been used to study the complexes in the solid state and in solution. ESR spectroscopy has been used to study the corresponding Ni(III) and Pd(III) complexes.

Synthesis and characterization of the novel macrobicyclic ligand, **26**, and its nickel complex are discussed in Chapter 5.

In Chapter 6, synthesis and characterization of Fe, Co, Ni, and Pd complexes of the ligand [10]-aneS_3, **23**, are discussed. ESR and NMR spectroscopic investigations and electrochemical properties of the Fe, Co, Ni, and Pd complexes in various oxidation states have been studied. ^{1}H and ^{59}Co nmr line broadening methods have been used to determine directly the self-exchange rate constants for the Fe(III)/(II) and the Co(III)/Co(II) complexes respectively.

In Chapter 7, the synthesis of [10]-aneSN_2, **25**, and the crystal structure of its Ni complex are discussed and the scope for further research is explored.

CHAPTER 2

EXPERIMENTAL METHODS

2.1. SYNTHESIS OF LIGANDS AND TRANSITION METAL COMPLEXES:

2.1.1. Synthesis of 1,4,7,10,13,16-hexaazacyclooctadecane, ([18]-aneN$_6$), 27:

The ligand [18]aneN$_6$.3H$_2$SO$_4$ used was supplied by Aldrich Chemical Co.. The trisulfate salt was dissolved in water and made basic (pH ~ 13) with sodium hydroxide solution. The free ligand was obtained as a colorless solid by continuously extracting the aqueous solution with chloroform.

2.1.2. Synthesis of a complex of [18]-aneN$_6$: [Cr([18]-aneN$_6$)]Br$_3$, 29 :

CrCl$_3$.6H$_2$O (0.124g, 0.5 mmol) was dissolved in 10 mL dmso at 190 °C. The volume of the solution was reduced to about 5 mL. A 0.5 mmol (0.134g) solution of the ligand in ethanol (5 mL) was added to the metal containing solution at 60 °C. The temperature was raised slowly to 170 °C during which time a yellow precipitate formed. Stirring was continued for 0.5 hours at 170 °C. The yellow solid was then filtered off and washed with small amounts of ethanol and ether. This was air-dried and then dissolved in water (~4 mL) at 50 °C. A saturated solution of sodium bromide (2 mL) was added. Yellow-orange crystals suitable for crystal structure determination were obtained on slow evaporation. The crystals were filtered off and dried under vacuum.

Yield 0.28 g; 70%.

Analysis for $C_{12}H_{30}N_6CrBr_3$:

Calcd. : C, 26.19; H, 5.49; N, 15.27.

Found : C, 26.23; H, 5.45; N, 15.29.

2.1.3. Synthesis of 1,4,7,11,14,17-hexaazacycloeicosane, [20]-aneN$_6$, 28:

The ligand 1,4,7,11,14,17-hexaazacycloeicosane was synthesised by previously adopted procedures[50,51]. The synthetic route is outlined in Scheme 2.1. The ligand was characterised by mass spectrometry and ^1H and ^{13}C nmr spectroscopy.

2.1.4. Syntheses of complexes of [20]-aneN$_6$:

a) [Cr([20]-aneN$_6$)]Br$_3$.H$_2$O, 30:

$CrCl_3.6H_2O$ (0.6g, 2.2 mmol) was dissolved in 10 mL dmso at 190 °C. The volume of the solution was reduced to about 8 mL by evaporation at 190 °C. The ligand, (2.2 mmol; 0.64g) in ethanol (5 mL) was added to the metal-ion solution with stirring at 60 °C. The temperature was raised slowly to 170 °C. The yellow solid was then filtered off and washed with small amounts of ethanol and ether. This was then dissolved in a saturated aqueous solution of NaBr. Yellow crystals of $[Cr([20]aneN_6)]Br_3.H_2O$ suitable for crystal structure determination were obtained upon slow evaporation.

Yield : 0.9 g; 66%.

Analysis for $C_{14}H_{34}N_6CrBr_3.H_2O$:

Scheme 2.1. Synthetic route to 28.

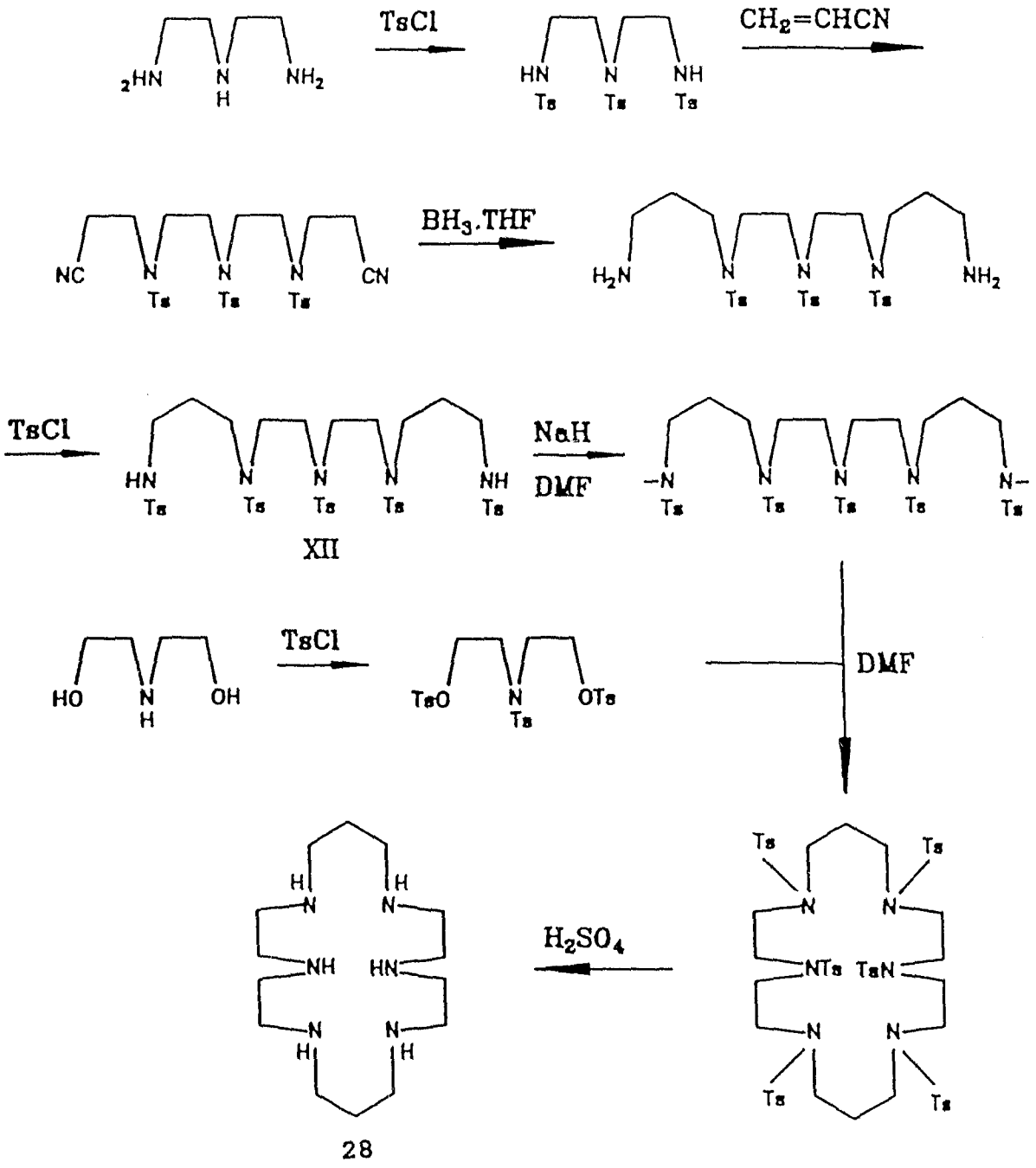

Calcd. : C, 28.33; H, 6.11; N, 14.17.

Found : C, 28.29; H, 6.02; N, 14.11.

b) $[Cu([20]\text{-}aneN_6)](ClO_4)_2$, 31:

The ligand [20]-$aneN_6$ (0.35g, 1.2 mmol) was dissolved in methanol (10 mL) at 50 °C. To this solution, $Cu(ClO_4)_2.6H_2O$ (0.37g; 0.98 mmol) in methanol (10 mL) at 50 °C was added under stirring. A blue precipitate was formed immediately. The solution was stirred for 30 minutes after which time the blue solid was filtered off and dried under vacuum. This was recrystallised from an acetonitrile solution containing sodium perchlorate.

Yield 0.41 g; 71%.

Analysis for $C_{14}H_{34}N_6CuCl_2O_8$:

Calcd. : C, 30.63; H, 6.24; N, 15.31; Cl, 12.91.

found : C, 30.92; H, 6.18; N, 15.38; Cl, 12.82.

c) $[Mn_2([20]\text{-}aneN_6)Cl_4]$, 32:

$MnCl_2.4H_2O$ (0.197g, 1 mmol) was dissolved in 5 mL of dry methanol. The solution was heated at 60 °C under an argon atmosphere. A solution of [20]-$aneN_6$ (0.286 g, 1 mmol) dissolved in 5 mL of ethanol was added slowly to the above solution. A colorless precipitate was obtained which was filtered under vacuum. This was washed with small amounts of methanol and ether and dried under vacuum.

Yield : 350 mg; 65 %.

Analysis for $Mn_2Cl_4C_{14}H_{34}N_6$:

Calcd. : C, 31.24; H, 6.36; N, 15.61.

Found : C, 31.38; H, 6.23; N, 15.56.

d) [Mn([20]-aneN$_6$)](PF$_6$)$_2$.NaPF$_6$.2H$_2$O, 33:

To an aqueous solution of the dimer, **32**, (100 mg) was added a saturated solution of $NaPF_6$. A colorless precipitate was obtained which was filtered off, washed with ethanol and ether and dried under vacuum.

Yield : 45 mg; 38 %.

Analysis for $C_{14}N_6H_{34}MnP_2F_{12}.NaPF_6.2H_2O$:

Calcd. : C, 19.91; H, 4.27; N, 9.94.

Found : C, 19.91; H, 4.27; N, 9.94.

2.1.5. Synthesis of 4,8-diaza-1-thiacyclodecane, ([10]-aneSN$_2$), 25:

The ligand [10]-aneSN$_2$ was synthesised by non-template methods using a modification of the Richman and Atkins method.[31] The synthetic route is outlined in Scheme 2.2.

a) 2-(p-toluenesulfonylamino)ethyl-p-toluenesulfonate, 34:

The compound **34** was synthesised by a modification of the procedure of Hope and Horncastle.[52] To a stirred suspension

Scheme 2.2. Synthetic route to **25**.

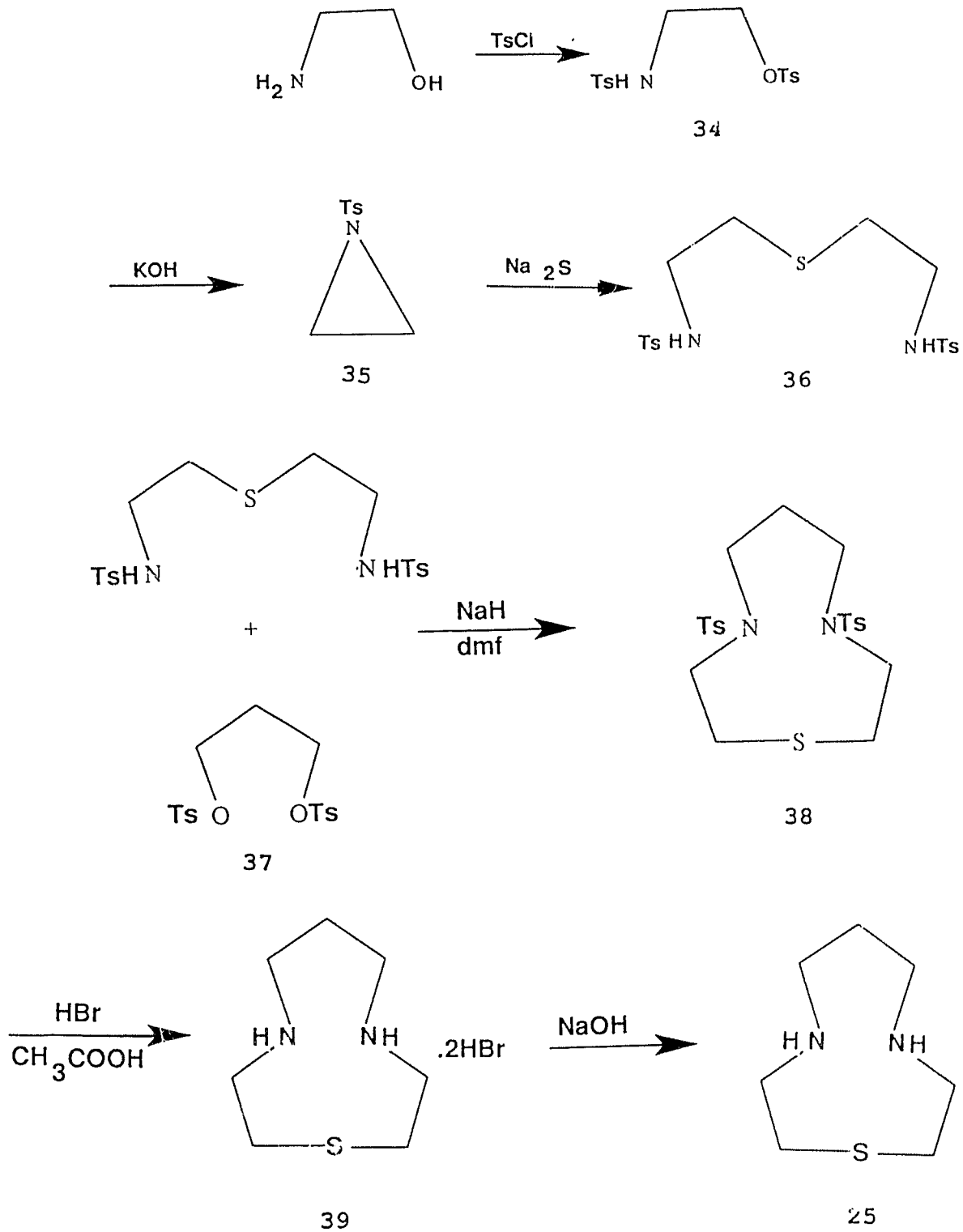

of TsCl (802.6 g, 4.2 mol) in pyridine (500 mL), cooled to -40 °C, was added dropwise a solution of 2-aminoethanol (122.2 g, 2 mol) in pyridine (200 mL) (cooled to 0 °C). After the addition was complete, the temperature was maintained at -10 °C for 2 h and overnight at 0 °C. Crushed ice was added, the solid which had formed was filtered, washed with water and dissolved in $CHCl_3$ (1 L). This solution was washed thrice with water, dried over anhydrous Na_2SO_4 and taken to dryness. The solid obtained was dissolved in a minimum of boiling CCl_4 and the compound crystallised upon cooling.

Yield : 517 g; 70 %.

m.p. : 87 °C.

^1H nmr ($CDCl_3$) : δ 7.6 (dd, 8H), 5.3 (t, 1H), 4.0 (t, 2H), 3.2 (m, 2H), 2.4 (s, 6H).

b) N-(p-toluenesufonyl)aziridine, 35:

N-(p-toluenesulfonyl)aziridine, also known as N-tosylaziridine, was synthesised by published procedures.[50] To a vigorously stirred mixture of compound **34** (130 g, 0.35 mmol) in toluene (1.2 L) was added a solution of KOH (89 g, 1.6 mol) in water (500 mL) over 1 h period. The two-phase mixture was stirred vigorously for another 2 h and the organic layer was separated using a separating funnel. The organic layer was washed thrice with water, dried over anhydrous Na_2SO_4 and evaporated to a small volume (50 mL) whereupon crystals of

the compound **35** were obtained upon standing. The crystalline solid was filtered and washed with a minimum of water and diethylether and dried under vacuum.

Yield : 57.5 g; 83 %.

m.p. : 63 °C.

^{1}H nmr ($CDCl_3$) : δ 7.6 (dd, 4H), 2.4 (s, 4H), 2.3 (s, 3H).

ms(CI) : 198 (M+1), 226 (M+29).

c) N,N'-di(p-toluenesulfonyl)bis(2-aminoethyl)sulphide, 36:

N-tosylaziridine, **35**, (53 g, 0.3 mol) was added in small portions to an aqueous ethanolic solution of 33.3 g (0.14 mol) $Na_2S.9H_2O$ (500 mL EtOH, 150 mL water). The mixture was refluxed for three hours. The solution was then evaporated to a small volume (75 mL) and made acidic (pH ~ 1) with aqueous HCl. This solution was extracted thrice with CH_2Cl_2 (200 mL) and then dried over anhydrous Na_2SO_4. The CH_2Cl_2 layer was evaporated to dryness to yield compound **36** as a crude solid. This was dissolved in boiling ethanol and upon cooling crystals of compound **36** were obtained.

Yield : 40.3 g; 70 %.

m.p. : 111 °C

^{1}H nmr ($CDCl_3$) : δ 2.39 (s, 6H, CH_3), 2.51 (t, *J* 6 Hz, 4H, CH_2-S), 3.03 (q, *J* 6 Hz, 4H, CH_2-N), 5.27 (t, *J* 6 Hz, 2H, -NH), 7.2 - 7.7 (m, 8H, Ar).

^{13}C nmr ($CDCl_3$) : δ 21.5 (2C, CH_3), 31.7 (2C, CH_2-S), 42.2 (2C,

CH_2-N), 127.0 and 129.8 (4C + 4C, Ar), 136.8 and 143.6 (2C + 2C, quat., Ar).

ms(CI) : 429 (M+1), 457 (M+29), 469 (M+41).

Analysis for $C_{18}H_{24}S_3O_4N_2$:

Calcd. : C, 50.44; H, 5.64; N, 6.53.

Found : C, 50.25; H, 5.61; N, 6.40.

d) 1,3-di[(p-toluenesulfonyl)oxy]propane, ($TsOCH_2CH_2CH_2OTs$), 37:

This was prepared by a modification of Nelson's method.[53] 15.2 g (0.2 mol) of propane-1,3-diol was dissolved in 1 L of CH_2Cl_2 contained in a 2-neck 2 L flask. The solution was cooled under a stream of dry N_2 to 0 °C and 100 mL of triethylamine was added through a dropping funnel. Solid p-toluenesulfonylchloride (114.0 g, 0.6 mol) was added in small portions over a period of 1 h. The mixture was stirred at 0° C under a stream of dry N_2 for 8 h. The solution was left to stir for another 8 hours whilst it equilibrated to room temperature. The triethyl ammonium chloride formed in the reaction was filtered off. The filtrate was washed twice with 200 mL of 2 M HCl and then twice with 200 mL distilled water and finally with 250 mL of saturated Na_2CO_3 solution. The CH_2Cl_2 layer was dried over anhydrous sodium sulfate. The solvent was evaporated off leaving a colorless crystalline product.

Yield : 61.5 g; 80 %.

m.p. : 91 °C.

^{13}C nmr : δ 21.6 (2C, $\underline{C}H_3$), 28.7 (1C, C-$\underline{C}$-C), 66.0 (2C, $\underline{C}$-C-$\underline{C}$), 128.1 and 130.1 (4C, Ar), 132.9 and 145.3 (2C + 2C, quat, Ar).

e) 4,8-di(p-toluenesulfonyl)-4,8-diaza-1-thiacyclodecane, 38:

Sodium hydride (0.2 mmol, 8.3 g of 60% dispersion in oil) was added to a vigorously stirred solution of **36** (35.5 g, 0.08 mol) in dmf (600 mL) to form the disodium salt. The solution was slowly heated to 70 °C, after the main effervescence, and stirring was continued for three hours. The solution was then stirred at 105 °C and a solution of $TsOCH_2CH_2CH_2OTs$ (31.87 g, 0.083 mol), **37**, in dmf (500 mL) was added over 2 h. The yellow solution formed was stirred at 105 °C for a further 2 h. The dmf solution was concentrated to a small volume (~ 200 mL) and added dropwise to a stirred mixture of ice/water (2 L). The colorless precipitate obtained was filtered off, washed with water, cold ethanol and ether and dried under vacuum. The solid was recrystallised from boiling ethanol.

Yield 27.5 g; 70%.

m.p. : 286 °C.

^1H nmr : δ 2.37 (p, 2H, CH_2), 2.39 (s, 6H, CH_3), 3.03 (m, 4H, CH_2-S), 3.07 (t, 4H, N-$\underline{CH_2}CH_2\underline{CH_2}$-N), 3.29 (m, 4H, CH_2-N), 7.28 - 7.65 (m, 8H,Ar).

^{13}C nmr : δ 21.4 (2C, $\underline{C}H_3$), 28.6 (1C, $-CH_2-\underline{C}H_2-CH_2-$), 31.0 (2C, $\underline{C}H_2-S$), 47.4 (2C, $N-\underline{C}H_2-CH_2-\underline{C}H_2-N$), 54.1 (2C, $\underline{C}H_2-N$), 127.6 and 129.7 (4C + 4C, Ar), 133.1 and 143.7 (2C + 2C, quat. Ar).

ms (CI) : 469 (M+1), 497 (M+29).

Analysis for $C_{21}H_{28}N_2S_3O_4$:

Calcd. : C, 53.82; H, 6.02; N, 5.97; S, 20.52; O, 13.65.

Found : C, 54.05; H, 5.91; N, 5.96.

f) 4,8-diaza-1-thiacyclodecane dihydrobromide, 39:

The cyclised tosylate **38** (7 g, 0.015 mol) was added to a solution of 30% HBr in acetic acid (250 mL) and phenol (10 g). The solution was heated under reflux for three days after which it was cooled to room temperature. This solution was added dropwise to a continuously stirred solution of diethyl ether and ethanol (350 mL; 6:1 v/v). A white-brown solid, **39**, was obtained.

This solid was dissolved in a minimum amount of 40% HBr solution and filtered. Ethanol was added dropwise until a solid started to form. The solution was refrigerated overnight. The colorless solid, **39**, obtained was filtered and washed with small amounts of ethanol and ether and dried under vacuum.

Yield : 2.21 g; 46%, based on compound **38**.

^1H nmr : δ 2.19 (p, 2H, $C-C\underline{H}_2-C$), 3.06 (m, 4H, $C\underline{H}_2-S$), 3.30 (m,

4H, $C\underline{H}_2$-C-$C\underline{H}_2$), 3.47 (t, 4H, $C\underline{H}_2$-N).

^{13}C nmr : δ 21.8 (1C, C-$\underline{C}$-C), 29.2 (2C, $\underline{C}H_2$-S), 42.6 (2C, N-$\underline{C}$-C-$\underline{C}$-N), 44.6 (2C, $\underline{C}H_2$-N).

g) 4,8-diaza-1-thiacyclodecane, 25:

Compound **39** (2.21 g) was dissolved in water (50 mL) and made basic (pH ~ 13) with aqueous NaOH. This aqueous solution was continuously extracted with $CHCl_3$ for a day. The $CHCl_3$ layer was dried over anhydrous Na_2SO_4 and evaporated to dryness leaving behind a pale yellow oil of the free ligand, **25**.

Yield : 1.3 g; 85%.

^{1}H nmr : δ 1.6 (m, 2H, C-$C\underline{H}_2$-C), 2.6 - 2.8 (m, 12H), 3.4 (s, 1H, -N$\underline{H}$).

^{13}C nmr : δ 26.4 (1C, C-$\underline{C}$-C), 34.3 (2C, $\underline{C}H_2$-S), 47.6 (2C, $\underline{C}$-C-$\underline{C}$), 49.4 (2C, $\underline{C}H_2$-N).

ms (CI) : 161 (M+1), 189 (M+29), 201 (M+41).

Another route to synthesise the ligand **25** is outlined in Scheme 2.3.:

Scheme 2.3. Synthetic route to **25**.

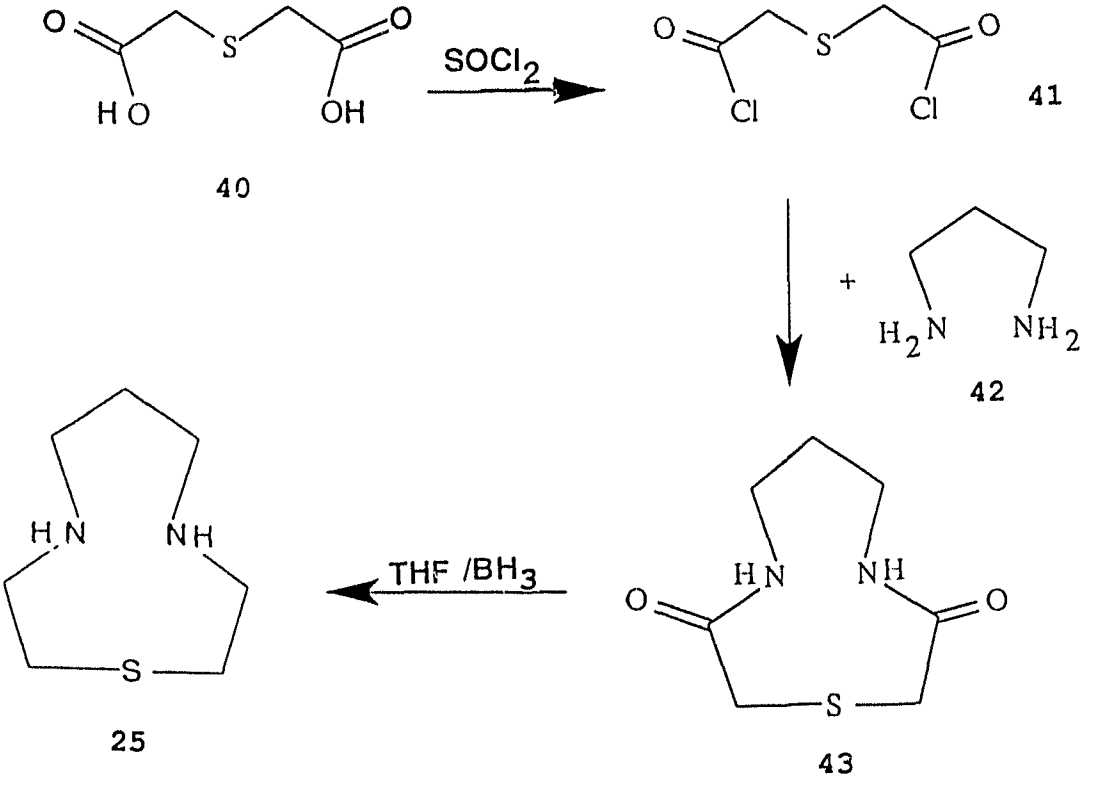

2.1.6. Synthesis of complex of ([10]-aneSN$_2$): [Ni([10]-aneSN$_2$)$_2$]Br$_2$.2H$_2$O, 44:

The free ligand, **25**, (0.5 g, 3.1 mmol) was dissolved in 50 mL EtOH and heated to 50 °C while stirring. A solution containing $Ni(ClO_4)_2.6H_2O$ (0.366g, 1 mmol) dissolved in 10 mL EtOH, was added dropwise to the ethanolic solution of the ligand and was refluxed for 1 h. The brown-purple solid obtained was filtered and recrystallised from ethanol/water mixture (10 mL, 9:1, v/v) containing NaBr. Upon cooling, purple crystals were obtained (suitable for X-ray diffraction studies) which were filtered off, washed with small amounts of

ethanol and ether and dried under vacuum.

Yield : 324 mg; 60 %.

Analysis for $NiC_{14}H_{32}N_4S_2Br_2.2H_2O$:

Calcd. : C, 29.20; H, 6.31; N, 9.74; Br, 27.79.

Found : C, 29.30; H, 6.06; N, 9.67; Br, 28.00.

2.1.7. Synthesis of 8-aza-1,5-dithiacyclodecane, ([10]-aneS$_2$N), 24:

The ligand **24** was synthesised according to the route outlined in Scheme 2.4.

Scheme 2.4. Synthetic route to **24**.

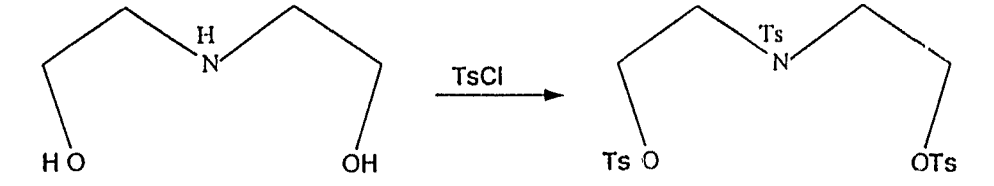

45

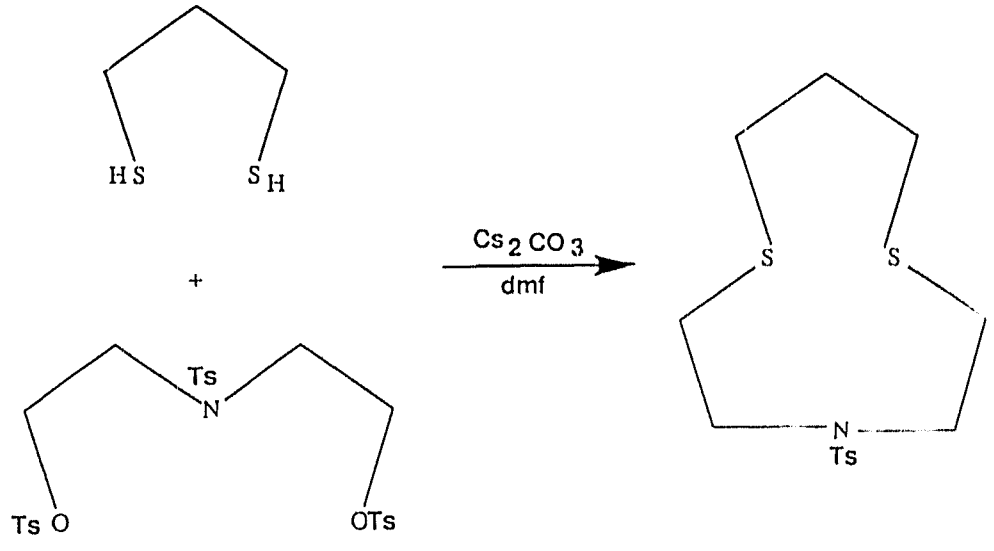

46

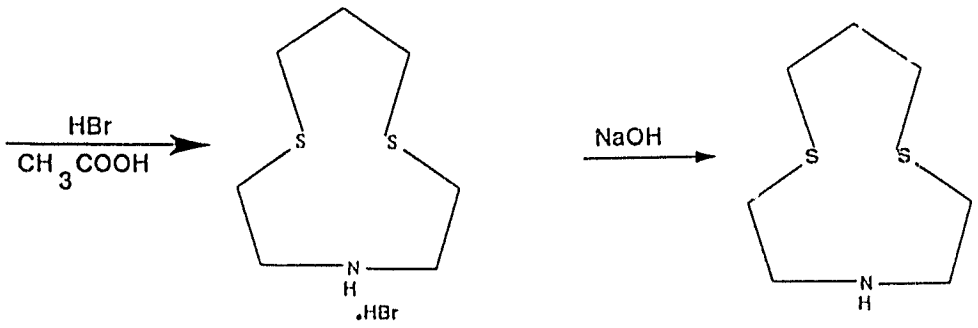

47 24

a) **2,2'-(p-toluenesulfonylimino)bis-ethyldi(p-toluenesulphonate), NTs(CH_2CH_2OTs)$_2$, 45:**

This compound was synthesised as described previously.[54]

b) **8-(p-toluenesulfonyl)-8-aza-1,5-dithiacyclodecane, 46:**

A dry, 5 L, three-necked, round bottom flask was equipped with a 500 mL additional funnel, a reflux condenser and a mechanical stirrer with a 7-cm Teflon blade. The entire system was kept under a positive pressure of dry nitrogen. The flask was charged with 2.2 L of dmf, and 13.04 g (40 mmol) of cesium carbonate (oven-dried at 150 °C overnight). The mixture was stirred vigorously and heated to 55 - 60 °C. A solution containing a mixture of 1,3-propanedithiol, 4.32 g, (40 mmol) and compound, **45**, 22.7 g, (40 mmol) in 600 mL dmf was prepared. Half of this mixture was added through the additional funnel over a period of 8 h. The reaction mixture was then charged with another portion of 13.04 g (40 mmol) of cesium carbonate and the second half of the solution mixture was added over a period of 8 h. The solution was stirred at

60 °C for a further 6 h, and then filtered. The filtrate was reduced to a small volume (100 mL). The resultant solution was added dropwise to a vigorously stirred mixture of ice/water mixture (2 L). The colorless solid obtained was filtered off and dried under vacuum. The solid was recrystallised from boiling ethanol to give colorless crystals of the compound, **46**.

TLC : One spot.

Yield : 8.6 g; 65 %.

m.p. : 138 °C.

^{1}H nmr : δ 1.88 (p, 2H, C-C$\underline{H_2}$-C), 2.40 (s, 3H, -C$\underline{H_3}$), 3.06 (m, 4H, -C$\underline{H_2}$-N), 3.15 (m, 8H, -C$\underline{H_2}$-S), 7.24 - 7.67 (m, 4Ar).

^{13}C nmr : δ 21.5 (1C, CH_3), 29.5 (1C, C-$\underline{C}$-C), 31.3 (2C, $\underline{C}$-C-$\underline{C}$), 33.8 (2C, CH_2-S), 53.2 (2C, $\underline{C}H_2$-N), 127.7 and 129.7 (2C + 2C, Ar), 133.8 and 143.7 (1C + 1C, Ar).

ms(CI) : 332 (M+1), 360 (M+29), 372 (M+42).

c) 8-aza-1,5-dithiacyclodecane, 24:

The cyclised tosylate **46**, 2.6 g (7.9 mmol) was added to a solution of 30% HBr in acetic acid (30 mL) containing phenol (3.0 g) and the solution was stirred at 70 °C for 30 h. The solution was cooled to room temperature and added dropwise to a stirred mixture of ether/ethanol (300 mL, 5:1, v/v) cooled in an ice bath. A colorless solid **47** was obtained which was

filtered off and washed with ether and dried under vacuum.

Yield : 1.2 g; 59 %.

^{1}H nmr : δ 1.73 (m, 2H, C-C$\underline{H_2}$-C), 2.85 - 2.95 (m, 8H, C$\underline{H_2}$-S), 3.42 - 3.47 (m, 4H, C$\underline{H_2}$-N).

^{13}C nmr : δ 25.6 (1C, C-$\underline{C}$-C), 29.8 (2C, $\underline{C}$-C-$\underline{C}$), 30.7 (2C, $\underline{C}H_2$-S), 46.0 (2C, $\underline{C}H_2$-N).

Analysis for $C_7H_{15}S_2N.HBr.H_2O$:

Calcd. : C, 30.41; H, 5.84; N, 5.07.

Found : C, 30.15; H, 5.81; N, 5.04.

The hydrobromide salt **47** (1.1 g, 4.3 mmol) was dissolved in water and made basic (pH ~ 13) with concentrated NaOH solution. This was continuously extracted with $CHCl_3$ overnight. The $CHCl_3$ layer was dried over anhydrous Na_2SO_4 and evaporated to dryness, leaving behind a colorless sticky solid of the free ligand **24**.

Yield : 0.7 g; 93 %.

^{1}H nmr : δ 1.63 (p, 2H, C-C$\underline{H_2}$-C), 2.55 (t, 4H, C$\underline{H_2}$-N), 2.83 (t, 8H, C$\underline{H_2}$-S-C$\underline{H_2}$), 3.68 (s, 1H, -N$\underline{H}$).

^{13}C nmr : δ 28.4 (1C, C-$\underline{C}$-C), 29.7 (2C, $\underline{C}$-C-$\underline{C}$), 33.6 (2C, $\underline{C}H_2$-S), 48.7 (2C, $\underline{C}H_2$-N).

ms(CI) : 178 (M+1), 206 (M+1), 218 (M+41).

2.1.8. Syntheses of complexes of ([10]-aneS$_2$N), 24:

a) [Ni(24)$_2$].(ClO$_4$)$_2$, 48:

An ethanolic solution (20 mL) of Ni(ClO$_4$)$_2$.6H$_2$O (280 mg, 0.77 mmol) was added dropwise to an ethanolic solution (50 mL) of the ligand **24** (300 mg, 1.7 mmol). The solution was refluxed for 1 h. The red-purple solid obtained was dried under vacuum. Diffusion of ether into acetonitrile solutions of the solid yielded violet crystals (suitable for X-ray diffraction studies) which were filtered, washed with small amounts of ethanol and ether and dried under vacuum.

Yield : 0.312 g; 51 %.

Analysis $NiC_{14}H_{30}S_4N_2Cl_2O_8$:

Calcd. : C, 27.46; H, 4.93; N, 4.57.

Found : C, 27.49; H, 4.69; N, 4.66.

b) [Pd(24)$_2$](PF$_6$)$_2$, 49:

A solution of the ligand **24** (173.5 mg, 0.98 mmol) in acetonitrile (25 mL) was added to a stirred suspension of Pd(OAc)$_2$ (100.0 mg, 0.45 mmol) in acetonitrile (20 mL). The solution was refluxed for 1 h. The color of the solution changed from orange to red-brown. A saturated solution of NH_4PF_6 in CH_3CN was then added. The solution was taken to a small volume and ether (5 mL) was added. A red solid was obtained which was filtered off and dried under vacuum.

Yield : 0.150 g; 44 %.

A small amount of this solid was dissolved in nitromethane (5 mL). Diffusion of ether yielded tiny purple crystals after three days, suitable for X-ray diffraction studies. The crystals were very sensitive to solvent loss. Some of these crystals were dried under vacuum.

Analysis calculated for $PdC_{14}H_{30}S_4N_2P_2F_{12}$:

Calcd. : C, 22.39; H, 4.02; N, 3.73.

Found : C, 22.38; H, 4.02; N, 3.74.

2.1.9. Synthesis of 1,4-bis(1-aza-4,8-dithia-4-cyclodecyl)ethane, 26:

Synthesis of the ligand **26** is given in Scheme 2.5.

Scheme 2.5. Synthetic route to **26**.

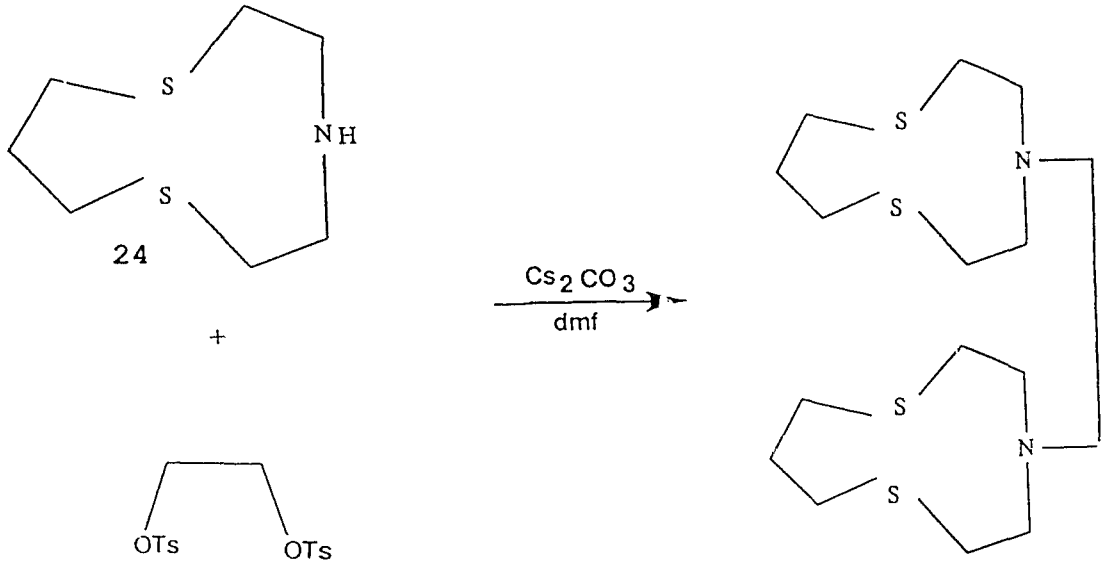

a) 1,2-di(p-toluenesulfonyloxy)ethane, 50:

Compound **50** was prepared as described in section **2.1.5(d)**, excepting that ethane-1,2-diol was used instead of propane-1,3-diol.

b) Ligand 26:

To a mechanically stirred suspension of Cs_2CO_3 (4.89 g, 15 mmol) in N,N'-dimethylformamide (75 mL) (freshly opened bottle) was added a solution of the ligand **24**, (1.77 g, 0.01 mol) in 25 mL dmf. The mixture was stirred vigorously at 80 °C for 4 h. A solution of **50**, (2.96 g, 8 mmol) in 50mL dmf was added over 1 h. The mixture was stirred for another 24 h at 100 °C. The dmf solution was filtered and taken to dryness on a rotary evaporator. The residue was dissolved in distilled dichloromethane (100 mL) and the CH_2Cl_2 layer was washed with saturated Na_2CO_3 solution and then thrice with water (200 mL). The CH_2Cl_2 layer was dried over anhydrous Na_2SO_4 and then taken to dryness leaving behind a pale yellow oil of the free ligand **26**.

Crude yield : 1 g; 53%.

Additional resonances were obtained in the ^1H and ^{13}C nmr and were attributed to the presence of 8-10% of the starting material. The crude ligand (1 g; 2.6 mmol) was dissolved in ethanol (50 mL) and its Ni complex prepared as described in section **2.1.10**. The violet band that was eluted with 0.05 M $NaClO_4$ was evaporated to dryness and dissolved in 25 mL of

ethanol. After filtering the residue, sodium perchlorate, the ethanolic solution was taken to dryness yielding a purple solid, of the Ni complex **51**.

Yield : 0.77 g; 51%.

This Ni complex, **51**, (500 mg) was dissolved in water (200 mL) and heated to reflux. A solution of NaCN (1 g; 20 mmol) in water (200 mL) was added slowly. The solution became turbid and a colorless solid began to separate out. The solution was refluxed for 4 h at which point the solution was no longer pink and was of a pale yellow color. The colorless solid obtained was filtered, washed with water (20 mL) and dissolved in dichloromethane. The CH_2Cl_2 layer was dried with anhydrous Na_2SO_4 and then evaporated to dryness yielding the pure ligand as a colorless solid. This was then dried under vacuum.

Yield : 0.13 g; 40 %.

Analysis for $C_{16}H_{32}S_4N_2.CH_2Cl_2$:

Calcd. : C, 46.38; H, 7.36; N, 6.01.

Found : C, 46.16; H, 7.37; N, 6.35.

^{1}H nmr : δ 1.86 (p, 4H, C-C$\underline{H_2}$-C), 2.63 (s, 4H, N-C$\underline{H_2}$-C$\underline{H_2}$-N), 2.67 (m, 8H, S-C$\underline{H_2}$-C-C$\underline{H_2}$-S), 2.74 (m, 8H, S-C$\underline{H_2}$-CH$_2$-N), 3.14 (t, 8H, S-CH$_2$-C$\underline{H_2}$-N).

^{13}C nmr : δ 30.3 (2C, C-$\underline{C}$-C), 30.8 (4C, S-$\underline{C}$-C-$\underline{C}$-S), 33.2 (4C, S-$\underline{C}$-C-N), 52.0 (2C, N-$\underline{C}$-$\underline{C}$-N), 57.1 (4C, S-C-$\underline{C}$-N).

2.1.10. Synthesis of metal complex of 26:

[Ni(26)]$(ClO_4)_2.2CH_3CN.H_2O$, 51:

The ligand **26**, (500 mg, 1.3 mmol) was dissolved in 50 mL ethanol and the solution was heated to 40 °C. Any insoluble residue was filtered off. A solution of $Ni(ClO_4)_2.6H_2O$ (293 mg, 2.7 mmol) in 20 mL EtOH was added dropwise to the ethanolic solution of the ligand. The solution was refluxed for 1 h. A red solid was obtained at the bottom of the flask with purple crystals on the sides of the flask. The solid was filtered and dissolved in a minimum quantity of water. This was loaded on to a C-25 Sephadex column. A violet and a green band separated upon using 0.05 M $NaClO_4$. The violet band was eluted using 0.05 M $NaClO_4$. The aqueous solution was taken to dryness and dissolved in a minimum quantity of ethanol. Sodium perchlorate crystals were filtered off. Purple crystals of **51** were obtained by slow evaporation of the ethanolic solution of the complex. These were filtered off and washed with small amounts of ethanol and ether and dried under vacuum. Diffraction quality crystals were grown by diffusion of ether into acetonitrile solutions of the complex.

Yield : 0.57 g; 60%.

I.R. : -NH band at 3280 cm^{-1} absent.

Analysis $NiC_{16}H_{32}S_4N_2Cl_2O_8.2CH_3CN.H_2O$:

Calcd. : C, 32.52; H, 5.46; N, 7.59.

Found : C, 32.74; H, 5.17; N, 7.40.

2.1.11. Synthesis of 1,4,7-trithiacyclodecane, ([10]-aneS$_3$), 23:

The synthetic route to ligand **23** is shown in Scheme 2.6. The cyclisation between the dithiol and 1,3-dibromopropane was carried out in DMF containing Cs_2CO_3 according to the methods of Buter and Kellogg.[33]

Scheme 2.6. Synthetic route to **23**.

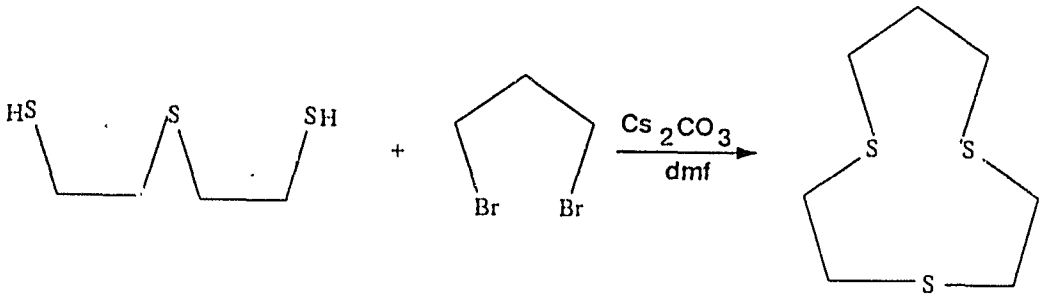

23

A dry, 5-L, three-necked round bottomed flask was equipped with a 500 mL addition funnel, a reflux condenser and a mechanical stirrer. The entire system was kept under a positive nitrogen atmosphere. The flask was charged with 2.0 L of dmf and 13.04 g (40 mmol) of dry Cs_2CO_3 (oven-dried at 100 °C for ten hours). The mixture was stirred and heated to 55 - 60 °C. A mixture of 2-mercaptoethyl sulfide (6.16 g, 40 mmol) and 1,3-dibromopropane (8.08 g, 40 mmol) in 500 mL dmf was prepared. Half of this mixture was added to the

mechanically stirred suspension of Cs_2CO_3 in dmf over a period of 10 h. The reaction mixture was then charged with another 13.04 g (20 mmol) of Cs_2CO_3 and the second half of the mixture of 2-mercaptoethyl sulfide and 1,3-dibromopropane was added over a period of 10 h. After the addition was complete the reaction mixture was stirred at 55 - 60 °C for about 6 h and was allowed to cool to room temperature and filtered. The N,N-dimethylformamide was distilled off under reduced pressure. The residual white solid was extracted with CH_2Cl_2 (5 × 100 mL) and the filtered extract was washed with 1.0M aqueous NaOH (2 × 100 mL) and then with water (3 x 150 mL). The CH_2Cl_2 layer was dried over anhydrous Na_2SO_4 and evaporated to dryness to give a colourless crystalline solid (10 g). This was taken up in 200 mL of boiling ethanol and the hot liquid was decanted. Upon cooling the solution to 5°C, colourless needle-shaped crystals of the product were obtained.

Yield : 6.2 g; 80 %; m.p. : 25 °C.

m/e(EI) : 194.

ms (CI) : 195 (M+1), 223 (M+29), 235 (M+41).

^{1}H nmr ($CDCl_3$) : δ 1.61 (p, 2H), 2.7 to 2.89 (m, 12H).

^{13}C nmr ($CDCl_3$) : 4-line spectrum, δ 27.5 (1C, -C-$\underline{C}H_2$-C), 29.3 (2C, -$\underline{C}H_2$-C-$\underline{C}H_2$), and two slightly magnetically inequivalent sets at δ 33.2 and 33.5 (4C, -S-$\underline{C}H_2$-$\underline{C}H_2$-S-).

2.1.12. Synthesis of complexes of [10]-aneS$_3$, 23:

a) Fe([10]-aneS$_3$)$_2$(ClO$_4$)$_2$, 52:

A methanolic solution (10 mL) of $Fe(ClO_4)_3.6H_2O$, 0.30 g (0.65 mmol), was added dropwise to 0.28 g (1.4 mmol) of [10]aneS$_3$ in 20 mL of CH_3OH. The solution was refluxed for 4 h, after which it was filtered to remove the colorless solid. The filtrate was taken to dryness. The violet residue was dissolved in CH_3CN containing $NaClO_4$. Diffusion of ether into the clear CH_3CN solution yielded violet crystals of the complex.

Yield : 0.17 g; 41%.

Analysis for $C_{14}H_{28}S_6FeCl_2O_8$:

Calcd. : C, 25.41; H, 4.57; S, 29.08.

Found : C, 25.18; H, 3.97; S, 28.80.

Pink crystals of the hexafluorophosphate salt were obtained by the addition of solid NH_4PF_6 to CH_3CN solutions of the complex.

b) Co([10]-aneS$_3$)$_2$(ClO$_4$)$_2$, 53:

A methanolic solution of $Co(ClO_4)_2.6H_2O$, 143 mg (0.39 mmol), was added to a solution of [10]-aneS$_3$, 164 mg (0.85 mmol) in 20 mL of CH_3OH. The solution was refluxed for 5h under a dinitrogen atmosphere and then filtered while hot. The filtrate was taken to dryness and the residue was dissolved in CH_3CN containing $NaClO_4$. Slow diffusion of ether yielded reddish brown needle-shaped crystals of the complex.

Yield : 150 mg; 60%.

Analysis for $C_{14}H_{28}S_6CoCl_2O_8$:

Calcd. : C, 26.00; H, 4.36.

Found : C, 26.01; H, 4.25.

c) $Co([10]\text{-}aneS_3)_2(ClO_4)_3$, 54:

An aqueous solution of $Na_2S_2O_8$, (3 mL), was added to 27 mg of $Co([10]\text{-}aneS_3)_2(ClO_4)_2$ in 2 mL of H_2O. The colour changed from red to orange. Addition of a saturated solution of $NaClO_4$ (1 mL) initiated the precipitation of orange-yellow crystals which were filtered off, washed with ethanol and dried under vacuum.

Yield : 28 mg; 90%.

Analysis $C_{14}H_{28}S_6CoCl_3O_{12}$:

Calcd. : C, 22.53; H, 3.78.

Found : C, 22.28; H, 3.66.

d) $Ni([10]\text{-}aneS_3)_2(ClO_4)_2$, 55:

A solution of $Ni(ClO_4)_2.6H_2O$, 183 mg (0.5 mmol), in ethanol (10 mL) was added dropwise to a solution of **25**, 230 mg (1.18 mmol) in 10 mL of ethanol. The solution was refluxed for half an hour. The pink complex that precipitated out was filtered and recrystallised from acetonitrile solution of the complex by diffusion of ether.

Yield : 0.23 g; 71%.

Analysis $C_{14}H_{28}NiCl_2O_8$:

Calcd. : C, 26.01; H, 4.36; S, 29.76.

Found : C, 25.92; H, 4.45; S, 29.34.

e) Pd([10]-aneS$_3$)$_2$(PF$_6$)$_2$, 56:

A suspension of the ligand **25**, 0.215 g (1.1 mmol) in 20 mL H_2O/MeOH (1/1 v/v), was stirred for 15 minutes at 45 °C. To this a solution of K_2PdCl_4, 0.167 g (0.51 mmol) in H_2O/CH_3OH (1/1 v/v, 20 mL), was added dropwise. The green solution was stirred at room temperature for 30 minutes and filtered. A yellow solid was also formed.[a] The filtrate was reduced to a small volume. Addition of NH_4PF_6 gave a green solid of the complex which could be recrystallised by diffusion of ether into CH_3CN solutions. Blue-green crystals of the complex Pd([10]aneS$_3$)$_2$(PF$_6$)$_2$ were obtained which were filtered off and dried under vacuum.

Yield : 244 mg; 61%.

Analysis for $C_{14}H_{28}S_6PdP_2F_{12}$:

Calcd. : C, 21.41; H, 3.59.

Found : C, 21.47; H, 3.59.

Note : [a] The yellow residue obtained could be recrystallised from hot acetonitrile solution containing NH_4PF_6.

Analysis for the yellow solid, $C_7H_{14}S_3PdClPF_6$:

Calcd. : C, 17.47; H, 2.93.

Found : C, 17.34; H, 2.86.

This may be a Pd dimer or $(Pd([10]\text{-ane}S_3)Cl)PF_6$.

2.2. Materials and Methods:

All chemicals were of reagent grade except where otherwise indicated. Infrared spectra were obtained as KBr discs or as neat samples on NaCl plates with a Perkin Elmer 283 grating spectrometer. ^1H nmr spectra were measured on a 60 MHz Perkin Elmer R12B or a 90 MHz Perkin Elmer R32 spectrometer. High field ^1H nmr and ^{13}C nmr spectra were obtained with a Brüker WM250 instrument or a Brüker 360 instrument. ^{59}Co nmr was obtained on a Brüker 360 instrument. All chemical shifts are reported relative to tetramethyl silane except in the case of Co where potassium hexacyanocobaltate(III) was used.

Electronic spectra were recorded on a Unicam SP800, Cary-17 or a Perkin Lambda 4B dual-beam spectrophotometer. EPR spectra were obtained with a Varian E6S spectrometer or a Bruker ER200tt spectrometer with an IBM/PC attachment. Diphenylpicrylhydrazyl radical (dpph) was used as a field marker (g = 2.0037). For the line broadening experiments the esr spectra were obtained on the Bruker and were integrated to

obtain the absorption spectra using the program EPRDAS (EPR Data Aquisition System, Version 1.22B, R.O. Schultz, Adaptable Laboratory Software, Inc., Rochester, N.Y.).

Mass spectra were recorded in a Finnegan 330GC-MS instrument by electron impact, methane or isobutane chemical ionization. Elemental analyses were performed by Microanalytical Services, Vancouver, B.C., Canada. Electrochemical measurements were recorded with Princeton Applied Research equipment which included the Model 173/179 potentiostat-galvanostat and Model 175 programmer or a Princeton Applied Research Model 273 potentiostat-galvanostat, interfaced with an IBM/PC. Cyclic voltammograms were run using the "Headstart" program supplied by Princeton Applied Research Company. The electrochemical cell employed the standard three electrode (hanging mercury drop or platinum), a Pt-wire auxiliary electrode and the reference electrode. The reference electrode was a saturated calomel or Ag/AgCl linked to the cell *via* a bridge containing saturated KCl. $Ag/AgNO_3$ (0.1 M) or a Ag wire was used as a reference electrode in non-aqueous systems containing 0.1 M NEt_4BF_4. Blank electrolyte solutions were scanned before each experiment and each time the ferrocenium/ ferrocene couple (Fc^+/Fc) was used either as an internal or external standard to calibrate the reference electrode, $E_{1/2}$ (Fc^+/Fc) = 0.15 V *vs* Ag^+/Ag. Acetonitrile was distilled over CaH_2 prior to use for

electrochemical purposes.

The kinetics of electron transfer reactions were studied by nmr line-broadening techniques.

2.3. Crystallography:

Crystals were mounted in glass Lindemann tubes (in some cases containing the solvent) and the unit cells and space groups were determined using Weissenberg and precession photography. The crystals were then transfered to a Picker 4-circle diffractometer automated with a PDP11/10 computer. Intensity measurements were carried out with Zr-filtered Mo radiation, λ = 0.71069 Å. Background counting was introduced at each end of the scan. A set of three standard reflections preceded each batch of 50 measurements, with no noticeable change in intensity observed during the collection in all cases. In some instances a Enraf-Nonius CAD4 diffractometer was used. The data collection was carried out at 22 ± 2 °C. Intensity measurements were made using Mo radiation λ = 0.709300 Å. Absorption corrections were made and solutions of the phase problem were thus achieved and the position of the single heavy atom located using Direct Methods of SHELX76[55], or MULTAN[56]. The atomic scattering factors used were those included in the SHELX76 program together with the metal *f*-curves from the International tables.[57] The completion of the structure and the refinement were carried out by difference

electron density maps and the method of least squares. The weighting scheme which gave the best analysis of variance in ranges of $|F|$ and θ was used and gave final residuals of about $R = 0.06$ in most cases. In the final cycles of full-matrix least-squares refinement all non-hydrogen atoms were refined with anisotropic thermal parameters. Hydrogen atoms were observed and refined isotropically, where possible, otherwise positions of the hydrogen atoms were calculated in some cases. Depending on the number of parameters, a blocked matrix was used in the final stages of refinement. The refinements converged with a maximum shift/esd of less than 0.1 on the final cycle. Details of each individual crystal structure and specific parameters are provided where appropriate. The following crystallographic tables have not been included in this dissertation:

Structure factor tables,

Anisotropic temperature parameters,

Fractional atomic coordinates of the hydrogen atoms,

Bond lengths and angles involving the hydrogen atoms, and

Intermolecular distances.

These will be deposited as supplementary material as the structures are published, and will be available from the author upon request.

CHAPTER 3

Synthesis and characterisation of transition metal complexes of hexadentate macrocyclic ligands

3.1. Introduction:

Complexes containing triaza macrocyclic ligands, M([9]-aneN_3)$_2$, have been studied extensively with respect to their redox properties and stabilization of less common oxidation states. Oxidation of square planar Ni(II) cyclam yields a stable octahedral Ni(III) species.[58,59] Owing to the extensive change in geometry upon going from square planar Ni(II) to octahedral Ni(III), the reorganisation terms involved in the outer sphere electron transfer energetics are expected to be large. However, small amounts of the octahedral ions are in equilibrium with the square planar species which reduces these energy requirements. This problem of geometry could be overcome where macrocyclic ligands are designed to achieve octahedral geometry in both the oxidation states. This can be done in several ways:

(i) Small tridentate macrocycles such as 1,4,7-triazacyclononane **22** have been used.[49,60] In the bis- (ligand) metal complexes octahedral geometry is imposed as a result of the facial disposition of the donor atoms.

(ii) Macrocycles that serve as cage ligands **57** have been used.[61]

(iii) Cryptates **8** that will encapsulate the metal atom and allow for maintaining the geometrical configuration in different oxidation states are being increasingly recognized.

(iv) Larger macrocyclic rings containing six donor atoms (hexadentate) may also wrap around the metal ion thereby

imposing an octahedral geometry around the metal atom.

These considerations have led to the investigations on hexadentate macrocyclic ligands **27** and **28** and their metal complexes.

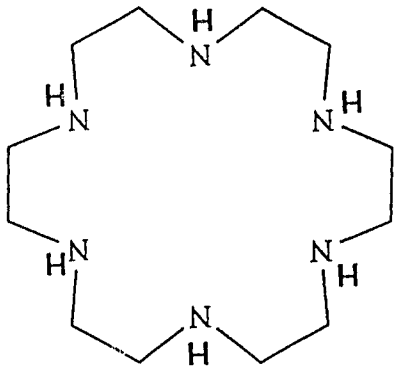

27

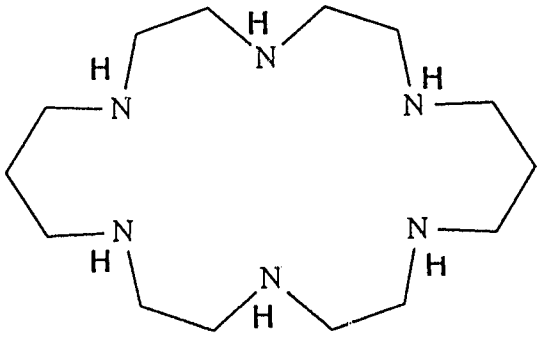

28

Hexadentate macrocycles containing six nitrogen donor atoms should coordinate in an octahedral fashion to the transition metal atom. Both Co(III) and Ni(II) monomeric complexes of **27** have been studied[62,63,64,65] and in both cases the meridional isomers were isolated, **58**, **59**, and **60**. The hexaamine macrocycles also serve to bind two metal atoms yielding discrete binuclear complexes.[66] Di-copper complexes of 20-, 22- and 24- membered hexaamine macrocycles have been considered suitable in the activation of small molecules. The mode of substrate binding can be controlled by varying the size of the macrocyclic ligands in which the metal ions have otherwise similar ligand coordination environments. With [20]-aneN$_6$, tetranuclear clusters containing Cu of the type $[Cu_4(O_2)_2(H_2O)_4(L)_2](ClO_4)_6.2CH_3NO_2$ have been obtained with the Cu atoms nearly square pyramidal in geometry.[67]

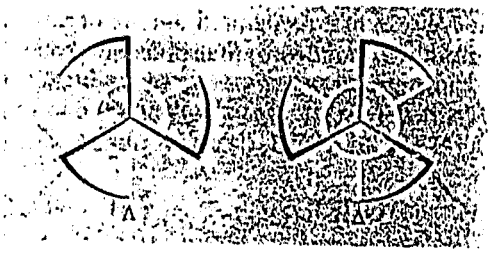

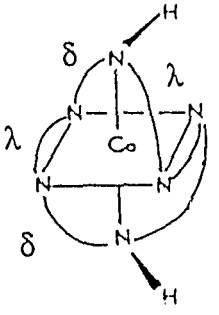

58

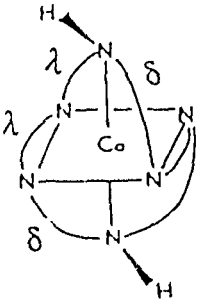

59

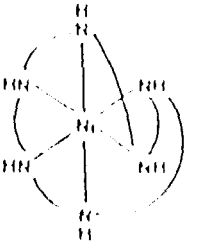

60

The binuclear complex $Pd_2([20]\text{-aneN}_6)Br_4.12H_2O$ was isolated in this laboratory.[68] This consisted of two square planar Pd atoms, each coordinated to three N atoms and one Br atom. The flexibility of the ligand allows for the formation of mono and multi-nuclear species.

It was, therefore, of interest to study the complexation properties of these ligands with transition metals ions.

3.2. Synthesis:

The ligand $[18]\text{-aneN}_6$ was obtained as the trisulphate salt from Aldrich Chemical Co.. The free ligand was obtained by continuously extracting a basic (pH ~ 13) solution of the sulphate salt with chloroform overnight.

The ligand [20]-aneN$_6$ was synthesised by previously published procedures.[51] Detosylation of the cyclised tosylate [20]-aneN$_6$ was carried out either by hydrolysis in sulfuric acid or using H_3PO_4 dried with P_2O_5. Good yields of the ligand (~60%) were obtained with both the methods. The end point of the detosylation was confirmed by periodically testing the solubilities of the reaction mixture in 1 M NaOH. If no colorless solid was obtained then, the detosylation was considered to have been completed.

Chromium complexes of both **27** and **28** were prepared by a modification of Pedersen's method.[69] The dmso solution containing $CrCl_3.6H_2O$ was heated to facilitate the formation of $Cr(dmso)_6Cl_3$ complex. The labile dmso ligand was then replaced by the N atoms of the hexadentate macrocyclic ligand to form the monomeric complex containiing CrN_6 core.

Both the Fe(II) complexes of **27** and **28** are blue in aqueous solutions but are very air sensitive. Analytically pure solids of the complexes could not be prepared.

The manganese dimer **32** was insoluble in dichloromethane, acetone, acetonitrile, and nitromethane but was soluble in dmso. The dimer decomposes in water forming the monomeric Mn([20]-aneN$_6$)$^{2+}$ complex.

3.3. Molecular structures of the complexes of 27 and 28:

3.3.1. Crystal structure of (Cr[18]-aneN$_6$)Br$_3$, 29:

A yellow crystal of compound **29** was placed in a

Lindemann's tube and mounted on a Picker 4-circle diffractometer automated with a PDP11/10 computer. Standard Weissenberg and precession photographic methods showed that the crystal belonged to the monoclinic system, space group I_12/m_1. The unit cell dimensions were refined using 24 pairs of reflections in the 2θ range 17 - 49°. Intensity measurements were carried out with Zr- filtered Mo radiation, λ = 0.71069 Å. The experimental details and treatment of the intensity data are summarized in Table 3.1.

The solution of the phase problem was achieved *via* direct methods, using MULTAN[56] which revealed the positions of chromium and bromine atoms. Subsequent Fourier syntheses revealed the positions of the carbon and nitrogen atoms. The hydrogen atoms could not be located and all non-hydrogen atoms were refined anisotropically. The number of reflections used was 751 ($I > 2\sigma(I)$) out of a total of 872, with 57 parameters to be refined in the final cycle. The refinement converged at

$$R = \Sigma||F_o| - |F_c||/\Sigma|F_o| = 0.0639,$$

with a maximum shift/esd of 0.023 and the maximum peak in the difference map was 0.007 eÅ^{-3}. The asymmetric unit consisted of one-fourth of the whole molecule.

The ORTEP diagram of the complex cation, $(Cr[18]aneN_6)^{3+}$ with atomic labelling for the non-hydrogen atoms is shown in Fig. 3.1. The fractional atomic coordinates and the isotropic temperature factors are given in Table 3.2. The bond lengths and bond angles are listed in Table 3.3.

Table 3.1. Experimental crystallographic data for [Cr([18]-aneN$_6$)]Br$_3$, **29**, and [Cr([20]-aneN$_6$)]Br$_3$, **30**.

Compound	**29**	**30**
Formula	$CrBr_3N_6C_{12}H_{30}$	$CrBr_3N_6O_2C_{14}H_{38}$
MW	550.1	596.2
Crystal color	yellow	yellow
Crystal system	monoclinic	monoclinic
Space group	I_12/m_1 (No. 12)	$P2_1/c$ (No. 14)
Cell dimensions		
a (Å)	12.486(4)	19.509(12)
b (Å)	9.550(2)	15.608(8)
c (Å)	8.038(3)	14.692(7)
β (°)	105.27(4)	99.30(8)
V (Å^3)	925	4415
Z	2	8
D_{calc} (g/cm^3)	1.976	1.794
D_{meas} (g/cm^3)	1.938	1.777
Crystal dimensions (mm^3)	0.17×0.12×0.11	0.06×0.20×0.21
Diffractometer	Picker, 4-circle	Picker, 4-circle
Radiation (λ, Å)	Mo-K$_\alpha$ (0.71069)	Mo-K$_\alpha$ (0.71069)
Filter	Zirconium	Zirconium
Measurement	2θ (2 - 50°)	2θ (2 - 40°)
Octants collected	±h,k,l	±h,k,l
std. reflections	060,002,400	006,060,900
no. refln. collected	872	4118
no. refln. I > nσ(I)	751 (n = 2)	2862 (n = 2)
no. parameters	57	446
Linear abs coeff. (cm^{-1})	73.72	58.65
Solution method	Direct methods	Direct methods
R^a	0.0639	0.0630
R_w^b	0.0713	0.0617

[a] $R = \Sigma\| F_o| - |F_c\| / \Sigma |F_o|$; [b] $R_w = [\Sigma w(|F_o| - |F_c|)^2 / \Sigma w(|F_o|)^2]^{1/2}$

where $w(29) = 4.02/(\sigma^2 F + 0.001F^2)$;

$w(30) = 1.68/(\sigma^2 F + 0.001F^2)$.

Fig. 3.1. CRTEP diagram of $[Cr(27)]^{3+}$ with 25% thermal ellipsoids showing the atom numbering scheme.

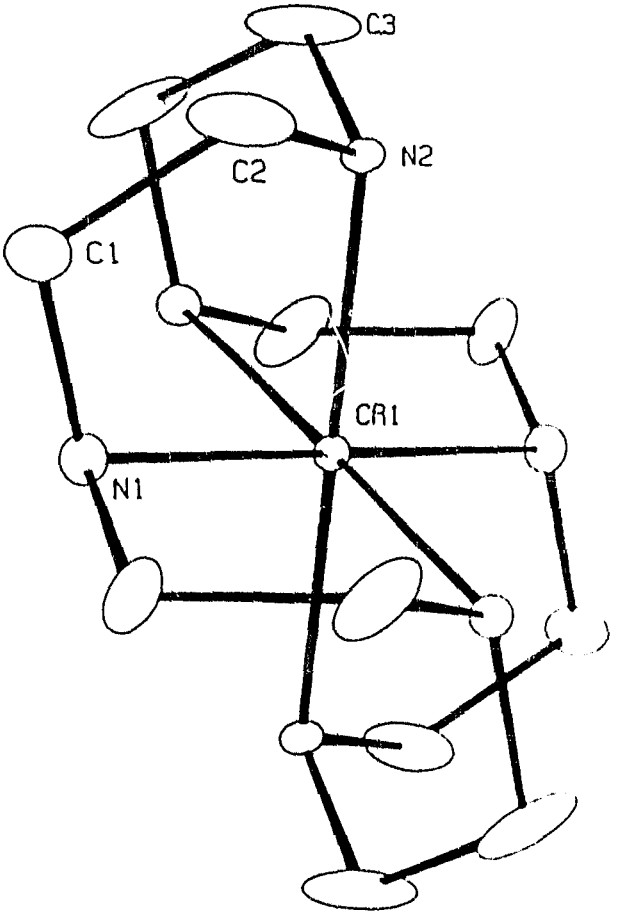

Table 3.2.

Fractional atomic coordinates and temperature parameters.

Atom	x/a	y/b	z/c	U_{eq}
Cr(1)	50000(0)	00000(0)	00000(0)	185(9)
Br(1)	00000(0)	00000(0)	00000(0)	384(7)
Br(2)	27929(11)	00000(0)	55857(17)	330(5)
N(2)	3310(8)	100000(0)	-96(14)	29(4)
N(2)	5042(6)	1669(7)	1697(9)	28(2)
C(1)	3036(8)	1195(13)	751(18)	57(5)
C(2)	3976(12)	1669(13)	2268(17)	66(6)
C(3)	5261(15)	2961(12)	625(18)	80(7)

Estimated standard deviations are given in parentheses.
Coordinates × 10^n where n = 5,5,4,4 for Cr,Br,N,C.
Temperature parameters × 10^n where n = 4,4,3,3 for Cr,Br,N,C.
U_{eq} = the equivalent isotropic temperature parameter.
$U_{eq} = 1/3 \sum_i \sum_j U_{ij} a_i^* a_j^* (a_i . a_j)$
Primed values indicate that U_{iso} is given
$T = \exp-(8\pi^2 U_{iso} \sin^2\theta/\lambda^2)$

Table 3.3.

Interatomic distances (Å)

Atoms		Distance
N(1)	-Cr(1)	2.091(9)
N(2)	-Cr(1)	2.090(6)
C(1)	-N(1)	1.416(12)
C(2)	-N(2)	1.517(12)
C(3)	-N(2)	1.439(13)
C(2)	-C(1)	1.519(17)
C(3)	-C(3)	1.457(31)

Estimated standard deviations are given in parentheses.

Bond angles (°)

Atoms			Angle
N(2)	-Cr(1)	-N(1)	82.8(3)
C(1)	-N(1)	-Cr(1)	110.6(6)
C(2)	-N(2)	-Cr(1)	108.7(6)
C(3)	-N(2)	-Cr(1)	110.3(6)
C(3)	-N(2)	-C(2)	114.6(9)
N(2)	-Cr(1)	-N(2)	80.6(4)
N(2)	-Cr(1)	-N(2)	99.5(4)
C(2)	-C(1)	-N(1)	112.9(10)
C(1)	-N(1)	-C(1)	107.4(12)
C(1)	-C(2)	-N(2)	108.2(8)

Estimated standard deviations are given in parentheses.

The mean Cr-N bond length is 2.091(9) Å, and the other bond lengths also fall in the expected range. This is similar to that observed in $Cr(en)_3^{3+}$,[70] (2.075(2)Å) and $Cr(NH_3)_6^{3+}$ ion.[71] The bite angle of the five membered chelate ring subtended at the central Cr atom has a mean = 81.9(10)° (mean of 4), in the present complex, thus, showing significant distortion from octahedral symmetry. The bite angle in the corresponding $Cr(en)_3^{3+}$ complex was found to be 82.4(10)°, (mean of 6).

Six coordinate chelate complexes of the transition elements can adopt stable structures in which the ML_6 coordination unit is significantly distorted from the usual octahedral symmetry. Such hexadentate complexes can be described by a "twist" angle of the two donor atom triangles whose planes are normal to the three-fold axis. For a perfect octahedral complex the twist angle ϕ as defined in Fig. 3.2. (the angle describing the twist of the faces perpendicular to the three-fold axis) is 60°. For the $(Cr[18]\text{-}aneN_6)Br_3$ complex the twist angle is 50° ± 1°.

As illustrated in Fig. 3.3., a facial or a meridional isomer is possible for the Cr complex of **27**, (the NH diastereoisomers are not shown for the sake of simplicity). For both Co(II) and Ni(II) complexes of **27** meridional isomers are obtained preferentially.[62,63,64,65] Yoshikawa,[62] obtained <1% of the symmetric isomer for the $Co([18]\text{-}aneN_6)^{3+}$ complex cation. The presence of large non-bonded hydrogen-hydrogen interactions in the facial isomer may result in the

Fig. 3.2. Definition of "twist" angle ϕ.

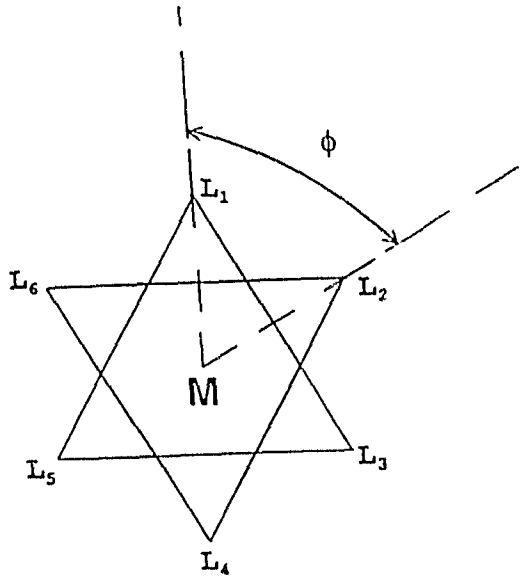

Fig. 3.3. Facial and meridional isomers of $[M([18]\text{-aneN}_6)]^{3+}$ complexes.

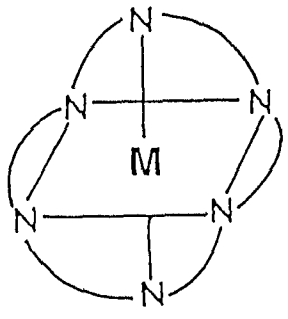

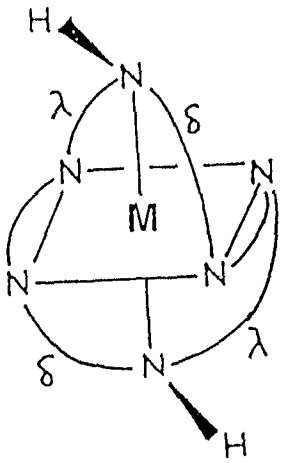

preferential formation of the meridional isomer. However, in the present case, the hexadentate ligand **27** wraps around the central Cr^{3+} ion in a facial manner. This is a rare example of the isolation and characterization of such a structure in [18]-aneN_6 complexes.

3.3.2. Crystal structure of [Cr([20]-aneN_6)]$Br_3.2H_2O$, 30:

Crystals of Cr([20]-aneN_6)Br_3 were grown from aqueous solutions containing sodium bromide. The crystals were handled as described in Section 2.3. Both Weissenberg and precession photography were used to obtain the space group for the crystal and to determine the unit cell dimensions. The crystal data were listed in Table 3.1. The cell was refined using 20 pairs of reflections in the range $2\theta = 10 - 40°$. The total number of reflections measured was 4118, but this reduced to 2862 ($I > 2\sigma(I)$) independent reflections. The solution of the phase problem was achieved by direct methods with SHELX-76.[55] Completion and refinement of the structure was made by difference electron density maps and by least squares minimizing $\Sigma w\Delta^2$, where,

$$\Delta = \| F_o | - | F_c \| \quad \text{and} \quad w = 1.68/(\sigma^2(F) + 0.001F^2).$$

The asymmetric unit was composed of two molecules of the complex containing 50 atoms. All non-hydrogen atoms except one carbon atom were refined with anisotropic thermal parameters. Since there were 446 parameters to be refined, a block matrix was used. Six blocks were used, each containing

a bromine atom and a few C/N atoms and were refined in each cycle. The rest of the structure was refined in alternating cycles of least squares, each containing one whole molecule of the metal complex. The refinement converged with a maximum shift/esd of 0.034 on the final cycle. R = 0.0630 and R_w = 0.0617. The largest peak in the final difference map was 0.74 eÅ^{-3}.

The chromium complex crystallized in the monoclinic space group, $P2_1/c$, a = 19.509 Å, b = 15.608 Å, c = 14.692 Å, $\alpha = \gamma = 90°$ and $\beta = 99.3°$, with two molecules in the asymmetric unit and it follows that each of these is individually devoid of symmetry. The molecular structures of these two molecules are shown in Figs. 3.4a. and 3.4b. The complex shows an octahedral microsymmetry with the six nitrogen atoms from the ligand coordinated to the central chromium atom. The fractional atomic coordinates for the Cr complex are given in Table 3.4. for two crystallographically independent formula units which comprise the asymmetric unit. Each formula unit consists of a triply charged Cr(III) cation, three bromide anions, and a water molecule. The isotropic temperature parameters given were calculated from the anisotropic parameters that were used.

The interatomic distances and the bond angles for the chromium complex are given in Tables 3.5. and 3.6., respectively. Data for each molecule are shown. The atomic labelling scheme of molecule 1 is shown in Fig. 3.4a.

Figures 3.4a. and 3.4b. ORTEP diagrams of $[Cr(\mathbf{28})]^{3+}$ with 25% thermal ellipsoids showing atom numbering scheme.

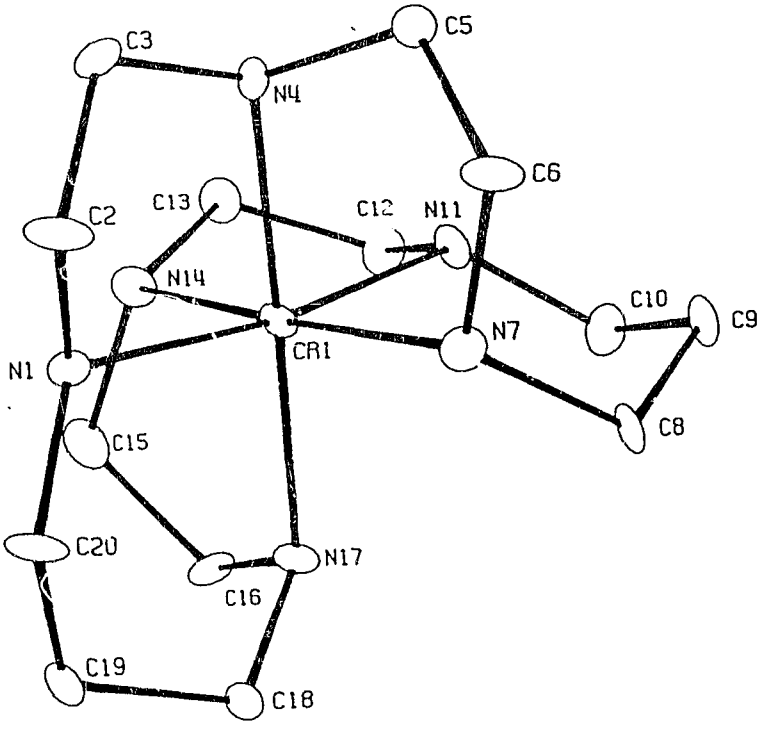

Fig. 3.4a.

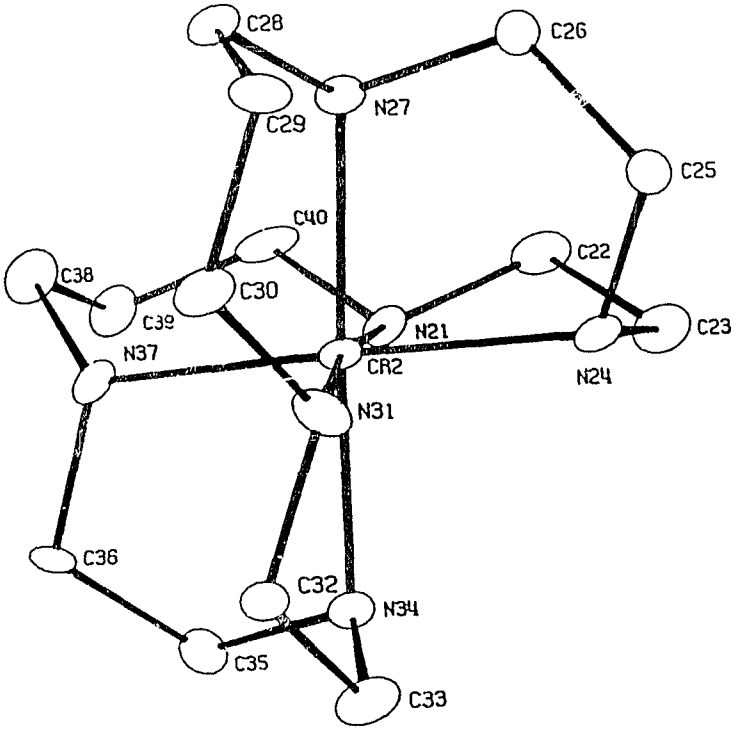

Fig. 3.4b.

Table 3.4.

Fractional atomic coordinates and temperature parameters.

Atom	x/a	y/b	z/c	Ueq
Br(1)	66618(10)	3808(11)	10262(12)	404(7)
Br(2)	99820(10)	11744(11)	44178(13)	470(8)
Br(3)	33414(11)	46788(14)	1493(15)	638(9)
Br(4)	11321(11)	14132(12)	7946(13)	516(8)
Br(5)	45035(12)	21237(12)	33208(15)	612(9)
Br(6)	79316(10)	31019(12)	10924(14)	539(8)
Cr(1)	62999(13)	41398(15)	26439(17)	242(9)
Cr(2)	-12273(14)	-9716(15)	25999(17)	275(10)
O(1)	8845(10)	2720(10)	4457(10)	112(8)
O(2)	3915(9)	2691(9)	337(10)	106(8)
N(1)	6422(7)	2888(7)	2167(8)	29(5)
N(4)	5817(7)	4336(7)	1289(8)	28(5)
N(7)	5275(7)	3944(8)	2871(9)	37(5)
N(11)	6241(7)	5448(7)	2940(9)	32(5)
N(14)	7305(7)	4466(8)	2446(9)	37(6)
N(17)	6761(7)	3847(8)	3990(8)	31(5)
C(2)	5871(10)	2731(11)	1333(11)	47(8)
C(3)	5866(8)	3542(11)	719(10)	34(7)
C(5)	5098(9)	4632(10)	1290(11)	34(4)
C(6)	4760(9)	4119(11)	1990(11)	43(7)
C(8)	5087(9)	4432(9)	3711(12)	35(7)
C(9)	5150(9)	5429(10)	3623(12)	41(7)
C(10)	5912(10)	5718(10)	3737(13)	49(8)

Table 3.4. (contd.)

C(12)	6965(9)	5858(11)	3077(12)	42(7)
C(13)	7370(10)	5431(10)	2391(12)	46(8)
C(15)	7813(10)	4077(11)	3229(13)	52(8)
C(16)	7523(9)	4071(11)	4143(11)	42(7)
C(18)	6662(9)	2926(10)	4322(11)	40(7)
C(19)	6890(9)	2229(10)	3697(12)	40(7)
C(20)	6411(10)	2106(10)	2785(12)	48(8)
N(21)	-1323(7)	293(8)	3038(9)	38(6)
N(24)	-1571(7)	-1260(9)	3832(9)	43(6)
N(27)	-2288(7)	-1084(7)	2035(9)	32(5)
N(31)	-1060(7)	-2282(8)	2364(10)	43(6)
N(34)	-172(7)	-997(8)	3196(9)	40(6)
N(37)	-846(7)	-594(7)	1414(9)	37(6)
C(22)	-1806(10)	314(11)	3749(13)	51(8)
C(23)	-1627(11)	-454(12)	4399(13)	58(8)
C(25)	-2280(9)	-1713(10)	3635(11)	37(7)
C(26)	-2709(9)	-1300(10)	2764(11)	39(7)
C(28)	-2438(9)	-1651(10)	1167(11)	40(7)
C(29)	-2220(9)	-2594(9)	1399(12)	39(7)
C(30)	-1437(9)	-2703(10)	1487(11)	42(7)
C(32)	-297(9)	-2437(11)	2423(11)	39(7)
C(33)	74(10)	-1911(11)	3254(12)	54(8)
C(35)	211(9)	-439(11)	2612(13)	46(8)
C(36)	-54(8)	-534(11)	1575(12)	42(8)
C(38)	-1179(10)	205(10)	941(12)	51(8)
C(39)	-1068(11)	999(11)	1580(13)	56(8)

Table 3.4. (contd.)

C(40)	-1537(10)	989(10)	2320(14)	54(8)

Estimated standard deviations are given in parentheses.

Coordinates × 10^n where n = 5,5,4,4,4 for Br,Cr,O,N,C.

Temperature parameters × 10^n where n = 4,4,4,3,3 for Br,Cr,O,N,C.

U_{eq} = the equivalent isotropic temperature parameter.

$U_{eq} = 1/3\ \Sigma_i\Sigma_j U_{ij} a_i^* a_j^* (a_i . a_j)$

Primed values indicate that U_{iso} is given

$T = \exp-(8\pi^2 U_{iso} \sin^2\theta/\lambda^2)$

Table 3.5.

Interatomic distances (Å).

Atoms	Distance	Atoms	Distance
N(1) -Cr(1)	2.102(12)	C(9) -C(8)	1.567(21)
N(4) -Cr(1)	2.082(12)	C(10) -C(9)	1.536(26)
N(7) -Cr(1)	2.102(14)	C(13) -C(12)	1.530(26)
N(11) -Cr(1)	2.095(12)	C(16) -C(15)	1.540(26)
N(14) -Cr(1)	2.091(14)	C(19) -C(18)	1.535(24)
N(17) -Cr(1)	2.087(12)	C(20) -C(19)	1.517(23)
N(21) -Cr(2)	2.094(13)	C(22) -N(21)	1.516(26)
N(24) -Cr(2)	2.079(15)	C(40) -N(21)	1.525(22)
N(27) -Cr(2)	2.109(13)	C(23) -N(24)	1.523(23)
N(31) -Cr(2)	2.109(13)	C(25) -N(24)	1.538(22)
N(34) -Cr(2)	2.103(13)	C(26) -N(27)	1.489(23)
N(37) -Cr(2)	2.087(14)	C(28) -N(27)	1.541(20)
C(2) -N(1)	1.514(20)	C(30) -N(31)	1.526(21)
C(20) -N(1)	1.523(20)	C(32) -N(31)	1.496(22)
C(3) -N(4)	1.508(20)	C(33) -N(34)	1.504(22)
C(5) -N(4)	1.478(21)	C(35) -N(34)	1.504(24)
C(6) -N(7)	1.529(20)	C(36) -N(37)	1.528(22)
C(8) -N(7)	1.543(22)	C(38) -N(37)	1.521(20)
C(10) -N(11)	1.484(24)	C(23) -C(22)	1.537(25)
C(12) -N(11)	1.534(21)	C(26) -C(25)	1.553(22)
C(13) -N(14)	1.515(19)	C(29) -C(28)	1.554(22)
C(15) -N(14)	1.518(21)	C(30) -C(29)	1.522(25)
C(16) -N(17)	1.508(22)	C(33) -C(32)	1.551(23)
C(18) -N(17)	1.541(20)	C(36) -C(35)	1.534(25)
C(3) -C(2)	1.555(23)	C(39) -C(38)	1.548(24)
C(6) -C(5)	1.533(25)	C(40) -C(39)	1.530(30)

Estimated standard deviations are given in parentheses.

Table 3.6.

Bond angles (°).

Atoms	Angle	Atoms	Angle
N(4) -Cr(1) -N(1)	82.9(5)	N(34) -Cr(2) -N(27)	174.0(5)
N(7) -Cr(1) -N(1)	94.6(5)	N(34) -Cr(2) -N(31)	83.3(5)
N(7) -Cr(1) -N(4)	83.0(5)	N(37) -Cr(2) -N(21)	93.0(5)
N(11) -Cr(1) -N(1)	171.2(5)	N(37) -Cr(2) -N(24)	175.4(5)
N(11) -Cr(1) -N(4)	91.3(5)	N(37) -Cr(2) -N(27)	98.9(5)
N(11) -Cr(1) -N(7)	91.3(5)	N(37) -Cr(2) -N(31)	92.9(5)
N(14) -Cr(1) -N(1)	91.2(5)	N(37) -Cr(2) -N(34)	84.1(5)
N(14) -Cr(1) -N(4)	96.9(5)	C(2) -N(1) -Cr(1)	108.4(9)
N(14) -Cr(1) -N(7)	174.2(5)	C(20) -N(1) -Cr(1)	122.2(10)
N(14) -Cr(1) -N(11)	82.9(5)	C(20) -N(1) -C(2)	106.0(12)
N(17) -Cr(1) -N(1)	93.3(5)	C(3) -N(4) -Cr(1)	110.5(8)
N(17) -Cr(1) -N(4)	175.7(5)	C(5) -N(4) -Cr(1)	109.1(9)
N(17) -Cr(1) -N(7)	95.4(5)	C(5) -N(4) -C(3)	113.7(11)
N(17) -Cr(1) -N(11)	92.7(5)	C(6) -N(7) -Cr(1)	110.6(10)
N(17) -Cr(1) -N(14)	85.1(5)	C(8) -N(7) -Cr(1)	114.2(9)
N(24) -Cr(2) -N(21)	83.1(5)	C(8) -N(7) -C(6)	112.4(12)
N(27) -Cr(2) -N(21)	93.9(5)	C(10) -N(11) -Cr(1)	119.0(10)
N(27) -Cr(2) -N(24)	83.7(5)	C(12) -N(11) -Cr(1)	110.7(9)
N(31) -Cr(2) -N(21)	171.4(5)	C(12) -N(11) -C(10)	106.6(12)
N(31) -Cr(2) -N(24)	90.8(6)	C(13) -N(14) -Cr(1)	109.7(11)
N(31) -Cr(2) -N(27)	91.3(5)	C(15) -N(14) -Cr(1)	108.0(10)
N(34) -Cr(2) -N(21)	91.1(5)	C(15) -N(14) -C(13)	112.8(12)
N(34) -Cr(2) -N(24)	93.7(5)	C(16) -N(17) -Cr(1)	110.7(9)

Table 3.6. (contd.)

C(18) -N(17) -Cr(1)	116.6(9)	C(25) -N(24) -Cr(2)	110.1(9)
C(18) -N(17) -C(16)	109.9(12)	C(25) -N(24) -C(23)	110.0(13)
C(3) -C(2) -N(1)	105.9(12)	C(26) -N(27) -Cr(2)	110.9(9)
C(2) -C(3) -N(4)	110.0(12)	C(28) -N(27) -Cr(2)	114.6(10)
C(6) -C(5) -N(4)	110.4(12)	C(28) -N(27) -C(26)	114.3(12)
C(5) -C(6) -N(7)	111.5(13)	C(30) -N(31) -Cr(2)	119.3(9)
C(9) -C(8) -N(7)	113.1(13)	C(32) -N(31) -Cr(2)	109.1(9)
C(10) -C(9) -C(8)	111.7(13)	C(32) -N(31) -C(30)	108.6(13)
C(9) -C(10) -N(11)	111.4(13)	C(33) -N(34) -Cr(2)	108.9(10)
C(13) -C(12) -N(11)	107.1(13)	C(35) -N(34) -Cr(2)	107.1(9)
C(12) -C(13) -N(14)	110.0(14)	C(35) -N(34) -C(33)	113.5(14)
C(16) -C(15) -N(14)	112.1(15)	C(36) -N(37) -Cr(2)	112.1(9)
C(15) -C(16) -N(17)	111.3(12)	C(38) -N(37) -Cr(2)	115.4(11)
C(19) -C(18) -N(17)	114.2(14)	C(38) -N(37) -C(36)	111.6(13)
C(20) -C(19) -C(18)	114.9(14)	C(36) -C(35) -N(34)	113.1(13)
C(19) -C(20) -N(1)	111.1(13)	C(35) -C(36) -N(37)	109.2(14)
C(22) -N(21) -Cr(2)	109.1(9)	C(39) -C(38) -N(37)	111.9(13)
C(40) -N(21) -Cr(2)	119.2(10)	C(40) -C(39) -C(38)	112.4(16)
C(40) -N(21) -C(22)	109.3(13)	C(39) -C(40) -N(21)	111.7(14)
C(23) -N(24) -Cr(2)	111.0(11)		

Estimated standard deviations are given in parentheses.

Molecule 2 (Fig. 3.4b.), is labelled in a similar way (add 20 to each label except Cr1). In the second molecule, the chromium atom is labelled Cr2. The carbon atom labelled C(5) was not made anisotropic because of poor thermal ellipsoids for this atom. The mean Cr-N bond lengths, the chelate bite angles, and the twist angles for the Cr complexes of **27** and **28** and related complexes are compared in Table 3.7.

Table. 3.7. Comparison of bond lengths and bond angles in chromium complexes.

Complex cation	<Cr-N> (Å)	θ (°)	ψ (°)	ϕ (°)
$Cr(NH_3)_6^{3+}$	2.064(3)	-	-	-
$Cr(en)_3^{3+}$	2.075(2)	82.4(10)	-	-
$Cr(^*diamsar)^{3+}$	2.070(3)	84.1(1)	89.9(10)	50
$Cr([18]\text{-}aneN_6)^{3+}$	2.091(9)	81.9(1)	-	50(1)
$Cr([20]\text{-}aneN_6)^{3+}$	2.095(15)	83.5(6)	92.2(11)	56(1)

θ = Five-membered chelate angle,

ψ = Six-membered chelate angle, ϕ= Twist angle.

Figures in parentheses are errors in the last digit(s) quoted.

*diamsar = (1,8-diamino-3,6,10,13,16,19-hexaazacyclo[6,6,6] eicosane), ref. 72

The bite angle of the five-membered chelate ring subtended at the central Cr atom for the chromium complex of **28** has a mean of 84° ± 2°(mean of 8), similar to that of the chromium complex of **27**, thus showing significant distortion from octahedral symmetry. The angles subtended by the six membered chelate ring at the center has a mean of 92° ± 2° (mean of 4).

The twist angle for the (Cr[20]-aneN$_6$)Br$_3$ complex is 56° ± 1° and is larger than that for the [18]-aneN$_6$ complex due to the lesser strain in the 20-membered ring. The presence of two six membered chelate rings in the Cr[20]-aneN$_6$)Br$_3$ complex tends to relieve the strain energy when compared to the [18]-aneN$_6$ complex. This is in keeping with the observation that the $E_{1/2}$ for the Cr([18]-aneN$_6$)$^{3+/2+}$ couple is greater than that for the corresponding [20]-aneN$_6$ complex and the ligand field strength of Cr([20]-aneN$_6$)Br$_3$ complex is also larger.

Complexes related by the 'c' glide plane are enantiomers, so that the crystals are racemic. Six isomers are possible for complexes of [20]-aneN$_6$ and their structures are shown in Fig. 3.5. The stereochemical properties and the nomenclature adopted are also illustrated in the figure. All linkages are facial in structure I and structures II - VI have four facial linkages and two meridional linkages. Depending on the relative dispositions of the trimethylene linkages, *trans* and *cis* geometric isomers are possible. The six chelate rings in the complex are broken into two sets by assigning the chelate rings alternately to each set as one proceeds around the

Fig. 3.5. Possible structures for the complexes of 28:

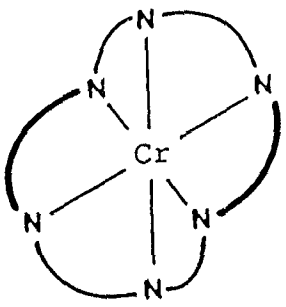

facial

I

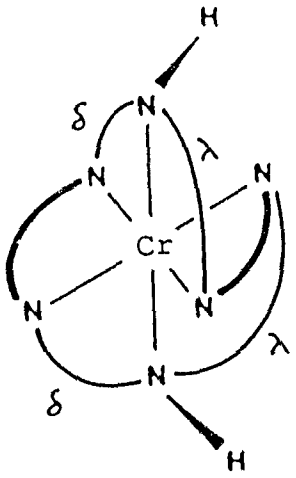

Λ-*mer*, *trans*, δ-NH

II

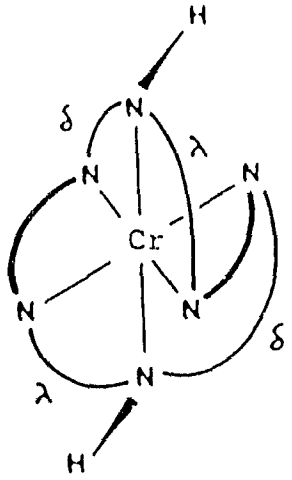

Λ-*mer*, *trans*, λ-NH

III

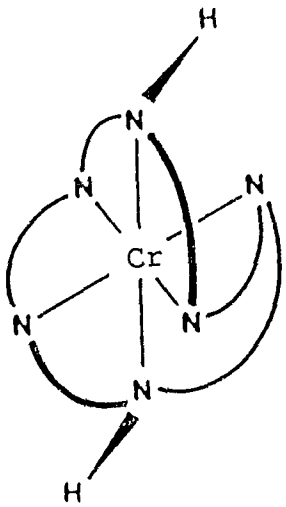

Λ-*mer*, *cis*-RR(λ-NH)

IV

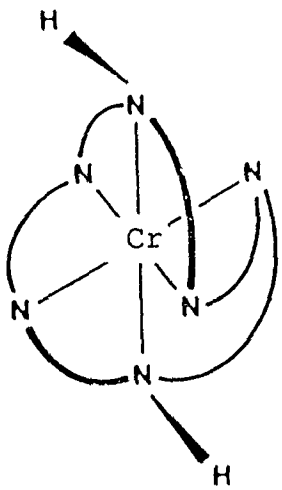

Λ-*mer*, *cis*-SS(λ-NH)

V

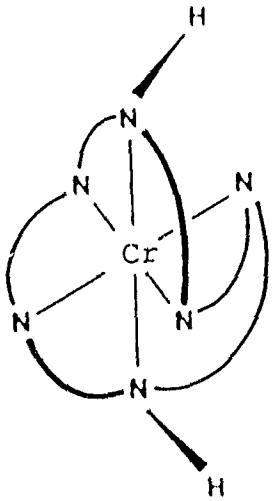

Λ-*mer*, *cis*-RS(δ-NH)

VI

macrocycle. Each set will then be arranged around a pseudo-3-fold axis in the same orientations as the three chelate rings in a tris-bidentate complex. Thus each set of three alternate chelate rings can be designated as Δ or Λ.[63] For the meridional structures, only one absolute configuration (Λ) is shown in Fig. 3.5. Information can then be appended to the Δ's and Λ's to indicate the nature and conformation of the individual chelate ring. The trimethylene bridging groups in the Cr([20]-aneN$_6$)Br$_3$ complex isolated are *cis* to one another. The complex is thus a Λ-mer, *cis*/ Δ-mer, *cis* racemate. Similar meridional isomers were obtained for the Ni([20]-aneN$_6$)$^{2+}$ and Co([20]-aneN$_6$)$^{3+}$ with the six-membered chelate rings *cis* to one another[73,74]. The conformations of the five-membered chelate rings for the meridional enantiomer **61** are shown below, while the six-membered rings adopt a chair conformation.

Cr1 - N4 - C5 - C6 - N7, λ

Cr1 - N1 - C2 - C3 - N4, δ

Cr1 - N17 - C16 - C15 - N14, δ

Cr1 - N14 - C13 - C12 - N11, λ, : Λ(λδ)Λ(δλ), mer, *cis* isomer.

Unlike the present case, the two trimethylene bridges in the Ni complex of [10]-aneN$_3$, **62**, are *trans* to one another.[75]

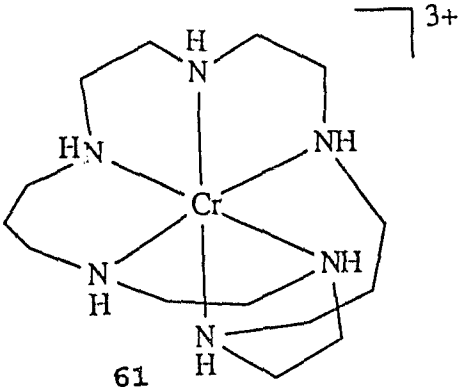

61

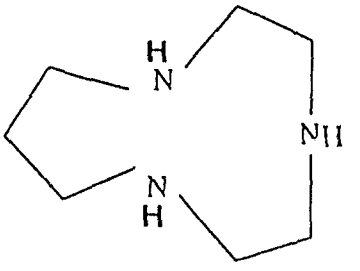

62

3.3.3. Crystal structure of $[Cu([20]\text{-}aneN_6)](ClO_4)_2$, 31:

Crystals of compound **31** were obtained by slow evaporation of ethanolic solutions of the complex. Analysis of the crystal structure showed the presence of a CuN_5 core in a distorted trigonal bipyramid geometry as shown in Fig. 3.6.

Fig. 3.6. ORTEP diagram of $[Cu(28)](ClO_4)_2$.

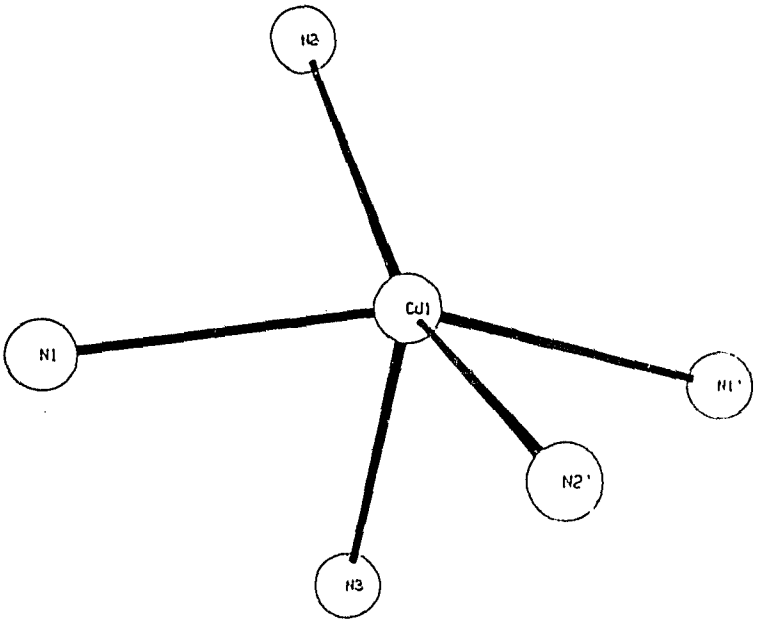

The crystal structure was solved to an *R* value of 0.13 at which point it was realised that the sixth nitrogen atom in the 20-membered macrocycle, together with the propane carbon atoms, were disordered and the structure could not be refined any further.

3.4. Spectroscopic studies:

Details of the uv-visible spectra for the various complexes are given in Table 3.8. The spectra of the chromium complexes obtained are similar to known octahedral MN_6 systems. A typical spectrum of the $[Cr[20]\text{-ane}N_6]^{3+}$ complex is shown in Fig. 3.7. The spectrum shows two bands, the one at lower energy has been assigned to the $^4T_{2g} \leftarrow {}^4A_{2g}$ transition and the other at higher energy to the $^4T_{1g} \leftarrow {}^4A_{2g}$ transition. The ligand field strength indicated by 10 Dq values for the chromium complexes of [18]-aneN_6 and [20]-aneN_6 were obtained from the $^4T_{2g} \leftarrow {}^4A_{2g}$ transition. The 10Dq value for the Cr complex of [20]-aneN_6, (21930 cm^{-1}) is greater than that of [18]-aneN_6, (21460 cm^{-1}) and is attributed to the strain-free 20-membered ring as opposed to the strained 18-membered macrocycle in the Cr complex.

Previous studies have shown that six coordinate complexes of Cu are blue-green (λ_{max} ~730 nm), five coordinate species blue (λ_{max} ~635 nm), and four coordinate complexes violet (λ_{max} ~500 nm).[36] A λ_{max} of 670 nm for the $Cu([20]\text{-ane}N_6)(ClO_4)_2$ is suggestive of a distorted CuN_6 or a CuN_5 core. The broad band

is typical of Cu(II) (d^9) metal ion. Similar results are obtained from X-ray crystal studies, where the copper atom is bound to 5 N atoms indicating the presence of a CuN_5 core. The energy of the absorption band for the Cu(II) complex of **28** (14881 cm^{-1}) is greater than that for the complex of **27** (14300 cm^{-1}) again indicating greater stability of the relatively strain-free 20-membered ring.

Table 3.8.

Table 3.8. Electronic absorption spectra of complexes.

Complex	λ_{max} (nm), (ε, L mol^{-1} cm^{-1})[a]	Ref.
$[Cr([9]\text{-}aneN_3)_2]^{3+}$	439(88), 340(64).	76
$[Cr([18]\text{-}aneN_6)]^{3+}$	466(227), 361(103).	PW
$[Cr([20]\text{-}aneN_6)]^{3+}$	456(104), 350(85).	PW
$[Fe([9]\text{-}aneN_3)_2]^{2+}$	601(6), 387(17), 288(560).	76
$[Fe([9]\text{-}aneN_3)_2]^{3+}$	500(sh), 430(82), 336(288).	76
$[Fe([18]\text{-}aneN_6)]^{2+}$	412, 308.	PW
$[Fe([20]\text{-}aneN_6)]^{2+}$	612.	PW
$[Cu([18]\text{-}aneN_6)]^{2+}$	699(140).	77
$[Cu([9]\text{-}aneN_3)_2]^{2+}$	618[b].	78
$[Cu([20]\text{-}aneN_6)]^{2+}$	672(150)[b].	PW

[a] H_2O (solvent), [b] CH_3CN (solvent), PW = present work

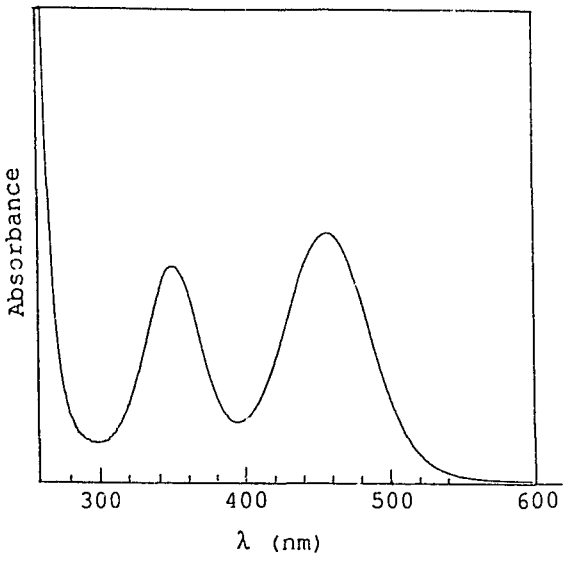

Fig. 3.7. UV-visible spectrum of $Cr([20]-aneN_6)Br_3$ in H_2O.

The electron spin resonance spectrum of **23** in CH_3NO_2 solutions (Fig. 3.8) is characteristic of an octahedral species with rhombic distortion, g_{zz} = 2.437; g_{xx} = 1.996; g_{yy} = 2.066. The g_{zz} feature is split into four lines by the copper nuclear hyperfine interaction (I = 3/2). There is also suggestion of super hyperfine interaction with the nitrogen nucleus (I = 1) on the high field side of the spectrum. For a tetragonally distorted d^9 metal complex with $g_{zz} > g_{xx}, g_{yy}$, the unpaired electron is present in the $d_{x^2-y^2}$ orbital (see Chapter 5).

Both the Fe(II) complexes of **27** and **28**, are blue in aqueous solutions but they are very air sensitive. Analytically pure solids of these complexes could not be prepared. The uv-visible spectrum of the blue Fe(II) complex of **28** shows an absorption peak at 612 nm which is

characteristic of low spin octahedral FeN_6 complexes.

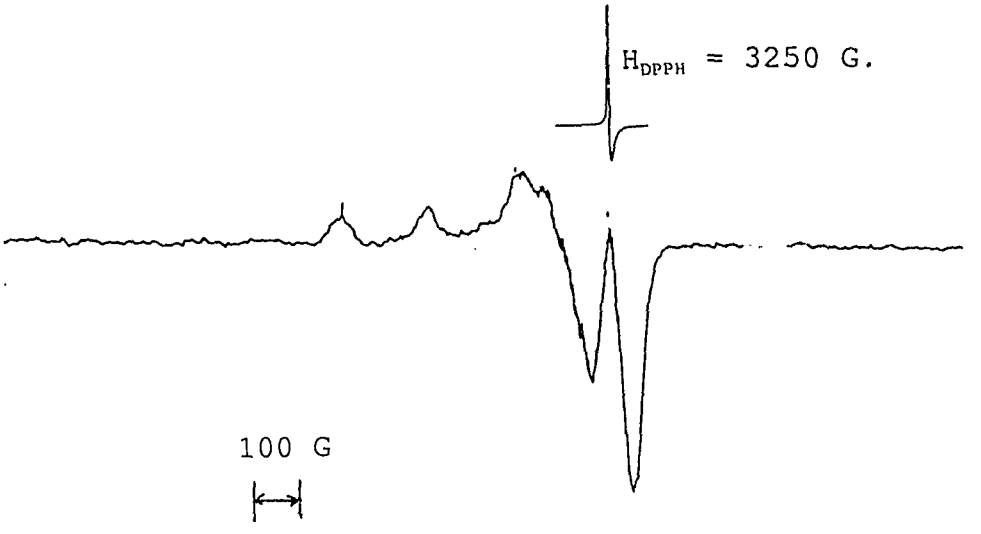

Fig. 3.8. ESR spectrum of $[Cu[20]\text{-}aneN_6](ClO_4)_2$ in CH_3NO_2.

The $[Fe([18]\text{-}aneN_6)]^{3+}$ complex cation is unstable in water and could not be recrystallised. It is insoluble in non-aqueous solvents. It decomposes in water to form the familiar red-brown gelatinous oxo and hydroxo species. The corresponding Fe(III) complex of **28** was obtained as a crude yellow solid but was insoluble in water and non-aqueous solvents and therefore could not be recrystallised to obtain an analytically pure sample. The affinity of Fe(III) for amines is very low.[18] Addition of aqueous ammonia to Fe(III) precipitates only the hydrous oxide. However, with small tridentate macrocyclic ligands, *e.g.*, $[9]\text{-}aneN_3$, **22**, bis-ligand, octahedral complexes of Fe(III) are formed.[79] The small tridentate ligand is suitably disposed to coordinate

with the Fe(III) ion. In the case of the large flexible [20]-aneN$_6$, polymeric products of Fe(III) are likely to be formed containing oxo and hydroxo bridges.

3.5. Electrochemistry :

The redox behaviour of the Cr, Mn and Cu complexes were studied by cyclic voltammetry. The peak-to-peak separations between the cathodic and the anodic waves of ~59 mV and i_{pa}/i_{pc} ratio of 1.0 indicates electrochemical reversibility for the one electron process, *e.g.* Fig. 3.9. Formal redox potentials for the present complexes and related ones are summarized in Table 3.9. For voltammograms that do not show a base line for the oxidation portion of the scan Nicholson[82] has developed a semi-empirical procedure which permits the computation of the ratio of the anodic and the cathodic currents (i_a/i_c) from a single-cycle voltamogram. The technique involves three easy-to-measure quantities; the cathodic current (i_c), the apparent anodic current (i_{aa}), and the current at the switching potential, i_{sw}, all measured from the cathodic base line as can be seen in Fig. 3.10. Using these parameters the true peak ratio can be given by:

$$i_a/i_c = i_{aa}/i_c + 0.485i_{sw}/i_c + 0.086. \quad \text{--- 3.1.}$$

Equation 3.1 was used to determine the i_a/i_c for the chromium complexes. When the redox potentials of $[Cr(\mathbf{22})_2]^{3+/2+}$ is compared with that of the corresponding complexes of **27** and **28**, it can be seen that the Cr(III) complex of **22** is more

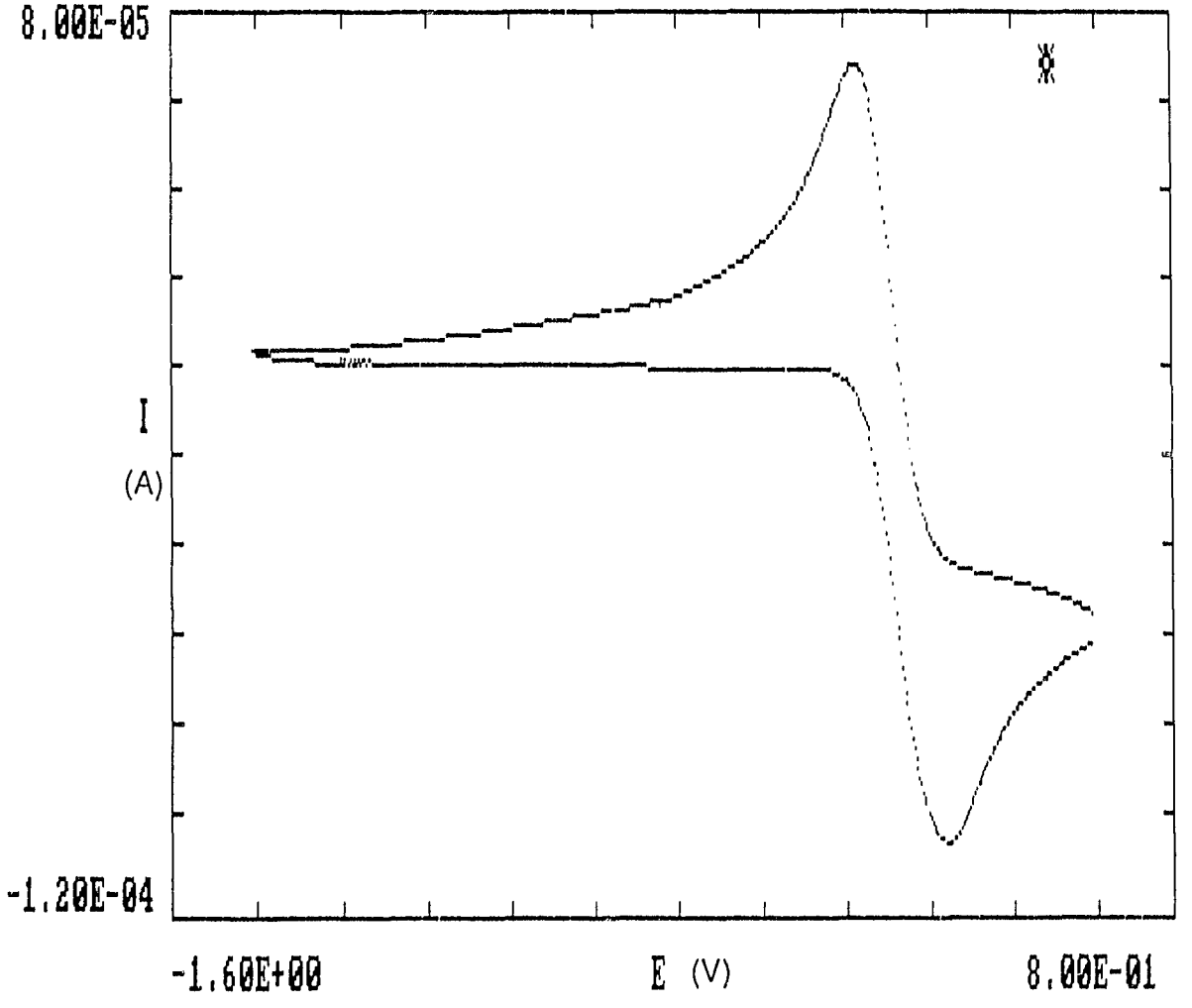

Fig. 3.9. Cyclic voltammogram of ferrocene at a Pt electrode in CH_3CN with $Ag/AgNO_3$ (0.1 M) reference electrode. Supporting electrolyte $(C_2H_5)_4N^+BF_4^-$. $E_{1/2}$ = 0.15 V.

Table 3.9. Redox potentials of complexes.

Complex	$E_{1/2}$ (V) *vs* NHE	ΔE_p (mV)[a]	Nature of wave	Ref.
$[Cr([9]\text{-}aneN_3)_2]^{3+/2+}$	−1.14[b]	63	reversible[c]	76
$[Cr(diamsar)]^{3+/2+}$	−1.11	70	reversible[c]	72
$[Cr([20]\text{-}aneN_6)]^{3+/2+}$	−1.02[b]	80	quasi-reversible[c]	PW
$[Cr([18]\text{-}aneN_6)]^{3+/2+}$	−0.92[b]	120	quasi-reversible[c]	PW
$[Cr(bipy)_3]^{3+/2+}$	−0.89[b]	59	reversible[c]	80
$[Mn([9]\text{-}aneN_3)_2]^{3+/2+}$	+0.62[d]	120[e]	quasi-reversible	76
$[Mn([20]\text{-}aneN_6)]^{3+/2+}$	+0.70[d]	–	irreversible	PW
$[Fe([9]\text{-}aneN_3)_2]^{3+/2+}$	+0.13[f]	60	reversible	76
$[Fe([18]\text{-}aneN_6)]^{3+/2+}$	+0.37[f]	95	quasi-reversible	PW
$[Cu([9]\text{-}aneN_3)_2]^{2+/+}$	−1.41[g]	–	irreversible	78
$[Cu([18]\text{-}aneS_4N_2)]^{2+/+}$	−0.31[g]	–	reversible	81
$[Cu([18]\text{-}aneN_6)]^{2+/+}$	−0.44[h]	–	reversible	77
$[Cu([20]\text{-}aneN_6)]^{2+/+}$	−0.67[g]	–	quasi-reversible	PW

[a]50 mV s^{-1}, [b]0.1 M $LiClO_4$, [c]Hanging-mercury-drop electrode, [d]0.1 M KCl at 3 °C, [e]scan rate 200 mV s^{-1}, [f]0.1 M $LiNO_3$, [g]CH_3CN, Fc^+/Fc, [h]SCE, PW = Present work.

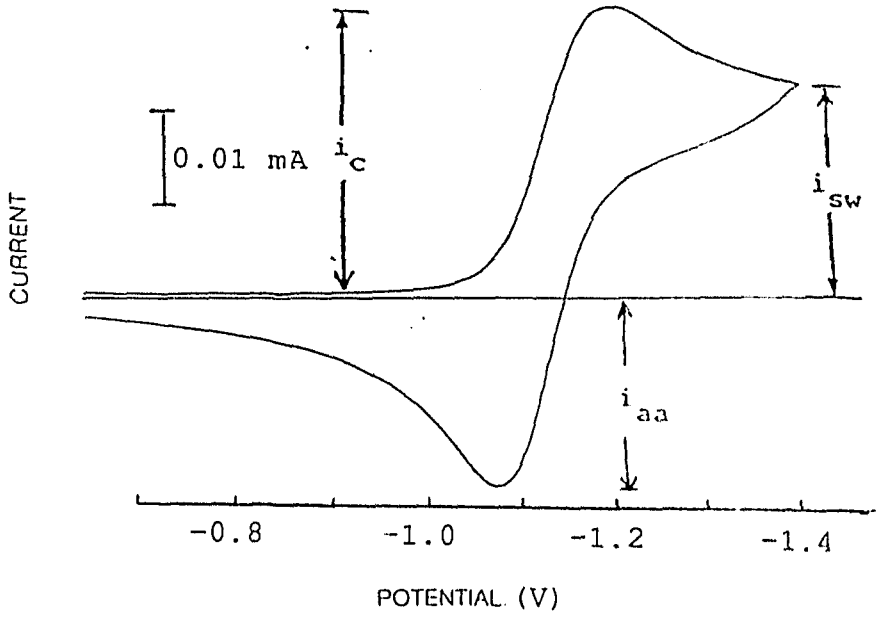

Fig. 3.10. Cyclic voltammogram of $[Cr(\mathbf{28})]^{3+/2+}$ in H_2O, scan rate 50 mV/s.

---

stable than that of **28**, which in turn is more stable than that of **27**. Similar results were obtained from absorption spectroscopy with ligand field strengths (10Dq) of [9]-aneN_3 (22779) cm^{-1} > [20]-aneN_6 (21930) cm^{-1} > [18]aneN_6 (21460) cm^{-1}. The presence of one or more six-membered chelate rings among five-membered rings in a complex tends to relieve strain energy. Thus in the complex of **27** the metal atom is subjected to a constrained octahedral environment. This is consistent with the kinetic observations that the strained $[Ni([18]\text{-ane}N_6)]^{2+}$ complex is more rapidly hydrolysed than $[Ni([20]\text{-ane}N_6)]^{2+}$.[73]

Cyclic voltammograms of the Cu complex in CH_3CN showed a quasi-reversible wave at $E_{1/2}$ = -1.08 V *vs* Fc^+/Fc, (Fc =

ferrocene) due to $[Cu(\mathbf{28})]^{2+/+}$, Fig. 3.11. $Ag/AgNO_3$ (0.1 M) was used as a reference electrode and NEt_4BF_4 (0.1 M) was used as the supporting electrolyte. Cu(I), being a d^{10} electronic configuration, is tetrahedral and such geometrical changes upon reduction may be reflected by the quasi-reversible nature of the voltammogram. The $E_{1/2}$ values of the Cu(II)/Cu(I) couple in $[Cu(\mathbf{28})](ClO_4)_2$, (-0.47 V *vs* SCE), are comparable to that of $[Cu_{(27)}](ClO_4)_2$, (-0.44 V *vs* SCE). The flexibility of the macrocyclic ring allows the formation of $[Cu(\mathbf{28})]^+$ ion, although of limited stability. The corresponding redox couple for the $[Cu([9]\text{-}aneN_3)_2]^{2+/+}$ is irreversible.[78] By incorporating soft donor atoms in the macrocyclic ring, the redox potentials move to more positive values. For example, the redox potential for the complex cation $[Cu(\mathbf{63})]^{2+}$ was found to be -0.31 V *vs* Fc^+/Fc.[81] Thus, both electronic effects and ring strain effects are important in the stabilization of a particular oxidation state.

The redox potential $E_{1/2}$, can be related to the ligand field splitting, 10Dq. A large ligand field splitting results in a higher degree of negative shift in the observed $E_{1/2}$ values.[83] Miyoshi *et al*[77] have obtained a linear relationship between the absorption maxima (λ_{max}) and the redox potentials ($E_{1/2}$ values) for the Cu(II) complexes of macrocyclic polyamines. Using a value of $E_{1/2}$ = -0.47 V (*vs* SCE) for the $[Cu(\mathbf{28})]^{2+/+}$ couple, a linear trend is observed between the $E_{1/2}$ and ν_{max} values, Table 3.10. and Fig. 3.12.

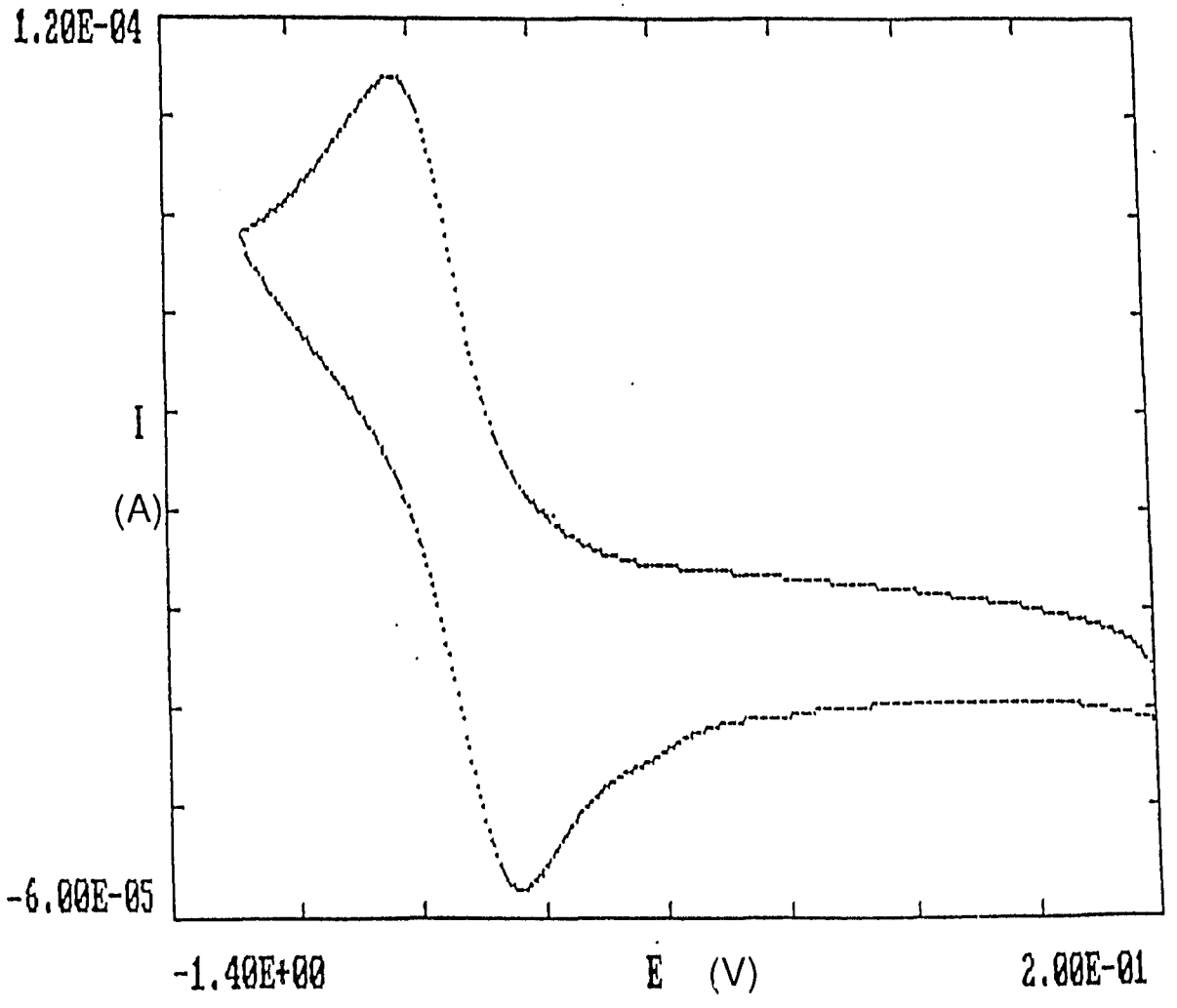

Fig. 3.11. Cyclic voltammogram of $[Cu(28)]^{2+/+}$ in CH_3CN with a $Ag/AgNO_3$ (0.1 M) reference electrode, NEt_4BF_4 (0.1 M), Pt electrode, scan rate 50 mV/s.

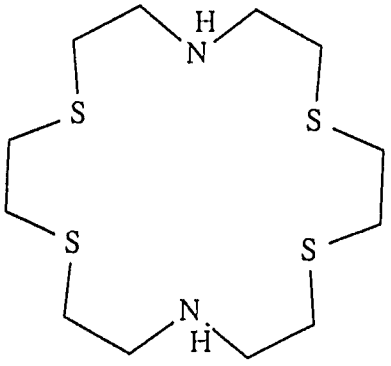

63

The $E_{1/2}$ values are most negative for square planar Cu(II) complexes with a large in-plane ligand field strength and increases to more positive values in distorted octahedral complexes.

Table 3.10. Correlation between $E_{1/2}$ and ν_{max} values in Cu polyamine macrocycles (L).[a]

L	$E_{1/2}$[b] (V)	ν_{max} (cm^{-1})
[18]-aneN_6	-0.440	14 300
[20]-aneN_6	-0.470[c]	14 881[c]
[15]-aneN_5	-0.570	17 000
[12]-aneN_4	-0.642	16 700
[14]-aneN_4	-0.729	19 500
o-[13]-aneN_4	-0.742	19 200

[a]Ref. 77, [b]$[CuL]^{2+/+}$, *vs* SCE, [c]Present work

o-[13]-aneN_4 = 1,4,7,10-tetraazacyclotridecane-11,13-dione.

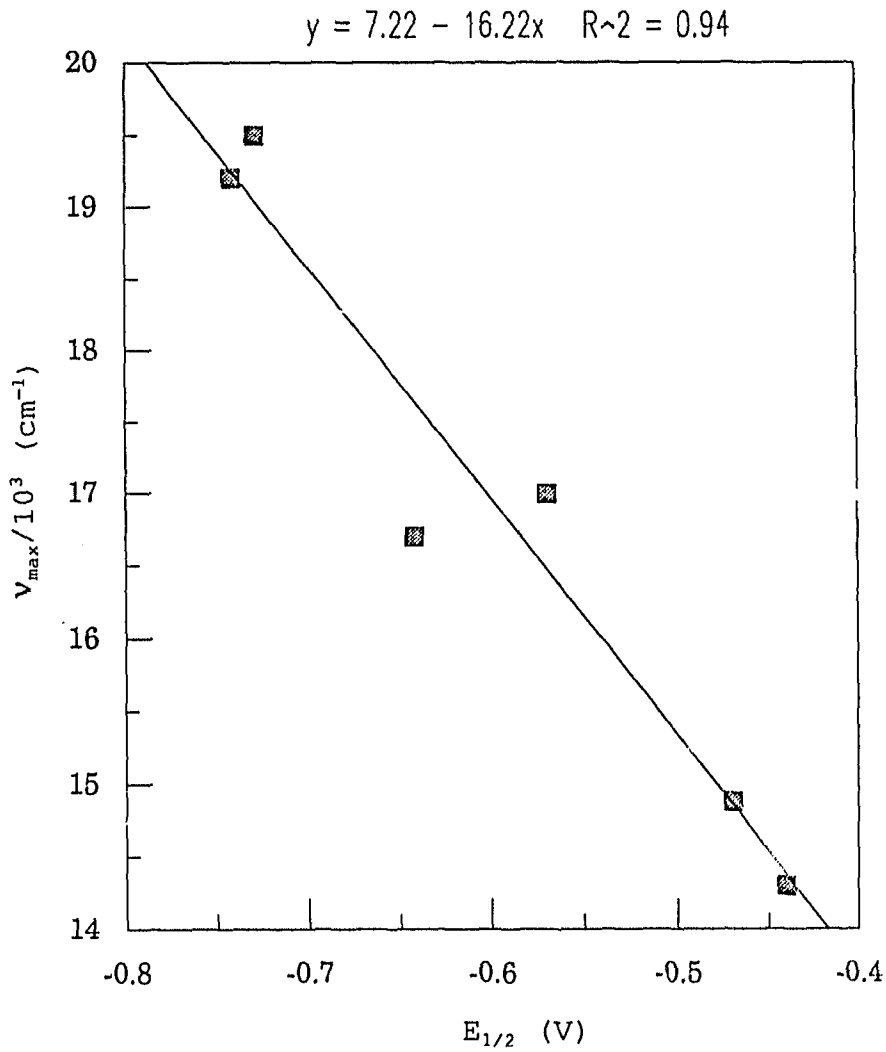

Fig. 3.12. Correlation between $E_{1/2}$ *vs* ν_{max} for the Cu complexes (data from Table 3.10.).

3.6. Conclusions:

The ligating abilities of large macrocyclic polyamines with transition metal atoms were studied. The effect of one or more propyl linkages in the macrocycle on the spectroscopic and redox properties and their relationship were investigated. Both electronic and ring constraint effects are important in the stabilization of various oxidation states.

Thus, monomeric Cr and Cu complexes of the hexaamines macrocyclic ligands were isolated and structurally characterised. The crystal structure of a facial isomer of the chromium complex of the 18-membered macrocycle was obtained for the first time.

CHAPTER 4

Synthesis of 1,5-dithia-8-azacyclodecane and the study of its Nickel and Palladium complexes

4.1. Introduction:

There have been extensive investigations on the transition metal complexes of homoleptic macrocycles containing N donor atoms.[21,22,84] With the availability of the homoleptic trithia ligand [9]-aneS_3,[85,86] **64**, in good yields, its complexation properties with 3d,[86,87] 4d,[88-93] and 5d[94] transition metal ions have been studied.

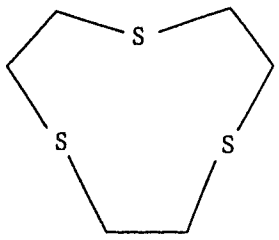

64

Bis- complexes of **22** (page 25) have been obtained with Fe,[76] Co,[95] Ni,[49] Pd,[96] Ru,[97] and Pt[98] ions. The steric demands of the ligand renders it stable towards ligand dissociation and facilitates oxidation of the metal centre. Thus stable $[M(\mathbf{22})_2]^{3+}$ octahedral complexes have been obtained, *e.g.*, M = Ni,[49] Pd,[99] and Ru.[97] These complexes serve as one electron outer sphere reagents in electron transfer reactions and the rates of self-exchange have been obtained for $[M(\mathbf{22})_2]^{3+/2+}$ complexes.

Although the facial disposition of the nine- membered ring induces formation of an octahedral structure with divalent first row transition metal ions, the ligand does not enforce octahedral geometry with the Pd(II) and Pt(II) ions owing to steric considerations of heavier element d^8 ions.

The crystal structure of the Pd(II) complex of **22** has the ligand coordinated in a bidentate, square planar manner and is similar to that in the Pt(II) complex ion. The chelate rings containing the apical N atoms in the Pd complex have an *'anti'* conformation (see Section 4.6. for definition). However, solution studies on the $[Pd(\mathbf{22})_2]^{2+}$ species provide evidence of fluxional behaviour at the Pd(II) centre.[96]

With the corresponding homoleptic thia ligand, **64**, Pt(II) forms an elongated square based pyramidal structure with two sulfur atoms from each ligand coordinated to the Pt(II) centre in a square plane and the third S atom from one of the ligands coordinated apically.[94] The $[Pd(\mathbf{64})_2]^{2+}$ ion is essentially square planar, with four thia donor atoms in an approximate square plane and two S atoms with significant apical interactions ($Pd\text{-}S_{ax}$ = 2.952(4) Å).[92] The structure shows a *'syn'* conformation of the rings containing the apical S atoms.

Although thioether ligands are poor σ- donors to metal ion centres, they can serve as π- donors *via* donation of the available lone pair on sulfur or as a π- acceptor[87] using empty d- orbitals on sulfur. The π- donor[86] capability of the S atoms is manifested in the stabilization of Pd(III),[100] Pt(IV),[94] Mo(IV),[101] and Nb(V)[102] complexes of [9]-aneS_3. By incorporating both hard and soft donor atoms in the macrocycle, stabilization of both low and high oxidation states in the transition metal complex ions can be achieved. Such a mixed donor environment could distort the geometry of

complexes, thereby, causing the metal ion to be in an "entatic" state. This would permit stabilization of uncommon oxidation states and unusual geometries in these complexes. Nickel enzymes have been identified in certain methanogenic bacteria where mixed donor coordination environments around the central metal atom are thought to be present.[103]

The stereochemical and redox properties of Pd complexes of [18]-aneS_4N_2, **63**, have been studied by Reid *et al.*[104] The Pd(II) ion in the complex is coordinated to an N_2S_2 donor set in a square plane and the remaining thioether donor atoms interact at long range with Pd(II) ($Pd-S_{ax}$ = 2.954(4) Å, $Pd-S_{ax}$ = 3.000(3) Å). Synthesis and reactivity of the nine- membered ligand [9]-aneS_2N, **65**, and its nickel complex have been studied recently.[105]

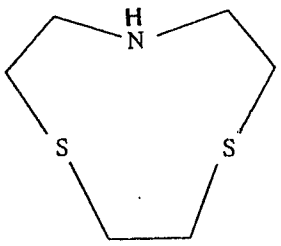

65

There has been no investigation to date on the mixed donor ten- membered macrocycles. The ligating abilities of mixed donor macrocycles containing S and N donor atoms are not very well understood. The lower symmetry of these ten-membered ligands offer new stereochemical characteristics that are not present in the more symmetrical analogs. Hence the synthesis and reactivity of the hitherto unknown ligand, [10]-aneS_2N,

24, and its Ni and Pd complexes were carried out. The present study provides the first example of an elongated octahedral Pd(II) complex containing two axial N atoms bent towards the axis with *'syn'* conformation of the nitrogen containing chelate rings. Crystallographic evidence is also presented in support of the possible mechanism proposed by Hunter *et al*[96] for the fluxional process within the chelate ring of the $[Pd(\mathbf{22})_2]^{2+}$ cation.

4.2. Synthesis:

The synthetic route to ligand **24** is outlined in Scheme 2.4., (Chapter 2). The tritosylate of diethanol amine, **45**, was synthesised according to published procedures. Care was taken to ensure that both the diol groups were tosylated. The cyclization was carried out using Cs_2CO_3 as a base according to the methods of Buter and Kellogg.[33] Several methods for the detosylation of the cyclised amine were attempted. When sulfuric acid was used, the cyclised tosylate degraded completely. Reductive elimination with sodium naphthalenide in DME[106] was not successful and the yields were extremely poor (0-5%). Detosylation of the corresponding nine- membered tosylate ([9]-aneS_2NTs) was carried out using anhydrous phosphoric acid.[105] In the present case, yields of about 25% of the free ligand, **24**, were obtained with this reagent. Reduction with lithium aluminum hydride in THF[107] proved to be mild, but the detosylation was not complete even after a 4-day

reaction period. One of the most frequently used reagents for the cleavage of sulfonamides is hydrobromic acid in a mildly acidic organic solvent containing phenol.[108,109] Detosylation was carried out using 30% HBr in CH_3COOH containing phenol and yields of 55 - 60% of the free ligand were obtained. The end point of the detosylation was confirmed by periodically testing the solubilities of the reaction mixture in 1 M NaOH.

The Ni complex, **48**, was obtained by the method described in Section 2.1.8. The red Pd complex, **49**, was obtained from the reaction of $Pd(CH_3COO)_2$ and the ligand in CH_3CN. Diffusion of ether into nitromethane solutions of the red complex **49** yielded tiny red crystals which were very hygroscopic and sensitive to solvent loss.

4.3. Crystal structure of $[Ni(24)_2].(ClO_4)_2.(CH_3CN)_2$, 48:

Diffraction quality crystals of **48** were obtained from acetonitrile solutions. The purple crystal was sealed in a Lindemann tube and mounted and centered on a Nonius CAD4 diffractometer. The cell was refined using 25 centered reflections in the range θ = 22 - 43°. Intensity measurements were carried out with Mo radiation, λ = 0.71069 Å. The crystal data are given in Table 4.1. The asymmetric unit consisted of the complex cation, two perchlorate anions and two molecules of acetonitrile as solvents of crystallisation. Data reduction yielded 3132 reflections with $I > 3\sigma(I)$, which were used for solution and refinement of the structure.

Table 4.1. Experimental crystallographic data for $[Ni([10]\text{-}aneS_2NH)_2].(ClO_4)_2.(CH_3CN)_2$, **48**.

Compound	**48**
Formula	$Ni_1S_4N_2C_{14}H_{30}(ClO_4)_2(CH_3CN)_2$
MW	694.36
Crystal color	purple
Crystal system	monoclinic
Space group	$P2_1/n$ (No. 14)
Cell dimensions	
a (Å)	9.566(1)
b (Å)	22.037(2)
c (Å)	14.603(2)
α (°)	90
β (°)	106.90(1)
γ (°)	90
V (Å^3)	2945.45
Z	4
D_{calc} (g/cm^3)	1.566
Crystal dimensions (mm^3)	1.26×0.6×0.4
Diffractometer	Nonius, CAD4
Radiation (λ, Å)	Mo-K_α (0.71069)
Filter	Zirconium
Measurement	2θ (2 - 45°)
Octants collected	±h,k,l
std. reflections	0012,800,0120,008,084,0120
no. refln. collected	3740
no. refln. I > nσ(I)	3132 (n = 3)
no. parameters	334
Linear abs coeff. (cm^{-1})	10.87
Solution method	MULTAN
R^a	0.0668
R_w^b	0.0783

[a] $R = \Sigma\| F_o| - |F_c\| / \Sigma |F_o|$

[b] $R_w = [\Sigma w(|F_o| - |F_c|)^2 / \Sigma w(|F_o|)^2]^{1/2}$ where $w = 6.94/(\sigma^2 F + 0.001F^2)$

The solution of the phase problem was achieved using MULTAN[56] which revealed the position of the Ni atom. Subsequent Fourier syntheses revealed the positions of the carbon and nitrogen atoms. Hydrogen atoms were not included in the calculations. The asymmetric unit consisted of 37 atoms with 334 parameters to be refined. The refinement converged with a maximum shift/esd of 0.050 on the final cycle, $R = 0.0668$; $R_w = 0.0783$.

The ORTEP diagram of the complex cation $[Ni([10]\text{-}aneS_2NH)_2]^{2+}$ with atomic labelling is shown in Fig. 4.1. The fractional atomic coordinates and isotropic temperature parameters are shown in Table 4.2. The interatomic bond lengths and bond angles are shown in Table 4.3.

The complex consists of four S donor atoms and two N atoms from the two ten-membered ligands coordinated to the central Ni atom in an octahedral fashion. The two trimethylene bridges are *trans* to one another as are the N atoms. The bond lengths and the bond angles for the ten-membered macrocyclic complexes containing N and S donor atoms are given in Table 4.4. The Ni-N distance (2.125(6) Å) is comparable to the corresponding $[Ni(\mathbf{62})_2]^{2+}$ ion, (2.12(2) Å)[75] and slightly shorter than the $[Ni(\mathbf{25})_2]^{2+}$ complex (2.142(5) Å), (see Chapter 7). The Ni-S bonds (2.408(2) Å) are also similar to those observed in the Ni complexes of **25** (2.395(1) Å) and **23** (2.395(9) Å), (see Chapter 6). The $[Ni(\mathbf{24})_2]^{2+}$ ion thus exhibits characteristics intermediate between those of the

Fig. 4.1. ORTEP diagram of $[Ni([10]\text{-ane}S_2NH)_2]^{2+}$ cation with 25% thermal ellipsoids.

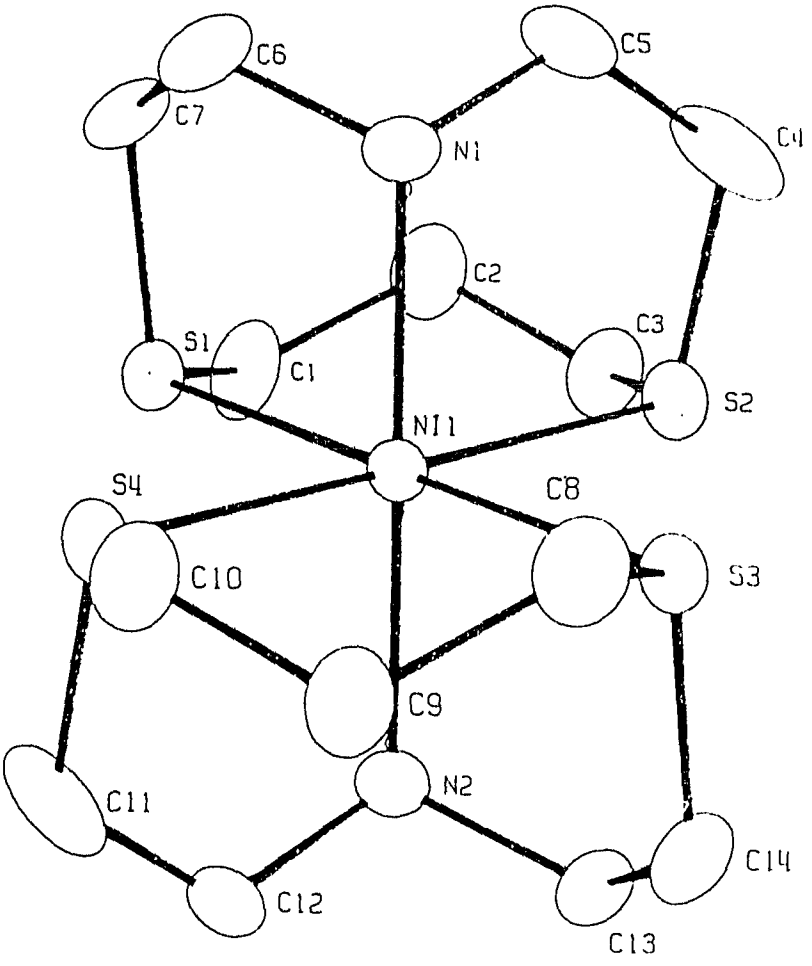

Table 4.2.

Fractional atomic coordinates and temperature parameters.

Atom	x/a	y/b	z/c	Ueq
Ni(1)	19600(9)	25949(4)	51507(6)	372(4)
Cl(1)	24422(23)	40127(10)	-3660(17)	590(9)
Cl(2)	15403(23)	8896(10)	8070(16)	587(9)
S(1)	12215(21)	34714(9)	41403(13)	454(7)
S(2)	25016(24)	31447(10)	66374(14)	539(8)
S(3)	26667(22)	17115(10)	61514(14)	481(8)
S(4)	13830(22)	20582(10)	36480(14)	503(8)
O(1)	3317(10)	4471(4)	-524(11)	161(7)
O(2)	1192(13)	4191(5)	-233(12)	200(9)
O(3)	2018(31)	3729(11)	-1188(15)	395(22)
O(4)	3033(16)	3563(7)	136(20)	297(16)
O(5)	2660(9)	679(4)	496(8)	125(5)
O(6)	838(10)	407(4)	1082(8)	129(5)
O(7)	570(15)	1223(6)	60(11)	188(8)
O(8)	2025(21)	1284(7)	1532(10)	258(12)
N(1)	-237(7)	2585(3)	5201(5)	48(2)
N(2)	4158(7)	2585(3)	5103(5)	50(3)
N(3)	-908(11)	4706(5)	2654(7)	93(4)
N(4)	-208(28)	1679(9)	7712(20)	263(18)
C(1)	1837(11)	4190(4)	4731(7)	70(4)
C(2)	1618(11)	4298(4)	5722(7)	75(4)
C(3)	2679(10)	3975(4)	6555(7)	69(4)
C(4)	782(13)	3008(7)	6853(9)	111(6)

Table 4.2. (contd.)

C(5)	-452(11)	2863(8)	6047(7)	111(6)
C(6)	-1229(9)	2868(5)	4342(7)	72(4)
C(7)	-726(8)	3464(4)	4047(7)	61(4)
C(8)	1931(10)	1016(4)	5539(7)	66(4)
C(9)	2135(11)	890(4)	4546(7)	69(4)
C(10)	1145(10)	1241(4)	3714(6)	65(4)
C(11)	3108(12)	2181(6)	3432(8)	100(6)
C(12)	4333(11)	2278(7)	4242(7)	98(6)
C(13)	5150(9)	2310(4)	5977(6)	58(3)
C(14)	4597(9)	1693(4)	6224(7)	64(4)
C(15)	40(12)	4823(5)	2340(7)	67(4)
C(16)	1189(15)	4959(7)	1918(11)	120(7)
C(17)	-8(20)	1140(11)	7658(12)	144(10)
C(18)	417(15)	535(6)	7666(11)	108(6)

Estimated standard deviations are given in parentheses.

Coordinates × 10^n where n = 5,5,5,4,4,4 for Ni,Cl,S,O,N,C.

Temperature parameters × 10^n where n = 4,4,4,4,3,3 for Ni,Cl,S,O,N,C.

U_{eq} = the equivalent isotropic temperature parameter.

$U_{eq} = 1/3 \sum_i \sum_j U_{ij} a_i^* a_j^* (a_i . a_j)$

Primed values indicate that U_{iso} is given

$T = \exp-(8\pi^2 U_{iso} \sin^2\theta/\lambda^2)$

Table 4.3.

Interatomic distances (Å)

Atoms	Distance	Atoms	Distance
S(1) -Ni(1)	2.408(2)	C(12) -N(2)	1.478(12)
S(2) -Ni(1)	2.407(2)	C(13) -N(2)	1.481(11)
S(3) -Ni(1)	2.410(2)	C(15) -N(3)	1.158(13)
S(4) -Ni(1)	2.411(2)	C(17) -N(4)	1.208(24)
N(1) -Ni(1)	2.125(6)	C(2) -C(1)	1.540(14)
N(2) -Ni(1)	2.124(6)	C(3) -C(2)	1.516(13)
O(1) -Cl(1)	1.374(8)	C(5) -C(4)	1.440(15)
O(2) -Cl(1)	1.325(9)	C(7) -C(6)	1.503(13)
O(3) -Cl(1)	1.309(14)	C(9) -C(8)	1.544(13)
O(4) -Cl(1)	1.265(14)	C(10) -C(9)	1.518(13)
O(5) -Cl(2)	1.361(7)	C(12) -C(11)	1.418(15)
O(6) -Cl(2)	1.378(7)	C(14) -C(13)	1.541(13)
O(7) -Cl(2)	1.415(11)	C(16) -C(15)	1.438(17)
O(8) -Cl(2)	1.344(10)	C(18) -C(17)	1.392(24)
C(1) -S(1)	1.816(9)		
C(7) -S(1)	1.828(8)		
C(3) -S(2)	1.845(10)		
C(4) -S(2)	1.788(9)		
C(8) -S(3)	1.810(9)		
C(14) -S(3)	1.819(9)		
C(10) -S(4)	1.820(9)		
C(11) -S(4)	1.788(9)		
C(5) -N(1)	1.446(12)		

Table 4.3. (contd.)

Bond angles (°)

Atoms	Angle	Atoms	Angle
S(2) -Ni(1) -S(1)	95.6(1)	O(7) -Cl(2) -O(6)	111.0(8)
S(3) -Ni(1) -S(1)	179.2(1)	O(8) -Cl(2) -O(5)	111.0(9)
S(3) -Ni(1) -S(2)	84.9(1)	O(8) -Cl(2) -O(6)	110.8(7)
S(4) -Ni(1) -S(1)	83.5(1)	O(8) -Cl(2) -O(7)	105.7(11)
S(4) -Ni(1) -S(2)	178.9(1)	C(1) -S(1) -Ni(1)	114.3(3)
S(4) -Ni(1) -S(3)	96.0(1)	C(7) -S(1) -Ni(1)	98.6(3)
N(1) -Ni(1) -S(1)	85.0(2)	C(7) -S(1) -C(1)	103.1(4)
N(1) -Ni(1) -S(2)	86.0(2)	C(3) -S(2) -Ni(1)	116.1(3)
N(1) -Ni(1) -S(3)	94.4(2)	C(4) -S(2) -Ni(1)	96.1(4)
N(1) -Ni(1) -S(4)	93.4(2)	C(4) -S(2) -C(3)	106.5(6)
N(2) -Ni(1) -S(1)	96.0(2)	C(8) -S(3) -Ni(1)	112.6(3)
N(2) -Ni(1) -S(2)	94.6(2)	C(14) -S(3) -Ni(1)	98.9(3)
N(2) -Ni(1) -S(3)	84.6(2)	C(14) -S(3) -C(8)	104.6(4)
N(2) -Ni(1) -S(4)	86.1(2)	C(10) -S(4) -Ni(1)	115.8(3)
N(2) -Ni(1) -N(1)	178.8(2)	C(11) -S(4) -Ni(1)	96.1(3)
O(2) -Cl(1) -O(1)	115.2(6)	C(11) -S(4) -C(10)	107.2(6)
O(3) -Cl(1) -O(1)	103.8(10)	C(5) -N(1) -Ni(1)	114.3(6)
O(3) -Cl(1) -O(2)	102.9(14)	C(6) -N(1) -Ni(1)	111.4(5)
O(4) -Cl(1) -O(1)	118.9(9)	C(6) -N(1) -C(5)	109.4(8)
O(4) -Cl(1) -O(2)	114.7(11)	C(12) -N(2) -Ni(1)	113.0(6)
O(4) -Cl(1) -O(3)	97.2(16)	C(13) -N(2) -Ni(1)	111.6(5)
O(6) -Cl(2) -O(5)	109.3(5)	C(13) -N(2) -C(12)	110.2(7)
O(7) -Cl(2) -O(5)	108.9(8)	C(2) -C(1) -S(1)	117.9(7)

Table 4.3. (contd.)

C(3)	-C(2)	-C(1)	116.1(8)	C(9)	-C(10)	-S(4)	119.3(6)
C(2)	-C(3)	-S(2)	117.7(6)	C(12)	-C(11)	-S(4)	117.2(7)
C(5)	-C(4)	-S(2)	118.1(7)	C(11)	-C(12)	-N(2)	120.5(8)
C(4)	-C(5)	-N(1)	120.5(8)	C(14)	-C(13)	-N(2)	112.6(7)
C(7)	-C(6)	-N(1)	115.7(7)	C(13)	-C(14)	-S(3)	112.2(6)
C(6)	-C(7)	-S(1)	113.0(6)	C(16)	-C(15)	-N(3)	178.0(11)
C(9)	-C(8)	-S(3)	118.6(6)	C(18)	-C(17)	-N(4)	172.2(23)
C(10)	-C(9)	-C(8)	116.1(8)				

Estimated standard deviations are given in parentheses.

Table 4.4. Comparison of bond lengths (Å) and bond angles (°) in Ni(II) bis complexes of ten-membered macrocycles.

	Ligands			
	62	**25**	**24**	**23**
Ni - N	2.123	2.142	2.125	-
Ni - S	-	2.395	2.408	2.395
N - Ni - N[a]	86.6	87.1	-	-
S - Ni - S[a]	-	-	95.8	94.1
S - Ni - N[b]	-	85.5	85.4	-
N - Ni - N[b]	82.4	-	-	-
S - Ni - S[b]	-	-	-	89.1

[a] six-membered chelate bite angle.

[b] five-membered chelate bite angle.

62 = [10]-aneN_3, **25** = [10]-aneN_2S, **24** = [10]-aneS_2N, **23** = [10]-aneS_3.

$[Ni(\mathbf{62})_2]^{2+}$ ion and $[Ni(\mathbf{23})_2]^{2+}$. As the N atoms are being replaced by the S donor atoms the bite angle for the five-membered chelate ring increases towards the ideal octahedral angle of 90° in the $[Ni(\mathbf{23})_2]^{2+}$ ion. In the Ni complex of **24**, the six-membered chelate $\angle S_1\text{-Ni-}S_2$ (95.8(2)°) is significantly larger than the $\angle N_1\text{-Ni-}N_2$ of the $[Ni(\mathbf{25})_2]^{2+}$ complex, (87.1(2)°), in accordance with the larger S atoms. In the $[Ni(\mathbf{23})_2]^{2+}$ ion the six-membered chelate bite angle, $S_1\text{-Ni-}S_2$ was found to be 94.1(1)°, smaller than that in the complex (**48**) under study. In this case, **48**, the axially-compressed nitrogen atoms force the equatorial sulfur atoms further apart giving rise to a larger equatorial $S_1\text{-Ni-}S_2$ six-membered chelate bite angle of 95.8(2)°. The S-Ni-N intraligand angles for both the Ni complexes of **24** and **25** compare well at 85.5(1)° and 85.4(8)° respectively. The Ni complex of the corresponding nine-membered ligand [9]-aneS_2N, **65**, shows an S-Ni-S equatorial angle of 87.4(0)° which is closer to that observed in the [9]-aneS_3 system, 88.0°. The larger ten-membered ring in the present case allows for the axial N atoms to reach over and occupy the apical position. However, for the $[Ni(\mathbf{65})_2]^{2+}$ complex the N donor atoms in the smaller ring are unable to completely occupy the apical position. These results are also substantiated by the absence of a reverse ESR spectrum ($g_\parallel > g_\perp$) for the corresponding $[Ni(\mathbf{65})_2]^{3+}$ ion.

There are four conformational possibilities for the ten-membered ligand in which the ligating atoms are all

endodentate facilitating facial coordination of the ligand. The various conformations have been discussed in the literature.[110,111,112] The conformation of the ten-membered ring, **24**, in its nickel complex is the [2233] conformation with the six-membered chelate ring in the chair form, Fig. 4.2.

Fig. 4.2. ORTEP diagram of $[Ni([10]\text{-ane}S_2NH)_2]^{2+}$ viewed down the pseudo-3-fold axis of the molecule.

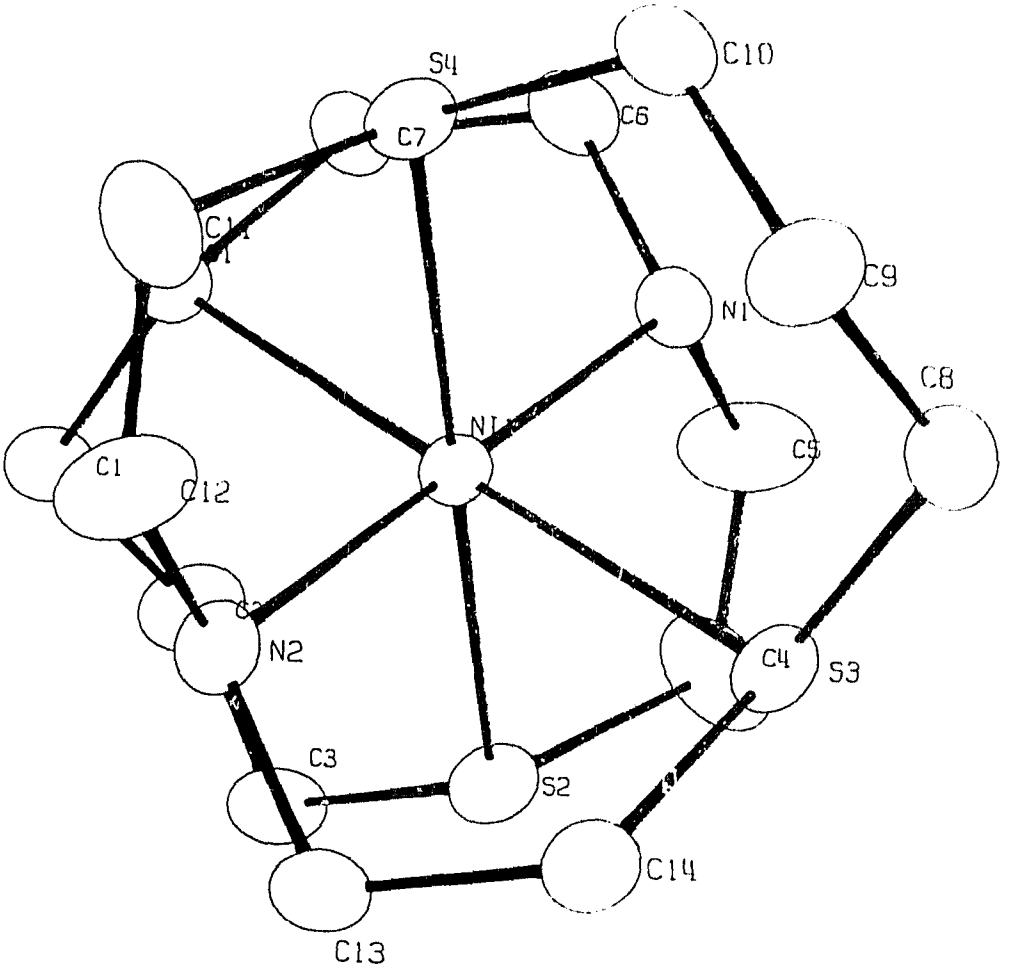

4.4. Ring conformations of $[Pd(24)_2](PF_6)_2$, 49:

Two conformations for the chelate rings of the macrocyclic complex, $M(X_3)_2^{2+}$ (M = Pd, X = donor atom of the tridentate macrocycle), are possible with respect to the MX_4 plane. The chelate rings containing the axial donor atoms can be on the same side or on opposite sides of the MX_4 plane as shown below:

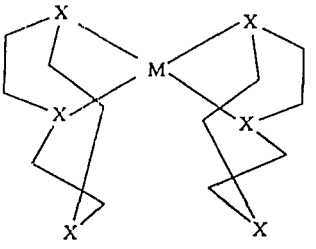

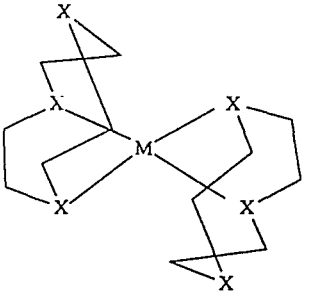

The conformation of the rings in the former case is termed as *'syn'* and in the latter *'anti'*. Again, two conformations for these rings can exist with respect to the axis. The chelate rings are said to be in the *'endo'* conformation if the rings are bent towards the metal centre and in an *'exo'* conformation if the chelate rings are bent away from the central metal ion as shown below:

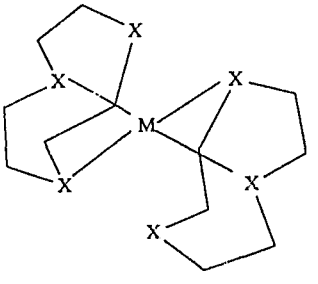

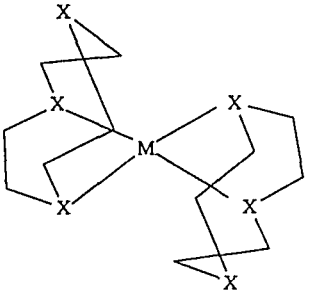

4.5. Crystal structures of Pd complexes of 24:

4.5.1. Crystal structure of $Pd([10]\text{-ane}S_2NH)_2(PF_6)_2.2CH_3NO_2$, 49a:

Blue crystals of the complex were obtained after 7 - 10 days by diffusion of ether into nitromethane solutions of the red complex. The crystal was very sensitive to solvent loss and was mounted in a Lindemann tube together with some solvent and sealed immediately. The crystal had lost 50% of its crystallinity by the end of data collection. Since the crystal was very sensitive to solvent loss the data were collected at speed-8 on the CAD4 Nonius diffractometer. The crystallographic data are listed in Table 4.5. The total number of reflections measured were 2317 and data reduction yielded 1283 reflections with $I > 1.5\sigma(I)$ which were used for solution and refinement of the structure. Solution of the phase problem was achieved by Patterson maps using SHELX76[55]. Completion and refinement of the structure were carried out by difference electron density maps and least squares analysis. Although the $[Pd(\mathbf{24})_2]^{2+}$ cation was ordered, one of PF_6^- counter ions was disordered. Together with four S atoms, the Pd atom and two P atoms were made anisotropic. All other atoms were refined isotropically. The final R value obtained was 0.0960. Important bond lengths and bond angles are given in Table 4.6.

The ORTEP diagram of the complex is shown in Fig. 4.3. The coordination geometry around the Pd atom is an elongated square pyramid with the S atoms in the axial position, bent

Table 4.5. Experimental crystallographic data for $[Pd([10]-aneS_2NH)_2](PF_6)_2.2CH_3NO_2$, **49**.

Compound	**49a**	**49b**
Formula	$Pd_1S_4N_2C_{14}H_{30}P_2F_{12}.2(CH_3NO_2)$	same as **a**
MW	873.0	873.0
Crystal color	blue	red
Crystal system	triclinic	monoclinic
Space group	P1	I2/a (No. 15)
Cell dimensions		
a (Å)	11.769(6)	18.322(3)
b (Å)	14.665(19)	8.072(3)
c (Å)	10.148(8)	22.041(2)
α (°)	80.10(9)	90
β (°)	95.01(5)	101.05
γ (°)	113.68(7)	90
V (Å^3)	1579.8	3199.5
Z	2	4
D_{calc} (g/cm^3)	1.835	1.787
D_{meas} (g/cm^3)	1.811	-
Crystal dimensions (mm^3)	0.7×0.8×0.15	0.06×0.16×0.24
Diffractometer	Nonius, CAD4	Nonius, CAD4
Radiation (λ, Å)	Mo-K_α (0.71069)	Cu-K_α (1.542)
Filter	Zirconium	Nickel
Measurement	2θ (2 - 40°)	2θ (2 - 80°)
Octants collected	±h,k,l	±h,k,l
std. reflections	453,091,057, 091,126,451.	1000,0014,640, 1006,028,2014
no. refln. collected	2317	897
no. refln. I > nσ(I)	1283 (n = 1.5)	-
no. parameters	208	196
Linear abs coeff. (cm^{-1})	10.30	9.38
Solution method	Patterson map	MULTAN
R^a	0.0960	0.159
R_w^b	0.0802	0.138

[a] $R = \Sigma\| F_o| - |F_c\| / \Sigma |F_o|$

[b] $R_w = [\Sigma w(|F_o| - |F_c|)^2 / \Sigma w(|F_o|)^2]^{1/2}$ $\quad w_{blue} = 1.41/(\sigma^2 F + 0.001F^2)$ $\quad w_{red} = 0.30/(\sigma 2F + 0.001F^2)$

Table 4.6. Important bond lengths (Å) and bond angles (°) for the blue $[Pd(\mathbf{24})_2]^{2+}$ cation.

Interatomic distances (Å)

Atoms	Distance	Atoms	Distance
S(1) -Pd(1)	2.44(2)	C(6) -S(4)	1.98(6)
S(2) -Pd(1)	2.84(2)	C(12) -S(4)	1.94(6)
S(3) -Pd(1)	2.20(2)	C(10) -N(2)	1.37(7)
N(1) -Pd(1)	2.00(4)	C(11) -N(2)	1.59(7)
N(2) -Pd(1)	2.17(5)	C(2) -C(1)	1.36(7)
C(1) -S(1)	1.80(6)	C(3) -C(2)	1.73(8)
C(4) -S(1)	1.84(4)	C(5) -C(4)	1.80(5)
C(3) -S(2)	1.78(4)	N(1) -C(5)	1.69(5)
C(14) -S(2)	1.78(4)	C(7) -C(6)	1.40(7)
C(8) -S(3)	1.92(5)	C(7) -C(8)	1.70(6)
C(9) -S(3)	1.81(5)	C(10) -C(9)	1.23(7)

Estimated standard deviations are given in parentheses.

Table 4.6. (contd.)

Bond angles (°)

Atoms	Angle	Atoms	Angle
S(2) -Pd(1) -S(1)	90.3(6)	C(5) -N(1) -Pd(1)	109(2)
S(3) -Pd(1) -S(1)	172.9(10)	C(13) -N(1) -Pd(1)	117(3)
S(3) -Pd(1) -S(1)	95.0(1)	C(13) -N(1) -C(5)	109(3)
N(1) -Pd(1) -S(1)	86.2(12)	C(10) -N(2) -Pd(1)	106(4)
N(1) -Pd(1) -S(2)	82.6(11)	C(11) -N(4) -Pd(1)	118(4)
N(1) -Pd(1) -S(3)	99.1(12)	C(11) -N(5) -C(10)	105(5)
N(2) -Pd(1) -S(1)	90.3(15)	C(2) -C(1) -S(1)	144(5)
N(2) -Pd(1) -S(2)	97.5(14)	C(3) -C(2) -C(1)	114(5)
N(2) -Pd(1) -S(3)	84.4(15)	C(2) -C(3) -S(2)	124(4)
N(2) -Pd(1) -N(1)	177 (2)	C(5) -C(4) -S(1)	105(2)
C(1) -S(1) -Pd(1)	110 (2)	C(4) -C(5) -N(1)	102(3)
C(4) -S(1) -Pd(1)	101.9(14)	C(7) -C(6) -S(4)	114(4)
C(4) -S(1) -C(1)	92 (2)	C(8) -C(7) -C(6)	107(4)
C(3) -S(2) -Pd(1)	120 (2)	C(7) -C(8) -S(3)	104(3)
C(14) -S(2) -Pd(1)	85.2(14)	C(10) -C(9) -S(3)	115(4)
C(14) -S(2) -C(3)	98 (2)	C(9) -C(10) -N(2)	130(6)
C(8) -S(3) -Pd(1)	117 (2)	C(12) -C(11) -N(2)	115(4)
C(9) -S(3) -Pd(1)	97 (2)	C(11) -C(12) -S(4)	116(4)
C(9) -S(3) -C(8)	118 (2)	C(14) -C(13) -N(1)	114(4)
C(12) -S(4) -C(6)	116 (3)	C(13) -C(14) -S(2)	113(3)

Estimated standard deviations are given in parentheses.

Fig. 4.3. ORTEP diagram of the blue $[Pd([10]\text{-ane}S_2N)_2]^{2+}$ cation.

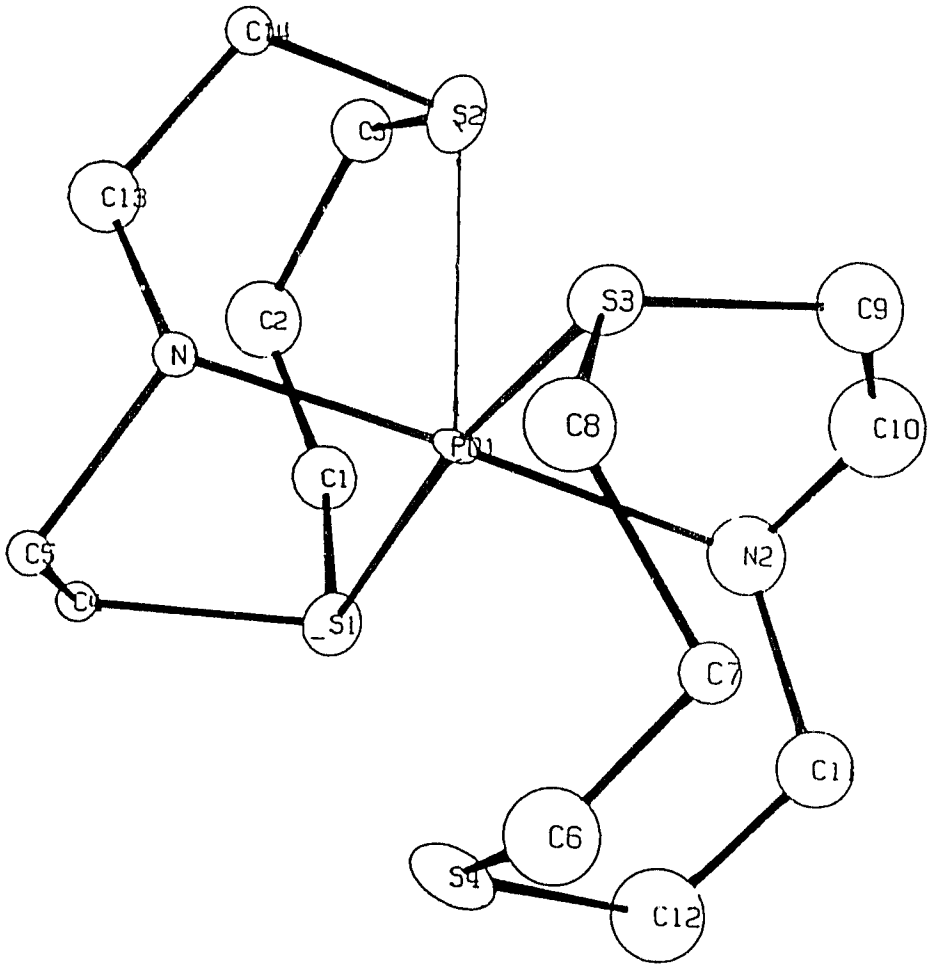

towards the Pd(II) metal ion having an overall *'endo'* conformation with respect to the axis (see Section 4.4.). The formation of this structure exhibits the affinity of the soft central Pd(II) ions for the soft thia donor atoms. In the analogous $[Pd([9]\text{-}aneN_3)_2]^{2+}$ ion, the Pd(II) is square planar with the remaining two nitrogen atoms not coordinated to the central Pd(II) atom.[99] The N atoms are bent away from the z-axis perpendicular to the PdN_4 plane in an *'exo'* conformation (Fig. 4.4.).

Fig. 4.4. ORTEP diagram of $[Pd([9]\text{-}aneN_3)_2]^{2+}$ cation.[99]

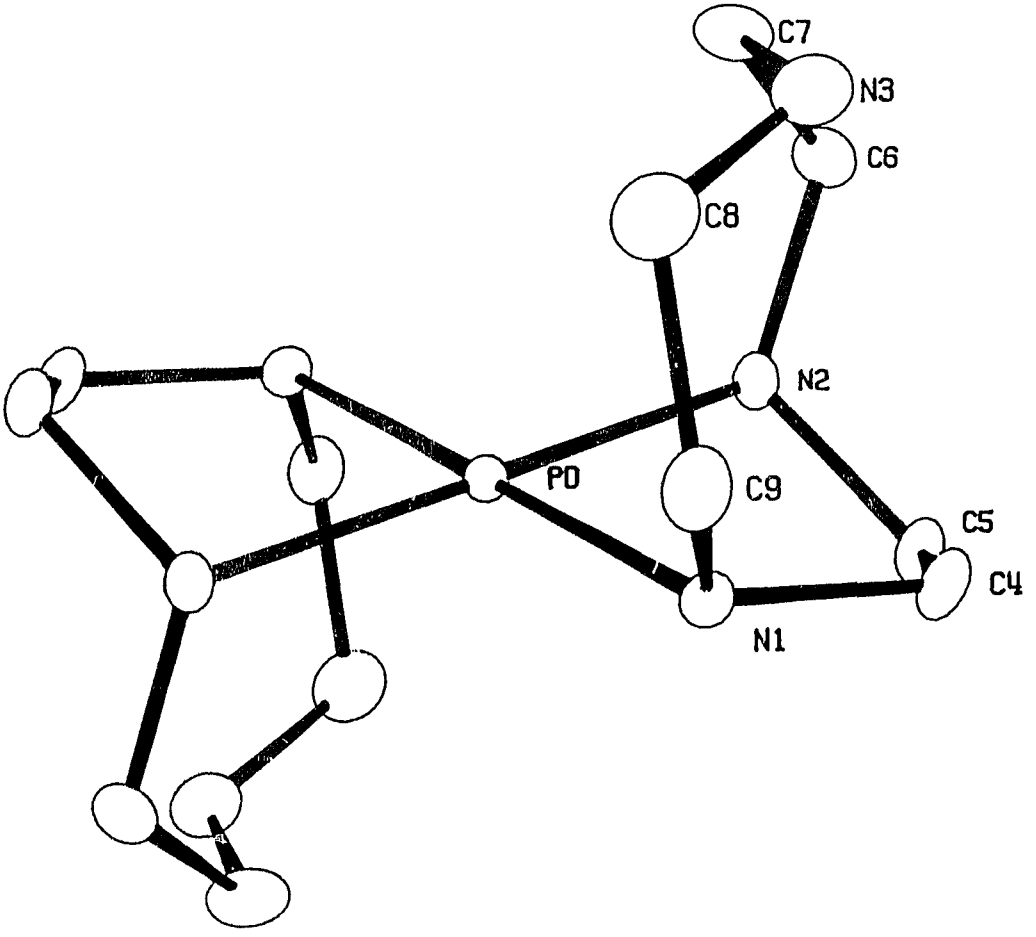

The Pd-N_{eq} bond length is 2.09(9) Å. The Pd-S_{eq} bond distance is found to be as expected (2.32(12) Å). The Pd-S2 bond length was found to be 2.84(2) Å while the other axial S atom (S4) interacts at long range with the Pd atom (3.05 Å). The Pd atom is pulled slightly above the plane (0.06 Å) towards the axial S2 atom forming an elongated square pyramidal geometry. The $S_{ax}(2)$-Pd-$S_{ax}(4)$ bond angle of 177° is very close to linear, as expected for an octahedral species. The Pd-S_{ax} bond length of 2.84(2) Å is smaller than the Pd-S_{ax} bond length, 2.952(4) Å, in the $[Pd([9]\text{-}aneS_3)_2]^{2+}$ complex[92] and the $[Pd([10]\text{-}aneS_3)_2]^{2+}$ complex (3.034(1) Å), (see Chapter 6), where significant interactions from the axial S donor atoms with the central Pd atom were noted. Whereas the $[Pd([9]\text{-}aneS_3)_2]^{2+}$ was essentially square planar with significant interactions from both the axial S atoms to form a pseudo octahedral complex ('*endo*' conformation), the Pd bis-complex of **24** exhibits a distorted square-based pyramidal environment of two coordinated N atoms and 3 coordinated S atoms. While a number of five-coordinated Pd(II) complexes with trigonal-bipyramidal geometry around the Pd(II) centre containing S, Se, P and As as donor ligands have been reported, very few square-based pyramidal complexes of Pd(II) are known.[113,114] Wieghardt[115] has reported the a Pd(II) complex of the ligand **66**, where the three nitrogen atoms from the nine-membered macrocycle and two from the pyridine moieties are coordinated to the Pd(II) centre in a square pyramidal fashion. The third

pendant arm is bent away from the Pd(II) centre. The Pd-N_{ax} bond length was found to be 2.580(3) Å. In the complex $[PdCl(PPh_3)_2(phen)](BF_4).(CH_3)_2CO$[116] the phenanthroline ligand is coordinated *via* one normal Pd-N bond (2.09(5) Å) and one very weak Pd-N bond (2.68(4) Å) to form a square pyramid.

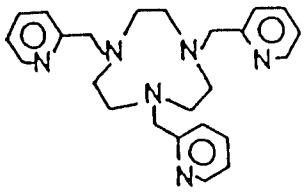

66

In their work, Reid *et al*[104] observed that the Pd complex of the 18-membered ring containing S_4N_2 core, **63** showed the S_2N_2 donor set in a square planar configuration around the central Pd(II) ion with the remaining two thioether ligands interacting at long range (2.977(23) Å) in the axial positions. The $\angle(S_{ax}\text{-Pd-}S_{ax})$ was 158.94(9)° thus giving a distorted octahedral geometry around the Pd atom. However, in the present case the corresponding ∠(S2-Pd-S4) of 177° and the Pd-S2 bond length of 2.84 Å is indicative of an elongated square pyramidal coordination around the metal atom. The $Pd([10]\text{-ane}S_2NH)_2^{2+}$, **49a**, complex isolated in the present study represents the first example of a mixed donor palladium complex containing a square-pyramidal PdS_3N_2 core. The driving force for formation of this structure is discussed in Section 4.6.

In order to grow more of the blue crystals discussed

above, the amorphous red complex was redissolved in CH_3CN and diffusion of ether yielded tiny red crystals after two days. These crystals were very hygroscopic and sensitive to solvent loss. Preliminary examination of this crystal indicated that it was different from the blue crystal identified earlier, and hence a detailed structural investigation was undertaken.

4.5.2. Crystal structure of Pd([10]-aneS$_2$NH)$_2$(PF$_6$)$_2$.2CH$_3$NO$_2$, 49b:

A suitable red crystal was mounted in a Lindemann tube and sealed immediately. The data were collected at speed-8 on the CAD4 Nonius diffractometer. The crystal data are given in Table 4.5. Data reduction yielded reflections with $I > 1.5\sigma(I)$ which were used for solution and refinement of the structure. Solution of the phase problem was achieved by Patterson maps using SHELX76[55]. Difference electron density maps and least squares analysis revealed the positions of the non-metal atoms. The asymmetric unit consisted of the complex cation, one PF_6 counter ion, and one nitromethane molecule, (solvent of crystallisation). The crystal structure was refined with anisotropic thermal parameters to a value of R = 0.15, when it was found that the thermal ellipsoids on the carbon atoms labelled C5 were poor. In the structure of the [Pd(22)$_2$(PF$_6$)$_2$ Blake *et al*[92] found the [Pd(22)$_2$]$^{2+}$ to be ordered but the PF_6^- counter ion to be disordered. In addition, the carbon atoms in the structure of the [Pd(22)$_2$](PF$_6$)$_2$ complex

were refined with isotropic thermal parameters, while, the Pd, S, P, and F atoms were refined anisotropically. A similar refinement process in the present case may prove useful. The ORTEP diagram of the complex cation, $[Pd(\mathbf{23})_2]^{2+}$ with atomic labelling is shown in Fig. 4.5. Important bond lengths and bond angles are given in Table 4.7.

The complex consists of four S atoms coordinated to the central Pd atom in a square plane. The Pd atom is in the square plane by symmetry. The mean of two Pd-S bond lengths was found to be 2.35 Å. The two N atoms are coordinated axially to the Pd atom (Pd-N = 2.55(12) Å). The ∠(S1-Pd-S2) was found to be 96.3(4)°. The ∠(S1-Pd-N1) and ∠(S2-Pd-N1) were found to be 79.1(8)° and 78.1(9)° respectively. Thus the coordination around the Pd atom may be described as an elongated octahedron. The Pd-N_{ax} distance of 2.545 Å compares well with the Pd-N_{ax} distance of 2.580(3) Å in the square based pyramidal structure of $[Pd(\mathbf{66})]^{2+}$ cation[115] and is shorter than the very weak Pd-N_{ax} bond of 2.68(4) Å in the crystal structure of $[PdCl(PPh_3)_2(phen)]^+$ cation.[116] Whereas the macrocycle **66** acts as a pentadentate ligand with one of the pendant arm bent away from the Pd(II) centre, in the present case both the axial N atoms are bent towards the Pd(II) metal centre giving rise to a unique instance where the chelate rings containing the N atoms are in the *'syn'* conformation, forming an elongated octahedral complex.

Fig. 4.5. ORTEP diagram of the red $[Pd([10]\text{-ane}S_2N)_2]^{2+}$ cation with 25% thermal ellipsoids.

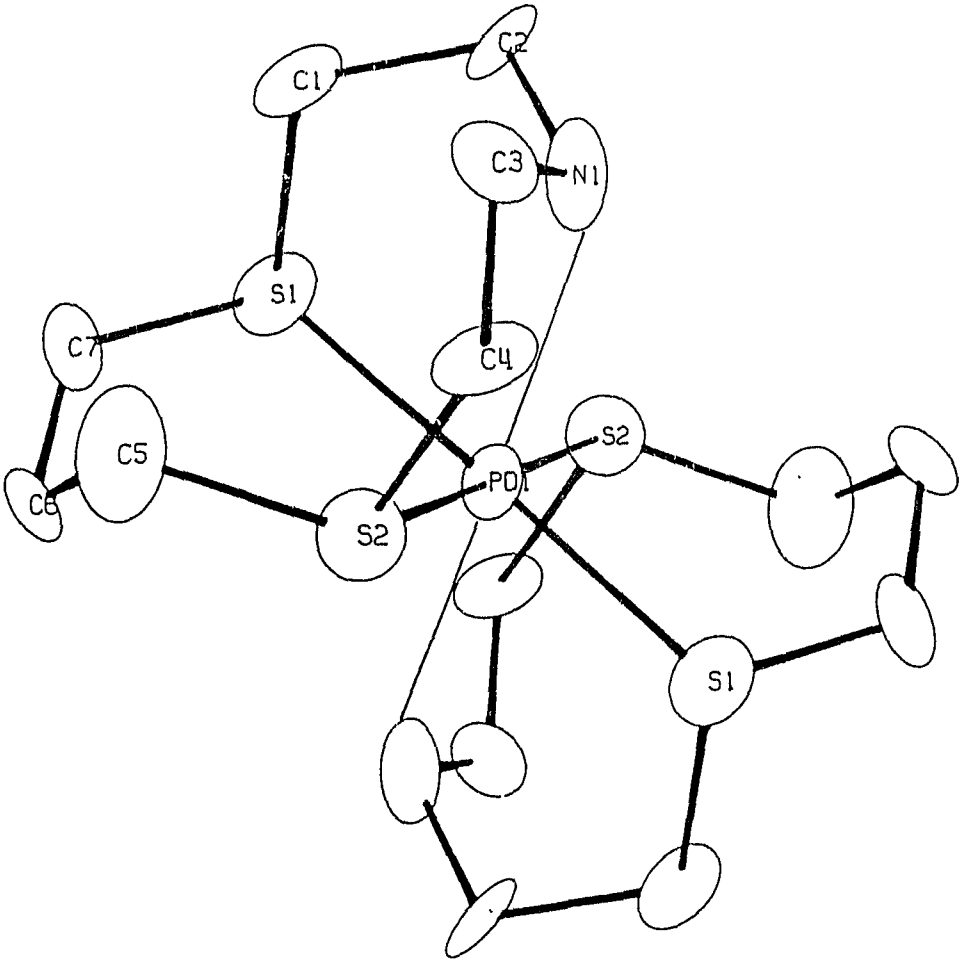

Interatomic distances (Å)

Atoms	Distance	Atoms	Distance
S(1) -Pd(1)	2.35(1)	C(2) -N(1)	1.46(4)
S(2) -Pd(1)	2.35(1)	C(3) -N(1)	1.56(5)
N(1) -Pd(1)	2.66(3)	C(2) -C(1)	1.60(5)
C(1) -S(1)	1.81(4)	C(3) -C(4)	1.47(5)
C(7) -S(1)	1.69(5)	C(6) -C(5)	1.62(7)
C(4) -S(2)	1.83(4)	C(6) -C(7)	1.53(7)
C(5) -S(2)	1.80(4)		

Estimated standard deviations are given in parentheses.

Bond angles (°)

Atoms	Angle	Atoms	Angle
S(2) -Pd(1) -S(1)	96.3(4)	N(1) -Pd(1) -S(1)	78.1(9)
N(1) -Pd(1) -S(2)	79.1(8)	C(6) -C(7) -S(1)	123(4)
C(1) -S(1) -Pd(1)	107.8(15)	C(3) -N(1) -C(2)	113(4)
C(7) -S(1) -Pd(1)	112(2)	C(2) -C(1) -S(1)	111(2)
C(7) -S(1) -C(1)	100(2)	C(1) -C(2) -N(1)	111(3)
C(4) -S(2) -Pd(1)	101(1)	C(4) -C(3) -N(1)	108(4)
C(5) -S(2) -Pd(1)	109(1)	C(3) -C(4) -S(2)	120(3)
C(5) -S(2) -C(4)	104(2)	C(6) -C(5) -S(2)	113(3)
C(2) -N(1) -Pd(1)	104(2)	C(7) -C(6) -C(5)	104(4)
C(3) -N(1) -Pd(1)	109(2)		

Estimated standard deviations are given in parentheses.

In the $[Pd(\mathbf{22})_2]^{2+}$ complex[96], the Pd atom is square planar with the two axial atoms pointing away from the Pd(II) centre with the chelate rings containing the axial N atoms in an *'anti'* conformation. The driving force for the formation and isolation of the unusual structure for the $[Pd(\mathbf{24})_2]^{2+}$ cation may arise from two factors: (i) The electron density on the Pd(II) metal centre would be relatively reduced compared to that of the $[Pd(\mathbf{22})_2]^{2+}$ ion, as a result of the π- acceptor properties of the equatorial S atoms (greater nephelauxetic effect of the S atoms compared to the N atoms) which would lead to lower electron-electron repulsion effects facilitating the axial N atoms to be bent towards the Pd(II) metal centre. (ii) Presumably, the presence of the propylene group in the ten-membered ring (compared to the nine membered ring, **22**) introduces a steric strain to the formation of the *'exo'* conformation of the nitrogen containing chelate rings. Rather, the steric effect fortuitously positions the chelate rings containing the N atoms in *'endo'* conformation facilitating formation of an elongated octahedral structure.

4.6. NMR spectra:

The ^1H nmr spectrum of the red $Pd([10]aneS_2NH)_2^{2+}$ cation distinguishes between equatorial protons and axial protons (Table 4.8.). These sets of protons are magnetically non-

Table 4.8. Chemical shifts in the ^{1}H nmr spectrum of the $[Pd(\mathbf{24})_2]^{2+}$ cation.

δ (ppm)	Number of protons	Assignment
2.24 2.64	4 (m)	$-C-C\underline{H}_2-C$
2.93	4 (m)	$-N-C\underline{H}_2$ (axial w.r.t. the ring)
3.30	20 (m)	$-S-C\underline{H}_2$ and $-N-CH_2$ (equatorial w.r.t. the ring)
5.70	2 (s)	-NH

equivalent because they are oriented differently toward the metal centre. The protons on the central $-C-\underline{C}H_2-C$ propyl ring (4 H) appears as two widely separate multiplets centered at 2.64 ppm and 2.24 ppm. A 4 H multiplet due to axial $-N-CH_2-$ protons is centered upfield at 2.93 ppm. The protons attached to the coordinated S and the four equatorrial $-N-CH_2$ protons appear as a multiplet downfield (3.1 - 3.5 ppm) centered at 3.3 ppm (20 H). A broad singlet due to -NH- (2 H) is seen at 5.7 ppm.

The ^{13}C nmr of the $[Pd(\mathbf{24})_2]^{2+}$ cation (Fig. 4.6.) shows four signals due to the four inequivalent sets of carbon atoms. The $C-\underline{C}H_2-C$ carbon appears at 27.2 ppm for this complex similar to the Pd complex of **23** (26.8 ppm). Two sets of carbons, equatorial and axial can be distinguished. The carbon atoms of the ethylene bridge next to the coordinated S

atom appears at 32.8 ppm. The S_{eq}-$\underline{C}H_2$ carbon appears at 37.3 ppm. The signal at 49.7 ppm for the $\underline{C}H_2$-N-$\underline{C}H_2$ carbons deserves comment. This is far downfield compared to the $\underline{C}H_2$-S_{eq} carbon atoms for the [10]-aneS_3 complex (32.8 ppm), because of the greater electronegativity of the N atom compared to that of the S atom. Based on ^{13}C nmr evidence, the following solution structure could be proposed for the Pd([10]-aneS_2NH)$_2$(PF_6)$_2$, **49b**, complex:

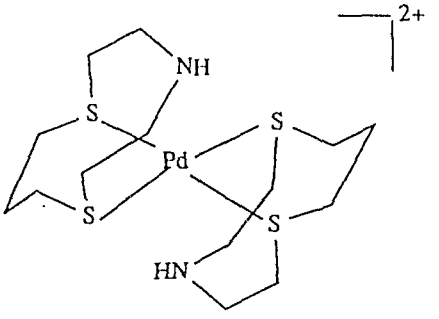

Fig. 4.6. ^{13}C nmr spectrum of the red [Pd(**24**)$_2$)]$^{2+}$ ion in CD_3NO_2. Solvent peak marked with asterisk.

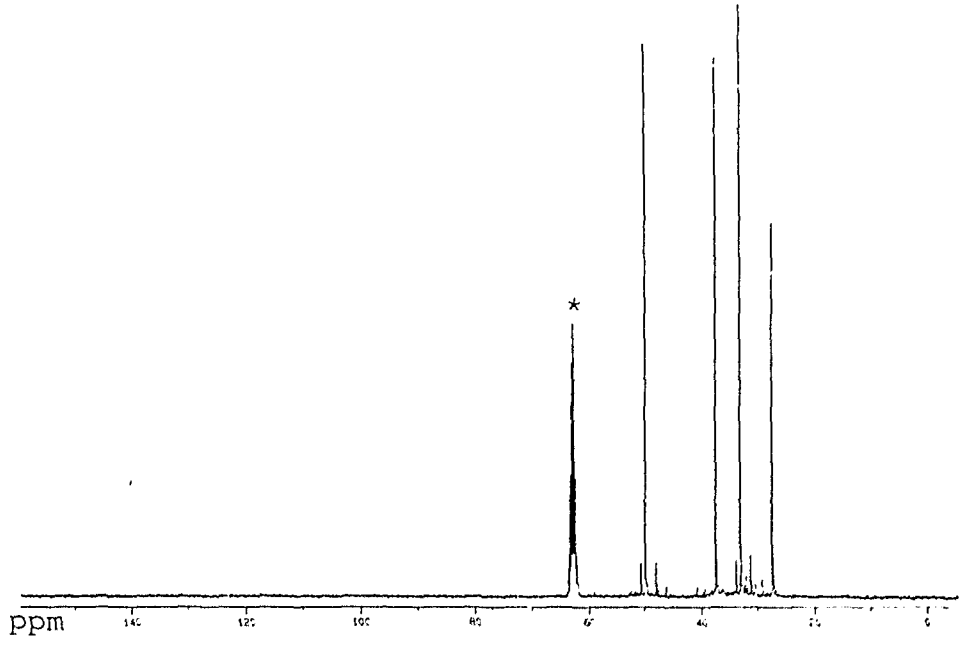

The ^{1}H and ^{13}C nmr spectra are consistent with the structure discussed in Section 4.5.2., (Fig. 4.5.). The peaks at δ 31.1, 33.7, 47.9 and 50.5 are attributed to the blue isomer present (6%) in the solution. From this red solution, blue crystals were obtained after 7 d. The ^{13}C nmr of the blue isomer at 22 °C, (Fig. 4.7.) showed resonances at δ 27.6 (C-C-C), 34.1 (S_{ax}-C), 36.2 (S_{eq}-C), 49.6 (N-C_{ax}) and 51.3 (N-C_{eq}). This is consistent with the structure shown in Fig. 4.3. The materials isolated in either case were insufficient to carry out variable temperature measurements. Since a blue crystal (with a different structure Fig. 4.3.) of the complex was obtained after several days (~7 d) from the same solution, the red isomer can be deemed the kinetic product and the blue isomer the thermodynamic product. The isomerization is, therefore, due to the metal hopping between any two of the three donor atoms of the cyclic ligand (Fig. 4.8a.). The process can be viewed as a "quasi-substitution reaction" within a pseudo-six-coordinate sphere. Although fluxional behaviour among Pt complexes has been well documented,[117,118] only a few cases among the Pd complexes have been postulated.[119,120] Evidence for rapid fluxional behaviour in a Pd macrocyclic complex was first observed by Hunter *et al*[96] where a possible mechanism for the interconversion was proposed. The results of the present work support the proposed mechanism inasmuch as a structure for the two N atoms in the apical positions (*endo* with respect to the axis), was

obtained (Fig. 4.5.) and subsequent substitution of this nitrogen onto the palladium, yields the structure shown in Fig. 4.3. The isomerisation process for the $[Pd(\mathbf{24})_2]^{2+}$ cation is depicted in Fig.4.8b. The intermediate, **X**, shown in Fig. 4.8b. is, perhaps, unstable due to the large repulsion between the ligating atoms on the same side of the PdS_3N plane. However, protonation of the N atoms in the ligand may sustain the *'syn'* structure **X**.[96]

Fig. 4.7. ^{13}C nmr of the blue isomer **49a** in CD_3NO_2/CD_3OD. Solvent peaks marked with asterisks.

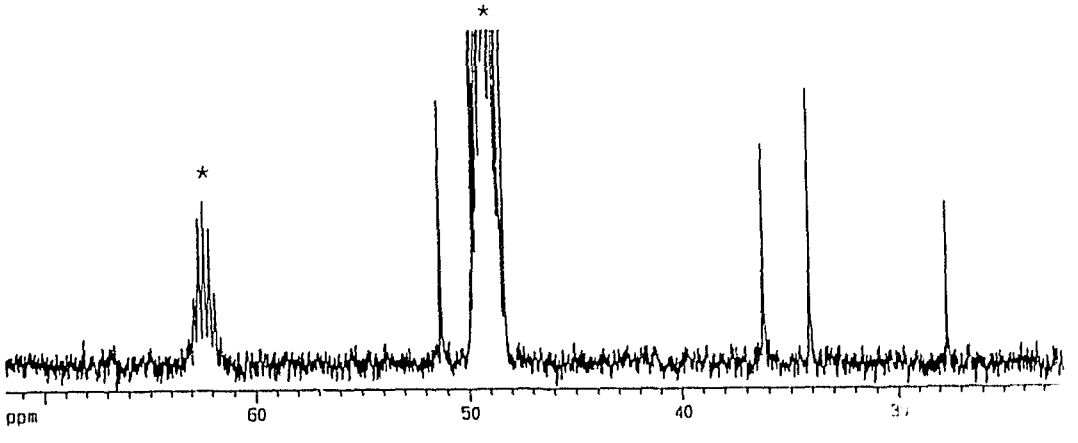

Fig. 4.8a. Isomerisation in **49**.

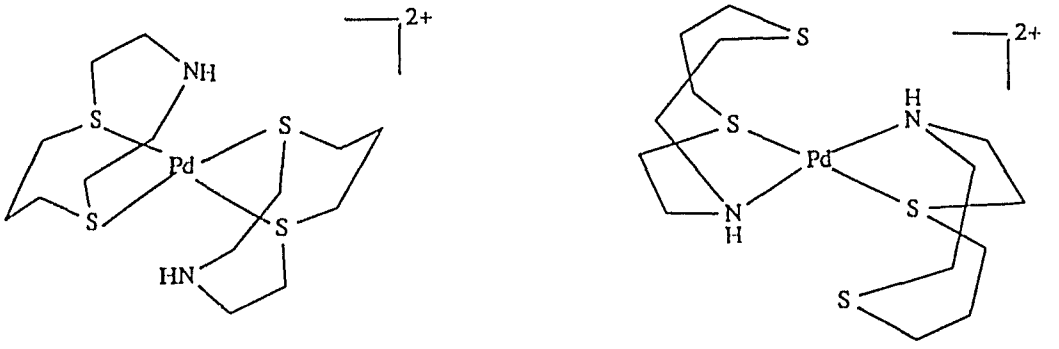

Kinetic product (Red isomer)

Thermodynamic product (Blue isomer)

Fig. 4.8b. Proposed mechanism of isomerisation of **49**.

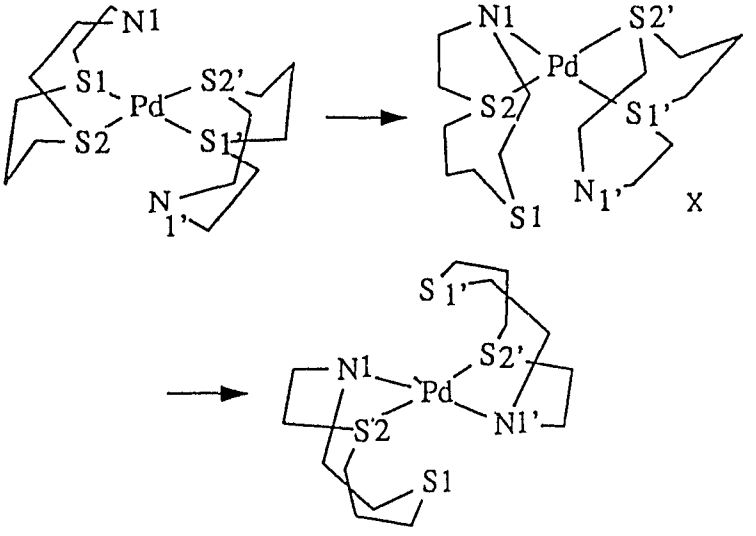

The variable low temperature ^{13}C nmr of the blue isomer, **49a**, Fig. 4.9., reveals an interesting phenomenon. As the temperature is lowered from 22 °C to 0 °C the spectrum becomes broad and at -20 °C the peaks at δ 34.1, 36.2 and 51.3 due to the carbon atoms, S_{ax}-$\underline{C}H_2$, S_{eq}-$\underline{C}H_2$ and N-$\underline{C}H_2$ respectively, become broader. At -40 °C the three peaks at δ 34.1, 36.2, and 51.3 disappear while the broad peak due to the -C-$\underline{C}H_2$-C carbon atom at δ 27.6 is just discernible. When the temperature is raised back to 22 °C the four-line carbon spectrum is regenerated. As the low-spin diamagnetic Pd(II) complex is cooled the axial S atoms are coordinated to the Pd(II) ion yielding a high-spin octahedral paramagnetic Pd(II) species at -40 °C as shown below:

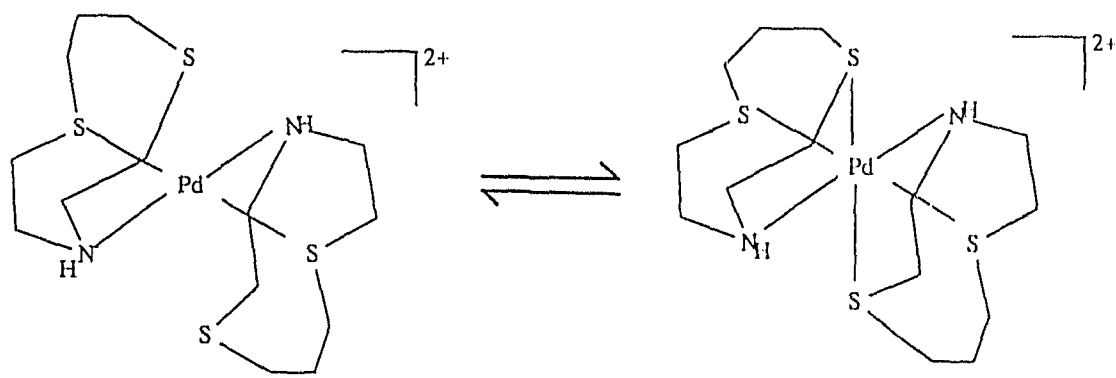

Fig. 4.9. Variable temperature ^{13}C nmr of the blue isomer **49a**. Solvent peak marked with asterisk.

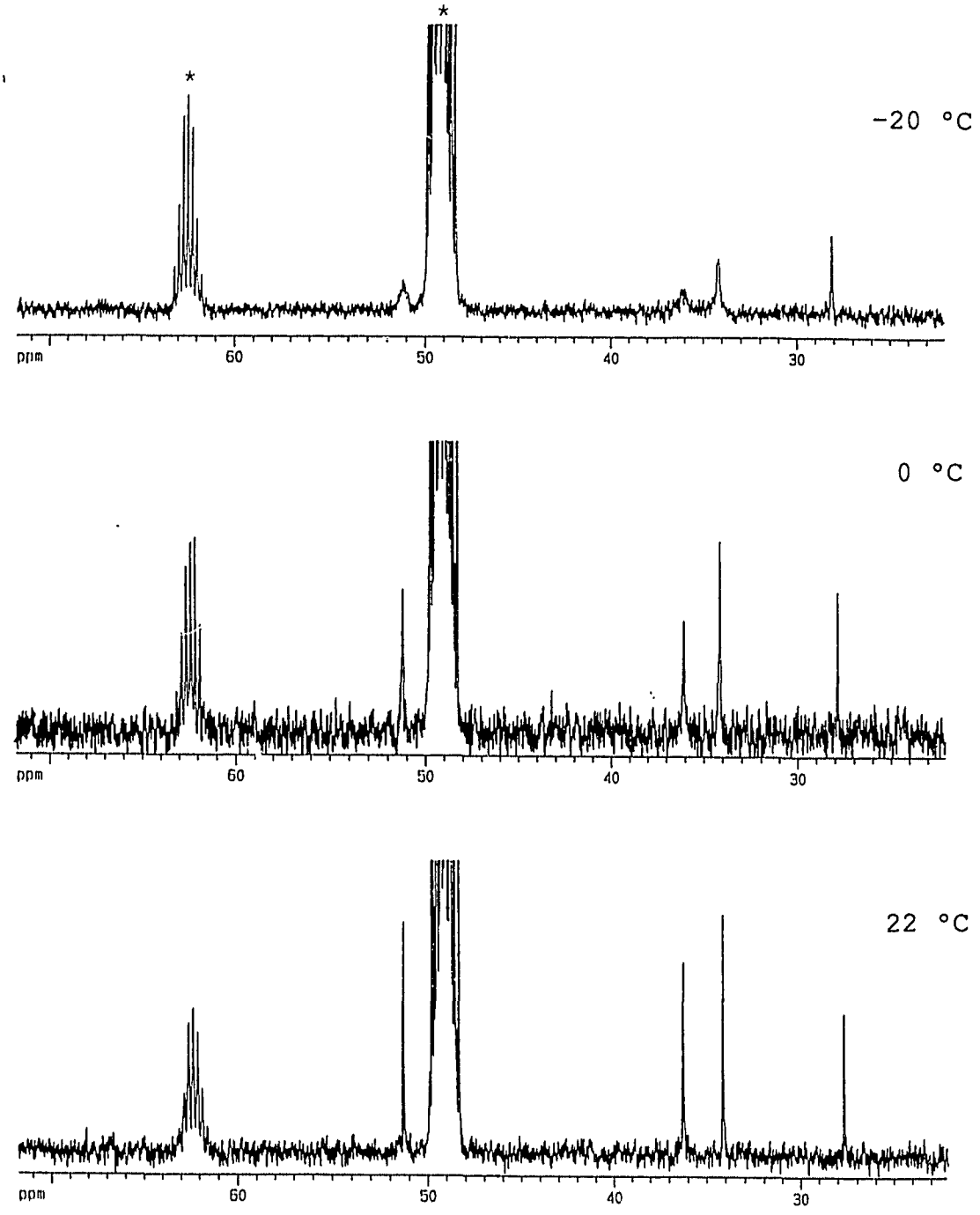

Fig. 4.9. (contd.)

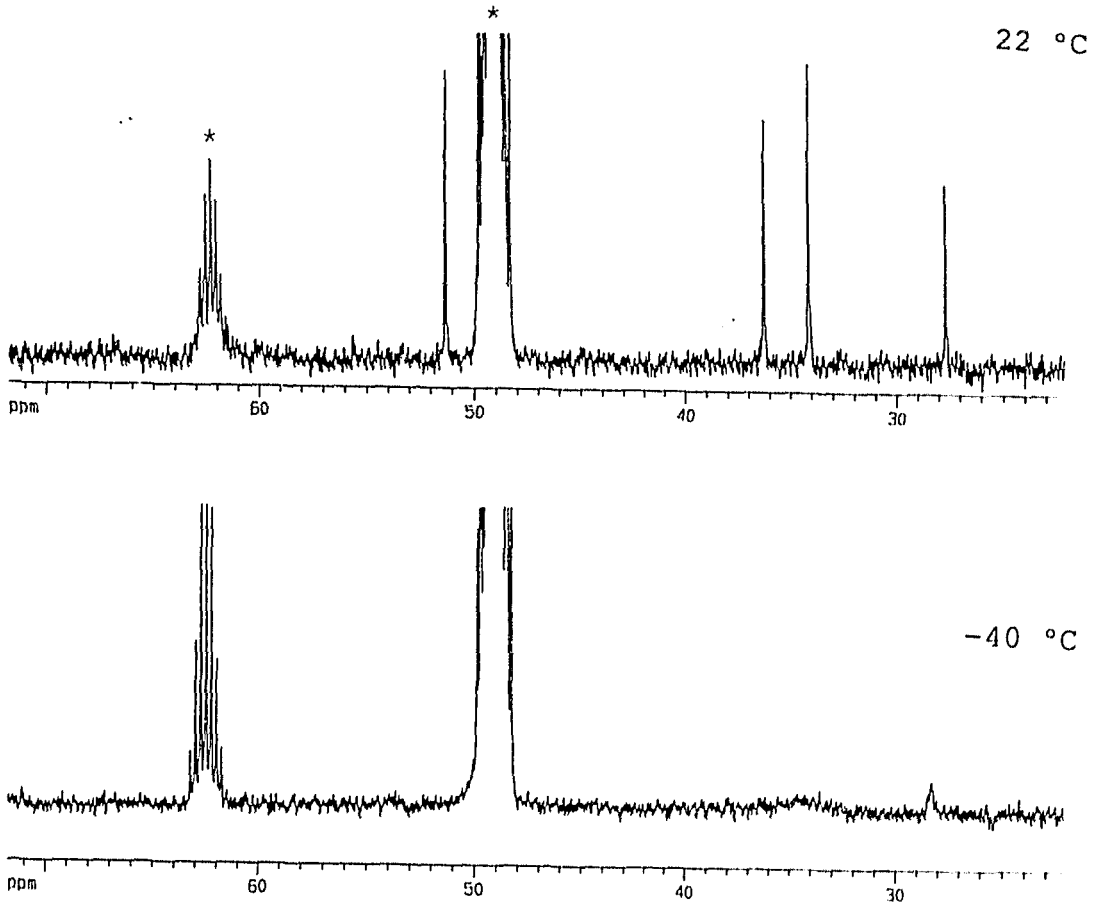

4.7. Electronic spectra:

Details of the electronic spectra of the Ni and Pd complexes of [10]-aneS_2NH, **24**, are provided in Table 4.9. The absorption spectra for the other members of the ten-membered series and similar examples are also shcwn in Table 4.9. For the complex **48** three bands are observed in the region 400 - 900 nm. The complex absorbs strongly below 400 nm which is attributed to charge tran fer bands. The band at 808 nm is attributed to the d-d transition $^3T_{2g} \leftarrow {}^3A_{2g}$ (ν_1). The ligand field strength, 10Dq, obtained from this transition is found to be 12376 cm^{-1}. The band at 19011 cm^{-1} is due to $^3T_{1g} \leftarrow {}^3A_{2g}$ transition (ν_2). The Racah parameter, B, for the Ni(II) complex of **24** has been found to be 778 cm^{-1} from the following equation:[123]

$$B = \frac{(2\nu_1^2 + \nu_2^2 - 3\nu_1\nu_2)}{15\nu_2 - 27\nu_1}$$

$$= 778 \text{ cm}^{-1}$$

The band at 418 nm (23923 cm^{-1}) is due to the $^3T_{1g}(P) \leftarrow {}^3A_{2g}$.

Table 4.9. Electronic spectra and ligand field parameters.

Complex	λ_{max} (nm); (ε ($M^{-1}cm^{-1}$))	10Dq (cm^{-1})	B[a] (cm^{-1})	β (cm^{-1})	Ref.
$[Ni(62)_2]^{2+}$	870(sh), 800, 513, 327	12500	937	0.90	75
$[Ni(25)_2]^{2+}$	880(13), 818(14), 529(14), 343(27)	11844	835	0.80	PW[b]
$[Ni(24)_2]^{2+}$	808(10), 526(14), 418(25)	12376	778	0.75	PW[c]
$[Ni(23)_2]^{2+}$	850(sh), 800(37), 530(66)	12500	717	0.69	PW[d]
$[Ni(65)_2]^{2+}$	840(23), 524(15), 297(680)	11930	-	-	105
$[Ni(24)_2]^{3+}$	558(44), 393(49), 336(57), 258(1769) 228, 192(995)	-	-	-	PW[c]
$[Ni(84)_2]^{2+}$	952, 850, 520	11560	820	-	122
$[Pd(24)_2]^{2+}$	710(sh), 550(114)	-	-	-	PW[c,e]
$[Pd(63)_2]^{2+}$	514(124), 332(4250), 266(10000), 233(10850)	-	-	-	104
$[Pd(23)_2]^{2+}$	598(84), 314(10800), 277(11300), 209(8000)	-	-	-	PW[d]

[a] $B_{free\ ion}$ = 1038 cm^{-1},[121] [b] Chapter 7, [c] this Chapter, [d] Chapter 6,

[e] Blue isomer, PW = Present work.

The ligand field strengths for the Ni complexes of the ten-membered series first decreases upon replacing one N atom with one S atom and then increases as more N atoms are replaced with S atoms. This is in keeping with the lack of strain in the homoleptic S_3 and N_3 ligand systems, (larger ligand field strength) and possible strain in the mixed donor complexes, (smaller ligand field strength).

Replacing the harder donors with softer S donor atoms allows for delocalisation of the t_{2g} electron density into the empty low lying ligand orbitals. Such delocalisation reduces electron-electron repulsions. In other words, the thioethers exhibit a greater nephelauxetic effect compared to the aza donor atoms. This is manifested in the values of the Racah parameter, B, for the Ni complexes of **23**, **24**, **25**, and **62** (Table 4.9.). The B values decrease in the order [10]-aneN_3 > [10]-aneSN_2 > [10]-aneS_2N > [10]-aneS_3. The nephelauxetic ratio β ($\beta = B_{complex}/B_{free\ ion}$)[123] for the $[Ni(\mathbf{24})_2]^{2+}$ ion was found to be 0.75.

The electronic spectrum of the blue complex Pd([10]-ane$S_2NH)_2(PF_6)_2$ in acetonitrile shows a band at 18169 cm^{-1}, (ε = 114 $M^{-1}cm^{-1}$) and weak absorption at 14084 cm^{-1} (sh). The band at 18169 cm^{-1} is assigned to a d-d transition of the low spin square-based PdS_4N chromophore. Strong absorptions below 400 nm are attributed to charge transfer bands.

4.8. Redox studies :

Oxidation of $[Ni(\mathbf{24})_2]^{2+}$ complex in aqueous medium (with Co^{3+} or $S_2O_8^{2-}$) or in non aqueous medium (NO^+/CH_3CN) yielded a red species of $[Ni(\mathbf{24})_2]^{3+}$ complex cation. In dry deaerated CH_3CN, the Ni(III) complex cation is stable for about two hours. The solution is extremely sensitive to moisture and decomposes to the Ni(II) complex cation. The $[Ni(\mathbf{24})_2]^{3+}$ complex cation shows an interesting esr spectrum characteristic of a tetragonally compressed octahedral geometry, with $g_{\parallel} = 2.127$ and $g_{\perp} = 2.061$, Fig. 4.10. For this low-spin d^7 metal ion, the unpaired electron is located primarily in the $d_{x^2-y^2}$ orbital. The $g_{\parallel}$ feature is the reverse of that normally observed for axial spectra obtained for Ni(III), (*i.e.*, $g_{\parallel} < g_{\perp}$). Coupling to the axial N atoms (I = 1) through the metal orbital is not discernible. This may be due to a smaller coupling constant. The $[Ni([9]\text{-ane}S_2N)_2]^{3+}$ complex cation also shows an axially elongated spectrum with $g_{\parallel}$ (2.019) < $g_{\perp}$ (2.121).[105] Also in that case the $g_{\parallel}$ feature shows hyperfine interaction with the N atoms (I = 1). Thus for the same ligating atoms, the axial distortion is significantly different for the nine and ten-membered rings. This may again reflect the ability of the N atom in the more flexible ten-membered ring to permit more complete occupation of the apical position. Since no hyperfine interaction with the N atoms was observed the possibility of two axial S atoms in a compressed octahedral coordination cannot be ruled out.

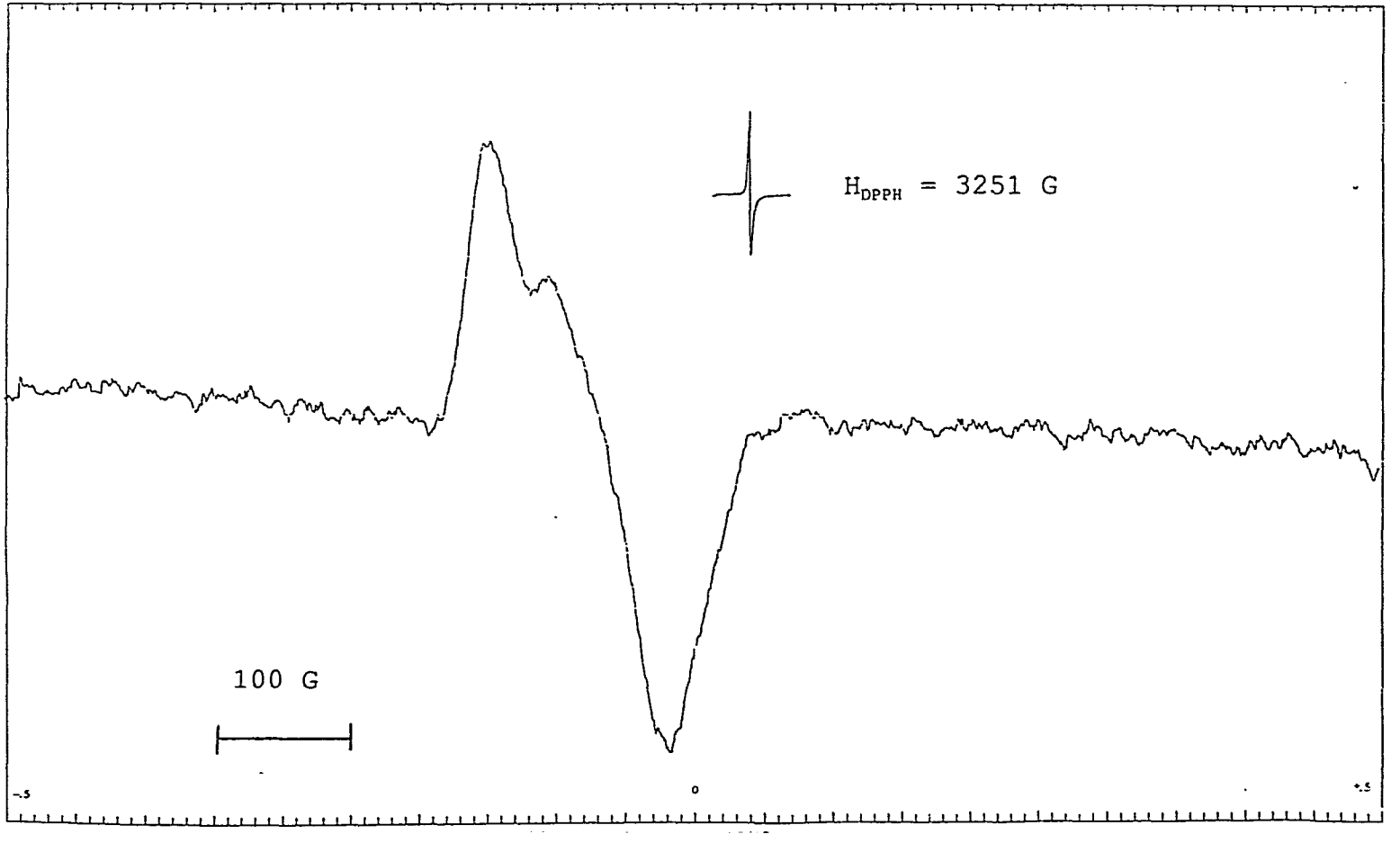

Fig. 4.10. ESR spectrum of $[Ni(\mathbf{24})_2]^{3+}$ ion in CH_3CN at 77 K.

The uv-visible spectrum of the chemically generated $[Ni(\mathbf{24})_2]^{3+}$ cation shows absorption bands at 558 nm (17921 cm^{-1}), 393 nm (25445 cm^{-1}), 336 nm (29762 cm^{-1}) and 314 nm (31847 cm^{-1}) assigned to $^2{}_aT_{1g} \leftarrow {}^2A_{1g}$, $^2{}_aT_{2g} \leftarrow {}^2A_{1g}$ and $^2{}_bT_{1g} \leftarrow {}^2A_{1g}$, respectively. The bands at 258 nm, 228 nm and 192 nm are assigned to charge transfer transitions.

Oxidation of the blue $[Pd(\mathbf{24})_2]^{2+}$ cation (**49a**) in acetonitrile with NO^+ yielded an orange species which was stable for a few minutes at room temperature. The esr spectrum of this orange species at 77 K is characteristic of an octahedral $[Pd(\mathbf{24})_2]^{3+}$ cation, which is near isotropic with $g_{near\ iso} = 2.096$, Fig. 4.11. The $g_\parallel$ feature and the $g_\perp$ feature cannot be distinguished distinctly from one another but there is indication of hyperfine interaction with the Pd nucleus (I = 3/2) in the higher field region of the spectrum. The esr spectrum of $[Pd(\mathbf{24})_2]^{3+}$ cation obtained by the oxidation of the red isomer **49b** (with NO^+ in CH_3CN at 77 K) is also near isotropic, $g_{near\ iso} = 2.050$, Fig. 4.12a. Hyperfine interaction with the axial N atoms is seen in the high field region. Addition of anhydrous Na_2SO_4 causes an anisotropy in the esr spectrum with $g_\parallel = 2.054$ and $g_\perp = 2.035$, Fig. 4.12b. The sequence $g_\parallel > g_\perp > g_e$ is indicative of the unpaired electron occupying the $d_{x^2-y^2}$ orbital. The structure, therefore, undergoes a tetragonal compression in ionic media. The presence of both isotropic and anisotropic spectra suggests dynamic Jahn-Teller distortion of the low spin d^7 ion at low

ionic strengths.

Fig. 4.11. ESR spectrum of $[Pd(\mathbf{24})_2]^{3+}$ cation (**49a** + NO^+) in CH_3CN at 77 K.

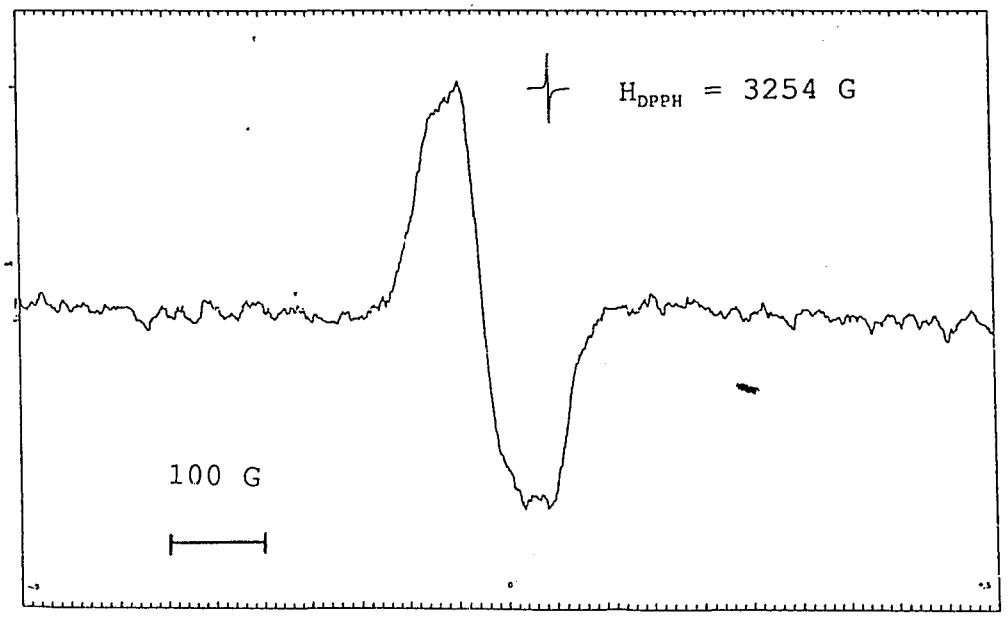

Fig. 4.12a. ESR spectrum of $[Pd(\mathbf{24})_2]^{3+}$ cation (**49b** + NO^+) in CH_3CN at 77 K.

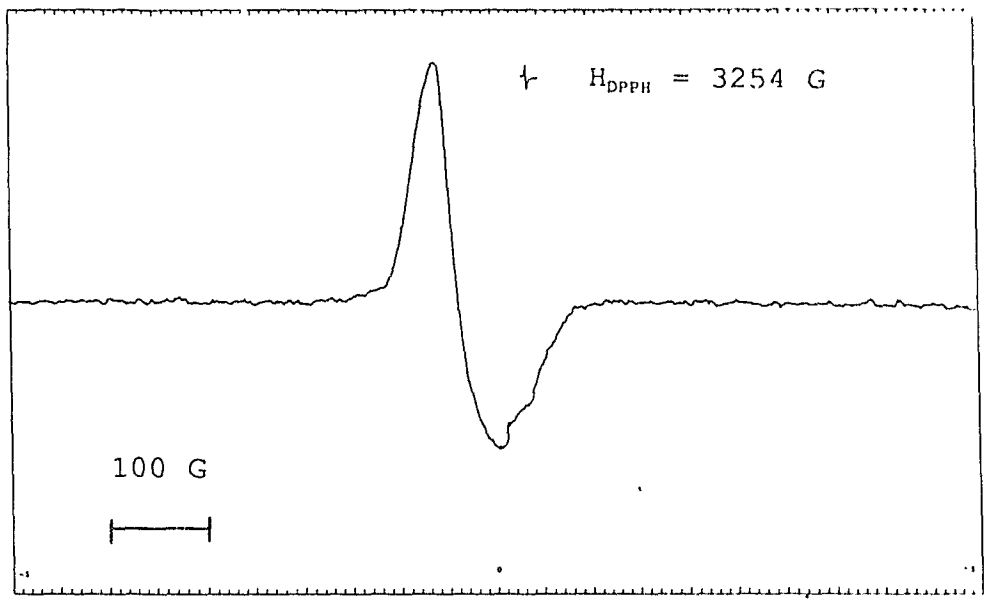

Fig. 4.12b. ESR spectrum of $[Pd(\mathbf{24})_2]^{3+}$ cation in the presence of Na_2SO_4 at 77 K.

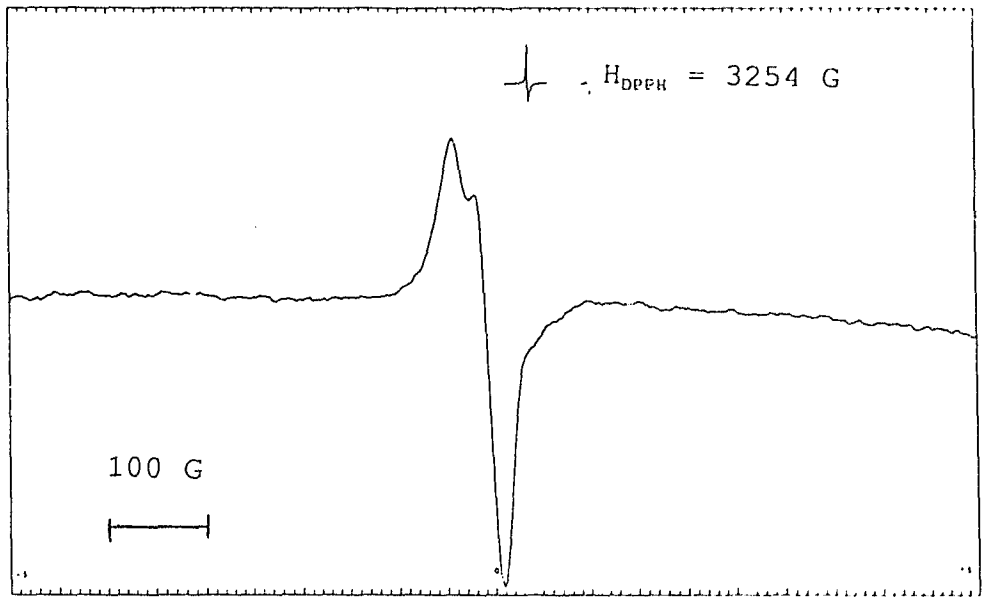

4.9. Electrochemistry:

Cyclic voltammograms of the Ni bis complex of **24** in acetonitrile showed an oxidation and a reduction wave at $E_{1/2}$ = 1.01 V *vs* Ag^{+}/Ag^{0} due to the $[Ni(\mathbf{24})]_2^{3+/2+}$ couple, Table 4.10. (The potentials are all reported *vs* Ag^{+}/Ag^{0} (0.1 M $AgNO_3$) in CH_3CN. Ferrocene was used as an external standard and $E_{1/2}$ (Fc^{+}/Fc) = 0.15 V).

Table 4.10. Half wave potentials of the complexes.

Complex	$E_{1/2}$ (V) (*vs* Ag^{+}/Ag)	ΔE (mV)	$E_{1/2}$ (V) (*vs* Fc^{+}/Fc)	Ref.
$[Ni(\mathbf{24})_2]^{3+/2+}$	1.01	114	0.86	PW
$[Ni(\mathbf{65})_2]^{3+/2+}$	1.04	110	0.88	105
$[Pd(\mathbf{24})_2]^{3+/2+}$	0.53	130	0.38	PW
$[Pd(\mathbf{64})_2]^{3+/2+}$	–	84	0.605	100
$[Pd(\mathbf{22})_2]^{3+/2+}$	–	70	0.37[b]	99
$[Pd(\mathbf{24})_2]^{4+/3+}$	0.93	260	0.78	78
$[Pd(\mathbf{22})_2]^{4+/3+}$	–	70	0.64[b]	99
$[Pd(\mathbf{24})_2]^{2+/+}$	-1.03	–	-0.88	PW

[a] in CH_3CN containing 0.1 M NEt_4BF_4, reference electrode – $Ag/AgNO_3$ (0.1 M).

[b] *vs* NHE.

This wave is quasi reversible with ΔE = 114 mV. At lower potentials an irreversible reduction wave due to Ni(I) complex cation is seen at E_{pc} = 0.306 V (E_{pc} = cathodic peak) and an irreversible oxidation wave at E_{pa} = -0.188 V (E_{pa} = anodic peak) at scan rates of 100 mV/sec. The reduced species is not stable for coulometric evaluation of the number of electrons in the species. The large separation between the reduction and the oxidation peak is suggestive of a rearrangement in the structure of the complex. Ni(I) being d^9 probably prefers a tetrahedral geometry.

The cyclic voltammograms of $[Pd([10]\text{-ane}S_2NH)_2](PF_6)_2$, **49a**, complex in acetonitrile showed two successive 1e redox waves arising from $Pd^{3+/2+}$ and $Pd^{4+/3+}$ couples. The half wave potential for the $Pd^{3+/2+}$ couple was found to be 0.53 V *vs* Ag^+/Ag^0 (ΔE = 130 mV), Fig. 4.13a. The peak to peak separation of 130 mV and a current ratio, i_{pc}/i_{pa} ~1, indicates a quasi-reversible wave. $E_{1/2}$ for the $Pd^{4+/3+}$ couple was found to be 0.93 V *vs* Ag^+/Ag^0, (ΔE = 260 mV), Fig. 4.13b. The current ratio (i_{pa}/i_{pc}) was not equal to unity indicating the instability of the Pd(IV) complex formed. At very negative potentials an irreversible wave (E_{pc} = -1.03 V *vs* Ag^+/Ag^0) is seen due to the formation of the Pd(I) species, Fig. 4.13c.

The half wave potentials for Pd complexes of ligands containing S and N donor atoms are shown in Table 4.10. The electrochemical properties of the $[Pd(\mathbf{24})_2]^{2+}$ ion are intermediate between the homoleptic N_3 and S_3 complexes. The

Fig. 4.13. Cyclic voltammograms of the $Pd(24)_2(PF_6)_2$ complex.

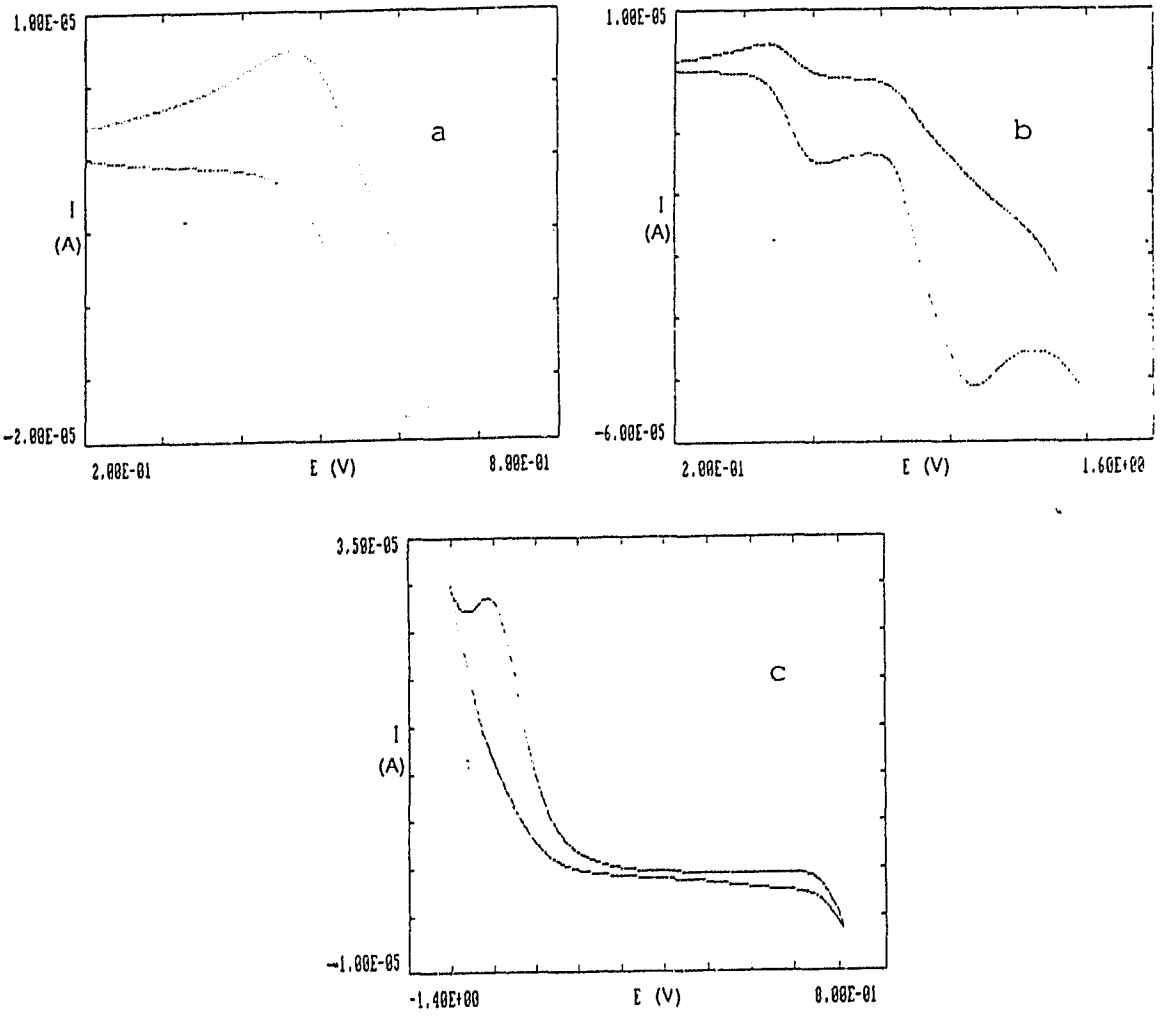

Pd(IV) species based on **24** is less stable when compared to the Pd(IV) complex based on [9]-aneN_3, **22**. Pd(IV) is not stabilised by complexes based on [9]-aneS_3, **64** or [10]-aneS_3, **23** and hence not observed. Thus, homoleptic aza ligands stabilize higher oxidation states by virtue of being pure σ donors whereas homoleptic thia ligands stabilize lower oxidation states because of π- acid properties of thia donors. Direct structural evidence for the π- acceptor properties of thioether crowns have been provided recently by Blake, *et al*[124] in the complex, $[Fe([9]\text{-ane}S_3)_2](ClO_4)_3$. [The co-ordinated S-donor atoms can thus act either as a π- acceptor using empty d- orbitals on sulphur, or as a π- donor via donation of the available lone-pair on sulphur]. Thus, both lower, Pd(I), and higher oxidation states, Pd(III) and Pd(IV), are accessible with the present heteroleptic ligand **24** albeit with limited stability.

4.10. Conclusions:

The hitherto unknown mixed donor macrocyclic ligand [10]-aneS_2NH, **24**, was successfully synthesised and its Ni(II) and Pd(II) complexes were structurally characterised. Two ligands coordinate to the Ni(II) metal ion occupying the trigonal faces to form octahedral complexes with the two N atoms in *trans* positions. The low-spin d^7 Ni(III) complex ion is in a compressed octahedral geometry as opposed to an elongated octahedral complex obtained for the Ni(III) complex of the

nine-membered [9]-aneS_2N, **65**. Both the spectroscopic and the redox properties of the Ni complexes were intermediate between those of the trithia and triaza ligands. Two isomers were obtained for the Pd complex. The octahedral preference of the two tridentate macrocycles and the use of S atoms in stabilizing Pd(II) ion is manifest in the isolation of *syn* isomers for the Pd complexes, and the formation of a paramagnetic Pd(II) ion at low temperatures. Evidence for the presence of Pd(I), Pd(III) and Pd(IV) complex ion species have been provided by cyclic voltammetry, although of limited stability. A rare case of a low spin Pd(III) complex ion in a compressed octahedral geometry has been stabilized.

CHAPTER 5

Synthesis of a novel macrobicyclic ligand and its nickel complex

5.1. Introduction :

Homoleptic and heteroleptic mono-macrocyclic ligands have been discussed in Chapters 3 and 4. Extensive investigations on macrocycles with flexible pendant functional groups have been made and representative examples of these ligands are shown below:[125, 126, 127]

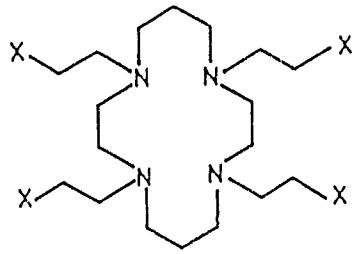

X = $-\overset{O}{\overset{\|}{C}}NH_2$, $-CH_2NH_2$

66 67

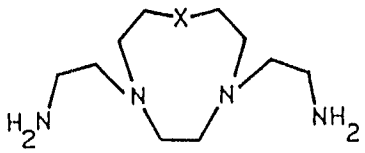

X = NH, S 68

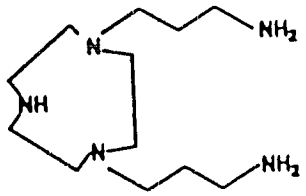

69

Binucleating macrocycles where the two rings are linked both by single and double units have been studied. Each macrocyclic ring of the ligand binds a metal ion (**9**, **10**, and **11**, Chapter 1).

Another type of macrobicyclic ligand with a 'clam', 'butterfly' or 'ear-muff' configuration can also be synthesised. In such an arrangement, the metal ion is held between the two macrocyclic rings in a sandwich configuration (with the respective rings connected by the polymethylene bridge), **70**. If the cation is of the 'correct' size relative

to the dimensions of the macrobicycle, then the 'ear-muff' configuration can occur. Studies on crown ethers, *e.g.*, **71**, have shown that the formation or lack of formation of a 'clam' type structure serves as a discrimination mechanism for particular metal ions,[128] although with some alkali metal ions binuclear complexes of the type **72** have been formed exclusively.

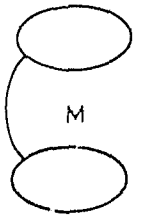

70

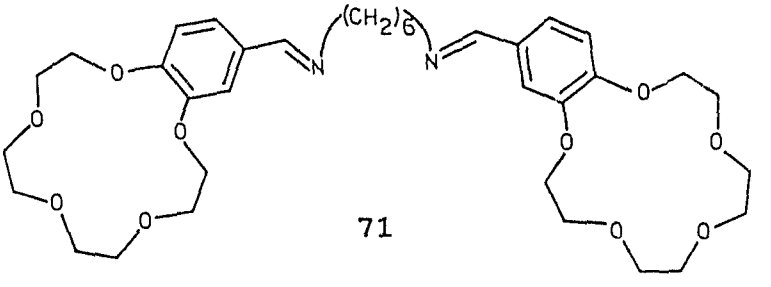

71

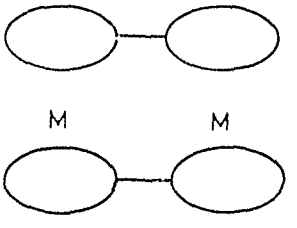

72

The 'ear-muff' configuration could allow the bound metal to be readily released on demand and are thus suitable in some cases as metal-ion transport systems. It is believed that metal complexes having configuration, **70**, might show enhanced shielding of the cation, both from the solvent and the counter ion present, thus stabilizing unusual oxidation states. Therefore study of transition metal complexes of such macrobicyclic ligands are of interest. Wieghardt *et al*[129] have synthesised Cr, Mn, Fe, Co and Ni complexes of the ligand **73**

(dtne). Only recently crystallographic evidence for the formation of a mononuclear Fe octahedral complex with the macrobicyclic ligand **73** was obtained.[130] The ligand **24** with one amino group was found suitable for the formation of the macrobicycle unlike **73**, where selective protection of the amino groups was required. In the present study the ligand **26** was synthesised and its Ni complex characterized crystallographically. Preliminary investigation of the Pd complex was also carried out.

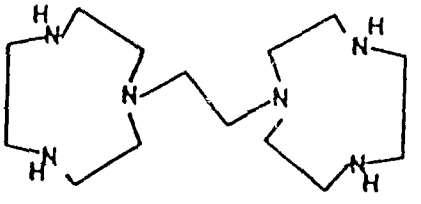

73

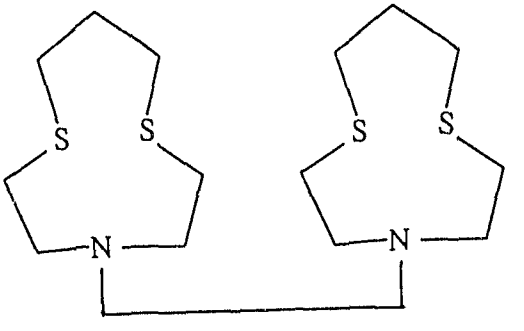

26

5.2. Synthesis :

Reaction of the ligand **24** with $TsOCH_2CH_2OTs$, **50**, in 2:1 ratio yielded the bis-macrocyclic species **26**. The purity of the ligand and the yield depended on the quality of the starting ligand, [10]aneS_2NH, **24**. The ditosylate of 1,2-ethanediol was prepared by previously published procedures[54] and characterised by ^1H nmr and melting point determination. The coupling reaction was carried out in the presence of cesium carbonate as base in dmf solution, with slow addition of the ditosylate **50**, (taken in slight excess, section **2.1.9.**). Vigorous mechanical stirring proved vital to the formation of the product and completion of the reaction. The

crude product was used as prepared for complexation with $Ni(ClO_4)_2$. The resulting impure Ni complex was purified on a Sephadex (C-25 resin) column. The Ni(II) complex of the ligand eluted as one single band with 0.05 M $NaClO_4$. Pure crystals of the complex were obtained by slow evaporation of the eluate. Decomplexation of this Ni(II) complex with NaCN in aqueous solutions precipitated the pure ligand **26**. This was used for subsequent preparations of the Ni and Pd complexes.

The ^1H nmr and ^{13}C nmr spectra of the ligand **26** are shown in Fig. 5.1a. and 5.1b. respectively. The chemical shift values are given in Chapter 2, section **2.1.9**. The $C-CH_2-C$ quintet of the propylene linkage is seen at 1.86 ppm (4 H). The singlet at 2.63 ppm (4 H) is due to the $N-C\underline{H_2}$ protons of the ethylene linkage. The $S-C\underline{H_2}$ protons are coupled and appear as a complicated multiplet centred at 2.71 ppm (16 H). A triplet further downfield at 3.14 ppm (8 H) is attributed to the protons of the macrocyclic ring attached to the electronegative N atom. The 5- line ^{13}C nmr spectrum is characteristic of the ligand **26** with five inequivalent carbon atoms. The triplet at δ 77.01 is due to the solvent $CDCl_3$.

5.3. Crystal structure of $Ni(26)(ClO_4)_2.2CH_3CN$, 51:

A deep purple crystal of the Ni complex obtained by slow evaporation of acetonitrile solutions was sealed in a Lindemann tube to prevent loss of acetonitrile. This was mounted and centered on a Nonius CAD4 diffractometer. The

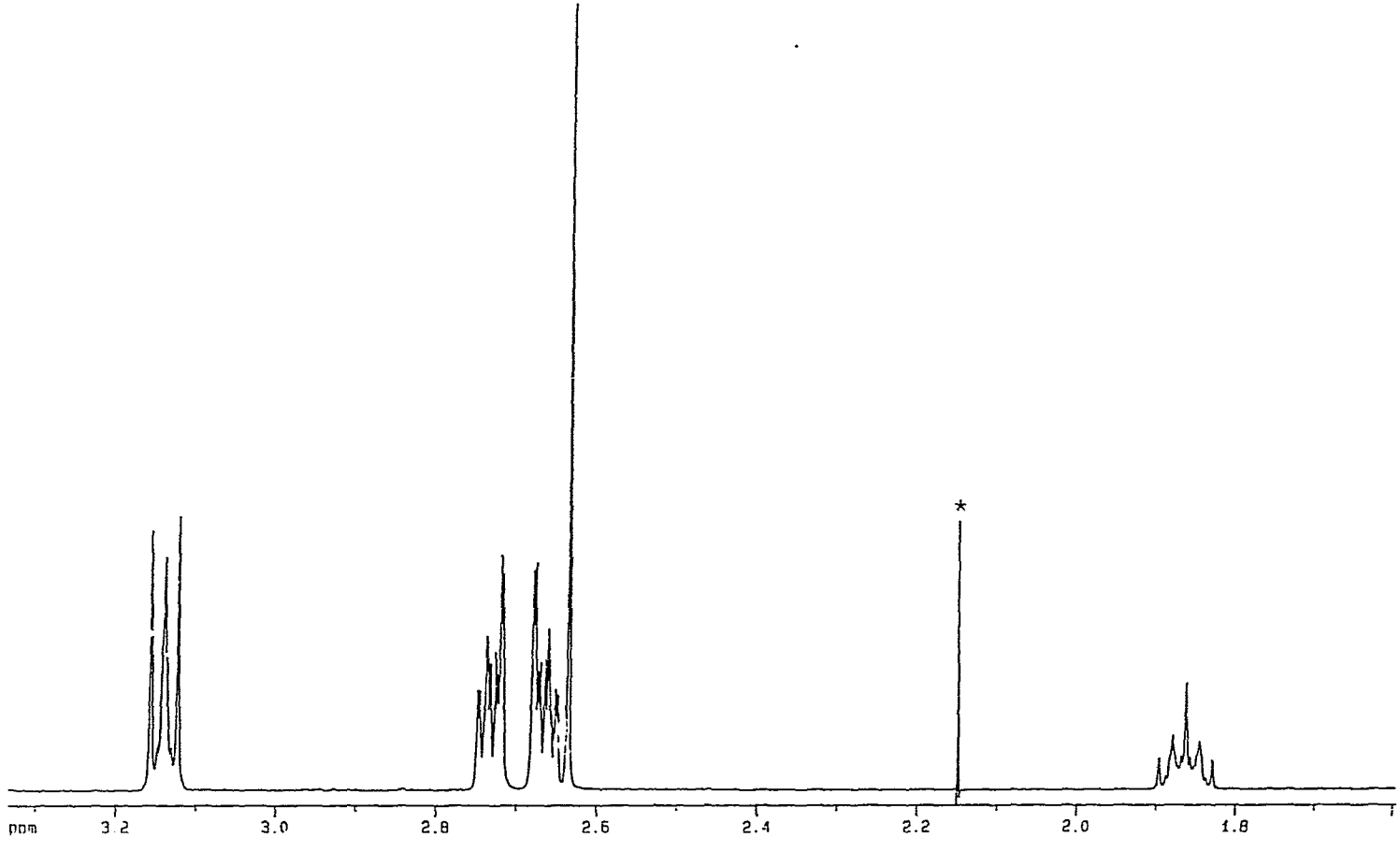

Fig. 5.1a. ^{1}H nmr of **26**. (* = acetone impurity)

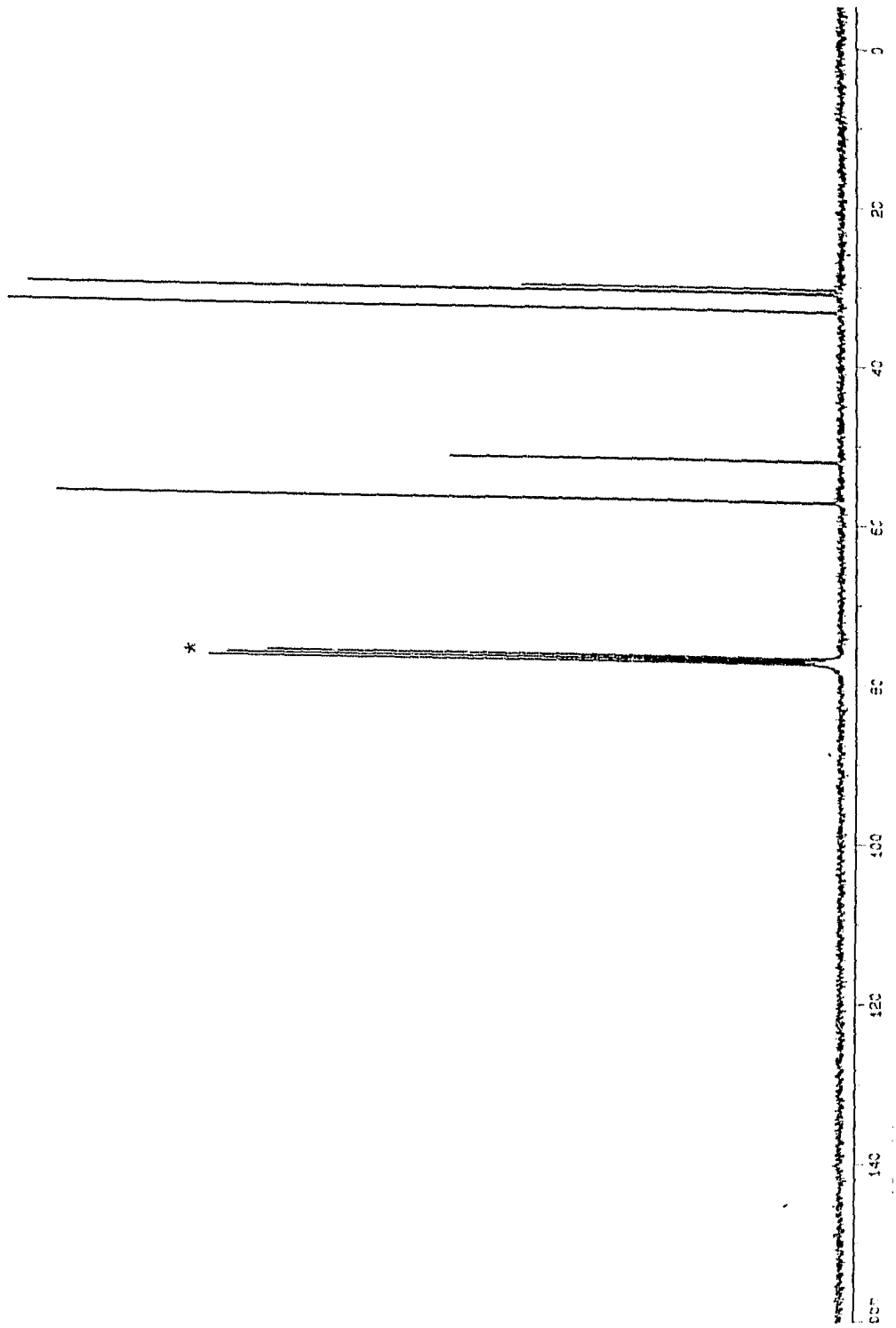

Fig. 5.1b, ^{13}C nmr of **26**. (* = $CDCl_3$).

Table 5.1. Experimental crystallographic data for $[Ni(\mathbf{26})_2].(ClO_4)_2.(CH_3CN)_2$, **51**.

Compound	**51**
Formula	$Ni_1S_4N_2C_{20}H_{38}(ClO_4)_2.(CH_3CN)_2$
MW	720.4
Crystal color	violet
Crystal system	monoclinic
Space group	C2/c (No. 15)
Cell dimensions	
a (Å)	18.483(2)
b (Å)	11.395(2)
c (Å)	15.505(3)
α (°)	90
β (°)	111.65(1)
γ (°)	90
V (Å^3)	3035.1
Z	4
D_{calc} (g/cm^3)	1.566
D_{meas} (g/cm^3)	1.576
Crystal dimensions (mm^3)	0.8×0.5×0.3
Diffractometer	Nonius, CAD4
Radiation (λ, Å)	Mo-K_α (0.71069)
Filter	Zirconium
Measurement	2θ (2 - 50°)
Octants collected	±h,k,l
std. reflections	0100,1200,008,686,1202,084
no. refln. collected	2540
no. refln. I > nσ(I)	2042 (n = 3)
no. parameters	174
Linear abs coeff. (cm^{-1})	10.56
Solution method	direct methods
R^a	0.0583
R_w^b	0.0666

[a] $R = \Sigma\|F_o|-|F_c\|/\Sigma|F_o|$; [b] $R_w = [\Sigma w(|F_o|-|F_c|)^2/\Sigma w(|F_o|)^2]^{1/2}$ where $w = 0.75/(\sigma^2 F + 0.001F^2)$

experimental details are provided in Table 5.1. Intensity measurements were made with Mo radiation filtered through a graphite monochromator, λ = 0.71069 Å. The cell was refined by using 25 centered reflections in the range 2θ = 30° - 49°. The total number of reflections measured was 2540, but this reduced to 2042 independent measurements after suppression, I > 3σ(I). The intensity measurements were corrected for Lorentz and polarization effects and for absorption.

The phase problem was solved by direct methods. The atomic scattering factors, together with the Ni *f*- curves were taken from ref. 57. Completion and refinement of the structure was done by difference electron density maps and by least squares minimizing $\sum w\Delta^2$, where $\Delta = |F_o| - |F_c|$ and $w = 0.747/[\sigma^2(F) + 0.001\ F^2]$. The asymmetric unit consisted of half a molecule, one perchlorate anion and one acetonitrile molecule, as solvent of crystallisation. Hydrogen atoms were not included in the calculations. All non-hydrogen atoms were refined using anisotropic thermal vibration parameters. The refinement converged to R = 0.0583; R_w = 0.0666 with a maximum shift/esd of 0.010 on the final cycle. A final difference map had a maximum peak of 0.1 eÅ^{-3}.

The Ni complex was found to be monoclinic and crystallised in the space group C2/c. In this centrosymmetric space group the Ni atom is in a special position (Wyckoff type *e*) of multiplicity 4 and site symmetry 2. The asymmetric unit is made up of half a molecule and is repeated by a 2-fold

symmetry axis to form the molecule. The molecule lacks an inversion centre, (no $\bar{1}$ symmetry) and the coordinates of the second half of the molecule are obtained not by $\bar{1}$ symmetry but by transposing x,y,z to -x,y,0.5-z. The fractional atomic coordinates of the complex are given in Table 5.2. The ORTEP diagram of the complex together with the atomic labelling scheme is shown in Fig. 5.2., and only the atoms of the asymmetric unit are labelled. The isotropic temperature parameters given were calculated from the anisotropic parameters.

The bond lengths and bond angles for the complex are given in Table 5.3. The Ni-N bond length of 2.112(5) Å is comparable to the normal Ni-N bond length (2.12 Å) expected for high spin Ni(II).[131] The Ni-S bond lengths are also as expected, (2.41 Å). The constraint imposed by the ligand causes the N atoms to be *cis* to each other.

The bond angle subtended at the Ni(II) ion by the two S atoms linked by a propylene group is 97.1° whereas, the five-membered chelate bite angles of the macrocyclic rings are 84.9° and 85.7°. Although the Ni(II) ion is octahedral in geometry there is a severe distortion induced by the bridge linking the two macrocycles. This strain is reflected in the *trans* S-Ni-N angles which average to 164°. However, the presence of the six-membered chelate ring allows the ten-membered ring to expand and the S atoms encapsulate the metal

Table 5.2.

Fractional atomic coordinates and temperature parameters.

Atom	x/a	y/b	z/c	Ueq
Ni(1)	0(0)	12478(8)	25000(0)	249(4)
Cl(1)	38655(9)	12068(15)	38116(12)	447(6)
S(1)	9970(9)	-310(14)	34593(11)	364(6)
S(2)	3776(8)	12175(14)	11658(10)	363(6)
O(1)	3494(6)	127(7)	3868(9)	156(7)
O(2)	3308(4)	2081(6)	3665(6)	102(4)
O(3)	4138(5)	1103(10)	3099(6)	143(5)
O(4)	4485(4)	1362(9)	4640(6)	145(5)
N(1)	838(3)	2595(4)	2987(3)	32(2)
C(1)	1548(4)	-850(7)	2883(5)	54(3)
C(2)	1725(4)	-230(7)	2113(5)	49(3)
C(3)	1018(4)	-45(7)	1226(5)	49(3)
C(4)	1012(4)	2489(6)	1427(4)	44(2)
C(5)	1377(4)	2745(6)	2471(4)	41(2)
C(6)	1335(3)	2329(6)	3984(4)	41(2)
C(7)	1689(4)	1125(6)	4108(4)	42(2)
C(8)	372(4)	3685(5)	2944(5)	43(3)
C(9)	3127(5)	1312(7)	745(6)	62(4)
C(10)	3913(4)	1600(7)	850(6)	59(3)
N(2)	2504(5)	1094(9)	658(7)	106(5)

Table 5.2. (contd).

Estimated standard deviations are given in parentheses.

Coordinates × 10^n where n = 5,5,5,4,4,4 for Ni,Cl,S,O,N,C.

Temperature parameters × 10^n where n = 4,4,4,4,3,3 for Ni,Cl,S,O,N,C.

U_{eq} = the equivalent isotropic temperature parameter.

$U_{eq} = 1/3\ \Sigma_i\Sigma_j U_{ij} a_i^* a_j^* (a_i . a_j)$

Primed values indicate the . U_{iso} is given

$T = \exp-(8\pi^2 U_{iso} \sin^2\theta/\lambda^2)$

Fig. 5.2. ORTEP diagram of [Ni(26)]$(ClO_4)_2.2CH_3CN$ with 25% tnermal ellipsoids.

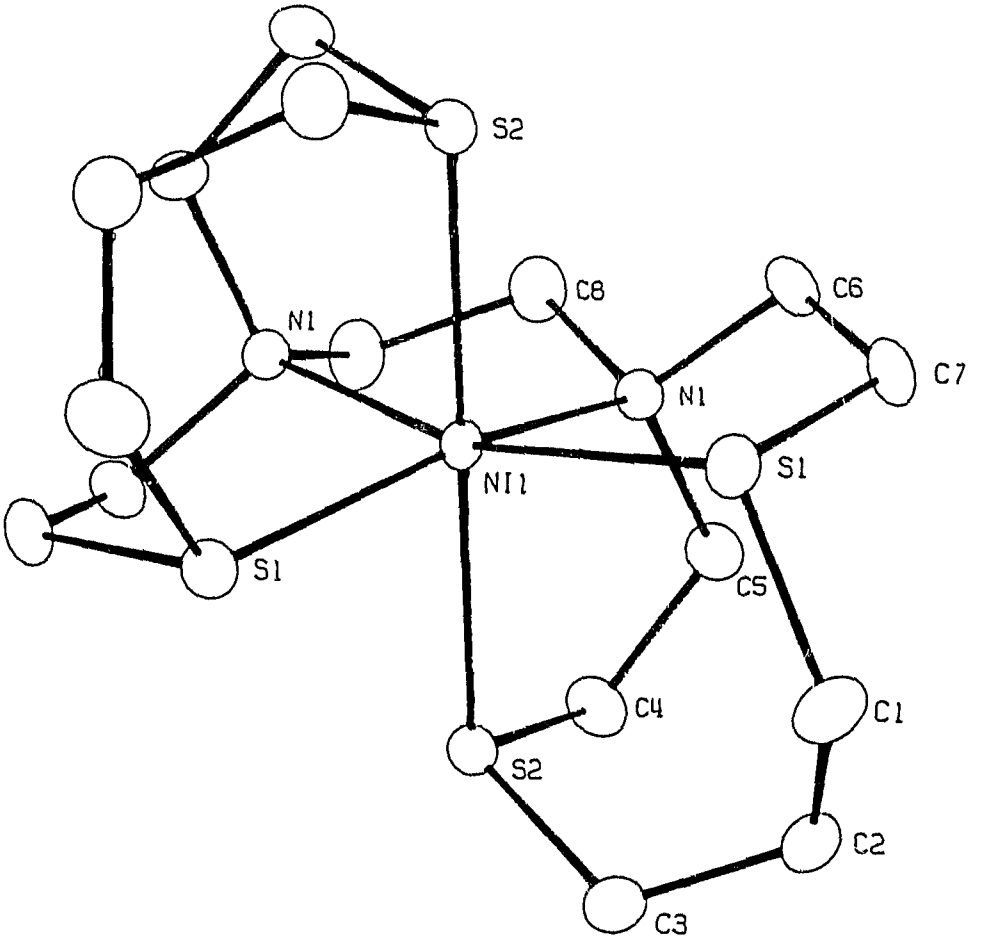

Table 5.3.

Interatomic distances (Å).

Atoms	Distance	Atoms	Distance
S(1) -Ni(1)	2.589(2)	C(5) -N(1)	1.500(7)
S(2) -Ni(1)	2.415(1)	C(6) -N(1)	1.509(7)
N(1) -Ni(1)	2.112(5)	C(8) -N(1)	1.498(7)
O(1) -Cl(1)	1.428(8)	C(2) -C(1)	1.523(10)
O(2) -Cl(1)	1.390(6)	C(3) -C(2)	1.522(10)
O(3) -Cl(1)	1.378(7)	C(5) -C(4)	1.535(8)
O(4) -Cl(1)	1.380(7)	C(7) -C(6)	1.501(9)
C(1) -S(1)	1.838(7)	C(8) -C(8)	1.546(13)
C(7) -S(1)	1.853(7)	C(10) -C(9)	1.440(11)
C(3) -S(2)	1.843(7)	N(2) -C(9)	1.135(11)
C(4) -S(2)	1.813(7)		

Estimated standard deviations are given in parentheses.

Table 5.3. (contd).

Bond angles (°)

Atoms			Angle	Atoms			Angle
S(2)	-Ni(1)	-S(1)	97.1(1)	C(5)	-N(1)	-Ni(1)	115.8(4)
N(1)	-Ni(1)	-S(1)	85.7(1)	C(6)	-N(1)	-Ni(1)	108.1(3)
N(1)	-Ni(1)	-S(2)	84.9(1)	C(6)	-N(1)	-C(5)	107.1(4)
O(2)	-Cl(1)	-O(1)	106.5(5)	C(8)	-N(1)	-Ni(1)	104.7(3)
O(3)	-Cl(1)	-O(1)	107.5(6)	C(8)	-N(1)	-C(5)	111.4(5)
O(3)	-Cl(1)	-O(2)	113.5(5)	C(8)	-N(1)	-C(6)	109.6(5)
O(4)	-Cl(1)	-O(1)	107.9(7)	N(1)	-Ni(1)	-N(1)	86.8(3)
O(4)	-Cl(1)	-O(2)	111.7(5)	C(2)	-C(1)	-S(1)	117.6(5)
O(4)	-Cl(1)	-O(3)	109.5(5)	C(3)	-C(2)	-C(1)	114.3(6)
C(1)	-S(1)	-Ni(1)	116.4(2)	C(2)	-C(3)	-S(2)	118.4(5)
C(7)	-S(1)	-Ni(1)	97.1(2)	C(5)	-C(4)	-C(2)	112.6(4)
C(7)	-S(1)	-C(1)	103.3(3)	C(4)	-C(5)	-N(1)	114.9(5)
S(1)	-Ni(1)	-S(1)	104.8(1)	C(7)	-C(6)	-N(1)	112.8(5)
C(3)	-S(2)	-Ni(1)	110.5(2)	C(6)	-C(7)	-S(1)	113.5(4)
C(4)	-S(2)	-Ni(1)	99.5(2)	N(2)	-C(9)	-C(10)	179.4(11)
C(4)	-S(2)	-C(3)	103.2(3)				

Estimated standard deviations are given in parentheses.

ion making the *trans* S-Ni-S angles to be 178°. Thus the trigonal twist between the two ten-membered macrocyclic rings imposed by the ethylene bridge was found to be 20° (Fig. 5.3.). The ORTEP diagram of the ligand in the complex as viewed down the pseudo-3-fold axis is shown in Fig. 5.4. Since the Ni(II) ion is d^8 high spin, one cannot distinguish between the axial and the equatorial ligating atoms based on the Ni(II) crystal structure. Upon oxidation low spin Ni(III) complex is formed. The electron configuration of the low spin Ni(III) being d^7, it is amenable to ESR studies and provides evidence for axial elongation or compression and the nature of the axial ligating atoms.

In the centrosymmetric space group related by the '*c*' glide plane the crystals obtained are racemic, so that both the Λ and Δ configurations are present in equal numbers. The two six-membered chelate rings are *cis* to each other and adopt a Λ configuration in the crystal structure obtained. The conformation of the ligand in the complex is [1324].[112]

5.4. Electronic spectra:

The absorption spectra, Dq values and interelectronic repulsion parameters for the various complexes are listed in Table 5.4. The Ni(II) species is purple, indicative of an octahedral Ni(II) species in solution. The absorption spectrum of Ni(**26**)$^{2+}$ complex, Fig. 5.5., shows two spin-allowed transitions at 12207 cm^{-1} (ε = 41 $M^{-1}cm^{-1}$) and 18505 cm^{-1}

Fig. 5.3. The twist angle in the two rings of the macrocycle.

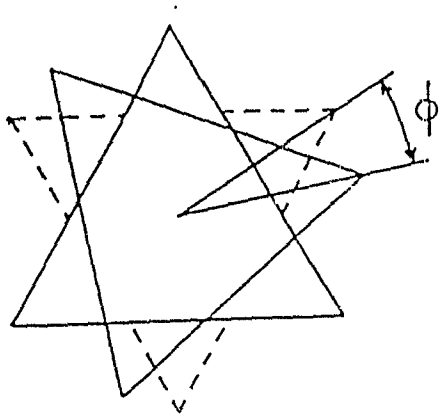

Fig. 5.4. ORTEP diagram of the $[Ni(\mathbf{26})]^{2+}$ cation as viewed along the pseudo-3-fold axis.

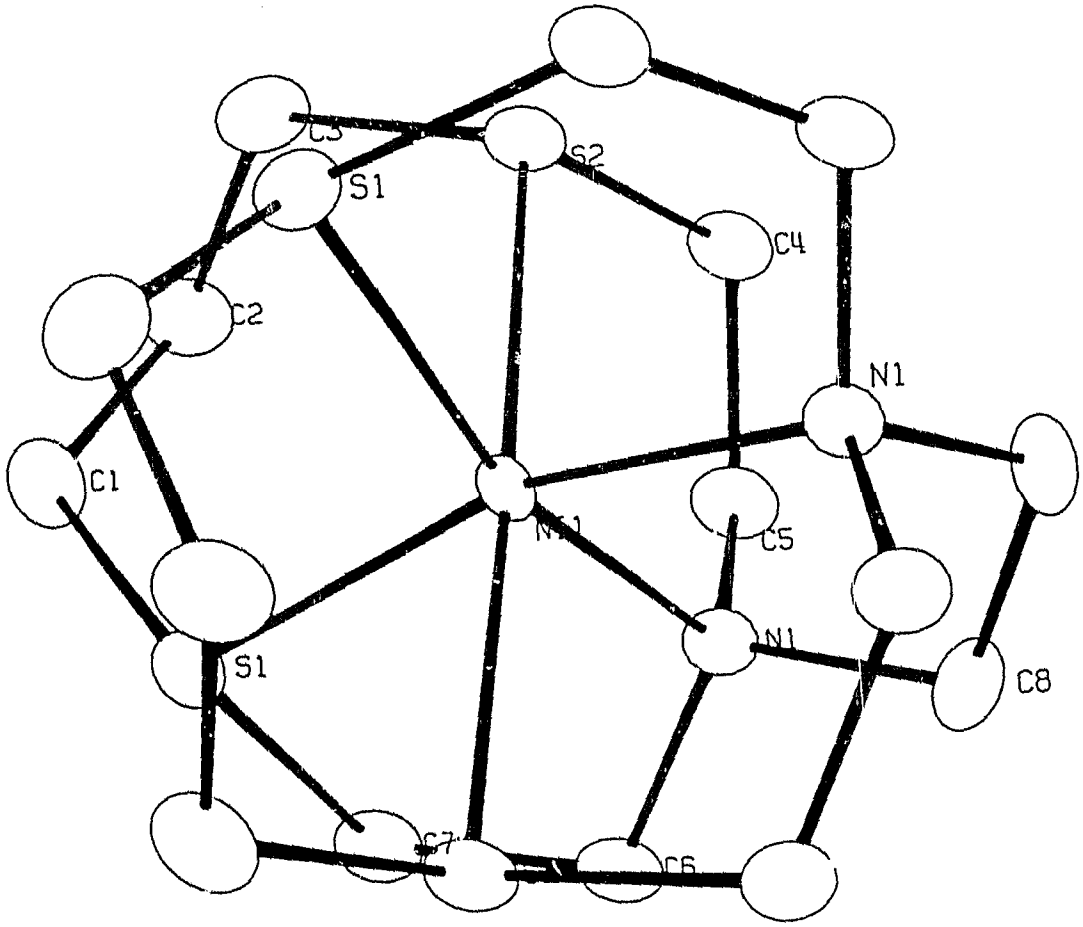

Table 5.4. Absorption spectra, Dq values and interelectronic repulsion parameters for various complexes.

Complex	λ_{max} (nm); (ε ($M^{-1}cm^{-1}$))	10Dq (cm^{-1})	B[a] (cm^{-1})	β (cm^{-1})	Ref.
$[Ni(26)_2]^{2+}$	828(43), 543(37), 318(4412), 270(3145), 191(5356)	12077	715	0.69	PW_b
$[Ni(24)_2]^{2+}$	808(10), 526(14), 418(25)	12376	778	0.75	PW[c]
$[Ni(65)_2]^{2+}$	840(23), 524(15), 297(680)	11930	-	-	105
$[Ni(23)_2]^{2+}$	850(sh), 800(37), 530(66)	12500	717	0.69	PW[d]
$[Ni(73)_2]^{2+}$	917(31), 848(31), 516(18), 363(16)	-	-	-	129
$[Ni(22)_2]^{2+}$	870, 800, 505, 325	12500	993	-	75
$[Ni(26)]^{3+}$	548(2011), 394(3369), 323(2987) 274(2118), 204	-	-	-	PW[b]
$[Ni(24)_2]^{3+}$	558, 393, 336, 258, 228, 192	-	-	-	PW[c]
$[Ni(62)_2]^{3+}$	290(11900)	-	-	-	152
$[Ni(73)_2]^{3+}$	1020(12), 623(62), 311(9000)	-	-	-	129

[a] $B_{free\ ion}$ = 1038 cm^{-1},[123] [b] this Chapter, [c] Chapter 4 [d] Chapter 6

PW = Present work.

Fig. 5.5. Electronic spectrum of $[Ni(\mathbf{26})]^{2+}$ complex.

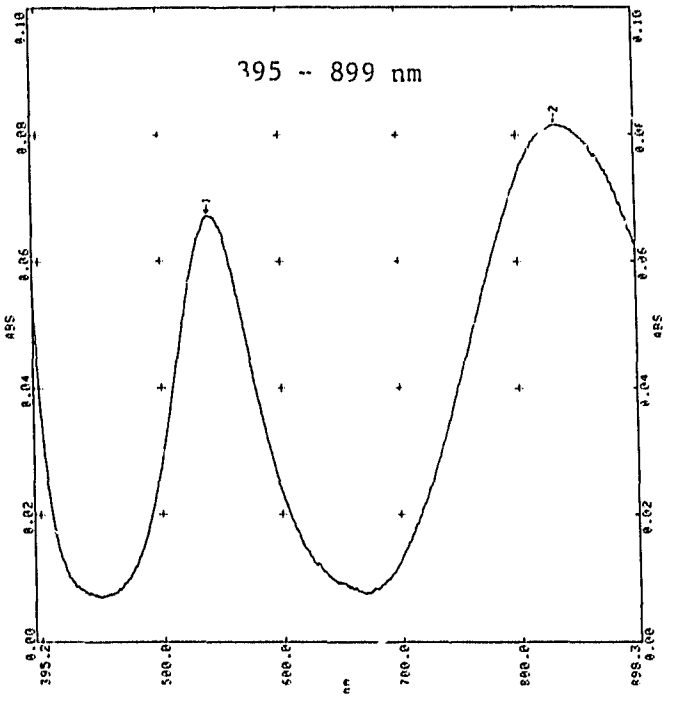

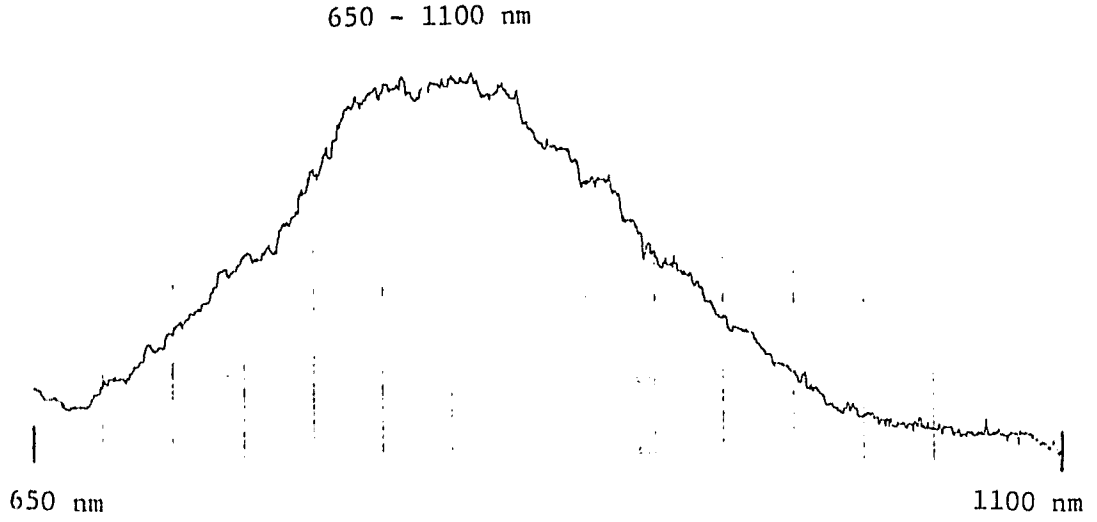

(ε = 37 $M^{-1}cm^{-1}$) due to $^3T_{2g} \leftarrow {}^3A_{2g}$ and $^3T_{1g}(F) \leftarrow {}^3A_{2g}$ transitions respectively in CH_3CN. The occurrence and the similarity of these transitions with analogous complexes are consistent with the presence of an octahedral NiS_4N_2 core, Table 5.4. The ligand field strength Dq has been evaluated from the $^3T_{2g} \leftarrow {}^3A_{2g}$ transition to be 1221 cm^{-1}. The values of 10Dq and the Racah parameter B (715 cm^{-1}) are intermediate between the homoleptic N_3 ligands and homoleptic S_3 ligands and are slightly less than those of the $Ni([10]\text{-}aneS_2N)_2^{2+}$ complex. Small differences in the 10Dq values for the $Ni(\mathbf{26})^{2+}$ complex with *cis* N atoms may be due to the strain in the macrobicyclic ligand where the N atoms are linked by an ethylene bridge, (smaller Dq). The heteroleptic nature of the ligand also contributes to the relatively lower 10Dq value. The molar absorption coefficients of the $^3T_{2g} \leftarrow {}^3A_{2g}$ bands are significantly larger than the corresponding $Ni([10]\text{-}aneS_2NH)_2^{2+}$ and $Ni([9]\text{-}aneS_2N)_2^{2+}$ ions and is comparable to that of the $Ni([10]\text{-}aneS_3)_2^{2+}$ ion, Table 5.4. This can be attributed to both the presence of tertiary amine donor atoms and a severe distortion of the NiS_4N_2 core. The ethylene bridge linking the two macrocyclic units enforces a trigonal twist of the two rings with respect to each other (see Fig. 5.3.). Large molar absorption coefficients have been noted for the homoleptic macrobicyclic ligand, dtne (**73**), compared to the $[Ni(\mathbf{22})]^{2+}$ ion and this was attributed to the trigonal twist of the two nine-membered rings. Unusually high extinction coefficients have also been

noted for Co(**69**)$^{3+}$ where the trigonal twist angle calculated from its structural parameters was found to be 11.1°.[132]

5.5. Redox studies:

Oxidation of [Ni(**26**)]$^{2+}$ in aqueous medium using Co^{3+}, $S_2O_8^{2-}$ or NO^+ in CH_3CN solutions yielded a red esr active species due to the formation of a low spin d^7 octahedral [Ni(**26**)]$^{3+}$ complex cation. Both the anisotropy and the magnitude of the g values of Ni(III) can be taken to indicate the degree of the metal-centered oxidation or reduction. The order of the g values gives detailed structural information allowing distinction between tetragonally elongated and tetragonally compressed geometry. Splitting of the d orbitals for a low spin d^7 ion is shown in Fig. 5.6.

Frozen solutions of the red Ni(III) complex species at 77 K showed an anisotropic EPR spectrum with $g_\parallel$ = 2.148 and $g_\perp$ = 2.063, Fig. 5.7. This spectrum with $g_\parallel > g_\perp > g_e$ is consistent with a compressed octahedron having a $d_{x^2-y^2}$ ground state. The ethylene bridge linking the two N atoms forces a *cis* geometry and also forces the two macrocyclic rings to wrap around the metal giving rise to an inverted esr spectrum. Such an inverted spectrum characteristic of compressed octahedral species is found among other cis complexes *viz.*, [Ni([12]-aneN$_4$)(CH$_3$CN)$_2$]$^{3+}$ cation.[133] A similar spectrum has been obtained for frozen solutions of [Ni$_2$(III)(**74**)$_2$(μ-oxalato)]$^{4+}$ in acetonitrile in this laboratory.[51] Another example of an

octahedral complex with axial compression is $[Ni(bpy)_3](ClO_4)_3.2CH_3CN.0.5CH_2Cl_2$ with two short axial Ni-N

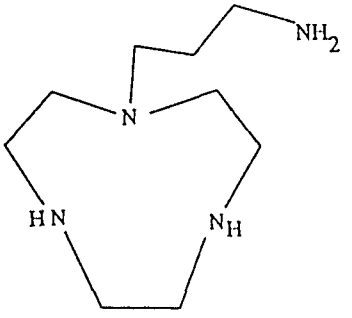

74

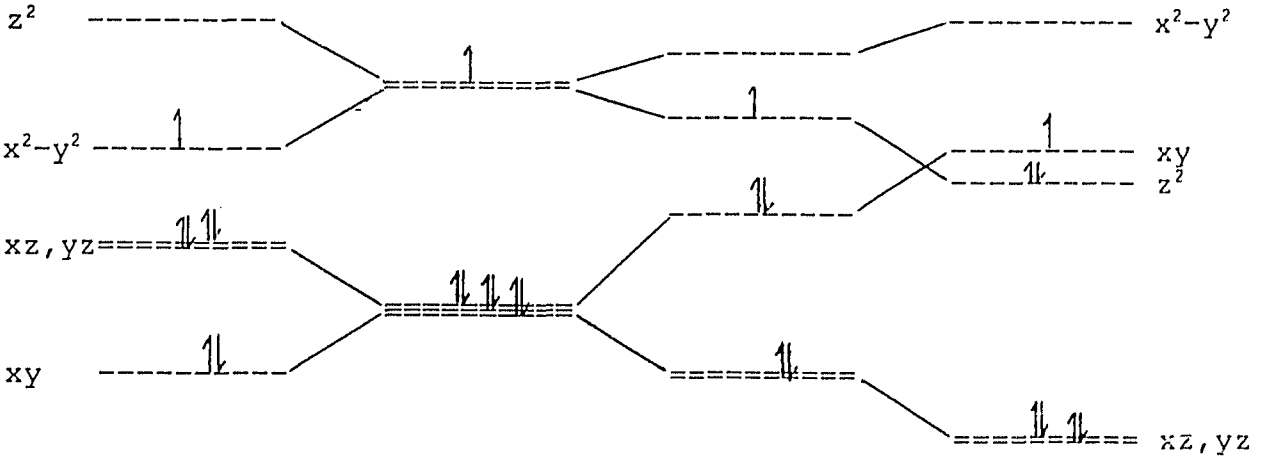

Tetragonally compressed	Octahedral	Tetragonally elongated	Square planar
$g_{zz} > g_{xx}, g_{yy}$	d^7	$g_{xx}, g_{yy} > g_{zz}$	$g_{zz} > g_{xx}, g_{yy}$
$g_{xx}, g_{yy} > g_{zz}$	d^9	$g_{zz} > g_{xx}, g_{yy}$	$g_{zz} > g_{xx}, g_{yy}$

Fig. 5.6. The splitting of d orbitals in tetragonally compressed, tetragonally elongated and square-planar geometries for a d^7 ion and the resulting relative g values for d^7 and d^9 configurations.

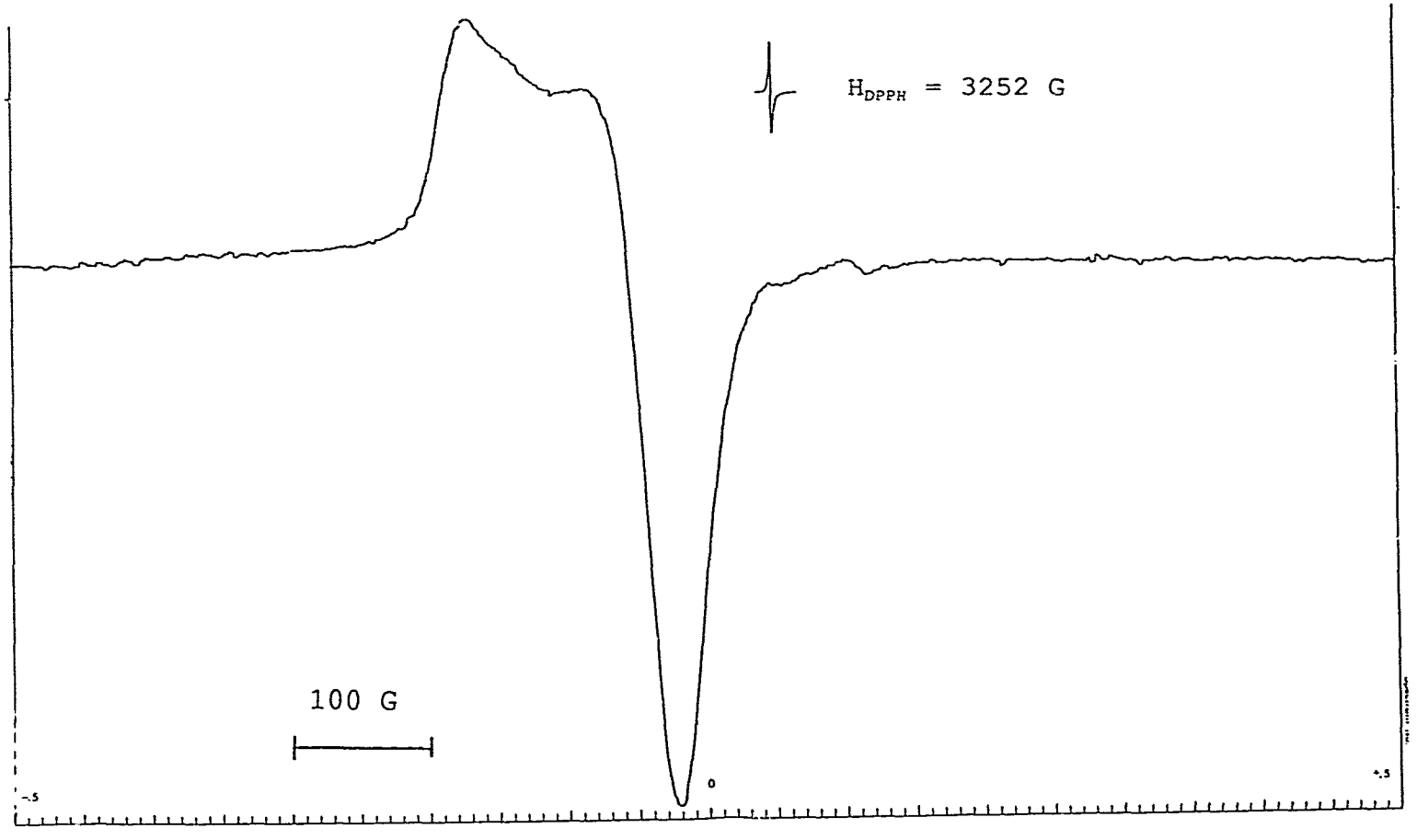

Fig. 5.7. ESR spectrum of [Ni(**26**)]$^{3+}$ complex ion in CH_3CN.

bond lengths of 1.92 Å and four long Ni-N bond lengths of 2.01 Å. Based on this structure the authors[58] concluded that the single unpaired electron was in the $d_{x^2-y^2}$ orbital. ESR spectra of its frozen solutions at 77 K showed $g_{\parallel}$ (2.02) < $g_{\perp}$ (2.13) indicative of a d_{z^2} ground state. This may be due to the smaller energy difference between an elongated and compressed D_{4h} geometry.

For the corresponding $[Ni(65)]^{3+}$ ion, although one expects an inverted esr spectrum with $g_{\perp} > g_{\parallel} > g_e$ consistent with the compressed octahedral geometry, an elongated spectrum has been observed.[105] However, hyperfine coupling with the axial N atoms was seen in the $g_{\parallel}$ feature. Although the Ni(III) structure is not known the Ni-N_{ax} distance is expected to be shorter than the Ni-S_{eq} distance. Static or dynamic disorder in the equatorial bonds may lead to an elongated coordination. This phenomenon of a 'planar dynamics' of 'antiferrodistortive order of elongated octahedra' is known to occur in low-spin d^7 cations with E_g ground state.[134]

The g value is a function of the spin-orbit coupling constant ζ and the ligand-field splitting 10Dq. For a compressed octahedron with a $d_{x^2-y^2}$ ground state, the g- tensor is given by :[135]

$$g_{\parallel} = g_e + 8\mu + 2\mu' \qquad \text{— 5.1.}$$

$$g_{\perp} = g_e + 2\mu + 2\mu' \qquad \text{— 5.2.}$$

where, $\mu = (1/2)\zeta[1.38/E_3 + 0.62/E_4]$ and $\mu' = \zeta^2/\delta^2$.

ζ is the spin-orbit coupling constant and δ is the energy

separation between the low-spin ground state ($^2A_{1g}$) and the first excited high-spin state (split level of the octahedral $^4T_{1g}$ parent state); E_3 and E_4 are the transitions from $^2A_{1g}$ to the octahedral $_a{}^2T_{2g}$ and $_b{}^2T_{2g}$ parent states. Substituting the g values in eqns. 5.1. and 5.2., μ and μ' were calculated to be 0.0142 and 0.0162 respectively. Using the values of E_3 = 25381 cm^{-1} and E_4 = 36497 cm^{-1} (from the electronic absorption spectrum, Fig. 5.8.) in the above equations, a high-spin-low-spin separation of 3140 cm^{-1} and ζ = 400 cm^{-1}, were obtained. The covalency parameter, K, was determined from:[121]

$$\zeta = K^2\zeta_c, \quad (\zeta_c = 705\ cm^{-1})$$

to be 0.75. For the $[Ni(\mathbf{22})_2]^{3+}$ complex the effective spin-orbit coupling parameter was found to be 450 cm^{-1} and K, 0.8.

Similar calculations for the $[Ni(\mathbf{24})_2]^{3+}$ ion were performed for comparison. Using the values of $g_\parallel$ = 2.127, $g_\perp$ = 2.061, E_3 = 25445 cm^{-1} and E_4 = 31847 cm^{-1} (see Chapter 4), the values of δ and ζ were found to be 2210 cm^{-1} and 300 cm^{-1} respectively. A value of 0.65 was obtained for the covalency parameter (K).

Formal redox potentials for $[Ni(\mathbf{26})]^{2+}$ ion and related complexes are summarised in Table 5.5. The cyclic voltammogram for the $[Ni(\mathbf{26})]^{3+/2+}$ couple is shown in Fig. 5.9. The $E_{1/2}$ value was found to be 1.30 V *vs* NHE [1.05 V *vs* Ag^+/Ag, ferrocene was used as an external standard; $E_{1/2}$ (Fc^+/Fc) = 0.15 V; $E_{1/2}$ (Fc^+/Fc) = 0.4 V *vs* NHE] and is larger than the corresponding value for the $[Ni(dtne)]^{3+/2+}$ couple (dtne = **73**).

This is attributed to the presence of S ligating atoms. The π- acceptor properties of the S atoms destabilize Ni(III) with respect to Ni(II) resulting in the higher redox potential for the former complex. Although the replacement of a secondary amine with a tertiary amine donor is expected to destabilize the Ni(III) state, the redox potential for the $[Ni(26)]^{3+/2+}$ couple is comparable to that of the Ni-bis complex of **24**, indicating the ligand constraint imposed by the ethylene bridge in the macrobicyclic ligand **26**.

Fig. 5.8. Absorption spectrum of the $[Ni(26)]^{3+}$ ion.

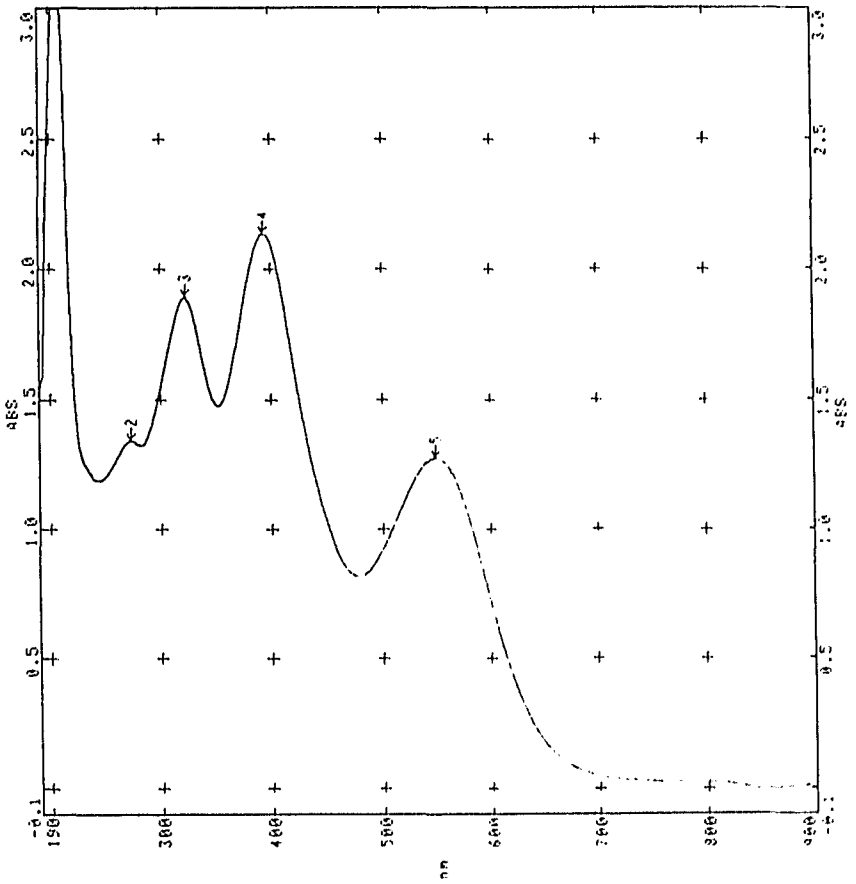

Table 5.5. Formal redox potentials (V) for $[Ni(\mathbf{26})]^{2+}$ and related complexes.

Complex	$E_{1/2}$ (V) (*vs* Fc^+/Fc)	ΔE (mV)	$E_{1/2}$ (V) (*vs* NHE)	Ref.
$[Ni(\mathbf{26})]^{3+/2+,a}$	0.90	90	1.30	PW
$[Ni(\mathbf{24})_2]^{3+/2+,a}$	0.86	114	1.26	PW
$[Ni(\mathbf{22})_2]^{3+/2+}$	-	75	0.95	76
$[Ni(\mathbf{73})]^{3+/2+}$	-	85	1.10	129

[a] in CH_3CN (0.1 M NEt_4BF_4), ref. electrode $Ag/AgNO_3$ (0.1 M).

Fig. 5.9. Cyclic voltammogram of the $[Ni(\mathbf{26})]^{3+/2+}$ couple in CH_3CN containing 0.1 M NEt_4BF_4. Ref. 0.1 M Ag^+/Ag.

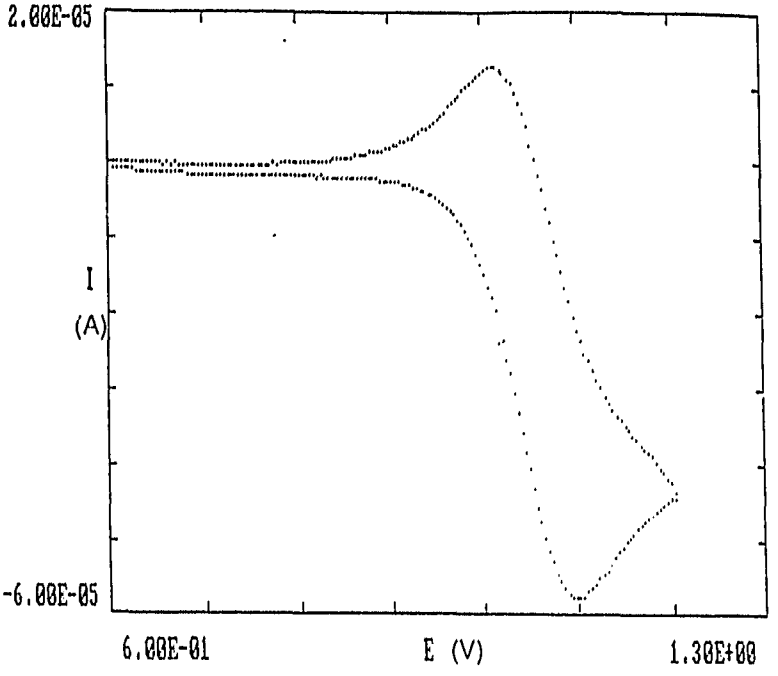

The $[Pd(\mathbf{26})]^{2+}$ complex was prepared by the reaction of the ligand **26** with $Pd(OAc)_2$ in CH_3CN. The solution was refluxed for 1 h during which time all of the $Pd(OAc)_2$ was dissolved. Addition of NH_4PF_6 to the yellow solution yielded yellow-brown hygroscopic solid. The reaction was not performed under strictly anaerobic conditions and esr spectrum of the orange-yellow filtrate (Fig. 5.10.) showed an inverted spectrum with $g_{\parallel} > g_{\perp} > 2$. The spectrum is typical of a low spin d^7 $[Pd(\mathbf{26})]^{3+}$ cation in a compressed octahedral environment. The sequence $g_{\parallel} > g_{\perp} > g_e$, [$g_e$(free-electron value) = 2.0023], is compatible with the unpaired electron in a $d_{x^2-y^2}$ orbital. Such a compressed geometry for Pd(III) complexes is unusual and reflects the steric constraints imposed by the ligand with *cis* N atoms. The spectrum of the corresponding $[Pd(\mathbf{24})_2]^{3+}$ cation is near octahedral and does not show distinct g anisotropy even in high ionic strengths. Both $[Pd(\mathbf{23})_2]^{3+}$ cation (Chapter 6) and $[Pd(\mathbf{22})_2]^{3+}$ ion[99] show an axial spectrum with $g_{\perp} > g_{\parallel} > g_e$. Pd(III) ion in a compressed octahedral coordination has been observed by Sastry[136] upon γ- irradiation of NH_4Cl crystals doped with Pd(II). Pd(III) ions have been stabilized in a number of complexes with S ligating atoms where axial elongation has been observed.[104] The esr spectrum of $[Pd(\mathbf{63})_2]^{3+}$ was anisotropic with $g_1 = 2.064$, $g_2 = 2.052$, and $g_3 = 2.019$. Based on the esr spectra structure **75** for the $[Pd(\mathbf{26})]^{3+}$ cation could be proposed. Further understanding requires isolation and characterization of these Pd complexes.

Fig. 5.10. ESR spectrum of $[Pd(26)]^{3+}$ complex in CH_3CN + NO^+.

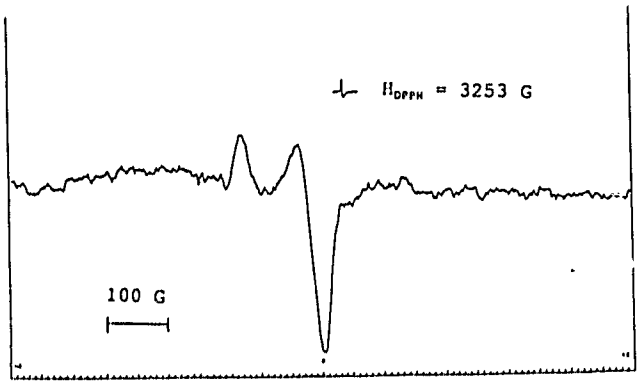

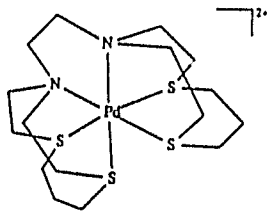

75

5.6. Conclusions:

The macrobicyclic ligand **26** was successfully synthesised. The ligand forms distorted octahedral complexes with Ni(II) and Pd(III) with the N atoms *cis* to each other as opposed to the complexes of [10]-aneS_2NH, **24**, where the N atoms are *trans* to each other. The constraint imposed by the ethylene bridge is reflected on the large twist angle of the macrocyclic rings with respect to each other and on the large molar absorption coefficients observed for the Ni(II) complex. Both the Ni(III) and Pd(III) complexes are in a compressed octahedral geometry with the unpaired electron in the $d_{x^2-y^2}$ orbital.

CHAPTER 6

Synthesis and reactivity of transition metal complexes of 1,4,7-trithiacyclodecane

6.1. Introduction:

Interest in homoleptic transition-metal complexes containing crown thioether ligands has seen significant increase only in the past five years.[86-94,137-142] Although the synthesis of the nine-membered trithia ligand [9]-aneS_3, **64**, was provided a decade ago,[143] the coordinating ability of these thioether ligands remained unexplored for a long time owing to the poor yields obtained. Since then, due to the Cs_2CO_3 mediated methods introduced by Kellogg and co-workers[144] better yields of macrocyclic ligands have been obtained.[145] Like the triaza macrocyclic ligands, crown thioether ligands are capable of stabilizing less common oxidation states in transition metal ions. The trithia systems provide examples of complexes where both higher and lower oxidation states are stabilised [(*e.g.*, Pt(III),[94] Pd(III),[100]] and also monomeric $[Rh(\mathbf{64})_2]^{2+}$ has been identified.[100] Octahedral Ag(I) bis-complexes of **64** have also been obtained. However, this species undergoes chemical oxidation by Ce(IV) in MeOH (-70 °C) affording the corresponding Ag(II) complex.[146] In much of this chemistry, particular attention has been paid to the structure of the complexes, including weak interactions in axial sites of d^8 ions which lend themselves to ready oxidation to d^7, hexacoordinate ions. Such an "entatic state" has been the subject of comment in the case of the Pt and Pd ions.[94,100]

Ligand conformational factors greatly influence the

stability of crown thioether complexes. Many crown thioethers, *e.g.*, 12-crown-4,[147] **76**, 14-crown-4,[148] **77**, 15-crown-5,[147] **78**, and 12-aneS_3,[149] **79**, are exodentate *i.e.*, the S atoms are pointed away from the macrocyclic cavity. Formation of transition metal complexes with these ligands requires a conformational change. Therefore, crown thio ethers tend to bridge metal atoms if the S atoms are exodentate. However, the S atoms in 9-aneS_3, **64**, are endodentate[150] (*i.e.*, pointing into the macrocyclic cavity) and hence transition metal complexes of bis-9-aneS_3 have been obtained readily. Homoleptic six-coordinate complexes of Fe(II), Fe(III), Co(II), Ni(II), Cu(II), Pd(II), Pt(II), Ag(I), Ru(II) and Rh(III) containing crown thioether ligands (*e.g.*, [9]-aneS_3) have been isolated and characterised. The constraints imposed by the crown thioether ligands forces coordination of the otherwise weakly binding donor atoms. Conformational effects of the carbon skeletons thus dictate the differences in properties exhibited by transition metal complexes of [9]-aneS_3 and those of [12]-aneS_3. Among the Ag(I) complexes of [9]-aneS_3 and [12]-aneS_3 Blower *et al*[93] found that while [9]-aneS_3 coordinates in a tridentate fashion yielding monomeric complexes, [12]-aneS_3 forms oligomers. Studies on the effect of cavity size on the complexing ability were made by Rawle *et al*[88] on Ru complexes of [9]-aneS_3 and [12]-aneS_3. It was found that while [9]-aneS_3, **64**, 'perches', [12]-aneS_3, **79**, 'engulfs'. This prompted the present attempts to synthesise [10]-aneS_3,

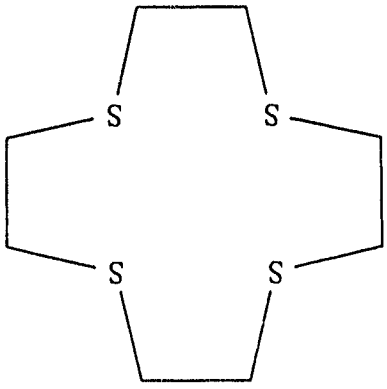

76

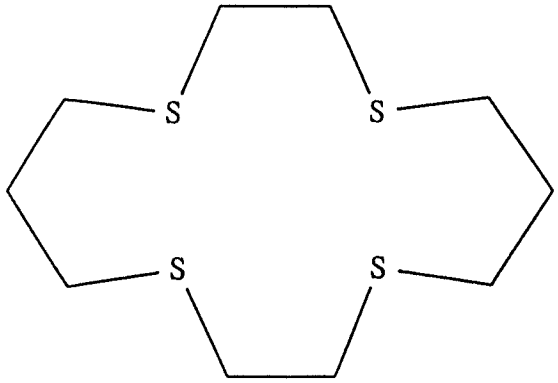

77

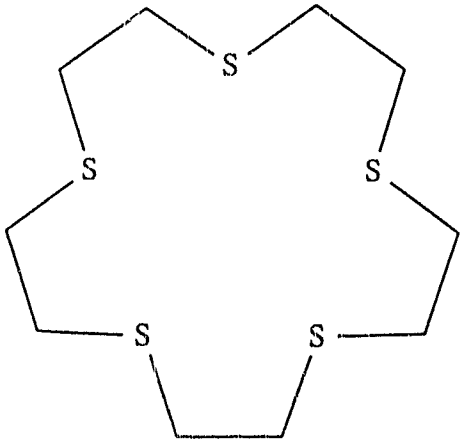

78

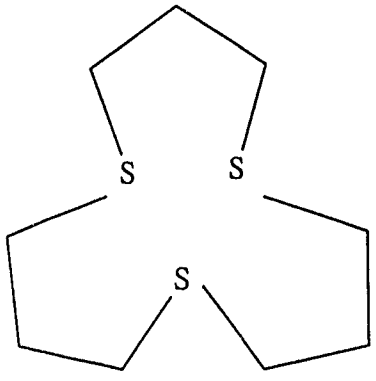

79

23, and study its transition metal complexes.[151] Also there are fewer data available for the corresponding ten-membered ring systems. The self exchange rates for the $[Ni([10]\text{-}aneN_3)_2]^{2+}$ couple have examined in this laboratory by means of a series of cross reactions.[152] In an interesting study, Wieghardt and coworkers[95] have analysed the electron transfer barriers in $CoN_6^{3+/2+}$ and $CoS_6^{3+/2+}$ couples in terms of the Marcus-Sutin model[47,153] for outer sphere electron transfer. It is important that direct methods for determining electron self-exchange rates be used wherever possible to augment data for the Marcus cross correlation. Only recently ^1H and ^{13}C nmr line broadening techniques have been used in the study of electron transfer reactions.[43,97,154]

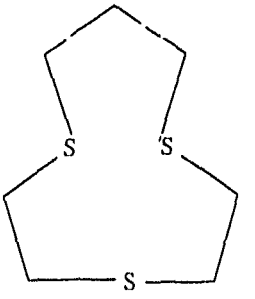

23

In the present chapter the *bis*-[10]-aneS_3 complexes with Fe(II), Co(II), Ni(II) and Pd(II) ions have been synthesised and characterised by their electronic spectra, NMR spectra and crystal structure. Oxidation, both electrochemical and chemical, produced the corresponding M^{3+} ions which have been characterised, where appropriate, by EPR techniques. Comparisons are made with the corresponding nine-membered ring complexes and preliminary kinetic data are presented.

The ^{59}Co NMR spectra of the Co(III) *bis*-thia complexes have been obtained and correlated with the electronic spectroscopic data. The rates of exchange in the electron transfer reactions for the $Co([10]\text{-}aneS_3)_2^{3+/2+}$ couples have been measured for the first time using ^{59}Co nmr.

6.2. Synthesis:

The ligand [10]-$aneS_3$ was synthesised by the methods of Buter and Kellogg[33] using Cs_2CO_3/dmf (Scheme 2.6., Chapter 2). The rate of addition of the mixture of the dithiol and the appropriate dibromo- compound was maintained at 2 mL/minute. Under the conditions of the experiment the percentage yield of the ten-membered macrocycle was very high (~80%). The twenty-membered macrocycle, [20]-$aneS_6$ was formed in quantities less than 10%. The colorless crystalline solid of [10]-$aneS_3$, **23**, could be obtained at low temperatures (5° C) upon crystallisation from an ethanolic solution of the ligand.

The bis-[10]-$aneS_3$ complexes of Fe(II), Co(II) and Ni(II) were made using the corresponding metal(II) perchlorate salt in methanol. In the case of Fe(II), although $Fe(ClO_4)_3.6H_2O$ was used as the starting material, the Fe(II) complex of the bis-trithia ligand was obtained. Similar observations were made by Wieghardt *et al*[87] in the reaction of $Fe(ClO_4)_3$ with [9]-$aneS_3$. This reflects the ability of the soft S donor atoms to stabilize low oxidation states (soft acid) by virtue of being a π- donor. The Co(II) bis- complex of [10]-$aneS_3$,

23, was prepared by reacting the metal perchlorate salt with a methanolic solution of the ligand. Orange crystalline $[Co[\mathbf{23}]_2]^{3+}$ complex was obtained by $S_2O_8^{2-}$ oxidation of the corresponding Co(II) complex.

During the preparation of the Pd complex a yellow solid was obtained initially and also a green solution (see Chapter II). The yellow solid analysed according to the formula $C_7H_{14}S_3PdClPF_6$ but could be a dimeric species having the following structure:

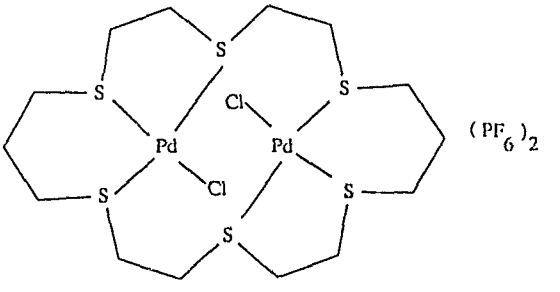

Similar Pd dimers of 18- membered and 20- membered hexaaza macrocycles were obtained in the laboratory[68] and were characterized structurally. Attempts to grow suitable crystals for X-ray studies were unsuccessful.

The green solid $[Pd([10]\text{-ane}S_3)_2](PF_6)_2$, **56**, was obtained from the green filtrate of the Pd bis- complex. Recrystallization from CH_3CN solutions afforded blue crystals of **56** and a yellow amorphous solid at the bottom of the beaker. Acetonitrile solutions of the green solid became more yellow when heated above room temperature and more blue when cooled below room temperature. A subsequent structural study

of the blue compound **56** showed it to be a *'endo'* isomer (with respect to the axis, see Chapter 4). The yellow amorphous solid is, possibly the corresponding *'exo'* isomer. Variable temperature ^{13}C nmr investigations should prove useful in understanding the *endo - exo* isomerization process.

6.3. Crystal structures:

6.3.1. Crystal structure of $Fe([10]\text{-}aneS_3)_2(ClO_4)_2$, 52:

A purple crystal of the complex was mounted in a Lindemann tube and photographed by Weissenberg and precession cameras to establish the symmetry and the cell dimensions. The crystal was then mounted on a Nonius CAD4 diffractometer. Crystal data are given in Table 6.1. The cell was refined using 22 centered reflections in the range $2\theta = 23° - 29°$. Data reduction yielded 1199 reflections with $I > 2\sigma(I)$ which were used for solution and refinement of the structure. The intensity measurements were corrected for Lorentz and polarization effects, and for absorption.

The solution of the phase problem was achieved using MULTAN.[56] The atomic scattering factors together with the Fe *f* curves were taken from ref. 57. Completion and refinement of the structure was done by methods of least squares minimizing. The asymmetric unit consisted of half a molecule of the complex cation and one perchlorate anion. The refinement converged with a maximum shift/esd of 0.027 on the final cycle and the *R* value was found to be 0.0553, R_w =

Table 6.1. Experimental crystallographic data for $[Fe([10]\text{-}aneS_3)_2].(ClO_4)_2$, **52**.

Compound	**52**
Formula	$Fe_1S_6C_{14}H_{28}Cl_2O_8$
MW	643.5
Crystal color	blue
Crystal system	monoclinic
Space group	$P2_1/c$ (No. 14)
Cell dimensions	
a (Å)	7.408(3)
b (Å)	9.482(5)
c (Å)	17.156(7)
α (°)	90
β (°)	97.87(3)
γ (°)	90
V (Å^3)	1193.7
Z	2
D_{calc} (g/cm^3)	1.731
D_{meas} (g/cm^3)	1.790
Crystal dimensions (mm^3)	0.144×0.125×0.626
Diffractometer	Nonius, CAD4
Radiation (λ, Å)	Mo-K_α (0.71069)
Filter	Zirconium
Measurement	2θ (2 - 45°)
Octants collected	±h,k,l
std. reflections	340,0012,080,0010,404,340
no. refln. collected	1466
no. refln. $I > n\sigma(I)$	1199 (n = 2)
no. parameters	142
Linear abs coeff. (cm^{-1})	13.24
Solution method	MULTAN
R^a	0.0553
$R_w{}^b$	0.0609

[a] $R = \Sigma\| F_o| - |F_c\| / \Sigma |F_o|$

[b] $R_w = [\Sigma w(|F_o| - |F_c|)^2 / \Sigma w(|F_o|)^2]^{1/2}$ where $w = 2.40/(\sigma^2 F + 0.001F^2)$

0.0609. A final difference map had a maximum peak of 0.64 eÅ^{-3}.

The molecular structure of $[Fe([10]\text{-ane}S_3)_2](ClO_4)_2$ together with the atomic labelling scheme is shown in Fig. 6.1. The metal atom is coordinated by six S atoms in a near octahedral fashion. The Fe atom occupies an inversion centre and the other half of the molecule is obtained by inverting at this centre. The fractional atomic coordinates, bond lengths and bond angles are given in Tables 6.2. and 6.3. The Fe-S bond lengths for the six membered rings are unequal, 2.275(2) Å and 2.260(2) Å; and are longer than that of the five membered ring, 2.243(2) Å. Although the low spin d^6 Fe(II) complex is expected to be undistorted, the asymmetry in the ligand induces a rhombic distortion in the complex. This is confirmed in the e.s.r. spectrum of the Fe(III) (oxidised) species with a low spin d^5 electronic configuration. The average S-Fe-S angle for the five-membered chelate ring is 89.4(3)° (mean of 2). The six-membered chelate bite angle was found to be 94.1(1)°. The two trimethylene bridges are *trans* to one another resulting in a mesomeric structure. In the corresponding octahedral Fe(II) complex of the symmetric ligand [9]-aneS_3, **64**, the differences in the Fe-S bond lengths were smaller and the lengths averaged to 2.250(9) Å. The average S-Fe-S angle was found to be 90.3(6)°.[87]

6.3.2. Crystal structures of $Ni([10]\text{-ane}S_3)_2(ClO_4)_2$, 55:

Pink crystals of the Ni complex were obtained by ether

Fig. 6.1. ORTEP diagram of $[Fe([10]\text{-}aneS_3)_2](ClO_4)_2$, **52**, with 25% thermal ellipsoids.

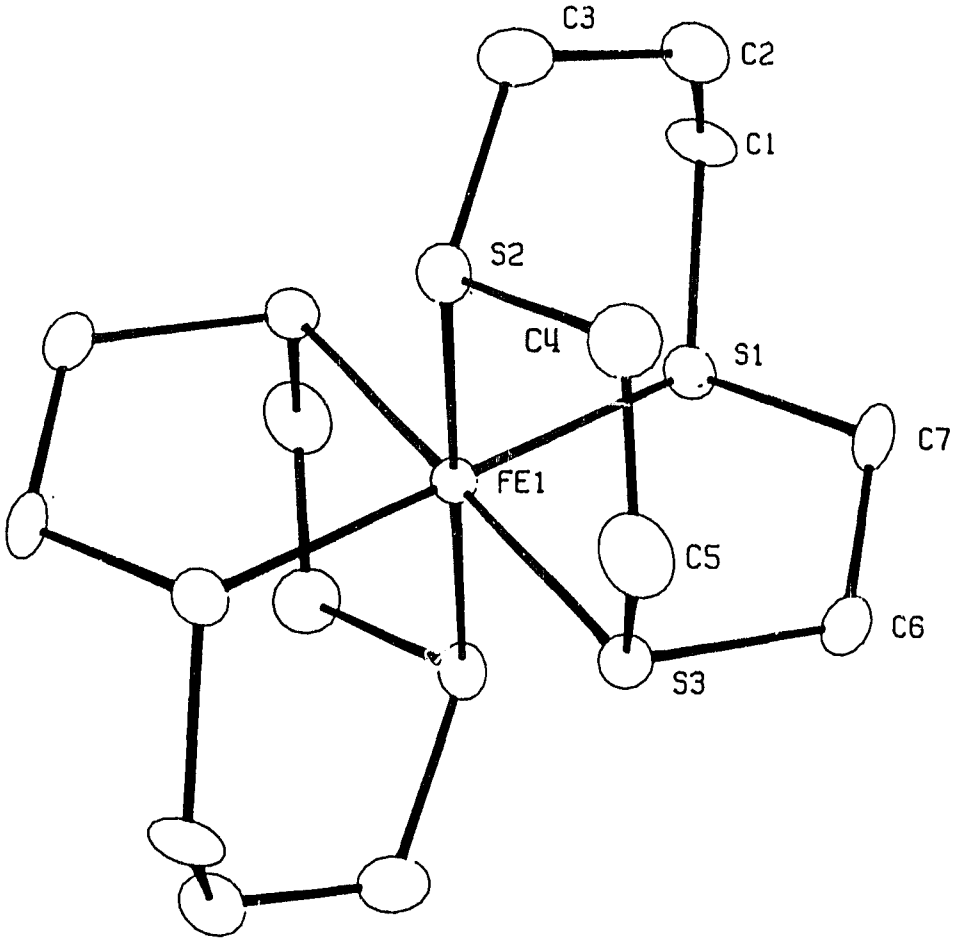

Table 6.2.

Fractional atomic coordinates and temperature parameters.

Atom	x/a	y/b	z/c	Ueq
F	00000(0)	00000(0)	00000(0)	265(5)
Cl(1)	46889(31)	7595(25)	33956(12)	424(8)
S(1)	2578(3)	1332(2)	158(1)	34(1)
S(2)	-1484(3)	1399(2)	769(1)	38(1)
S(3)	1129(3)	-1254(2)	1065(1)	37(1)
O(1)	5450(10)	1095(7)	4179(3)	56(2)
O(2)	5925(11)	1150(9)	2866(4)	83(3)
O(3)	2994(11)	1479(10)	3195(5)	95(4)
O(4)	4376(11)	-715(8)	3332(4)	79(3)
C(1)	2139(12)	3215(9)	223(5)	45(3)
C(2)	1006(13)	3667(10)	856(6)	48(3)
C(3)	-982(14)	3252(10)	691(6)	55(4)
C(4)	-546(12)	974(10)	1805(5)	48(4)
C(5)	-68(14)	-576(11)	1868(5)	52(4)
C(6)	3490(11)	-621(10)	1307(5)	43(3)
C(7)	3708(11)	944(10)	1142(5)	43(3)

Estimated standard deviations are given in parentheses.

Coordinates × 10^n where n = 5,5,4,4,4 for Fe,Cl,S,O,C.

Temperature parameters × 10^n where n = 4,4,3,3,3 for Fe,Cl,S,O,C.

U_{eq} = the equivalent isotropic temperature parameter.

$U_{eq} = 1/3\ \Sigma_i\Sigma_j U_{ij} a_i^* a_j^* (a_i . a_j)$

Primed values indicate that U_{iso} is given

$T = \exp-(8\pi^2 U_{iso} \sin^2\theta/\lambda^2)$

Table 6.3.

Interatomic distances (Å).

Atoms		Distance
S(1)	-Fe(1)	2.275(2)
S(2)	-Fe(1)	2.260(2)
S(3)	-Fe(1)	2.243(2)
O(1)	-Cl(1)	1.421(6)
O(2)	-Cl(1)	1.424(7)
O(3)	-Cl(1)	1.429(7)
O(4)	-Cl(1)	1.419(7)
C(1)	-S(1)	1.821(9)
C(7)	-S(1)	1.816(9)
C(3)	-S(2)	1.804(10)
C(4)	-S(2)	1.862(9)
C(5)	-S(3)	1.852(9)
C(6)	-S(3)	1.842(9)
C(2)	-C(1)	1.522(12)
C(3)	-C(2)	1.513(14)
C(5)	-C(4)	1.513(14)
C(7)	-C(6)	1.523(13)

Estimated standard deviations are given in parentheses.

Table 6.3. (contd.)

Bond angles (°).

Atoms			Angle
S(2)	-Fe(1)	-S(1)	94.1(1)
S(3)	-Fe(1)	-S(1)	89.1(1)
S(3)	-Fe(1)	-S(2)	89.6(1)
O(2)	-Cl(1)	-O(1)	109.8(4)
O(3)	-Cl(1)	-O(1)	110.0(5)
O(3)	-Cl(1)	-O(2)	110.0(5)
O(4)	-Cl(1)	-O(1)	109.4(4)
O(4)	-Cl(1)	-O(2)	108.7(5)
O(4)	-Cl(1)	-O(3)	108.8(6)
C(1)	-S(1)	-Fe(1)	113.4(3)
C(7)	-S(1)	-Fe(1)	105.7(3)
C(7)	-S(1)	-C(1)	101.9(4)
C(3)	-S(2)	-Fe(1)	114.0(3)
C(4)	-S(2)	-Fe(1)	106.4(3)
C(4)	-S(2)	-C(3)	103.1(5)
C(5)	-S(3)	-Fe(1)	105.0(3)
C(6)	-S(3)	-Fe(1)	104.3(3)
C(6)	-S(3)	-C(5)	104.8(4)
C(2)	-C(1)	-S(1)	116.1(6)
C(3)	-C(2)	-C(1)	114.3(8)
C(2)	-C(3)	-S(2)	116.4(7)
C(5)	-C(4)	-S(2)	109.3(6)
C(4)	-C(5)	-S(3)	114.6(6)
C(7)	-C(6)	-S(3)	113.4(6)
C(6)	-C(7)	-S(1)	108.9(6)

Estimated standard deviations are given in parentheses.

diffusion into a solution of the complex in nitromethane. The crystal with appropriate dimensions, 0.46 × 0.24 × 0.26 mm^3, was mounted in a Lindemann tube and Weissenberg and precession photography were done to establish the unit cell dimensions and the space group. The cell constants were refined on a Nonius CAD4 diffractometer using 25 centered reflections in the range $2\theta = 24° - 37°$. The crystal data are given in Table 6.4. Intensity measurements were carried out in the $\omega - 2\theta$ scan mode with Zr- filtered Mo radiation, $\lambda = 0.71069$ Å. A total of 2513 independent reflections were measured from which 1848 [$I > 2\sigma(I)$] were used after suppression.

The solution of the phase problem was achieved using MULTAN[56] and the structure was completed by difference electron density maps and refined by the method of least squares. The atomic scattering factors used were those included in the SHELX-76 program[55] together wuth the Ni *f* curve from ref. 57. All the non-hydrogen atoms were refined anisotropically. Fourier difference maps revealed half of the H atoms, but all were included in calculated positions (C-H = 1.08 Å), with isotropic thermal parameters. The final refinement converged to $R = 0.0651$ and $R_w = 0.0689$ with a maximum shift/esd of 0.027 on the final cycle. A final difference map had a maximum peak of 0.71 $eÅ^{-3}$.

The asymmetric unit consists of half a molecule of the complex cation with one perchlorate anion and one molecule of nitromethane. The Ni atom occupies an inversion centre and

Table 6.4. Experimental crystallographic data for $[Ni([10]\text{-}aneS_3)_2].(ClO_4)_2.(CH_3NO_2)_2$, **55**.

Compound	**55**
Formula	$Ni_1S_6C_{14}H_{28}(ClO_4)_2(CH_3NO_2)_2$
MW	768.4
Crystal color	magenta
Crystal system	monoclinic
Space group	$P2_1/c$ (No. 14)
Cell dimensions	
a (Å)	10.484(4)
b (Å)	15.272(1)
c (Å)	9.445(0)
α (°)	90
β (°)	101.49(1)
γ (°)	90
V (Å^3)	1533.68
Z	2
D_{calc} (g/cm^3)	1.664
D_{meas} (g/cm^3)	1.674
Crystal dimensions (mm^3)	0.46×0.24×0.26
Diffractometer	Nonius, CAD4
Radiation (λ, Å)	Mo-K_α (0.71069)
Filter	Zirconium
Measurement	2θ (2 - 50°)
Octants collected	±h,k,l
std. reflections	900,0100,008,760,404,4102
no. refln. collected	2513
no. refln. $I > n\sigma(I)$	1848 (n = 2)
no. parameters	178
Linear abs coeff. (cm^{-1})	11.81
Solution method	MULTAN
R^a	0.0651
R_w^b	0.0689

[a] $R = \Sigma\| F_o| - |F_c\| / \Sigma |F_o|$

[b] $R_w = [\Sigma w(|F_o| - |F_c|)^2 / \Sigma w(|F_o|)^2]^{1/2}$ where $w = 3.05/(\sigma^2 F + 0.001F^2)$

the other half of the complex cation was obtained by inversion at this centre. The molecular structure of the Ni complex with the atomic labelling scheme is shown in Fig. 6.2., while the fractional atomic coordinates, bond lengths and bond angles are contained in Tables 6.5. and 6.6. The Ni atom is coordinated to six S atoms, three from each ligand occupying a trigonal face, thus forming a distorted octahedral complex.

The average Ni-S bond length was 2.396(7) Å (mean of 3) and compares well with the $Ni([9]\text{-}aneS_3)_2^{2+}$ complex,[86] (2.386(14) Å). The rest of the bond lengths fall in the normal range as expected, except C3-C4, C4-C5 and C6-C7. This was due to disorder in the propyl and ethyl the rings. The site occupation factors for these C atoms were varied to model the positional disorder. The structure obtained is that of a meso stereoisomer in which the trimethylene bridges are *trans* to one another. For the $[Ni([12]\text{-}aneS_3)_2](BF_4)_2$ complex, one of the C-C single bond lengths was found to be 1.30(2) Å also due to disorder in that part of the ring.[123]

The mean five-membered chelate bite angle was found to be 89.2(11)° similar to that found in the $Ni([9]\text{-}aneS_3)_2^{2+}$ complex[86] (88.5(4)°), and the $Ni([18]\text{-}aneS_6)^{2+}$ complex.[123] The remaining six-membered chelate bite angle is larger by 4.6° (93.8(1)°), indicating the relief of strain in the six-membered chelate ring. A facial tridentate complexation of ligand **23** requires a conformation in which all of the ligating atoms are *syn* endodentate. The conformations that meet this

requirement are [2323], [2233], [1333] and [1324].[155]

Fig. 6.2. ORTEP diagram of $[Ni([10]\text{-}aneS_3)_2](ClO_4)_2$, **55**, with 25% thermal ellipsoids.

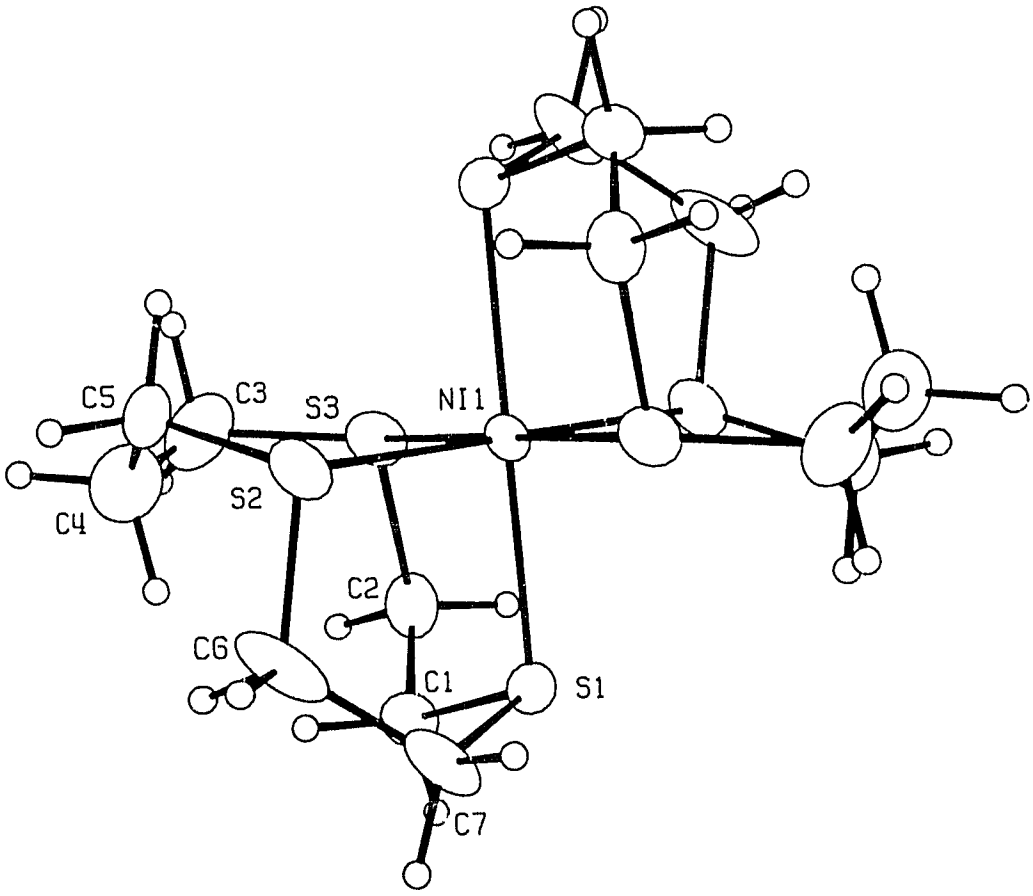

Table 6.5.

Fractional atomic coordinates and temperature parameters.

Atom	x/a	y/b	z/c	Ueq
Ni(1)	0(0)	0(0)	0(0)	383(4)
S(1)	-2118(20)	3520(14)	23399(22)	530(7)
S(2)	8989(24)	14312(14)	-1480(24)	605(8)
S(3)	20609(22)	-6643(15)	8775(23)	627(8)
Cl(1)	34984(20)	40070(15)	13151(22)	582(7)
O(1)	2227(10)	3804(8)	1368(12)	159(2)
O(2)	3680(13)	3863(12)	1(11)	200(3)
O(3)	3654(15)	4893(8)	1628(20)	246(3)
O(4)	4343(14)	3600(10)	2205(15)	228(3)
C(1)	745(9)	1360(5)	2696(9)	61(2)
C(2)	526(9)	1955(6)	1372(10)	66(2)
C(3)	2666(3)	1518(9)	42(14)	89(2)
C(4)	3447(14)	867(7)	1011(14)	111(3)
C(5)	3344(14)	-19(8)	333(19)	130(3)
C(6)	2155(10)	-600(11)	2765(3)	90(3)
C(7)	918(8)	-458(6)	3285(10)	66(2)
C(8)	5937(10)	1953(8)	3795(11)	83(2)
N(1)	7085(10)	1955(6)	3149(11)	90(2)
O(5)	8146(10)	1948(7)	4014(13)	149(2)
O(6)	6970(14)	1935(9)	1981(11)	204(3)
C(3')	625(23)	-342(14)	3766(15)	45(4)'
C(4')	1509(20)	-963(15)	3214(26)	52(4)'
C(5')	2633(21)	-522(18)	2759(4)	41(4)'
C(6')	3250(16)	147(11)	550(24)	31(4)'
C(7')	2564(12)	1012(20)	317(46)	635(5)'

Estimated standard deviations are given in parentheses.

Coordinates × 10^n where n = 5,5,4,4,4 for S,Cl,O,C,N.

Temperature parameters × 10^n where n = 4,4,4,4,3,3 for Ni,S,Cl,O,C,N.

U_{eq} = the equivalent isotropic temperature parameter.

$U_{eq} = 1/3 \sum_i \sum_j U_{ij} a_i^* a_j^* (a_i . a_j)$

Primed values indicate that U_{iso} is given

$T = \exp-(8\pi^2 U_{iso} \sin^2\theta/\lambda^2)$

Disorder occupancy for C3, C4, C5, C6 and C7 = 74%

Table 6.6.

Interatomic distances (Å).

Atoms		Distance
S(1)	-Ni(1)	2.403(2)
S(2)	-Ni(1)	2.396(2)
S(3)	-Ni(1)	2.386(2)
C(1)	-S(1)	1.832(8)
C(7)	-S(1)	1.830(1)
C(3')	-S(1)	1.830(1)
C(2)	-S(2)	1.798(9)
C(3)	-S(2)	1.829(1)
C(7')	-S(2)	1.830(1)
C(5)	-S(3)	1.830(1)
C(6)	-S(3)	1.831(1)
C(5')	-S(3)	1.830(1)
C(6')	-S(3)	1.830(1)
O(1)	-Cl(1)	1.380(9)
O(2)	-Cl(1)	1.353(10)
O(3)	-Cl(1)	1.390(12)
O(4)	-Cl(1)	1.273(10)
C(2)	-C(1)	1.560(13)
C(4)	-C(3)	1.500(1)
C(7')	-C(3)	0.832(37)
C(5)	-C(4)	1.500(1)
C(6')	-C(4)	1.190(22)
C(7')	-C(4)	1.056(24)
C(6')	-C(5)	0.356(27)
C(7')	-C(5)	1.772(30)
C(7)	-C(6)	1.500(1)
C(4')	-C(6)	1.037(23)
C(5')	-C(6)	0.517(21)
C(3')	-C(7)	0.635(21)
C(4')	-C(7)	1.001(21)
C(5')	-C(7)	1.969(24)
N(1)	-C(8)	1.466(13)
O(5)	-N(1)	1.256(12)
O(6)	-N(1)	1.124(12)
C(4')	-C(3')	1.500(1)
C(5')	-C(4')	1.500(1)
C(7')	-C(6')	1.500(1)

Estimated standard deviations are given in parentheses.

Table 6.6. (contd.)

Bond angles (°).

Atoms	Angle	Atoms	Angle
S(2) -Ni(1) -S(1)	88.0(1)	C(4') -C(6) -S(3)	119.3(17)
S(3) -Ni(1) -S(1)	90.1(1)	C(4') -C(6) -C(7)	41.7(12)
S(3) -Ni(1) -S(2)	94.1(1)	C(5') -C(6) -S(3)	81.8(4)
C(1) -S(1) -Ni(1)	102.6(3)	C(5') -C(6) -C(7)	151.3(36)
C(7) -S(1) -Ni(1)	99.0(4)	C(5') -C(6) -C(4')	147.7(37)
C(7) -S(1) -C(1)	101.4(5)	C(6) -C(7) -S(1)	116.3(8)
C(3') -S(1) -Ni(1)	118.3(7)	C(3') -C(7) -S(1)	80.0(4)
C(3') -S(1) -C(1)	100.4(9)	C(3') -C(7) -C(6)	150.2(28)
C(3') -S(1) -C(7)	20.0(7)	C(4') -C(7) -S(1)	146.5(17)
C(2) -S(2) -Ni(1)	101.7(3)	C(4') -C(7) -C(6)	43.6(13)
C(3) -S(2) -Ni(1)	117.6(5)	C(4') -C(7) -C(3')	131.6(16)
C(3) -S(2) -C(2)	105.4(5)	C(5') -C(7) -S(1)	115.7(8)
C(7') -S(2) -Ni(1)	91.9(10)	C(5') -C(7) -C(6)	7.3(9)
C(7') -S(2) -C(2)	107.7(14)	C(5') -C(7) -C(3')	143.8(29)
C(7') -S(2) -C(3)	26.3(12)	C(5') -C(7) -C(4')	48.2(12)
C(5) -S(3) -Ni(1)	109.4(6)	O(5) -N(1) -C(8)	113.8(10)
C(6) -S(3) -Ni(1)	101.7(4)	O(6) -N(1) -C(8)	120.4(13)
C(6) -S(3) -C(5)	111.7(7)	O(6) -N(1) -O(5)	125.8(13)
C(5') -S(3) -Ni(1)	113.8(9)	C(7) -C(3') -S(1)	80.0(4)
C(5') -S(3) -C(5)	96.6(8)	C(4') -C(3') -S(1)	109.2(14)
C(5') -S(3) -C(6)	16.2(7)	C(4') -C(3') -C(7)	30.0(13)
C(6') -S(3) -Ni(1)	104.4(7)	C(7) -C(4') -C(6)	94.8(21)
C(6') -S(3) -C(5)	11.2(9)	C(3') -C(4') -C(6)	108.4(23)
C(6') -S(3) -C(6)	103.8(9)	C(3') -C(4') -C(7)	18.5(8)
C(6') -S(3) -C(5')	89.8(10)	C(5') -C(4') -C(6)	10.6(12)
O(2) -Cl(1) -O(1)	108.6(8)	C(5') -C(4') -C(7)	102.0(21)
O(3) -Cl(1) -O(1)	106.4(8)	C(5') -C(4') -C(3')	113.6(21)
O(3) -Cl(1) -O(2)	109.5(10)	C(6) -C(5') -S(3)	81.9(4)
O(4) -Cl(1) -O(1)	114.2(9)	C(7) -C(5') -S(3)	97.8(9)
O(4) -Cl(1) -O(2)	111.1(10)	C(7) -C(5') -C(6)	21.5(27)
O(4) -Cl(1) -O(3)	106.8(11)	C(4') -C(5') -S(3)	97.2(12)
C(2) -C(1) -S(1)	110.3(6)	C(4') -C(5') -C(6)	21.7(26)
C(1) -C(2) -S(2)	114.0(6)	C(4') -C(5') -C(7)	29.8(10)
C(4) -C(3) -S(2)	115.5(10)	C(4) -C(6') -S(3)	129.2(16)
C(7') -C(3) -S(2)	76.9(6)	C(5) -C(6') -S(3)	84.4(5)
C(7') -C(3) -C(4)	43.0(15)	C(5) -C(6') -C(4)	146.4(13)
C(5) -C(4) -C(3)	109.7(13)	C(7') -C(6') -S(3)	107.5(20)
C(6') -C(4) -C(3)	110.0(16)	C(7') -C(6') -C(4)	44.4(12)
C(6') -C(4) -C(5)	7.5(8)	C(7') -C(6') -C(5)	135.7(64)
C(7') -C(4) -C(3)	32.5(20)	C(3) -C(7') -S(2)	76.8(6)
C(7') -C(4) -C(5)	86.0(23)	C(4) -C(7') -S(2)	154.6(37)
C(7') -C(4) -C(6')	83.6(15)	C(4) -C(7') -C(3)	104.6(26)
C(4) -C(5) -S(3)	110.5(7)	C(5) -C(7') -S(2)	136.7(18)
C(6') -C(5) -S(3)	84.4(5)	C(5) -C(7') -C(3)	137.7(29)
C(6') -C(5) -C(4)	26.0(7)	C(5) -C(7') -C(4)	57.6(13)
C(7') -C(5) -S(3)	96.7(11)	C(6') -C(7') -S(2)	138.6(22)
C(7') -C(5) -C(4)	36.5(12)	C(6') -C(7') -C(3)	141.2(26)
C(7') -C(5) -C(6')	36.2(53)	C(6') -C(7') -C(4)	52.0(12)
C(7) -C(6) -S(3)	118.2(7)	C(6') -C(7') -C(5)	8.1(12)

Estimated standard deviations are given in parentheses.

The conformation of the complexed ligand is [2233] for the complex under study.

6.3.3. Crystal structure of $[Co([10]\text{-}aneS_3)_2](ClO_4)_2$, 53:

Dark brown crystals of diffraction quality were grown by vapor diffusion of diethyl ether into nitromethane solutions of the complex. Preliminary photography using Weissenberg and precession methods were carried out to establish the unit cell dimensions and the space group. The crystal was found to be isomorphous with the $[Ni([10]\text{-}aneS_3)_2](ClO_4)_2.2CH_3NO_2$ crystal. The cell constants were refined on a Nonius CAD4 diffractometer using 25 centered reflections in the range $2\theta = 16° - 36°$. The crystal data are given in Table 6.7. A total of 2407 reflections were measured out of which 1545, $I > 2\sigma(I)$, were used.

The coordinates for the Co atom and the three S atoms were used from that of the isomorphous Ni complex. The atomic scattering factors used were those included in the SHELX-76 program[55] together with the Co *f* curve from ref.57. All non-hydrogen atoms were refined anisotropically. The final refinement converged to $R = 0.0829$ and $R_w = 0.0812$ with a maximum shift/esd of 0.073 on the final cycle. A final difference map had a maximum peak of 0.63 $eÅ^{-3}$.

The asymmetric unit consists of half a molecule of the complex cation with one perchlorate anion and one molecule of nitromethane. The molecular structure of the cobalt complex

Table 6.7. Experimental crystallographic data for $[Co([10]\text{-}aneS_3)_2].(ClO_4)_2.(CH_3NO_2)_2$, **53**.

Compound	**53**
Formula	$Co_1S_6C_{14}H_{28}Cl_2O_8.2CH_3NO_2$
MW	768.65
Crystal color	brown
Crystal system	monoclinic
Space group	$P2_1/c$ (No. 14)
Cell dimensions	
a (Å)	10.463(3)
b (Å)	15.292(4)
c (Å)	9.720(2)
α (°)	90
β (°)	102.16(1)
γ (°)	90
V (Å^3)	1520.3
Z	2
D_{calc} (g/cm^3)	1.679
D_{meas} (g/cm^3)	1.677
Crystal dimensions (mm^3)	0.64×0.24×0.06
Diffractometer	Nonius, CAD4
Radiation (λ, Å)	Mo-K_α (0.71069)
Filter	Zirconium
Measurement	2θ (2 - 50°)
Octants collected	±h,k,l
std. reflections	006,600,008,060,404,644
no. refln. collected	2407
no. refln. I > nσ(I)	1545 (n = 2)
no. parameters	199
Linear abs coeff. (cm^{-1})	11.19
Solution method	MULTAN
R[a]	0.0829
R_w[b]	0.0812

[a] $R = \Sigma\| F_o| - |F_c\| / \Sigma |F_o|$

[b] $R_w = [\Sigma w(|F_o| - |F_c|)^2 / \Sigma w(|F_o|)^2]^{1/2}$ where $w = 3.46/(\sigma^2 F + 0.001F^2)$

with the atomic labelling scheme is shown in Fig.6.3., while the fractional atomic coordinates, bond lengths and bond angles are contained in Tables 6.8. and 6.9. As in the corresponding nickel complex, the three S atoms from each ligand coordinate with the Co(II) ion in a facial manner to yield an octahedral complex. The structure is centrosymmetric with the Co(II) ion occupying an inversion centre resulting in a mesomeric structure.

The carbon atoms in the propyl ring (C3, C4, C5) and the ethyl ring (C6, C7) were disordered and the site occupation factors for these carbon atoms were varied to model the positional disorder. The Co-S bond lengths are all smaller than the Ni-S bond lengths in the Ni(II) complex, **55**. Ni(II) has an ionic radius of 0.830 Å which is intermediate between that of high spin and low spin Co(II) (0.885 Å and 0.790 Å respectively).[156] The shorter Co-S bond length suggests that the Co(II) ion may be in a low spin state in the present complex. The observed M-S bond lengths in the series increases in the order Fe < Co < Ni. This is in accordance with the ionic radii of low spin Fe(II), Co(II) and Ni(II) *viz.*, Fe < Co < Ni. The Co-S distances in the present complex are all different (Table 6.8.) and cannot be distinguished as equatorial or axial bonds. The unique bond length of 2.395(3) Å (greater than the calculated sum of covalent radii (2.360 Å) suggests that the complex is essentially axially elongated. Morever, the equatorial bond lengths are unequal (2.257 (3) Å

Fig. 6.3. ORTEP diagram of $[Co([10]\text{-}aneS_3)_2](ClO_4)_2$, **53**, with 25% thermal ellipsoids.

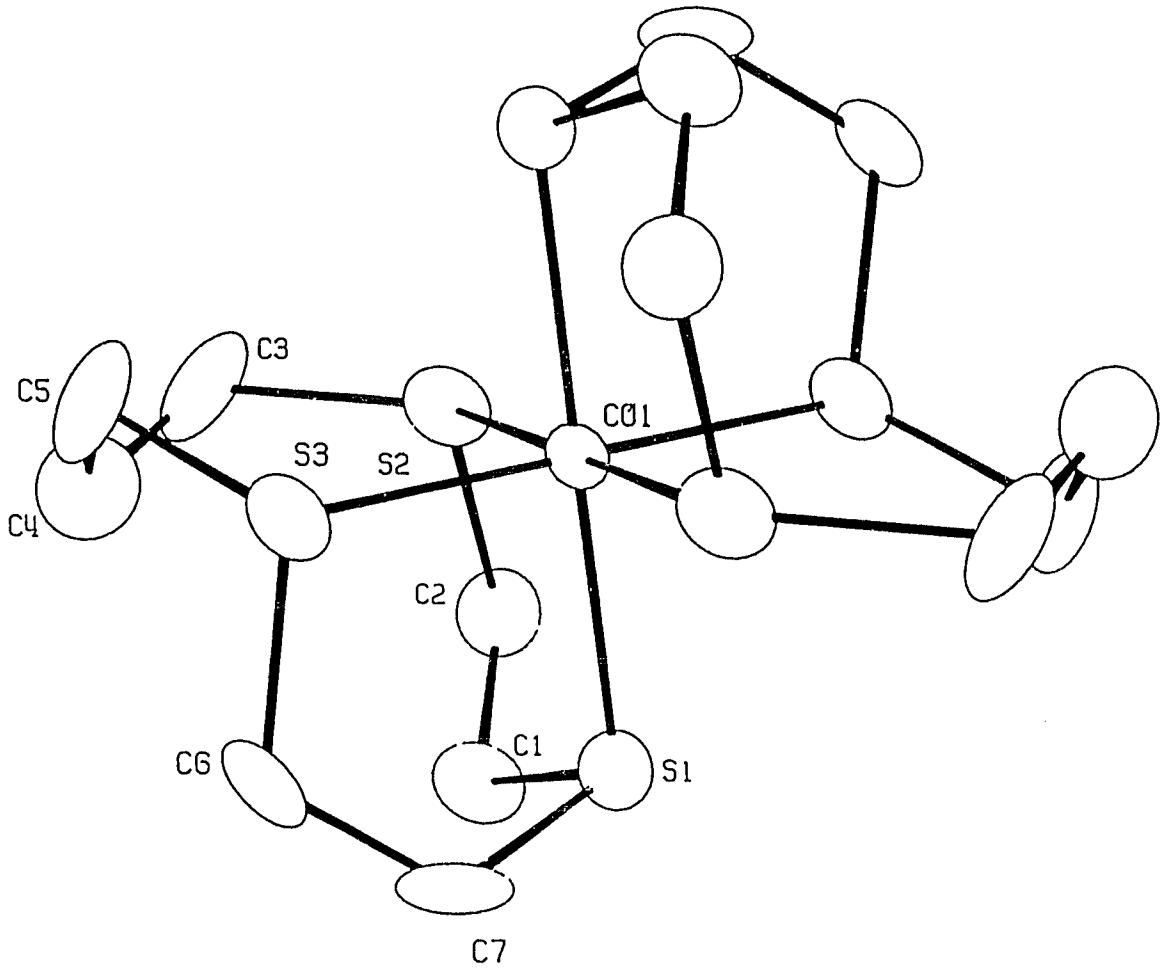

Table 6.8.

Fractional atomic coordinates and temperature parameters.

Atom	x/a	y/b	z/c	Ueq
Co(1)	0(0)	0(0)	0(0)	420(6)
S(1)	-2184(27)	3507(21)	22612(30)	659(11)
S(2)	8948(32)	14296(20)	-1532(33)	727(12)
S(3)	19592(28)	-6339(20)	8250(29)	665(11)
Cl(1)	35238(27)	40092(21)	13331(29)	654(10)
O(1)	2254(12)	3815(10)	1389(15)	168(3)
O(2)	3679(15)	3869(14)	20(14)	214(3)
O(3)	3679(19)	4872(12)	1704(23)	273(4)
O(4)	4363(16)	3596(12)	2239(17)	237(3)
C(1)	746(12)	1361(7)	2695(12)	72(3)
C(2)	557(12)	1964(7)	1393(13)	75(3)
C(3)	2669(4)	1532(12)	72(19)	111(3)
C(4)	3457(18)	849(9)	989(18)	114(3)
C(5)	3300(15)	-36(9)	311(21)	107(3)
C(6)	2180(12)	-570(14)	2741(3)	86(3)
C(7)	931(11)	-443(8)	3244(12)	75(3)
C(8)	5893(13)	1941(10)	3786(14)	93(3)
N(1)	7034(13)	1955(7)	3116(15)	104(3)
O(5)	8120(13)	1937(8)	4019(17)	165(3)
O(6)	6900(18)	1919(11)	1952(15)	233(3)
C(3')	566(29)	-336(18)	3742(20)	50(5)'
C(4')	1541(28)	-915(23)	3256(38)	82(6)'
C(5')	2688(27)	-583(29)	2708(7)	63(6)'
C(6')	3155(21)	181(15)	531(32)	36(5)'
C(7')	2606(11)	1090(22)	358(52)	177(6)'

Estimated standard deviations are given in parentheses.

Coordinates × 10^n where n = 5,5,4,4,4 for S,Cl,O,C,N.

Temperature parameters × 10^n where n = 4,4,4,4,4,4 for Co,S,Cl,O,C,N.

U_{eq} = the equivalent isotropic temperature parameter.

$U_{eq} = 1/3 \sum_i \sum_j U_{ij} a_i^* a_j^* (a_i . a_j)$

Primed values indicate that U_{iso} is given

$T = \exp-(8\pi^2 U_{iso} \sin^2\theta/\lambda^2)$

Disorder occupancy for C3, C4, C5, C6 and C7 = 73%

Table 6.9.

Interatomic distances (Å).

Atoms		Distance
S(1)	-Co(1)	2.320(3)
S(2)	-Co(1)	2.395(3)
S(3)	-Co(1)	2.257(3)
C(1)	-S(1)	1.845(11)
C(7)	-S(1)	1.830(1)
C(3')	-S(1)	1.830(1)
C(2)	-S(2)	1.809(12)
C(3)	-S(2)	1.830(1)
C(7')	-S(2)	1.830(1)
C(5)	-S(3)	1.830(1)
C(6)	-S(3)	1.830(1)
C(5')	-S(3)	1.830(1)
C(6')	-S(3)	1.830(1)
O(1)	-Cl(1)	1.374(11)
O(2)	-Cl(1)	1.337(13)
O(3)	-Cl(1)	1.368(16)
O(4)	-Cl(1)	1.273(11)
C(2)	-C(1)	1.545(16)
C(4)	-C(3)	1.500(1)
C(7')	-C(3)	0.738(42)
C(5)	-C(4)	1.500(1)
C(6')	-C(4)	1.133(25)
C(7')	-C(4)	1.036(26)
C(6')	-C(5)	0.439(33)
C(7')	-C(5)	1.873(35)
C(7)	-C(6)	1.500(1)
C(4')	-C(6)	1.057(34)
C(5')	-C(6)	0.540(31)
C(3')	-C(7)	0.697(27)
C(4')	-C(7)	0.960(29)
N(1)	-C(8)	1.476(17)
O(5)	-N(1)	1.281(16)
O(6)	-N(1)	1.112(15)
C(4')	-C(3')	1.500(1)
C(5')	-C(4')	1.500(1)
C(7')	-C(6')	1.500(1)

Estimated standard deviations are given in parentheses.

Table 6.9. (contd.)

Bond angles (°)

Atoms	Angle	Atoms	Angle
S(2) -Co(1) -S(1)	88.0(1)	C(7') -C(5) -C(4)	33.5(13)
S(3) -Co(1) -S(1)	91.5(1)	C(7') -C(5) -C(6')	28.1(49)
S(3) -Co(1) -S(2)	94.4(1)	C(7) -C(6) -S(3)	114.0(8)
C(1) -S(1) -Co(1)	104.6(4)	C(4') -C(6) -S(3)	119.9(24)
C(7) -S(1) -Co(1)	99.0(4)	C(4') -C(6) -C(7)	39.5(17)
C(7) -S(1) -C(1)	99.7(6)	C(5') -C(6) -S(3)	81.5(5)
C(3') -S(1) -Co(1)	119.7(9)	C(5') -C(6) -C(7)	163.8(23)
C(3') -S(1) -C(1)	99.6(11)	C(5') -C(6) -C(4')	137.6(57)
C(3') -S(1) -C(7)	22.0(9)	C(6) -C(7) -S(1)	115.9(9)
C(2) -S(2) -Co(1)	102.3(4)	C(3') -C(7) -S(1)	79.0(4)
C(3) -S(2) -Co(1)	118.1(6)	C(3') -C(7) -C(6)	154.1(31)
C(3) -S(2) -C(2)	103.5(7)	C(4') -C(7) -S(1)	150.0(25)
C(7') -S(2) -Co(1)	95.6(11)	C(4') -C(7) -C(6)	44.5(21)
C(7') -S(2) -C(2)	104.7(16)	C(4') -C(7) -C(3')	128.9(23)
C(7') -S(2) -C(3)	23.3(13)	O(5) -N(1) -C(8)	112.4(13)
C(5) -S(3) -Co(1)	112.3(7)	O(6) -N(1) -C(8)	120.6(16)
C(6) -S(3) -Co(1)	104.4(4)	O(6) -N(1) -O(5)	126.8(18)
C(6) -S(3) -C(5)	108.2(8)	C(7) -C(3') -S(1)	79.0(5)
C(5') -S(3) -Co(1)	119.5(12)	C(4') -C(3') -S(1)	108.2(20)
C(5') -S(3) -C(5)	94.0(11)	C(4') -C(3') -C(7)	29.9(18)
C(5') -S(3) -C(6)	17.0(10)	C(7) -C(4') -C(6)	96.0(32)
C(6') -S(3) -Co(1)	104.6(9)	C(3') -C(4') -C(6)	113.3(33)
C(6') -S(3) -C(5)	13.8(10)	C(3') -C(4') -C(7)	21.2(11)
C(6') -S(3) -C(6)	100.3(11)	C(5') -C(4') -C(6)	14.0(19)
C(6') -S(3) -C(5')	88.4(14)	C(5') -C(4') -C(7)	108.7(33)
O(2) -Cl(1) -O(1)	108.4(10)	C(5') -C(4') -C(3')	124.1(32)
O(3) -Cl(1) -O(1)	105.1(10)	C(6) -C(5') -S(3)	81.6(5)
O(3) -Cl(1) -O(2)	112.0(13)	C(4') -C(5') -S(3)	98.3(18)
O(4) -Cl(1) -O(1)	113.4(11)	C(4') -C(5') -C(6)	28.4(40)
O(4) -Cl(1) -O(2)	112.1(12)	C(4) -C(6') -S(3)	134.1(23)
O(4) -Cl(1) -O(3)	105.7(13)	C(5) -C(6') -S(3)	83.1(6)
C(2) -C(1) -S(1)	110.0(7)	C(5) -C(6') -C(4)	141.0(25)
C(1) -C(2) -S(2)	113.4(8)	C(7') -C(6') -S(3)	113.0(23)
C(4) -C(3) -S(2)	115.4(12)	C(7') -C(6') -C(4)	43.6(13)
C(7') -C(3) -S(2)	78.4(7)	C(7') -C(6') -C(5)	144.0(62)
C(7') -C(3) -C(4)	39.0(15)	C(3) -C(7') -S(2)	78.3(7)
C(5) -C(4) -C(3)	111.8(16)	C(4) -C(7') -S(2)	158.5(45)
C(6') -C(4) -C(3)	108.8(21)	C(4) -C(7') -C(3)	114.4(28)
C(6') -C(4) -C(5)	10.6(13)	C(5) -C(7') -S(2)	128.1(17)
C(7') -C(4) -C(3)	26.6(21)	C(5) -C(7') -C(3)	140.0(43)
C(7') -C(4) -C(5)	93.4(26)	C(5) -C(7') -C(4)	53.1(16)
C(7') -C(4) -C(6')	87.4(17)	C(6') -C(7') -S(2)	128.5(24)
C(4) -C(5) -S(3)	110.5(9)	C(6') -C(7') -C(3)	145.9(41)
C(6') -C(5) -S(3)	83.1(6)	C(6') -C(7') -C(4)	49.0(14)
C(6') -C(5) -C(4)	28.4(16)	C(6') -C(7') -C(5)	7.9(14)
C(7') -C(5) -S(3)	97.4(11)		

Estimated standard deviations are given in parentheses.

and 2.320(3) Å) resulting in a distorted octahedral complex in the solid state. However, in the $[Co([9]\text{-}aneS_3)_2]^{2+}$ complex[86] ion, the axial bonds are compressed from the calculated sum of covalent radii of 2.36 Å to 2.240(7) Å but the equatorial bonds are close to the sum of the calculated covalent radii (2.356(6) - 2.367(5) Å). In the $[Co([18]\text{-}aneS_6)]^{2+}$ complex ion the Co-S axial bond length is elongated (2.479(1) Å) and the equatorial Co-S bond lengths are 2.251(1) Å and 2.292(1) Å.[157] The Co-S bond lengths in the complex under study lie in between those of $[Co([9]\text{-}aneS_3)_2]^{2+}$ and $[Co([18]\text{-}aneS_6)]^{2+}$ complex ions.

The five-membered chelate ring bite angle S-Co-S was found to be 89.8(18)°, similar to that of the average S-Co-S angle in $[Co([9]\text{-}aneS_3)_2]^{2+}$ complex cation (89.0(20)°). The six-membered chelate ring angle, S-Co-S was found to be 94.4(1)° as expected. The conformation adopted by the ligand in the complex is [2233].

6.3.4. Crystal structure of $[Pd([10]\text{-}aneS_3)_2](PF_6)_2.2CH_3CN$, 56:

Deep blue crystals of the complex were obtained by diffusion of ether into acetonitrile solutions of the ligand containing NH_4PF_6. The crystal was mounted in a Lindemann tube and centered on a Nonius CAD4 diffractometer. The pertinent crystallographic data are given in Table 6.10. The cell was refined using 25 centered reflections in the range $2\theta = 24° - 42°$. The total number of reflections measured was 2638 but

Table 6.10. Experimental crystallographic data for $[Pd([10]\text{-}aneS_3)_2].(PF_6)_2.(CH_3CN)_2$, **56**.

Compound	**56**
Formula	$Pd_1S_6C_{14}H_{28}(PF_6)_2(CH_3CN)_2$
MW	867.2
Crystal color	deep blue
Crystal system	triclinic
Space group	$P\bar{1}$
Cell dimensions	
a (Å)	10.021(3)
b (Å)	10.800(3)
c (Å)	8.043(2)
α (°)	111.57(3)
β (°)	95.40(2)
γ (°)	81.28(2)
V (Å^3)	799.42
Z	1
D_{calc} (g/cm^3)	1.801
D_{meas} (g/cm^3)	1.815
Crystal dimensions (mm^3)	0.98×0.14×0.15
Diffractometer	Nonius, CAD4
Radiation (λ, Å)	Mo-K_α (0.71069)
Filter	Zirconium
Measurement	2θ (2 - 50°)
Octants collected	±h,k,±l
std. reflections	700,006,060
no. refln. collected	2638
no. refln. $I > n\sigma(I)$	2393 (n = 3)
no. parameters	187
Linear abs coeff. (cm^{-1})	12.52
Solution method	MULTAN
R^a	0.0517
R_w^b	0.0582

[a] $R = \sum\| |F_o| - |F_c| \| / \sum |F_o|$

[b] $R_w = [\sum w(|F_o| - |F_c|)^2 / \sum w(|F_o|)^2]^{1/2}$ where $w = 0.24/(\sigma^2 F + 0.001F^2)$

this reduced to 2393 ($I > 2\sigma(I)$) after suppression. After correction for absorption effects, the position of the Pd atom was obtained from a Patterson synthesis. The structure was completed with difference electron density maps and refined by the method of least squares minimizing $\Sigma w\Delta^2$, where $w = 1/\sigma^2(F)$ and $\Delta = ||F_o| - |F_c||$. The asymmetric unit consists of half a molecule of the complex cation, one PF_6^- anion and one molecule of CH_3CN as solvent of crystallization.

The molecule has an inversion centre at the Pd atom. The other half of the molecule is, therefore, generated by inversion at the Pd centre. Hydrogen atoms were not included in the calculations. All non-hydrogen atoms were refined anisotropically. The refinement converged to an R value of 0.0517 and $R_w = 0.0582$, with a maximum shift/esd of 0.043 in the final cycle. A final difference map had a maximum peak of 0.895 $eÅ^{-3}$.

The structure of the Pd complex is shown in Fig. 6.4., and the fractional atomic coordinates, bond lengths and bond angles are given in Tables 6.11. and 6.12. The Pd(II) ion, with d^8 electronic configuration, is low spin as a result of increased crystal field stabilization energy and invariably shows a square planar geometry. Thus the Pd(II) atom is surrounded by four S atoms (2 from each ligand) in a square planar geometry. The Pd-S equatorial bond length is 2.329(1) Å (mean of 2). The equatorial bond lengths are similar to those obtained for the corresponding $Pd([9]\text{-}aneS_3)_2^{2+}$ complex.[92]

Fig. 6.4. ORTEP diagram of $[Pd([10]\text{-}aneS_3)_2](PF_6)_2.2CH_3CN$, **56**, with 25% thermal ellipsoids.

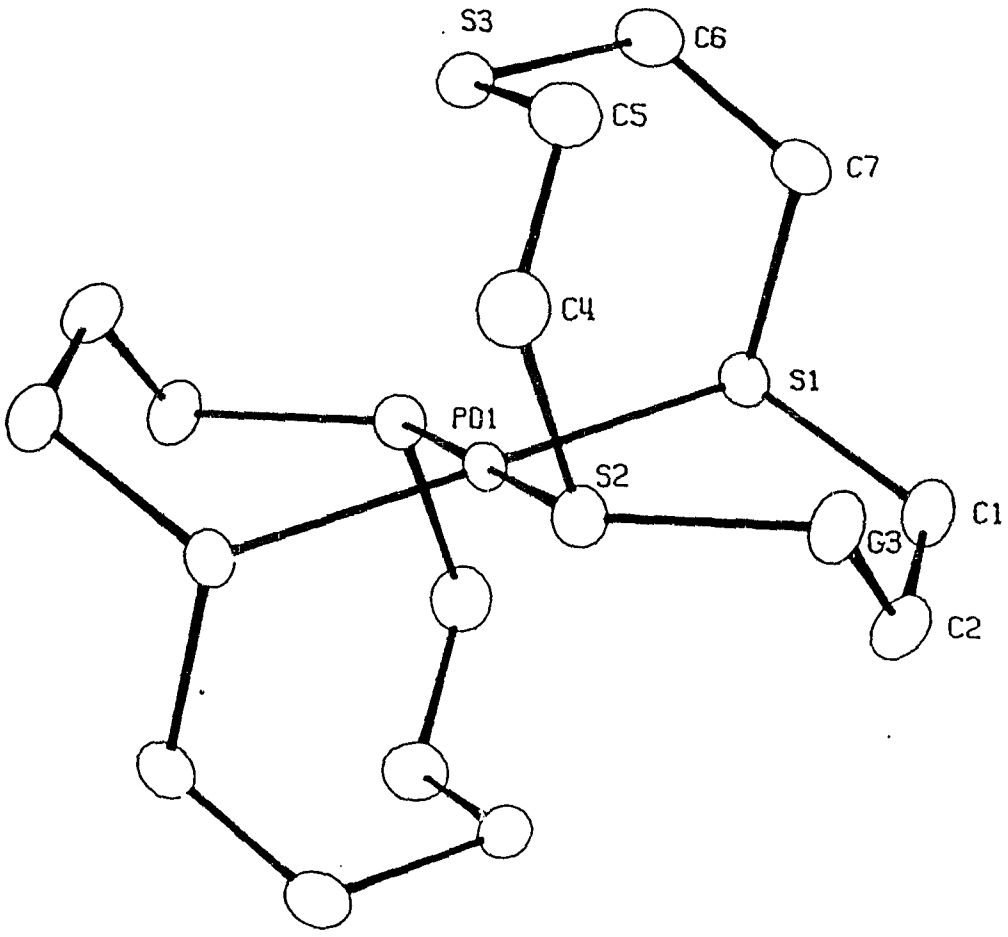

There is significant interaction from the axial S atoms with the central Pd(II) atom. The Pd...S distance is 3.034(1) Å compared to 2.952(4) Å in the corresponding $Pd([9]\text{-}aneS_3)_2^{2+}$ complex[92] and is due to the presence of the larger ten-

Table 6.11.

Fractional atomic coordinates and temperature parameters.

Atom	x/a	y/b	z/c	Ueq
Pd(1)	0(0)	0(0)	0(0)	299(2)
S(1)	-9023(13)	16839(13)	-10941(18)	366(5)
S(2)	-3331(15)	12650(14)	30091(18)	395(5)
S(3)	-29565(15)	-2751(15)	1048(21)	435(6)
P(1)	30937(20)	30159(20)	66070(25)	564(8)
F(1)	4555(7)	2906(11)	6289(20)	214(8)
F(2)	2819(10)	2010(10)	4749(11)	181(5)
F(3)	1569(8)	3183(13)	6957(14)	189(7)
F(4)	3277(17)	4151(14)	8428(12)	251(9)
F(5)	2731(14)	4208(10)	5967(15)	219(8)
F(6)	3366(17)	1996(15)	7428(23)	297(12)
C(1)	-359(7)	3288(6)	326(9)	52(3)
C(2)	212(7)	3400(6)	2213(9)	50(2)
C(3)	-682(7)	3056(6)	3363(8)	48(2)
C(4)	-1856(7)	831(7)	3594(8)	51(3)
C(5)	-3145(6)	877(7)	2384(9)	51(3)
C(6)	-3426(6)	790(7)	-1225(10)	54(3)
C(7)	-2729(6)	2027(7)	-701(9)	48(3)
C(8)	4315(8)	3944(8)	2254(11)	69(3)
C(9)	3225(8)	5094(7)	2679(10)	56(3)
N(1)	2396(8)	5943(8)	2988(10)	80(3)

Estimated standard deviations are given in parentheses.

Coordinates × 10^n where n = 5,5,4,4,4 for S,P,F,C,N.

Temperature parameters × 10^n where n = 4,4,3,3,3 for Pd,S,P,F,C,N..

U_{eq} = the equivalent isotropic temperature parameter.

$U_{eq} = 1/3 \sum_i \sum_j U_{ij} a_i^* a_j^* (a_i . a_j)$

Primed values indicate that U_{iso} is given

$T = \exp-(8\pi^2 U_{iso} \sin^2\theta/\lambda^2)$

Table 6.12.

Interatomic distances (Å).

Atoms		Distance
S(1)	-Pd(1)	2.330(1)
S(2)	-Pd(1)	2.328(1)
S(3)	-Pd(1)	3.034(1)
C(1)	-S(1)	1.821(6)
C(7)	-S(1)	1.846(6)
C(3)	-S(2)	1.831(6)
C(4)	-S(2)	1.812(7)
C(5)	-S(3)	1.806(7)
C(6)	-S(3)	1.826(7)
F(1)	-P(1)	1.490(8)
F(2)	-P(1)	1.520(7)
F(3)	-P(1)	1.551(8)
F(4)	-P(1)	1.543(9)
F(5)	-P(1)	1.538(9)
F(6)	-P(1)	1.460(8)
C(2)	-C(1)	1.539(10)
C(3)	-C(2)	1.519(9)
C(5)	-C(4)	1.548(10)
C(7)	-C(6)	1.504(9)
C(9)	-C(8)	1.483(10)
N(1)	-C(9)	1.110(9)

Estimated standard deviations are given in parentheses.

Table 6.12. (contd.)

Bond angles (°)

Atoms			Angle
S(2)	-Pd(1)	-S(1)	96.6(0)
S(3)	-Pd(1)	-S(1)	82.7(0)
S(3)	-Pd(1)	-S(2)	81.1(0)
C(1)	-S(1)	-Pd(1)	110.8(2)
C(7)	-S(1)	-Pd(1)	107.3(2)
C(7)	-S(1)	-C(1)	100.6(3)
C(3)	-S(2)	-Pd(1)	110.6(2)
C(4)	-S(2)	-Pd(1)	107.4(2)
C(4)	-S(2)	-C(3)	105.5(3)
C(5)	-S(3)	-Pd(1)	94.9(2)
C(6)	-S(3)	-Pd(1)	90.2(2)
C(6)	-S(3)	-C(5)	103.8(3)
F(2)	-P(1)	-F(1)	92.5(6)
F(3)	-P(1)	-F(1)	178.0(7)
F(3)	-P(1)	-F(2)	88.7(5)
F(4)	-P(1)	-F(1)	90.0(7)
F(4)	-P(1)	-F(2)	173.8(8)
F(4)	-P(1)	-F(3)	88.7(8)
F(5)	-P(1)	-F(1)	92.5(7)
F(5)	-P(1)	-F(2)	92.1(7)
F(5)	-P(1)	-F(3)	85.9(7)
F(5)	-P(1)	-F(4)	82.2(7)
F(6)	-P(1)	-F(1)	91.3(9)
F(6)	-P(1)	-F(2)	93.9(8)
F(6)	-P(1)	-F(3)	90.2(8)
F(6)	-P(1)	-F(4)	91.7(9)
F(6)	-P(1)	-F(5)	172.8(10)
C(2)	-C(1)	-S(1)	116.7(4)
C(3)	-C(2)	-C(1)	116.5(5)
C(2)	-C(3)	-S(2)	110.0(4)
C(5)	-C(4)	-S(2)	117.9(4)
C(4)	-C(5)	-S(3)	113.3(4)
C(7)	-C(6)	-S(3)	116.4(4)
C(6)	-C(7)	-S(1)	114.3(4)
N(1)	-C(9)	-C(8)	179.1(9)

Estimated standard deviations are given in parentheses.

membered ring.

The equatorial bond angle ∠S1 - Pd - S2 of 96.6(0)° is larger than that of the corresponding Pd(II) bis-[9]-aneS_3 complex (89.63(11)°) due to the presence of the six- membered chelate ring in the present complex. As a result the trigonal distortion in the ten-membered ring is less and the axial S atom moves closer to the axis perpendicular to the PdS_4 plane. This is manifest in the smaller angle between the axial Pd-S3 bond and the axis perpendicular to the PdS_4 plane (4.68°) compared to that in the $[Pd([9]\text{-ane}S_3)_2]^{2+}$ complex cation (7.80°). The larger ten- membered macrocycle thus enables the S atom to reach over and encapsulate the Pd atom.

In the present $[Pd([10]\text{-ane}S_3)_2]^{2+}$ complex ion, the axial C-S-C linkage adopts a "*endo*" conformation with respect to the axis (see Chapter 4) in the solid state in contrast to the "*exo*" conformation found in the $[Pd([9]\text{-ane}N_3)_2]^{2+}$ cation.[96] Owing to an axial interaction between the S atoms and the Pd atom, the geometry of the Pd atom can be described as an elongated octahedron. The molecule can be considered, therefore, to be in an "entatic" state because the "*endo*" conformer with significant axial interaction is predisposed to ready oxidation to six-coordinated d^7 octahedral ions, as will be discussed below.

6.4. NMR spectra:

6.4.1. ^{1}H and ^{13}C nmr spectra:

The ^{1}H nmr spectrum of $[Fe([10]\text{-}aneS_3)_2](ClO_4)_2$ in D_2O is characteristic of a low spin $(Fe[10]\text{-}aneS_3)_2^{2+}$ complex, Fig. 6.5. The protons are oriented differently towards the Fe(II) centre. Coupling can occur between these sets of protons giving rise to second order effects resulting in a more complicated spectrum. The C-$C\underline{H}_2$-C proton (4H) appear as a multiplet centered at 2.22 ppm. The S-$C\underline{H}_2$ protons can be divided into two magnetically inequivalent sets, one set (12H) due to protons on the axial position appearing as a multiplet centered at 2.63 ppm and another set (12H) due to protons in the equatorial position, with respect to the two planes of the coordinated ligand, (2.82 - 3.42 ppm). These 12 equatorial protons can be further divided into two subgroups, a multiplet centered at 2.91 ppm (4H) pointing away from the central atom and another centered at 3.32 ppm (8H) pointing towards the central metal atom. The seven-line ^{13}C nmr spectrum of the Fe(II) complex, Fig. 6.6. (δ 17.3, 24.2, 27.2, 34.4, 34.5, 34.9, 36.7), can be attributed to the presence of a *cis* (*gauche*) isomer in solution (C_2 symmetry).

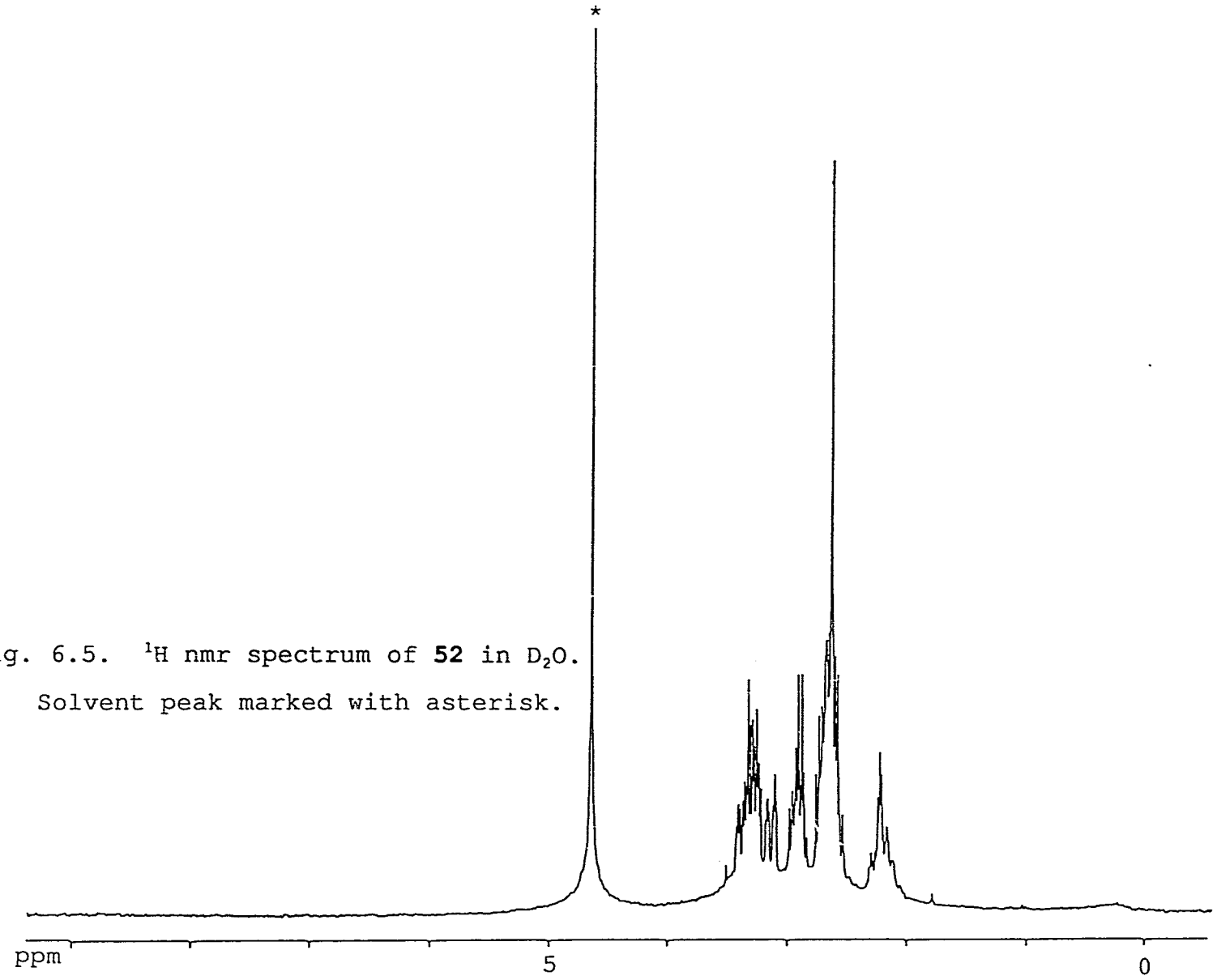

Fig. 6.5. ^{1}H nmr spectrum of **52** in D_2O.
Solvent peak marked with asterisk.

Fig 6.6. ^{13}C nmr spectrum of 52 in D_2O.

Solvent peak marked with asterisk.

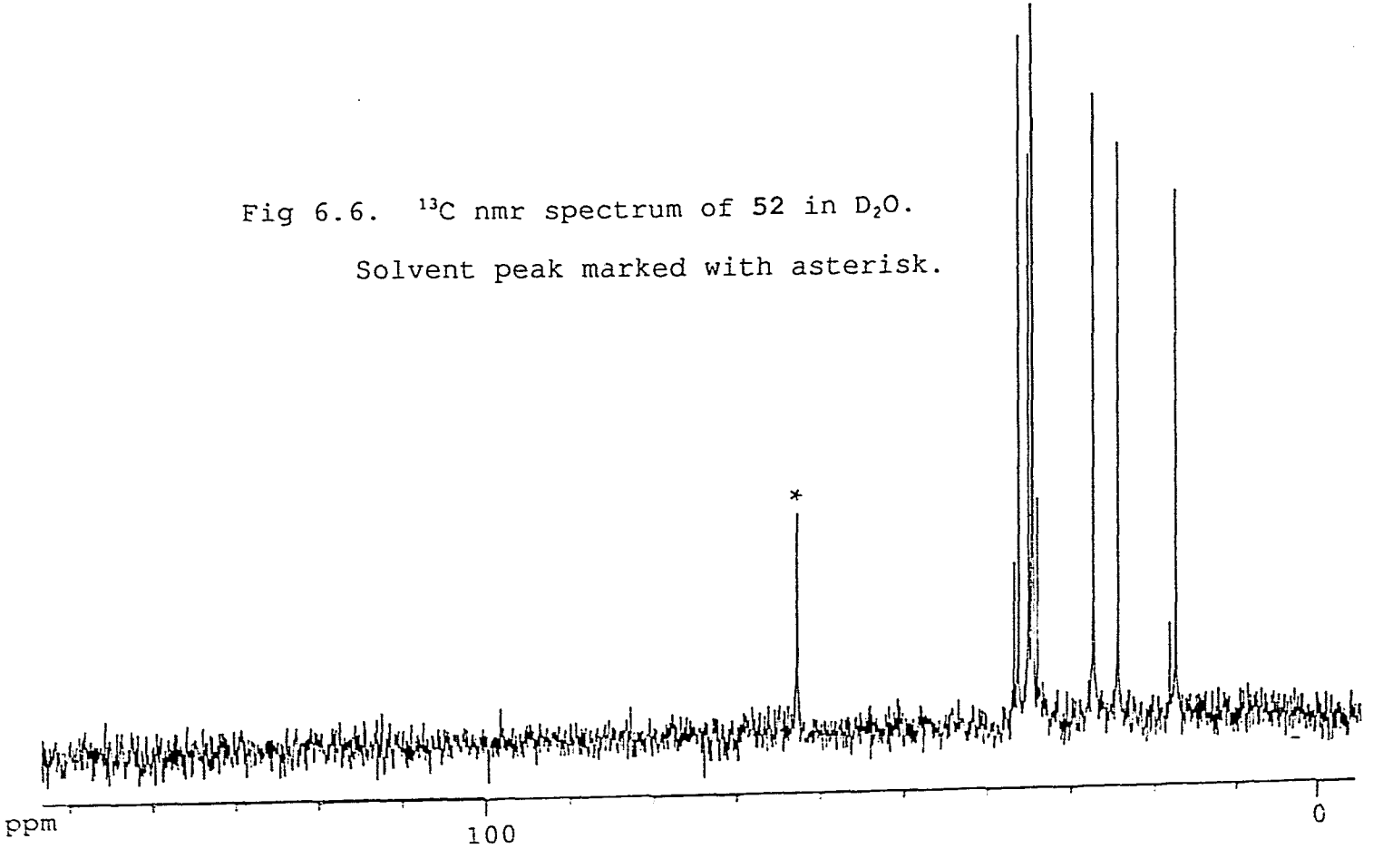

Based on the ^{13}C nmr the following solution structure for the Fe(II) complex is proposed:

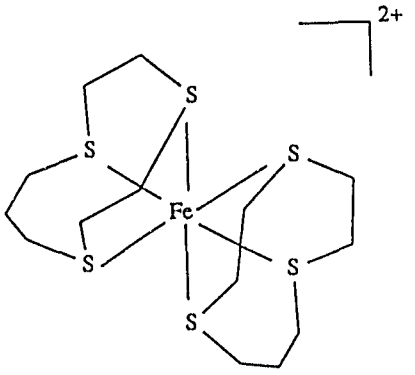

The peak at 17.3 ppm is due to the C-$\underline{C}H_2$-C methylene C atom. The peaks at 24.2 ppm and 27.2 ppm are due to the C atoms of the propylene bridge, adjacent to the S atoms. The remaining four peaks between δ 34.4 and 36.1 are due to the C atoms of the ethylene bridges. The peaks at δ 18.1, 33.9 and 36.7, (and another peak may be overlapped), in the ^{13}C nmr may be assigned to the meso stereoisomer, (*trans*). The *cis* (*gauche*) isomer can exist as Δ and λ enantiomers, Fig. 6.7. The designations Δ and λ indicate the two possible orientations of the two six- membered rings.[158] Recently, the optically active isomer of $[Fe([10]\text{-ane}S_3)_2]^{2+}$ was obtained and structurally characterised.[155] The ^{13}C nmr spectrum thus shows evidence for the presence of *gauche* arrangement of the six- membered ring in solution. However, in the present study, as is seen from the crystal structure, the meso stereoisomer of the Fe(II) complex was obtained where the two six- membered chelate rings are *trans* (*anti*) to one another. It is not unusual to obtain different structures in the solid state and in solution.

Fig. 6.7. Two possible enantiomers of **52**.

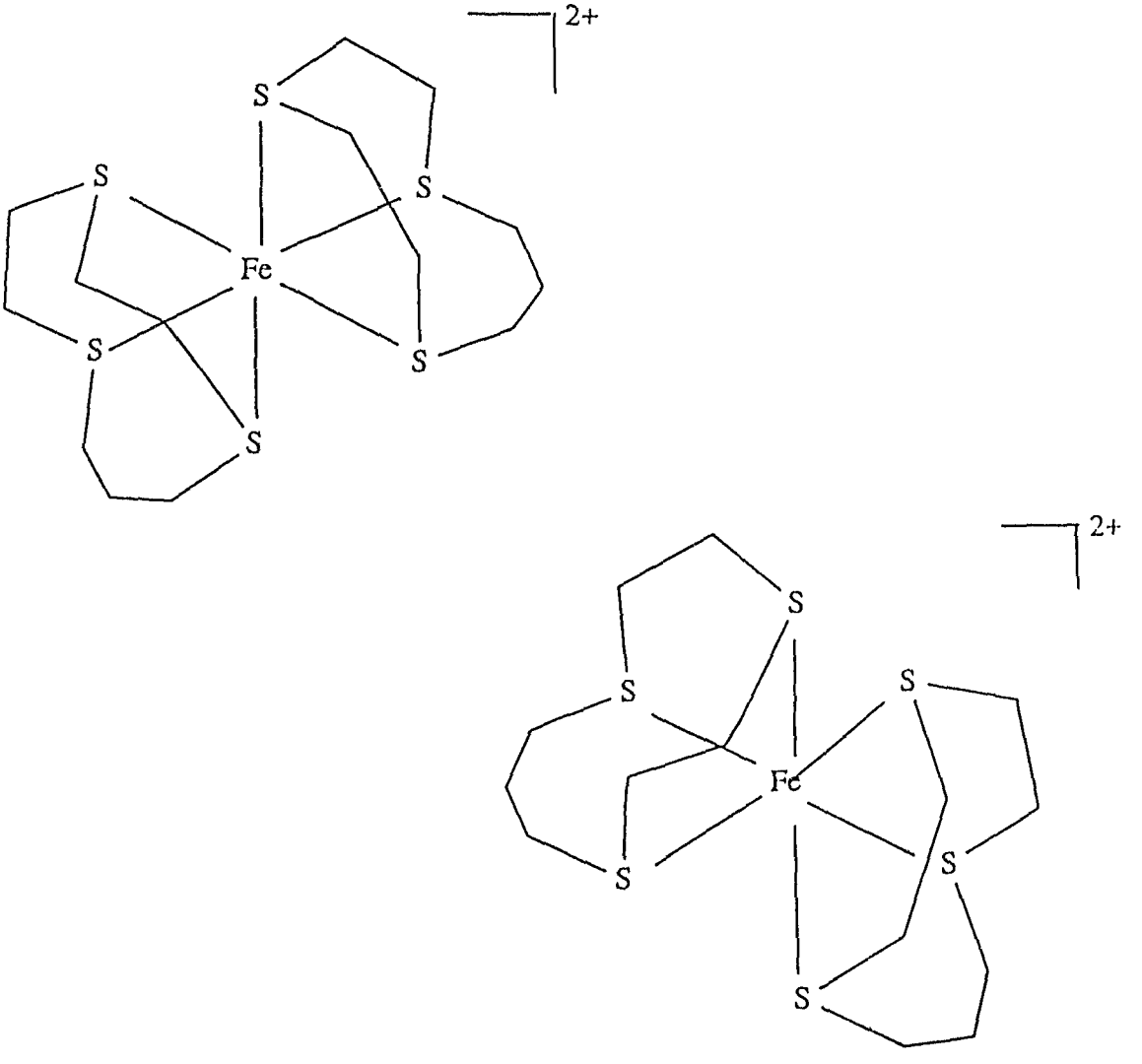

The ^{13}C nmr of Co(III) complex ion (Fig. 6.8.) shows seven lines at δ 17.0, 26.8, 29.2, 39.5, 40.6, 41.0 and 41.2 and are attributed to the presence of the *cis* isomer in solution (C_2 symmetry).

Fig. 6.8. ^{13}C nmr spectrum of $[Co([10]\text{-}aneS_3)_2](ClO_4)_3$, **54** in CD_3NO_2. Solvent peak marked with asterisk.

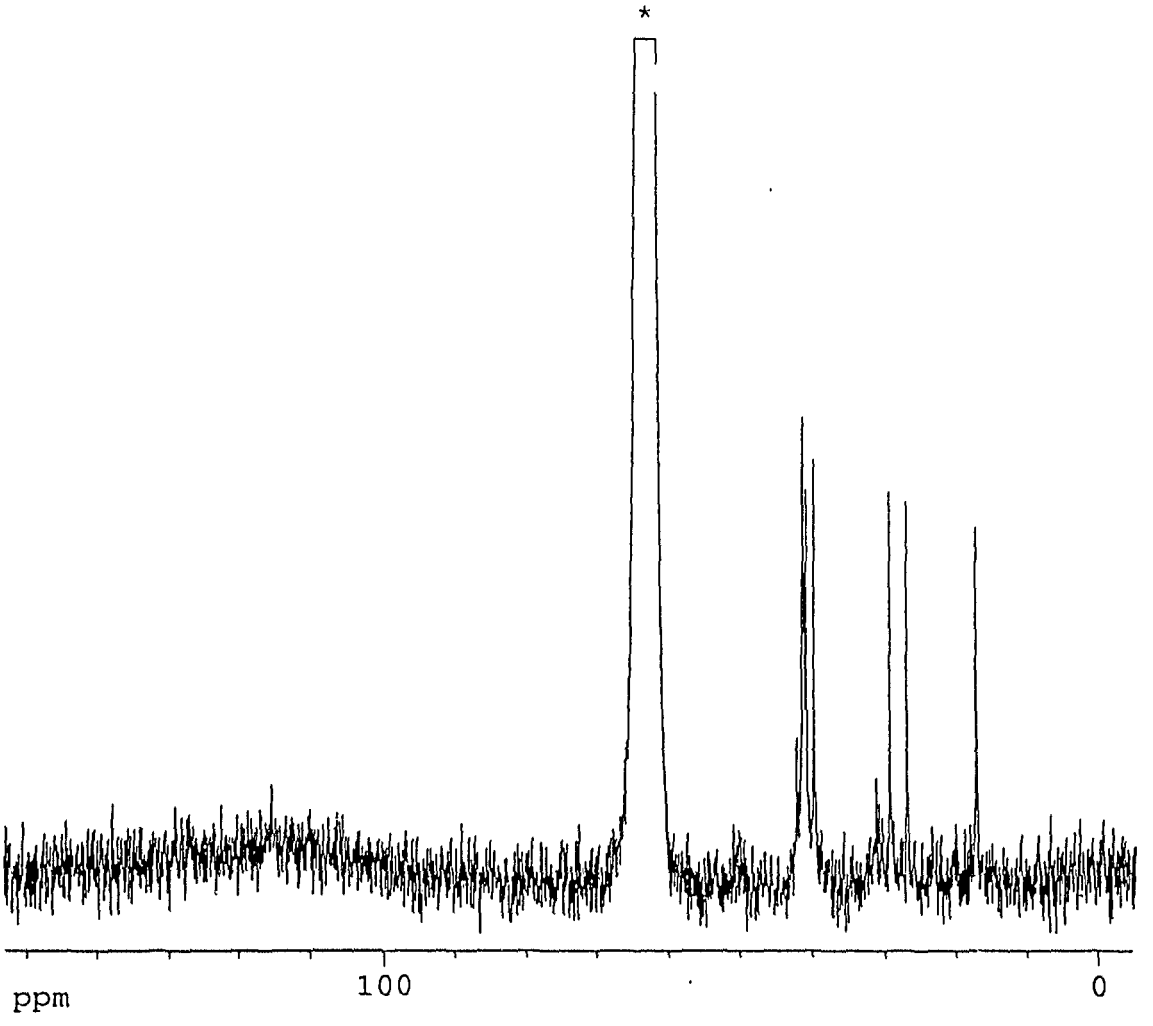

Based on the nmr the following structure for the Co(III) complex is proposed:

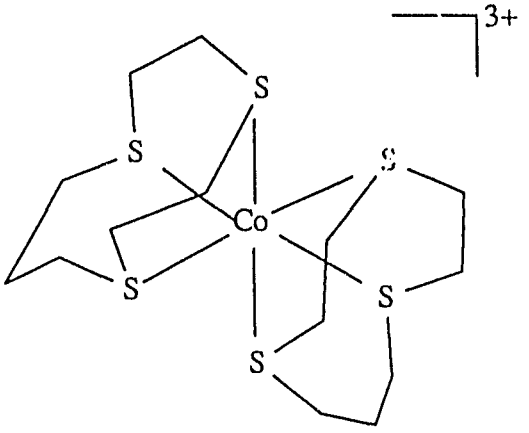

The peak at δ 17.0 is attributed to the C-$\underline{C}H_2$-C carbon of the propylene bridge. The peaks at δ 26.8 and 29.2 are due to the magnetically inequivalent C atoms of the propylene bridge, adjacent to the S atom. The remaining four peaks are due to the C atoms of the ethylene bridges. The conformations of the five- membered chelate rings interchange rapidly in solution and the ^{13}C nmr spectra reflect the average conformations. Similar seven line ^{13}C nmr spectrum has been obtained for the *cis* isomer of $[Co([10]\text{-ane}N_3)_2]^{2+}$ ion.[158] The peaks at δ 31.0 and 42.0 may be attributed to small amounts of the *trans* isomer. In general, the peaks are broad due to possible coupling with the Co nucleus (I = 7/2). No attempt was made to separate the *cis* and *trans* isomers.

The ^1H nmr of the Co(III) complex ion (Fig. 6.9.) is complicated due to the asymmetry of the ten- membered ring and also to the existence of both *cis* and *trans* isomers.

Fig. 6.9. ^{1}H nmr spectrum of complex **54** in D_2O.

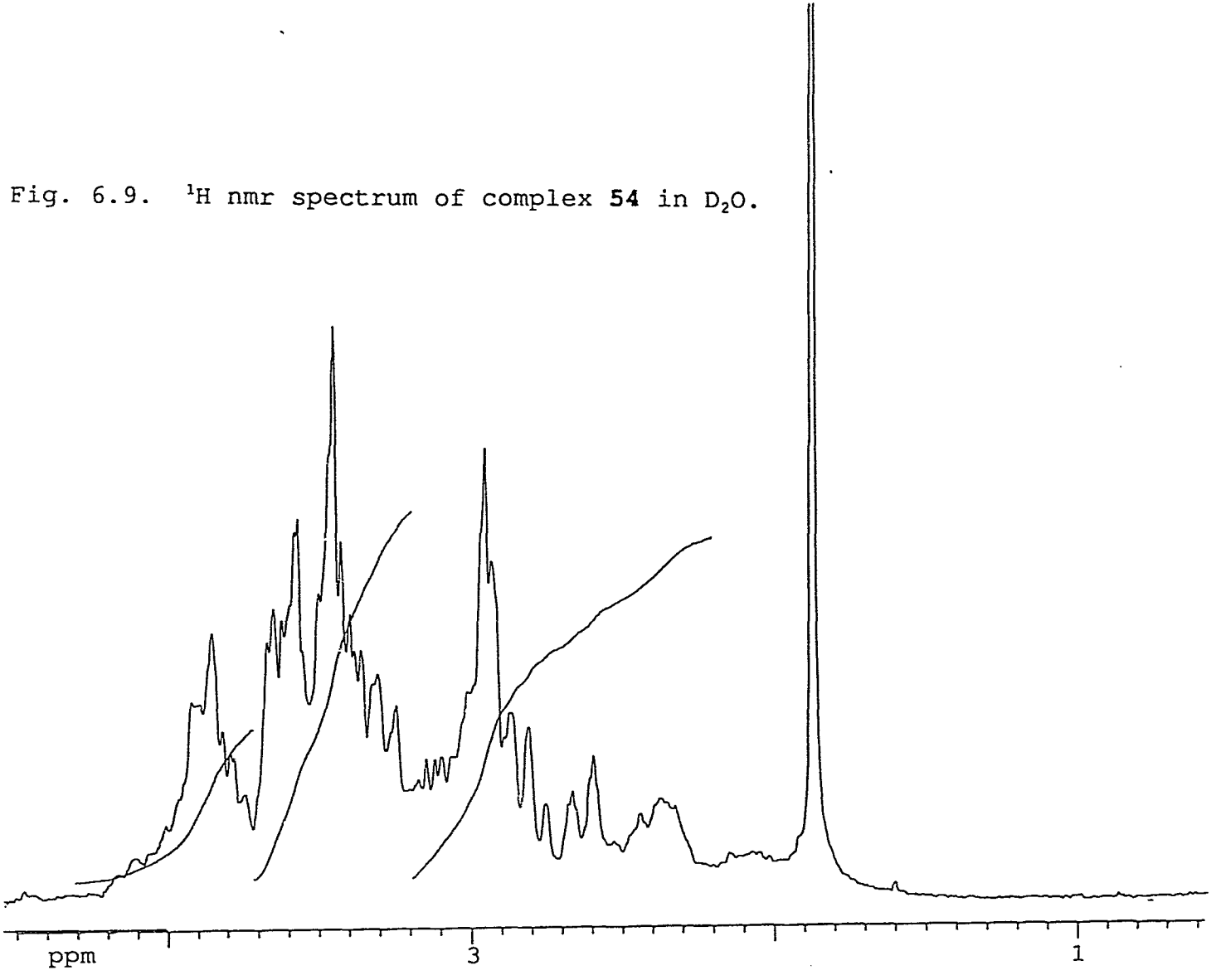

The corresponding ^1H nmr spectrum of $[Co([9]\text{-}aneS_3)_2]^{3+}$ ion is symmetrical and can be described in terms of the protons in axial and equatorial positions.[95]

The ^1H nmr spectrum of $Pd([10]\text{-}aneS_3)_2(PF_6)_2$ in d^3-nitromethane is complicated and can be explained in terms of protons pointing towards the metal ion and those that point away from it, (Fig. 6.10.). The C-C$\underline{H_2}$-C (4H) protons appear as two well separated multiplets centered at 2.19 ppm and at 2.70 ppm. The S-CH_2 protons can be divided into two magnetically inequivalent sets, one set (12H) due to protons in the axial position and another set (12H) due to protons in the equatorial positions appearing downfield (3.46 ppm). The axial set of 12 protons is further divided into two groups (4H and 8H), 4H pointing away from the central atom (2.89 ppm) and 8 protons pointing towards it (3.28 ppm).

At ambient temperature the proton nmr also shows an additional broad peak centered at 2.0 ppm. As the temperature is lowered this broad peak increases in intensity and moves downfield and becomes narrower below -20 °C, Fig. 6.11. At -45 °C this peak, now at δ 2.28 is well separated from the C-$\underline{C}H_2$-C proton multiplet at δ 2.11. The ambient temperature spectrum is regenerated upon raising the temperature. This peak is, therefore, assigned to the paramagnetic species with the axial S atoms bonding to the central Pd atom (Fig. 6.4.).

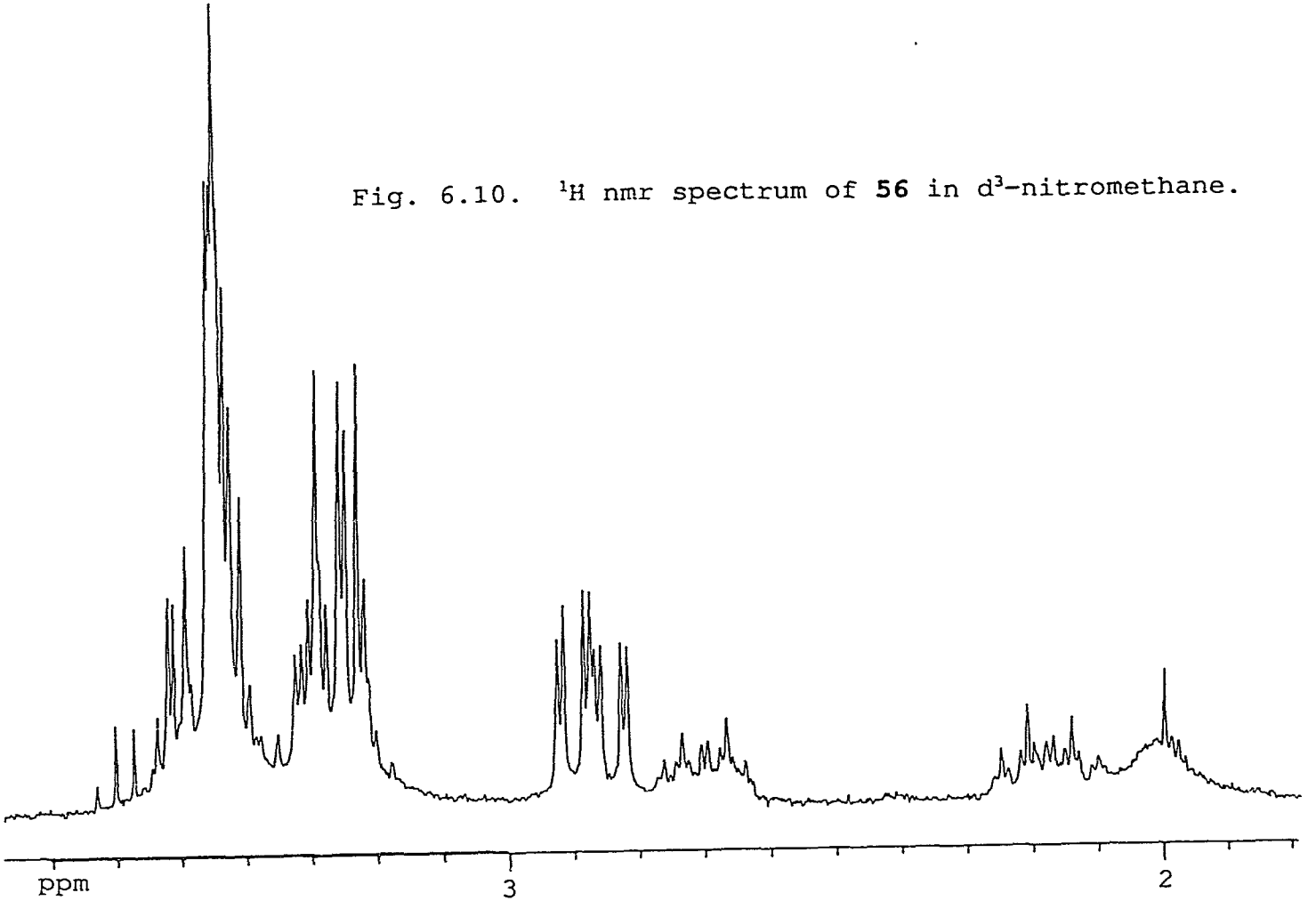

Fig. 6.10. ^{1}H nmr spectrum of **56** in d^{3}-nitromethane.

Fig. 6.11. Variable temperature ^1H nmr of $[Pd([23])_2](PF_6)_2$, **56** in CD_3NO_2 + CD_3OD mixture.

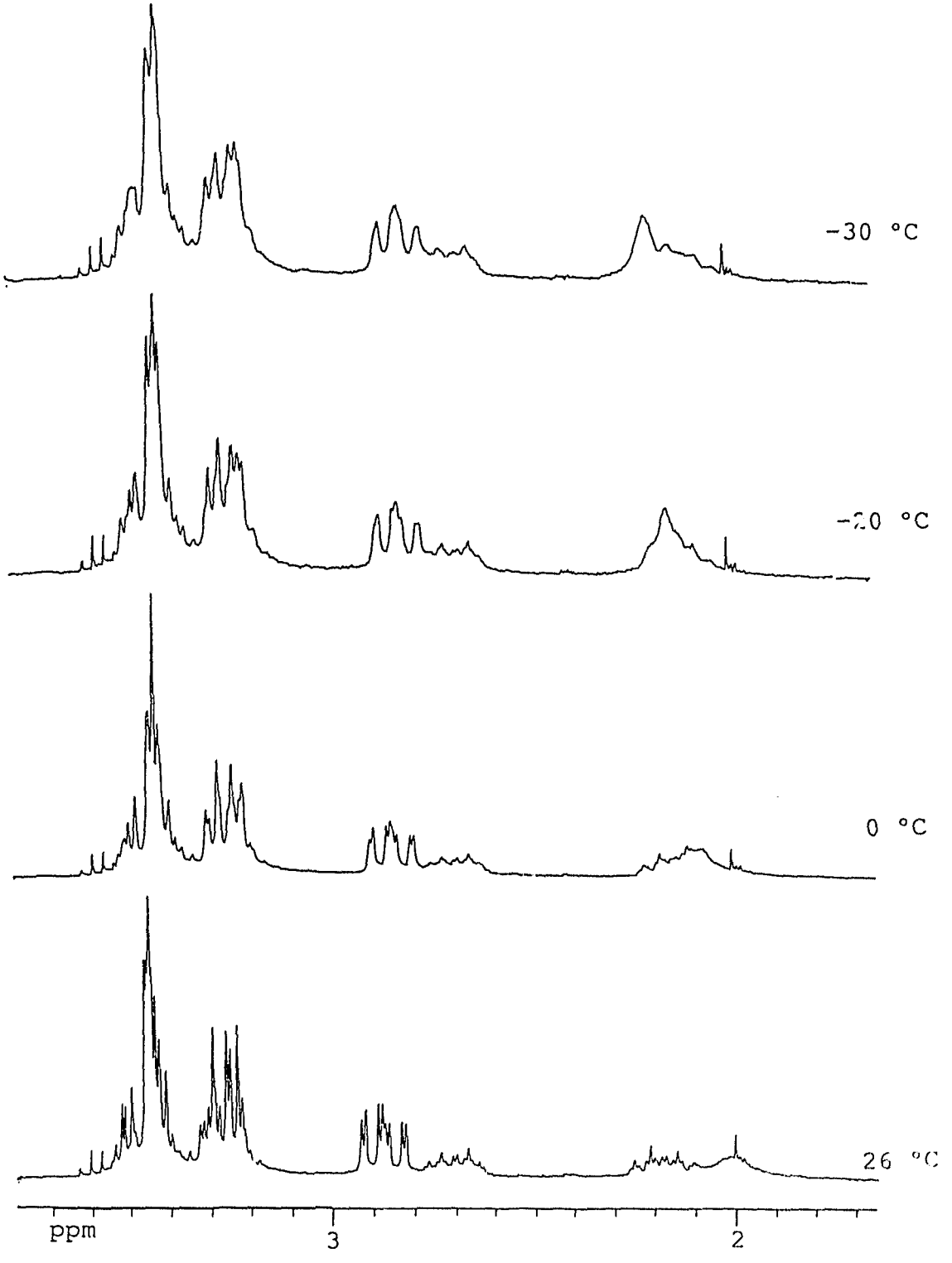

Fig. 6.11. (contd.)

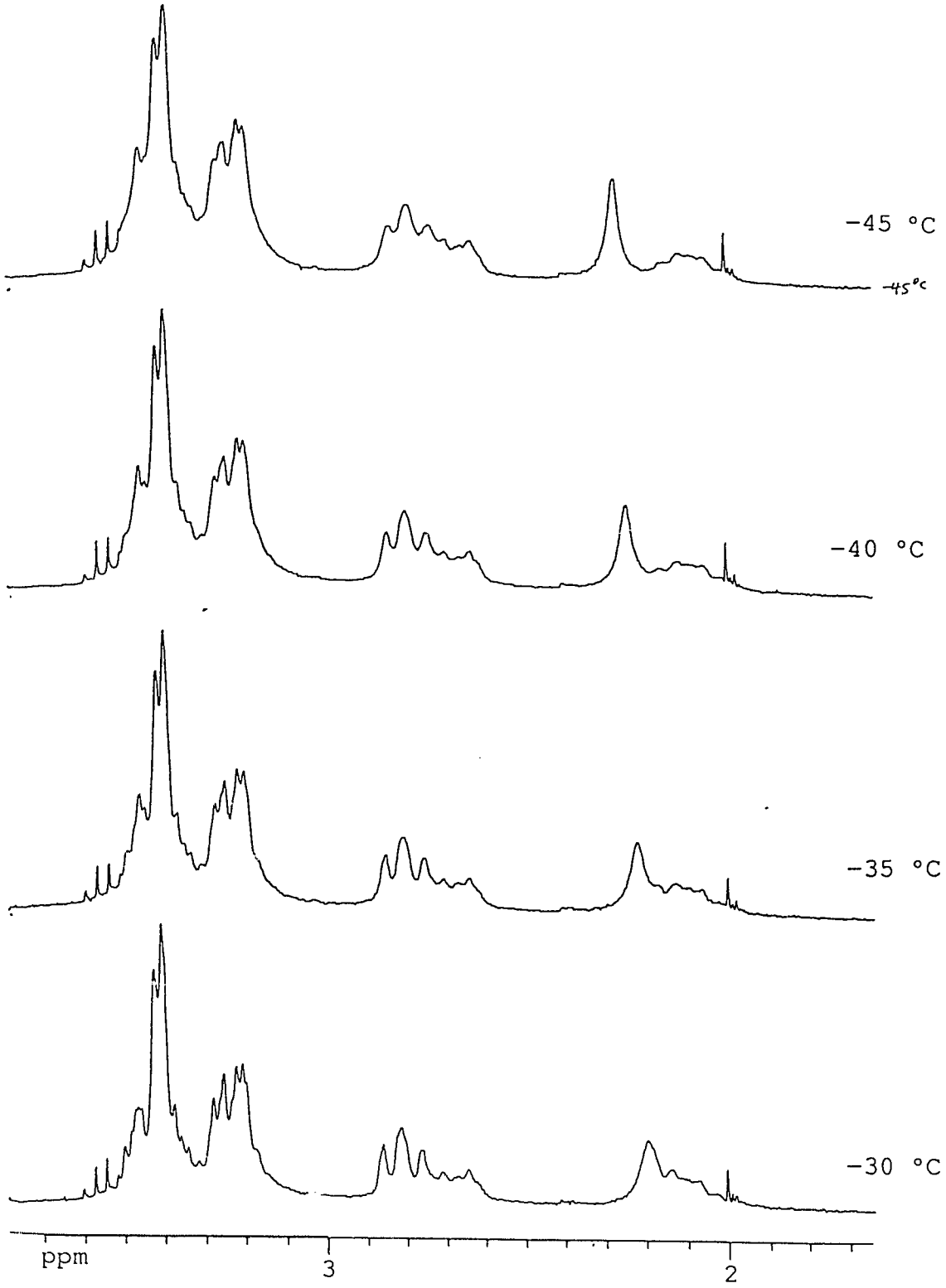

The ^{13}C nmr spectrum at ambient temperatures show four peaks at δ 26.8, 30.3, 33.7 and 38.2, Fig. 6.12. The peak at 26.8 ppm is assigned to the central C atom of the propylene bridge, labelled 'a' in **80**. The peak at 30.3 ppm is assigned to the C atoms adjacent to the apical S atoms, 'b' in **80**. The feature at 33.7 ppm is due to the ethylene C atoms adjacent to the coordinated S atoms, 'c' in **80**. The peak at 38.2 ppm is associated with the C atoms adjacent to the coordinated equatorial S atoms, 'd' in **80**. The solution spectrum at ambient temperatures is in agreement with the solid state structure, Fig. 6.4.

Fig. 6.12. ^{13}C nmr spectrum of **56** at ambient temperatures in CD_3CN. Solvent peak marked with asterisk.

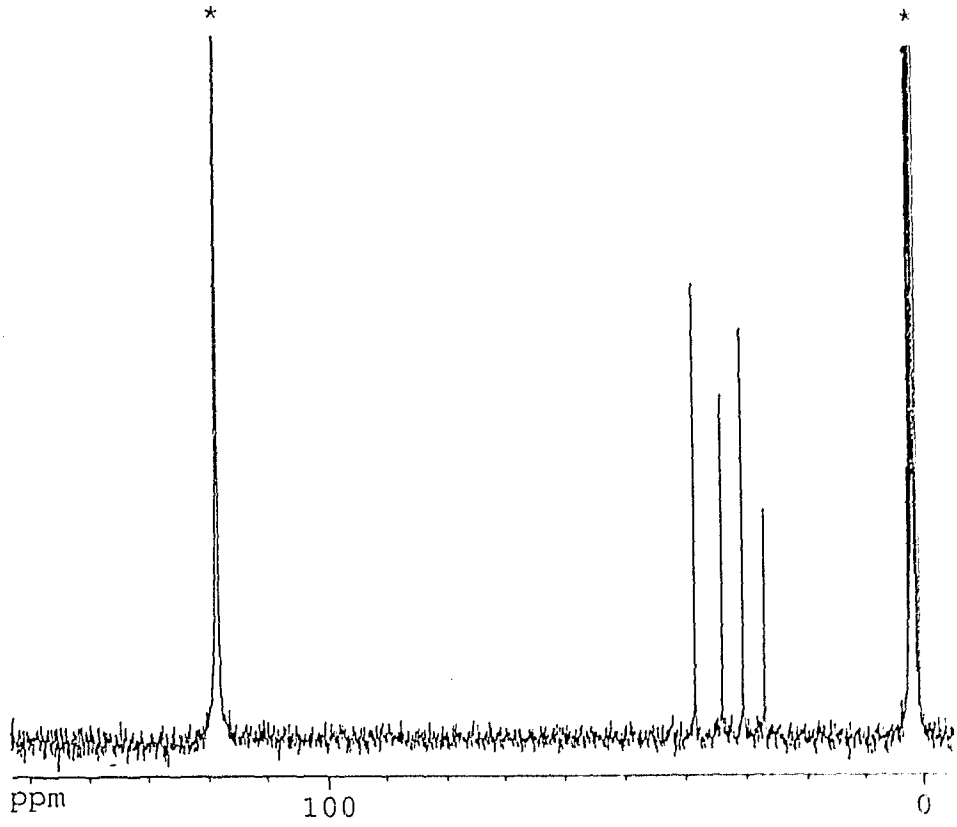

The low temperature nmr spectrum, Fig. 6.13., provides evidence for fluxionality of the coordinated ligand in the complex. As the temperature is lowered the four peaks become broader due to the formation of the paramagnetic species. At 0 °C the intensity ratio of the peaks is approximately 2:2:2:1 characteristic of the structure **80**, (*anti* with respect to the PdS_4 plane, see Chapter 4). As the temperature is lowered further two additional narrow peaks appear at δ 15.4 and 67.1 and increase in intensity at -40°C. The peaks are assigned to the '*syn*' structure **81** (*syn* with respect to the PdS_4 plane). For the '*syn*' structure the peak at 15.4 ppm arises from the C atom adjacent to the apical S atoms. The structure of the '*syn*' species necessitates this C atom to be close to the Pd atom resulting in a significant upfield shift. Similar upfield shifts for the '*syn*' isomer have been been observed by Hunter *et al*[96] in the low temperature ^{13}C nmr studies of the

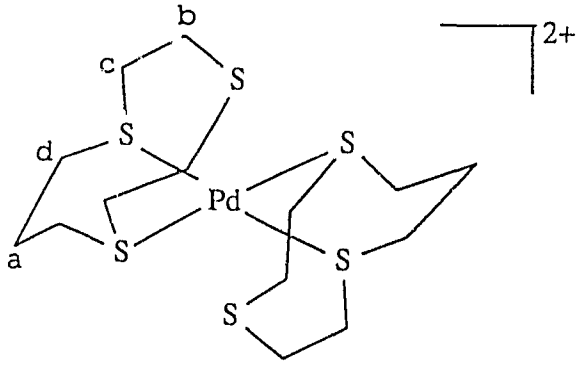

80

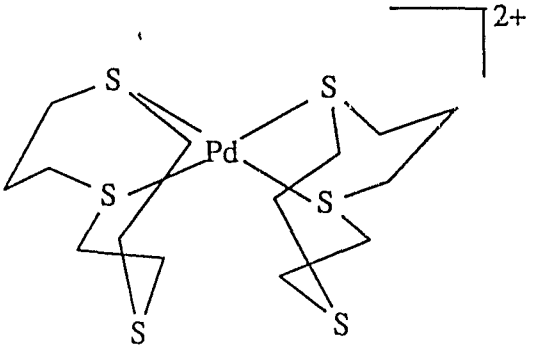

81

Fig. 6.13. Variable temperature ^{13}C nmr of **56** in CD_3NO_2 + CD_3OD mixture. Solvent peak marked with asterisk.

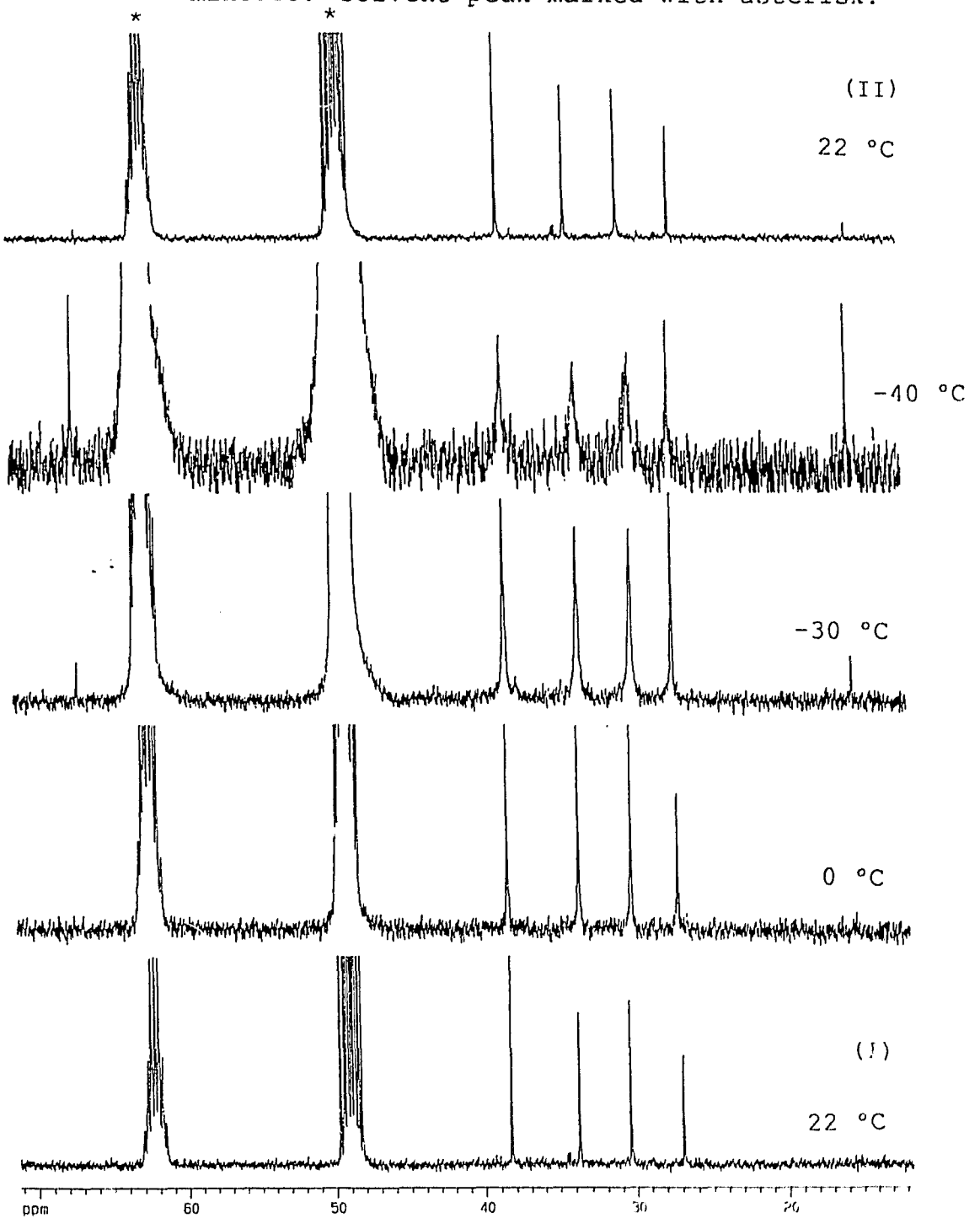

fluxional $[Pd([9]\text{-}aneN_3)_2]^{2+}$ complex ion, {([9]-aneN$_3$) = **22**}. The peak at 67.1 ppm may be assigned to the C atoms adjacent to the coordinated S atoms.

The variable temperature nmr can be explained by a fluxional process in the macrocyclic ring in which the metal effectively hops between any two of the three S atoms as illustrated in Fig. 6.14. A possible mechanism for the interconversion is shown in Fig. 6.15. The apical S atom is substituted onto the Pd atom forming a five- coordinate intermediate, B in Fig. 6.15. One of the S atoms then moves to the axial position forming a *syn* species where both the macrocycles are on the same side of the PdS_4 plane, C in Fig.6.15.

The other ring rotates in a similar fashion to form the *'anti'* isomer D in Fig. 6.15. Structure D can then revert back to A in Fig. 6.15 through the same process. Thus the variable temperature ^{13}C nmr provides evidence for such an interconversion from *'anti'* to *'syn'* species and *vice versa*. The interconversion thus proceeds through an interchange or an associate-interchange mechanism. The fluxional behaviour of the $Pd([\mathbf{23}])_2^{2+}$ ion together with significant interaction in axial sites leaves the d^8 Pd(II) complex ion in an entatic state facilitating ready oxidation of the Pd(II) ion to the octahedral Pd(III) complex.

Figs. 6.14. Fluxional process within the macrocyclic ring with respect to the Pd central atom.

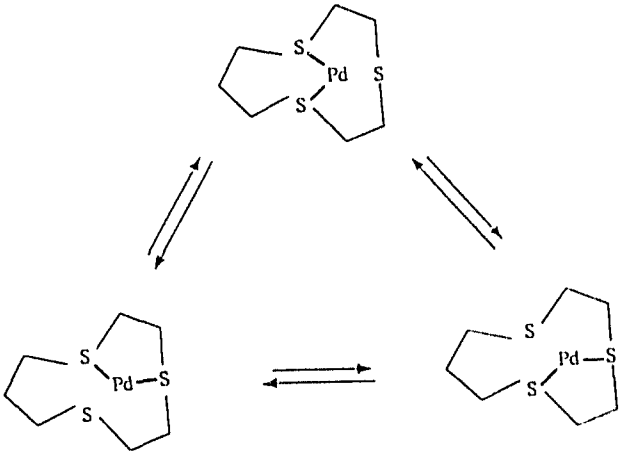

Fig. 6.15. Possible mechanism for the interconversion of the *anti* (A) to *syn* (C) configuration.

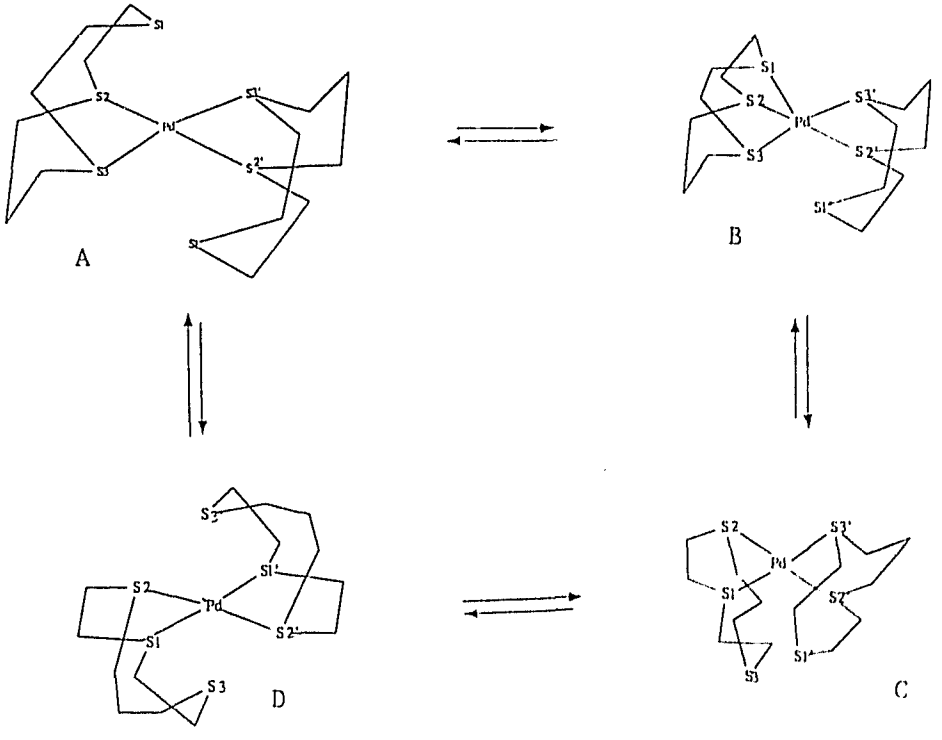

6.4.2. ^{59}Co nmr spectroscopy:

^{59}Co has a natural abundance of 100%. Its gyromagnetic ratio, γ = 6.3472 × 10^7 rad $T^{-1}s^{-1}$, places its resonance frequency in the neighbourhood of that for ^{13}C.[159] At 2.3488 T, ^{59}Co resonates at 23.727 MHz, whereas ^{13}C resonates at 25.144 MHz.

The receptivity of ^{59}Co is better than that of ^{13}C by a factor of 1570. This is attributed to the greater intrinsic sensitivity of the Co nucleus (0.277 *vs.* 1.59 × 10^{-2} for an equal number of ^{59}Co and ^{13}C nuclei at constant field) and to its greater natural abundance (100% *vs.* 1.1%). However, the quadrupole moment Q has a very large value of 0.404 barns which leads to large quadrupole interactions. The relaxation rate depends on the product of Q^2 and $[(2I + 3)/\{I^2(2I - 1)\}]$. Since ^{59}Co has a nuclear spin I = 7/2, this product is moderate (21.8)[159] and is comparable to those of ^{14}N (25.2) and ^{23}Na (19.2), making Co complexes amenable to study by their ^{59}Co nmr spectroscopy.

The ^{59}Co nmr spectrum of $Co([9]\text{-}aneS_3)_2(ClO_4)_3$, ([9]-$aneS_3$ = **64**), and $Co([10]\text{-}aneS_3)_2(ClO_4)_3$, **54**, are shown in Fig. 6.16. and 6.17., respectively. The spectrum of the Co complex based on **64** shows one single resonance at 1511 ppm relative to hexacyanocobaltate taken as 0 ppm, and is in good agreement with the value of 1502 ppm obtained by Küppers *et al.*[160] The complex based on [10]-$aneS_3$, **23**, shows two peaks at 2296 ppm and 2207 ppm of intensity ratio 6:1, due to the presence of

cis and *trans* isomers respectively. The ^{59}Co nmr linewidths depend on the electrostatic field gradients in the complexes. The electric field gradient for the *cis* isomer is usually smaller than that for the *trans* isomer.[159] A quadrupolar mechanism is the predominant mode of relaxation in Co(III) complexes devoid of full octahedral symmetry. As a result the ^{59}Co nmr linewidth for the *trans* isomer is broader to a greater extent than the *cis* isomer. This is in keeping with the observation that the ^{59}Co spectrum of **54** shows two peaks of different widths. The full width at half maximum (FWHM) for the peak centered at 2296 ppm is 624 Hz and for the peak centered at 2207 ppm is 1100 Hz. The broader peak is assigned to the *trans* (*anti*) isomer, since the Co complex can exist as *cis* (*gauche*) and *trans* (*anti*) isomers (Fig. 6.18.).

Fig. 6.16. ^{59}Co nmr spectrum of $[Co([\mathbf{64}])_2](ClO_4)_3$ in D_2O.

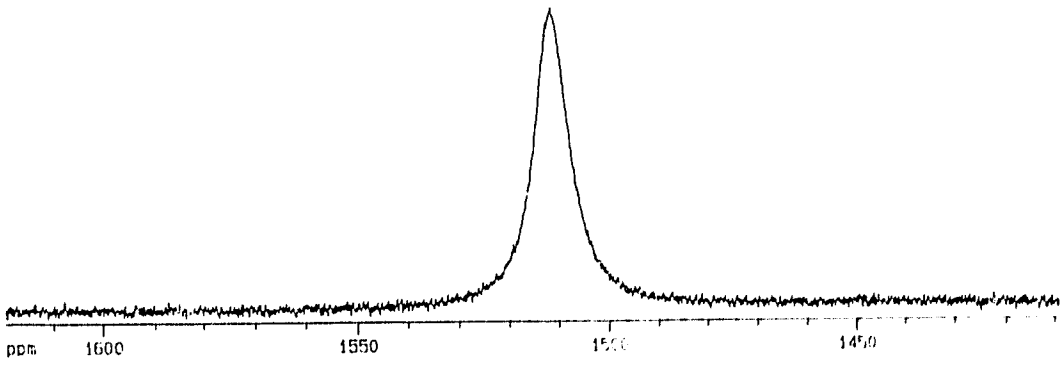

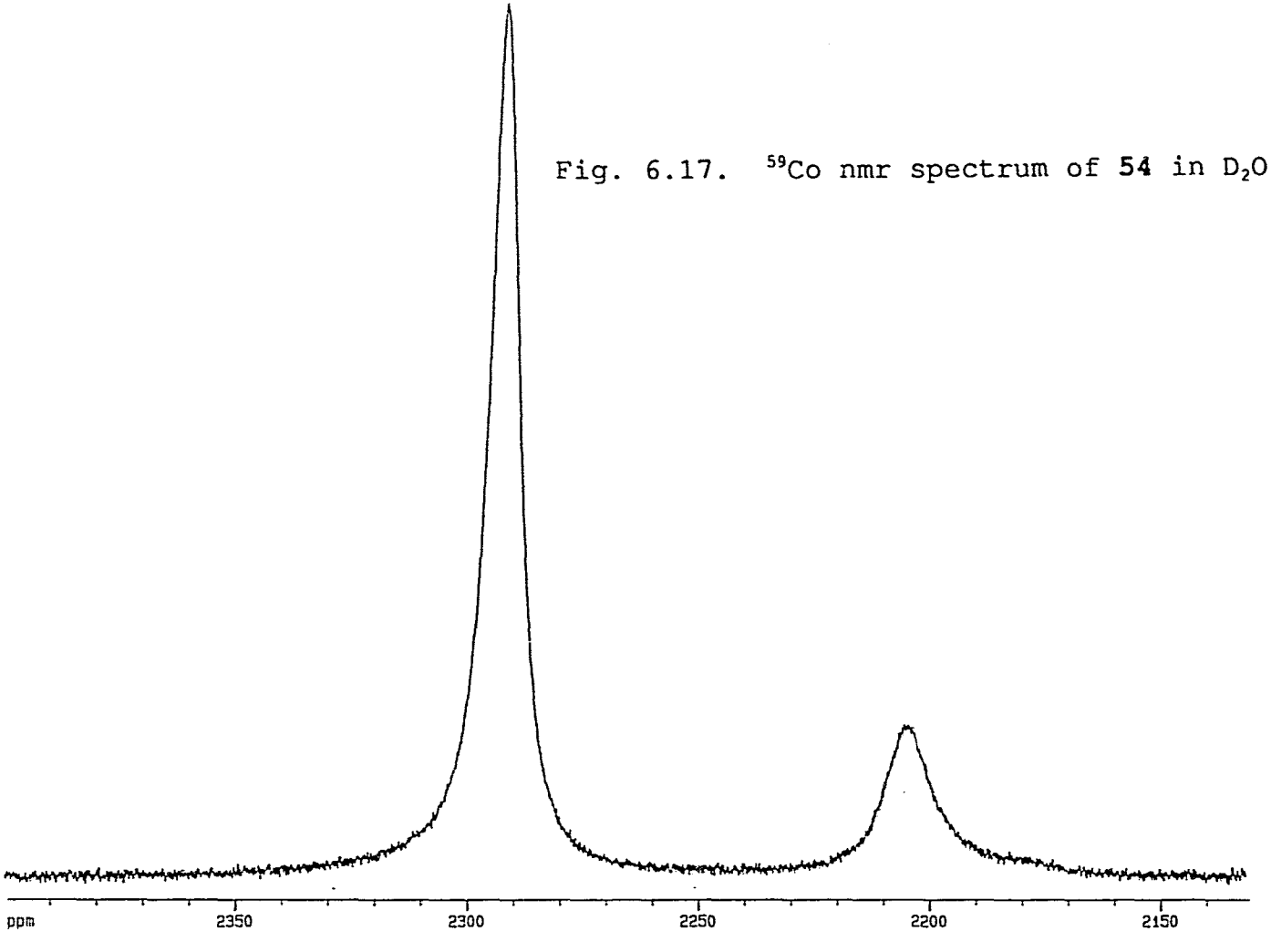

Fig. 6.17. ^{59}Co nmr spectrum of **54** in D_2O.

Fig. 6.18. *CIS* and *TRANS* isomers of **54**.

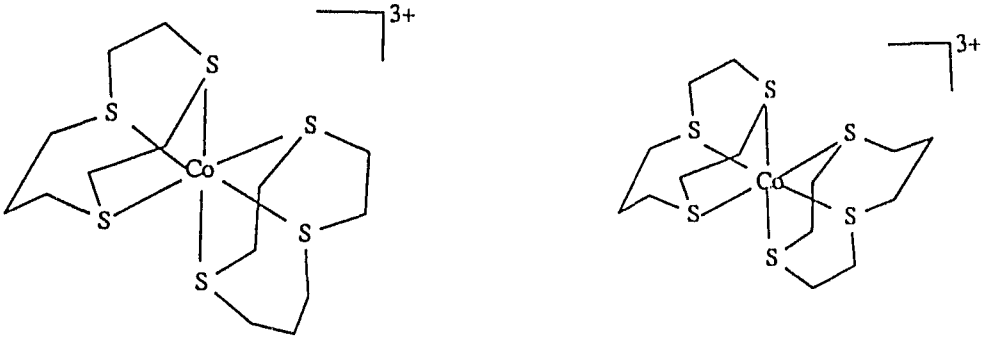

cis-**54** *trans*-**54**

6.5. Electronic spectra:

The electronic spectra of the various complexes together with the ligand field parameters are listed in Table 6.13. The electronic spectrum of $[Fe([10]\text{-ane}S_3)_2]^{2+}$ shows two bands at 542 nm and 409 nm due to d-d transitions attributed to $^1T_{1g} \leftarrow {}^1A_{1g}$ and $^1T_{2g} \leftarrow {}^1A_{1g}$ respectively. For the two transitions, the large molar absorptivity in this complex compared to that of the Fe(II) complex of [9]-aneS_3, **64**,[87] is attributed to the asymmetry of the ten membered ring as opposed to the symmetrical nine- membered ring. The two transitions can be expressed as follows:[121]

$E(^1T_{1g} \leftarrow {}^1A_{1g})$: $10Dq - C + 86B^2/10Dq = 18450\ cm^{-1}$ --- 6.1.

$E(^1T_{2g} \leftarrow {}^1A_{1g})$: $10Dq + 16B - C + 2B^2/10Dq = 24450\ cm^{-1}$ --- 6.2.

Assuming C = 4B, Dq is calculated to be = 1935 cm^{-1} and B = 424 cm^{-1}. The nephelauxetic ratio β (= B(complex)/B(free ion)) for the Fe(II) complex was found to be 0.40. This value is

Table 6.13. Electronic spectra and ligand field parameters for various complexes.

Complex	λ_{max} (nm), (ε, $Mol^{-1}cm^{-1}$)	Dq (cm-1)	B (cm^{-1})	β	*f*	h	Ref.
$[Fe(23)_2]^{2+}$	542(86), 409(97)	1965	460	0.38	1.97	-	PW
$[Fe(23)_2]^{2+}$	540(78), 395(103)	1943	490	0.46	1.94	-	155
$[Fe(64)_2]^{2+}$	523(53), 395(52)	2005	437	041	2.00	-	87
$[Fe(23)_2]^{3+}$	721(53), 613(42), 487(75)	2496	665	0.61	1.78	1.6	PW
$[Fe(64)_2]^{3+}$	634(700), 587(sh), 498(sh), 458(520), 340(7600)	2512	579	0.53	1.79	1.9	161, PW
$[Co(23)_2]^{2+}$	738(15), 638(sh), 565(sh), 483(133), 364, 284	-	-	-	-	-	PW
$[Co(23)_2]^{2+}$	510(sh, 370), 290(11800)	-	-	-	-	-	155
$[Co(64)_2]^{2+}$	730(11), 560(sh), 480(92), 338(6600), 264(6500)	-	-	-	-	-	87
$[Co(23)_2]^{3+}$	493(398), 374(sh,10247), 356(13077), 295(6004)	2190	404	0.37	-	1.8	PW
$[Ni(23)_2]^{2+}$	850(sh), 800(37), 530(66)	1250	717	0.69	1.40	2.6	PW
$[Ni(23)_2]^{2+}$	807(33), 544(54)	1239	656	0.63	1.42	-	155
$[Ni(23)_2]^{3+}$	567, 411, 346, 306, 283						
$[Pd(23)_2]^{2+}$	598(84), 314(10800), 277(11300), 209(8000)	-	-	-	-	-	PW

comparable with that obtained for the Fe(II) complex of [9]-aneS$_3$, **64**, and is characteristic of the π- acid properties of the S donor atoms. An empirical rule due to Jørgensen,[162] can be used to express Δ_0 as a product of two functions each of one variable,

$$10Dq = \Delta_0 = f(\text{ligand})g(\text{metal})\ (cm^{-1} \times 10^3), \qquad \text{--- 6.3.}$$

and can be used to estimate the spectrochemical parameter *f* for various ligands (*f* is a pure number relative to the hexa-aqua ion, *g* is in 10^3 cm^{-1}). Thus,

$$19347 \times 10^{-3} = fg,$$

$g(Fe^{2+})$[163] = 10.0, giving, f = 1.9.

The spectra of [Fe([10]-aneS$_3$)$_2$]$^{3+}$ in 1 M $HClO_4$ shows three bands at 721 nm (13869 cm^{-1}), 613 nm (16313 cm^{-1}), and 487 nm (20534 cm^{-1}), Fig. 6.19. Intense charge transfer bands were seen above 21000 cm^{-1}.

Fig. 6.19. Electronic spectrum of Fe(**23**)$_2^{3+}$ in 1 M $HClO_4$.

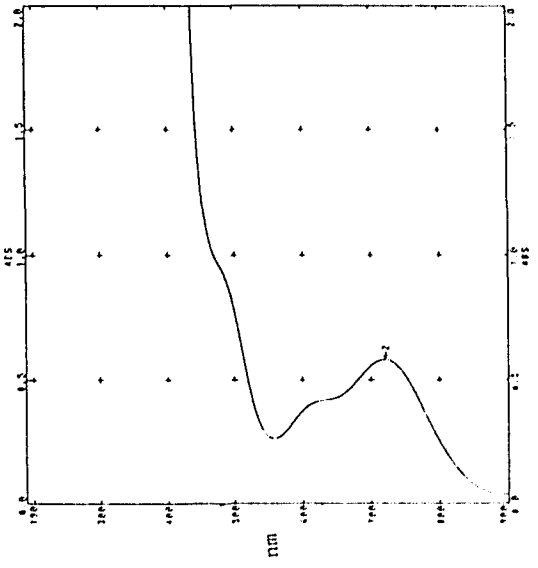

The spectrum is characteristic of a low spin d^5 ion with $^2T_{2g}$ ground state. The terms arising from the $t_{2g}^4e_g^1$ configuration[164] together with the energy relative to the $^2T_{2g}$ ground state are shown in Table 6.14. The 2^2T_{2g} states arise from the $d_{x^2-y^2}$ and d_{z^2} orbitals. Comparison with the electronic spectrum of $[Fe(CN)_6]^{3-}$ ion[164,165] enabled the assignment of the three bands in the $Fe([10]\text{-}aneS_3)_2^{3+}$ complex ion. The shoulder at 487 nm (20534 cm^{-1}) and the broad peak at 613 nm (16313 cm^{-1}) have been assigned to d-d transitions. The band at 721 nm (13867 cm^{-1}) (ε = 492 M^{-1} cm^{-1}) is attributed to L $\rightarrow$ M charge transfer transition, $t_{2g}\pi \leftarrow t_{1u}\sigma$. The lower intensity of this charge transfer band compared to the other intense charge transfer bands at energies greater than 21000 cm^{-1} seems appropriate for a $\sigma \rightarrow \pi$ -type transition. The d-d band at 613 nm is attributed to the $^4T_{2g} \leftarrow {}^2T_g$ transition and the one at 487 nm is attributed to the spin-allowed $^2T_{2g} \leftarrow {}^2T_{2g}$ transition. From the energy expressions for these two transitions, neglecting spin-orbit interactions, the ligand field strength 10Dq, and the Racah parameters B and C were determined:

$^4T_{2g} \leftarrow {}^2T_{2g}$ $\quad$ $10Dq + 3B - 4C = 16313\ cm^{-1}$ $\quad$ --- 6.4.

$^2T_{1g}(^2A_{2g}) \leftarrow {}^2T_{2g}$ $\quad$ $10Dq - 2.65B - C = 20534\ cm^{-1}$ $\quad$ --- 6.5.

$B = 665\ cm^{-1}$

$C = 2660\ cm^{-1}$

$10Dq = 24957\ cm^{-1}$.

The molar absorption coefficients for the two d-d transitions are larger than expected due to: a) the distorted octahedral

Table 6.14.

Terms and energies in low spin d^5 ions (from ref. 165)

Strong-field d-electron configurations	Terms arising (parentage)	Diagonal electrostatic energy, including off-interactions, relative to $^2T_{2g}(t_{2g}^5)$	Energy relative to E_g" with 1st order spin-orbit splitting
t_{2g}^5	$^2T_{2g}$	0	0
$t_{2g}^4e_g^1$	$^4T_{1g}(^3T_{1g})$	$\Delta - 5B - 4C$	$\Delta - 5B - 4C + 3\lambda/4$
	$^4T_{2g}(^3T_{1g})$	$\Delta + 3B - 4C$	$\Delta + 3B - 4C + 17\lambda/12$
	$(1)\,^2T_{1g}(^3T_{1g})$	$\Delta - 2.65B - C$	$\Delta - 2.65B - C + 4\lambda/3$
	$(1)\,^2T_{2g}(^1T_{2g})$	$\Delta + B - C$	$\Delta + B - C + \lambda$
	$(2)\,^2T_{1g}(^1T_{2g})$	$\Delta + 12.65B - C$	$\Delta + 12.65B - C + \lambda$
	$(2)\,^2T_{2g}(^3T_{1g})$	$\Delta + 13B - C$	$\Delta + 13B - C + 4\lambda/3$
	$^2A_{1g}(^1E_g)$	$\Delta + 17B - C$	$\Delta + 17B - C + \lambda$

Fe^{3+} species and b) intensity "stealing" from nearby charge transfer bands.

The tentative assignment of the bands observed in the $[Fe([9]\text{-}aneS_3)_2]^{3+}$ complex[161] have been reassigned as follows:

Band position	Transition	Energy level
458 nm (21834 cm^{-1})	$^2T_{2g} \leftarrow {}^2T_{2g}$	$10Dq - B - C + \lambda$
498 nm (20080 cm^{-1})	$(^2A_{2g})\,^2T_{1g} \leftarrow {}^2T_{2g}$	$10Dq - 2.65B - C + 4\lambda/3$
587 nm (17036 cm^{-1}	$^4T_{2g} \leftarrow {}^2T_{2g}$	$10Dq + 3B - 4C + 17\lambda/12$
634 nm (15773 cm^{-1})	$t_{2g}(\pi) \leftarrow t_{1u}(\sigma)$.	

Using the $^2T_{2g} \leftarrow {}^2T_{2g}$ and $^4T_{2g} \leftarrow {}^2T_{2g}$ transitions, 10Dq, B and C were found to be 25120 cm^{-1}, 579 cm^{-1} and 2316 cm^{-1} respectively. The band at 634 nm (ε = 700 M^{-1} cm^{-1}) was wrongly assigned to the $^1T_{1g} \leftarrow {}^2T_{2g}$ transition. The relatively large value for ε is only consistent with the $t_{2g}(\pi) \leftarrow t_{1u}(\sigma)$, $L \rightarrow M$, charge transfer transition. The discrepancies in the computations of 10Dq and B using different pairs of these transitions arise because the positions of the bands at 498 nm and 587 nm are not well defined.

For the Fe^{3+} complexes of $[9]\text{-}aneS_3$, **64**, and $[10]\text{-}aneS_3$, **23**, the ligand spectrochemical parameter *f* together with the Dq values and the interelectronic repulsion parameters are shown in Table 6.13. The spectrochemical parameter *f* was obtained using a $g(Fe^{3+})$ value of 14.[163] Thus,

$$f([9]\text{-}aneS_3) = 25120/(14 \times 10^3) = 1.79$$

and $f([10]\text{-aneS}_3) = 24957/(14 \times 10^3) = 1.78$.

The ligand nephelauxetic parameter *h* can be determined from the following empirical relationship:[162]

$$\beta = B/B_0 = [1 - \{h(\text{ligand}) \times k(\text{metal})\}] \quad \text{--- 6.6.}$$

For the ligand [10]-aneS$_3$, **23**, B = 665 cm^{-1}, B_0 = 1090 cm^{-1} (the free ion interelectronic repulsion parameter for Fe^{3+}), β(nephelauxetic ratio) = 0.61, $k(Fe^{3+})$[163] = 0.24 and *h* is estimated to be 1.6. Using the value of β = 0.53, *h* for the ligand [9]-aneS$_3$, **64**, was estimated to be 1.9.

The uv-visible spectra of [Co([10]-aneS$_3$)$_2$](ClO$_4$)$_2$ in CH$_3$CN shows four bands at 13550 cm^{-1}, 15674 cm^{-1}, 17699 cm^{-1} and 20704 cm^{-1} and are assigned to the $(_{2a}T_{1g})\,^2A_{2g} \leftarrow {}^2A_{1g}$, $(^2T_{2g})\,^2B_{2g} \leftarrow {}^2A_{1g}$, $(^2T_{2g})\,^2E_g \leftarrow {}^2A_{1g}$ and $(^2{}_bT_1g)\,^2A_{2g} \leftarrow {}^2A_{1g}$ respectively. The assignments are based on comparison with other low spin d^7 Co(II) complexes.[166,167,168] The ligand field splitting Δ, was obtained from the $^2A_{2g} \leftarrow {}^2A_{1g}$ transition and was found to be 13558 cm^{-1}. This value is comparable to that obtained for low spin Co(**64**)$_2^{2+}$, (13500 cm^{-1}).[168]

The 493 nm band in the spectrum of [Co(**23**)$_2$](ClO$_4$)$_3$, Table 6.13., is assigned to the $^1T_{1g} \leftarrow {}^1A_{1g}$ transition. The shoulder at 374 nm could be assigned to the $^1T_{2g} \leftarrow {}^1A_{1g}$ transition. The higher ε value may be due to intensity "stealing" from the nearby charge transfer band at 356 nm. Using equations 6.1. and 6.2., and assuming C = 4B, the ligand field strength, Dq, was found to be 2190 cm^{-1} and B = 404 cm^{-1}. The nephelauxetic ratio β for the Co(III) complex ion was found to be 0.37 (B_0

= 1100 cm^{-1}).[121]

The electronic spectra of $Ni([10]\text{-}aneS_3)_2(ClO_4)_2$ shows transitions due to $^3T_{2g} \leftarrow {}^3A_{2g}$ (12500 cm^{-1}, ν_1) and $^3T_{1g}(F) \leftarrow {}^3A_{2g}$ (18867 cm^{-1}, ν_2). These transitions involve excitation of an electron from a t_{2g} to an e_g orbital, *e.g.*, $t_{2g}^6e_g^2 \rightarrow t_{2g}^5e_g^3$. The band due to $^3T_1(P) \leftarrow {}^3A_{2g}$ is obscured by a charge transfer band. The Racah parameter for the spin allowed transition, B_{35}, (the numeral subscripts are derived from Bethe quantum numbers, $\gamma_3 \equiv e_g$ and $\gamma_5 \equiv t_{2g}$),[169] has been calculated from:

$$B_{35} = \frac{(2\nu_1^2 + \nu_2^2 - 3\nu_1\nu_2)}{(15\nu_2 - 27\nu_1)} = 717 \text{ cm}^{-1} \qquad \text{--- 6.7.}$$

B for free ion[121] = 1038 cm^{-1} and nephelauxetic ratio β_{35} for the complex has been found to be 0.69. A weak shoulder at 11765 cm^{-1} is assigned to the $^1E_g \leftarrow {}^3A_{2g}$ transition (energy = 8B + 2C).[121] This transition involves a change in the spin quantum number within the e_g set $\{t_{2g}^6e_g^2(S=1) \rightarrow t_{2g}^6e_g^2(S=0)\}$. From this spin forbidden transition B_{33} was found to be 735 cm^{-1} and β_{33} = 0.71. The value of β_{33} (0.71) is similar to that obtained for the trithia analogs[168] and to the triaza complexes, $Ni(\mathbf{22})_2^{2+}$ (0.69) and $[Ni(\mathbf{62})_2]^{2+}$ (0.69), ([10]-aneN3 = **62**). However, β_{35} for the trithia complex $Ni(\mathbf{23})_2^{2+}$ (0.69) is significantly lower than triaza analog, $[Ni(\mathbf{62})_2]^{2+}$, (0.9, B_{35} = 937 cm^{-1}). This is attributed to the higher degree of covalency of the Ni-S bond in the trithia complexes compared to the Ni-N bond in the triaza complexes.

The uv-visible spectrum of $Pd([10]ane\text{-}S_3)_2^{2+}$ ion shows one broad peak at 598 nm assigned to a d-d transition and three charge transfer bands at 314 nm, 277 nm and 209 nm, Fig. 6.20. No other absorption bands were observed at lower energies.

Fig. 6.20. Electronic spectrum of $[Pd([10]\text{-}aneS_3)_2]^{2+}$ complex.

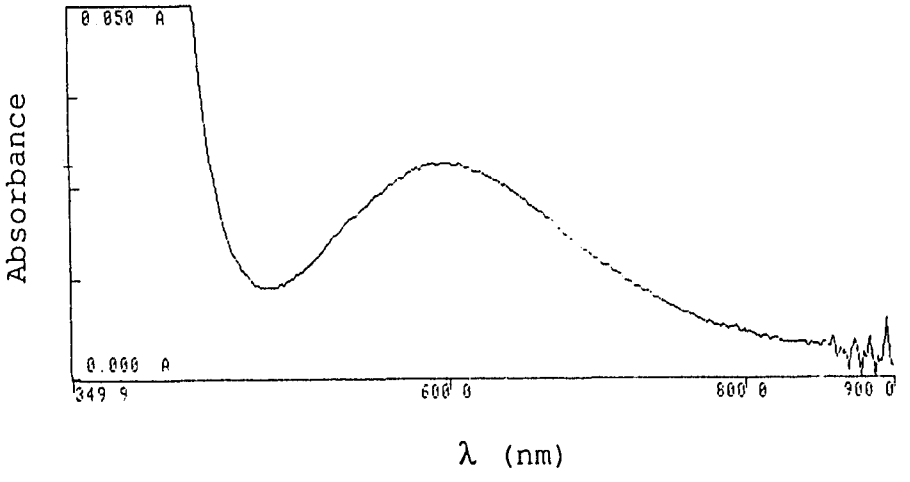

6.6. Correlation of the Co chemical shift with d-d electronic transitions:

There exists a linear relationship between the ^{59}Co chemical shift and the energy of the first optical transition in Co complexes.[170] The Ramsey theory[171] relates shielding to

optical spectroscopic data. According to this theory, the shielding constant for the Co nucleus can be given as

$$\sigma = \sigma_d + \sigma_p, \qquad \text{--- 6.8.}$$

where, σ_d is the diamagnetic contribution and σ_p is the paramagnetic contribution. For the Co nucleus in Co(III) complexes, variations of diamagnetic shielding from one complex to another are expected to be very small in comparison with variations of paramagnetic shielding. The ^{59}Co nmr chemical shifts can thus be described in terms of variations in paramagnetic shielding only. This arises from the distribution of electrons in the orbitals that are predominantly Co 3d orbitals and can be expressed as:

$$\sigma_p = (\mu_0/4\Pi)\,(4\mu_B^2)\langle r^{-3}\rangle_{3d}\langle 0|L^2|0\rangle/3\Delta_0 \qquad \text{--- 6.9.}$$

where, r is the radius of the octahedral d orbital and Δ_0 the splitting in the octahedral crystal field. By introducing an orbital reduction factor $k_{\sigma\pi}$ between the t_{2g} and e_g orbitals of the Co atom, to allow for covalency, the paramagnetic shielding term becomes

$$\sigma_p = -32\mu_B^2 k_{\sigma\pi}^2 \langle r^{-3}\rangle_{3d}/\Delta_0 \qquad \text{--- 6.10.}$$

where, μ_B is the Bohr magneton. Of the two spin-allowed excited states $^1T_{1g}(t_{2g}^5e_g^1)$ and $^1T_{2g}(t_{2g}^5e_g^1)$, only the former interacts with the ground state through the angular momentum operator. Hence, the significance of the Δ_0 splitting is that it measures the promotion energy ΔE from the ground state A_{1g} to the $^1T_{1g}$ excited state. As a consequence, the ^{59}Co magnetogyric ratios are directly related to the $^1T_{1g} \leftarrow {}^1A_{1g}$

electronic transition energies by

$$\gamma = \gamma_0(1-\sigma^d) + \gamma_0[B/\{\Delta E(^1T_{1g} \leftarrow {}^1A_{1g})\}] \qquad \text{--- 6.11.}$$

where, $B = 32\mu^2 \times k_{\sigma\pi}{}^2\langle r^{-3}\rangle_{3d}$.

Experimentally excellent correlations have been obtained between the ^{59}Co chemical shift and the $^1T_{1g} \leftarrow {}^1A_{1g}$ transition.[172,173] A typical correlation plot for Co complexes containing S ligating atoms is shown in Fig. 6.21. For the $Co([10]\text{-ane}S_3)_2{}^{3+}$ complex the $^1T_{1g} \leftarrow {}^1A_{1g}$ transition occurs at 480 nm. The value of the ^{59}Co magnetogyric ratio calculated from Fig. 6.21. is 10.146 MHz T^{-1}. This matches well with the

---

Fig. 6.21. Correlation between ^{59}Co magnetogyric ratios and $^1T_{1g} \leftarrow {}^1A_{1g}$ transition wavelength.[172]

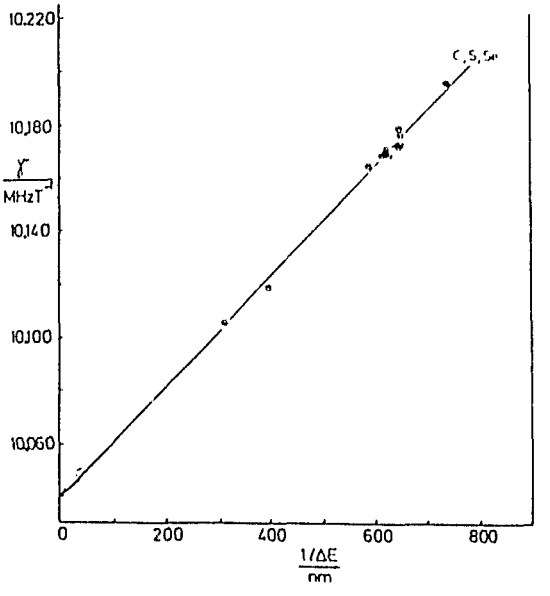

---

experimental value of 10.130 MHz T^{-1} obtained from the ^{59}Co nmr spectrum (Fig. 6.17.). Similarly, for the $Co([9]\text{-ane}S_3)_2{}^{3+}$ complex the $^1T_{1g} \leftarrow {}^1A_{1g}$ transition occurs at 476 nm. This corresponds to a value of 10.134 MHz T^{-1} for the magnetogyric

ratio of ^{59}Co and compares well with the experimental value of 10.121 MHz T^{-1}, (from Fig. 6.16.). Thus for a given set of ligating atoms, using the linear plot, the ^{59}Co chemical shift can be predicted if the energy of the first electronic transition is known for the complex and *vice versa*.

6.7. EPR spectra:

6.7.1. EPR spectrum of $[Fe([10]\text{-}aneS_3)_2](PF_6)_3$:

The esr spectrum of the $Fe([10]\text{-}aneS_3)_2^{3+}$ ion in CH_3CN (Fig. 6.22.) is characteristic of a distorted low spin d^5 (t_{2g}^5) Fe(III) ion. The low spin t_{2g}^5 configuration gives rise to a $^2T_{2g}$ ground state. Alternatively, this could be considered as a hole in the t_{2g} orbital. The t_{2g}^5 configuration is six fold degenerate since the "hole" can reside in any one of the six (including spin) states of the t_{2g} level. These energy levels are split by crystal field distortions and spin orbit coupling. If the crystal field distortion is axial ($O_h \rightarrow D_{4h}$) then the orbital degeneracy of the t_{2g} orbitals (d_{xy}, d_{yz}, d_{xz}) is lifted giving rise to one degenerate (d_{zx}, d_{yz}) and one non-degenerate (d_{xy}) level as shown below:

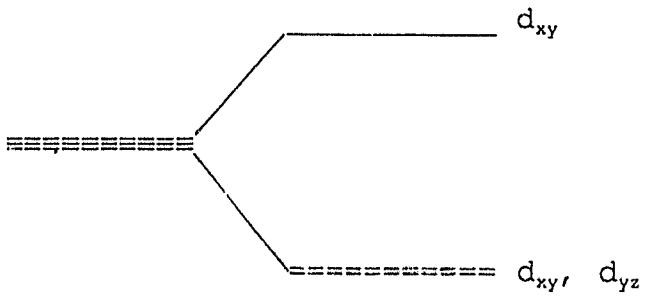

If the distortion is rhombic, then the orbital degeneracy is lifted completely as shown below:

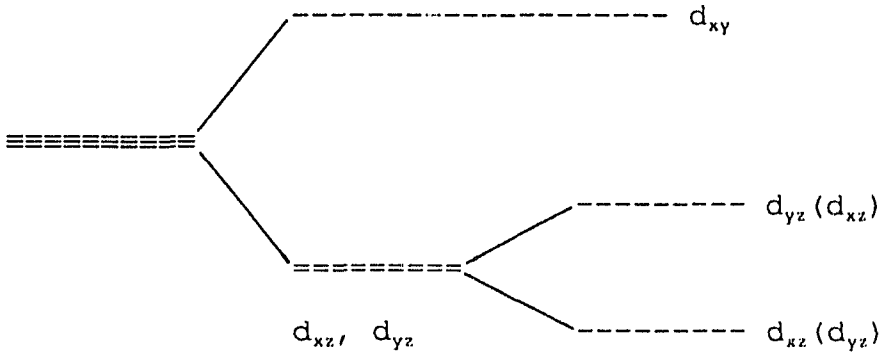

Fig. 6.22. ESR spectrum of $[Fe([10]\text{-ane}S_3)_2](PF_6)_3$ in CH_3CN.

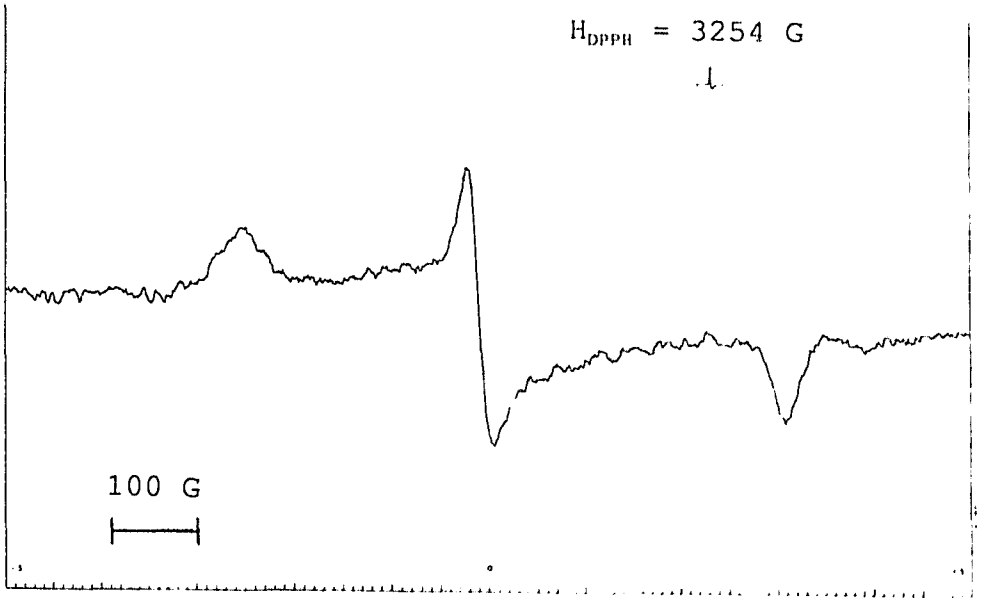

Thus the $^2T_{2g}$ ground state gives rise to three Kramer's doublets (spin degeneracy) and the lowest energy doublet can be described as:[174,175]

$$|+\rangle = A|1^+\rangle + (B/2^{1/2})(|2^-\rangle - |-2^-\rangle) + C|-1^+\rangle$$

$$|-\rangle = -A|-1^-\rangle + (B/2^{1/2})(|2^+\rangle - |-2^+\rangle) - C|1^-\rangle \quad \text{--- 6.12.}$$

with $A^2 + B^2 + C^2 = 1.$

In an orthorhombic symmetry the values of the coefficients A, B and C can be evaluated from the g_{xx}, g_{yy} and g_{zz} values.

$$A = (g_x + g_y - 2g_z)/4(g_x + g_y - g_z)^{1/2},$$

$$B = (g_x + g_y)/2(2(g_x + g_y - g_z))^{1/2},$$

$$C = (g_y - g_x)/4(g_x + g_y - g_z)^{1/2}. \quad \text{--- 6.13.}$$

The coefficients A, B and C can then be used to obtain the ordering of the energy levels originating from $^2T_{2g}$ ground state from the relationships:

$$\Delta/\lambda = [-A^2 + B^2 + C^2 + (AB + BC^2/A)/\sqrt{2}]/\sqrt{2}(-AB + BC^2/A) \quad \text{--6.14.}$$

$$R/\lambda = [2AC + \sqrt{2}BC]/(C^2 - A^2) \quad \text{--- 6.15.}$$

$$E/\lambda = 2/3(\Delta/\lambda) - (A/\sqrt{2}B), \quad \text{--- 6.16.}$$

where, λ is the spin-orbit coupling constant, R/λ is the rhombic distortion parameter and Δ/λ is the axial distortion parameter, E is the energy of the ground state Kramers doublet.

From the e.s.r. spectrum of the Fe(III) complex of **23** the g values were calculated, $g_{zz} = 1.956$, and $g_{xx} \neq g_{yy}$; $g_{xx} = 2.355$ and $g_{yy} = 2.164$. In order to obtain the correct combination of j values that satisfy the normalization condition:

$$A^2 + B^2 + C^2 = 1, \quad \text{--- 6.17.}$$

the values of g_x(2.355) and g_y(2.164) were substituted in the following equation:

$g_x^2 + g_y^2 + g_z^2 - g_xg_z - g_yg_z + g_xg_y - 4g_x - 4g_y + 4g_z = 0$ -- 6.18.

The value of g_z was calculated to be 1.939 and which is close to the g_z value of 1.956 obtained experimentally. This, therefore, means that the assumptions --- 'no-delocalization' and 'no excited state mixing'--- made are reasonable and eqns. 6.12. and 6.13. are valid. Six such orderings of g values are possible and the correct combination of g values that allow for $|\Delta/\lambda|$ to be maximum and R/λ to be positive was found to be: g_x = 2.355, g_y = 2.164 and g_z = 1.956. Substituting these values in equations 6.13., the ground state coefficients were found to be A = 0.0948, B = 1.000 and C = -0.0298. The ligand field distortion parameters were obtained from eqns. 6.14 and 6.15., Δ/λ = -8.839, and R/λ = 5.901, and from eqn. 6.16., the energy of the ground state doublet E/λ = -5.960. A rough estimate of λ can be made from a plot of μ_{eff} *vs* kT/λ for the axial distortion parameter of Δ/λ = -10, yielding a value for λ of -150 cm^{-1}, where μ_{eff} is assumed to be equal to that of $K_3Fe(CN)_6$, 1.90 B.M. at 80 K, and k is unity.[163] Thus the ligand field distortion parameters are found to be, Δ = 1326 cm^{-1}, R = -885 cm^{-1}, where,

$$\Delta = E(d_{xy}) - [\{E(d_{xz}) + E(d_{yz})\}/2] \quad \text{--- 6.19.}$$

and $$R = E(d_{xz}) - E(d_{yz}) \quad \text{--- 6.20.}$$

The complete energy pattern of the ground $^2T_{2g}$ levels can then be obtained,

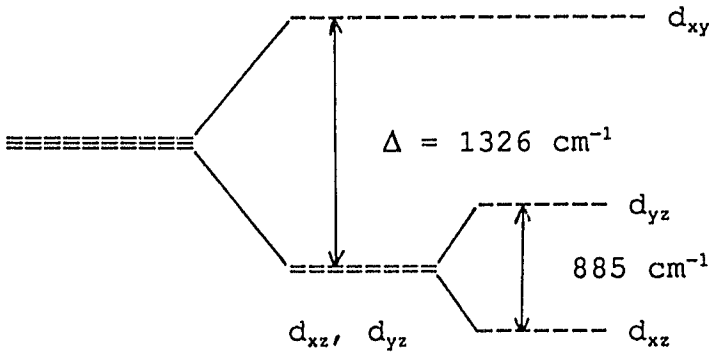

Chemical oxidation of $[Fe(\mathbf{23})_2]^{2+}$ complex ion with PbO_2 in concentrated (60%) $HClO_4$ yields the green $[Fe(\mathbf{23})_2]^{3+}$ ion which is esr active (Fig. 6.22a.). The spectrum is anisotropic with g_{xx} = 2.341, g_{yy} = 2.163 and g_{zz} = 1.960. Additional lines are also seen due to hyperfine interaction with the protons of the ligand in the complex. The g_{xx} feature is further split into three lines (g = 2.476, 2.341, 2.225) with the hyperfine coupling constant, A_{xx} = 150 G. The g_{zz} feature is also split into three hyperfine components (g = 2.054, 1.960, 1.867) with A_{zz} = 163 G. The line at g = 1.917 may belong to the central g_{yy} feature. Interaction of the unpaired electron in the low spin $[Fe(\mathbf{23})_2]^{3+}$ ion (t_{2g}^5) with two protons (I = 1/2), of the ligand molecule, give rise to the three-line patterns observed in both the g_{xx} and g_{zz} features.

The e.s.r. spectrum of $[Fe([9]\text{-ane}S_3)_2]^{3+}$ (Fig. 6.23) is axially elongated with $g_{xx} = g_{yy} = g_{\perp}$ = 2.354 and $g_{zz} = g_{\parallel}$ = 1.851. Substituting these values in eqn. 6.13., the coefficients of the ground state doublet A, B and C were determined: A = 0.0948, B = 1.000 and C = -0.0298. The ligand

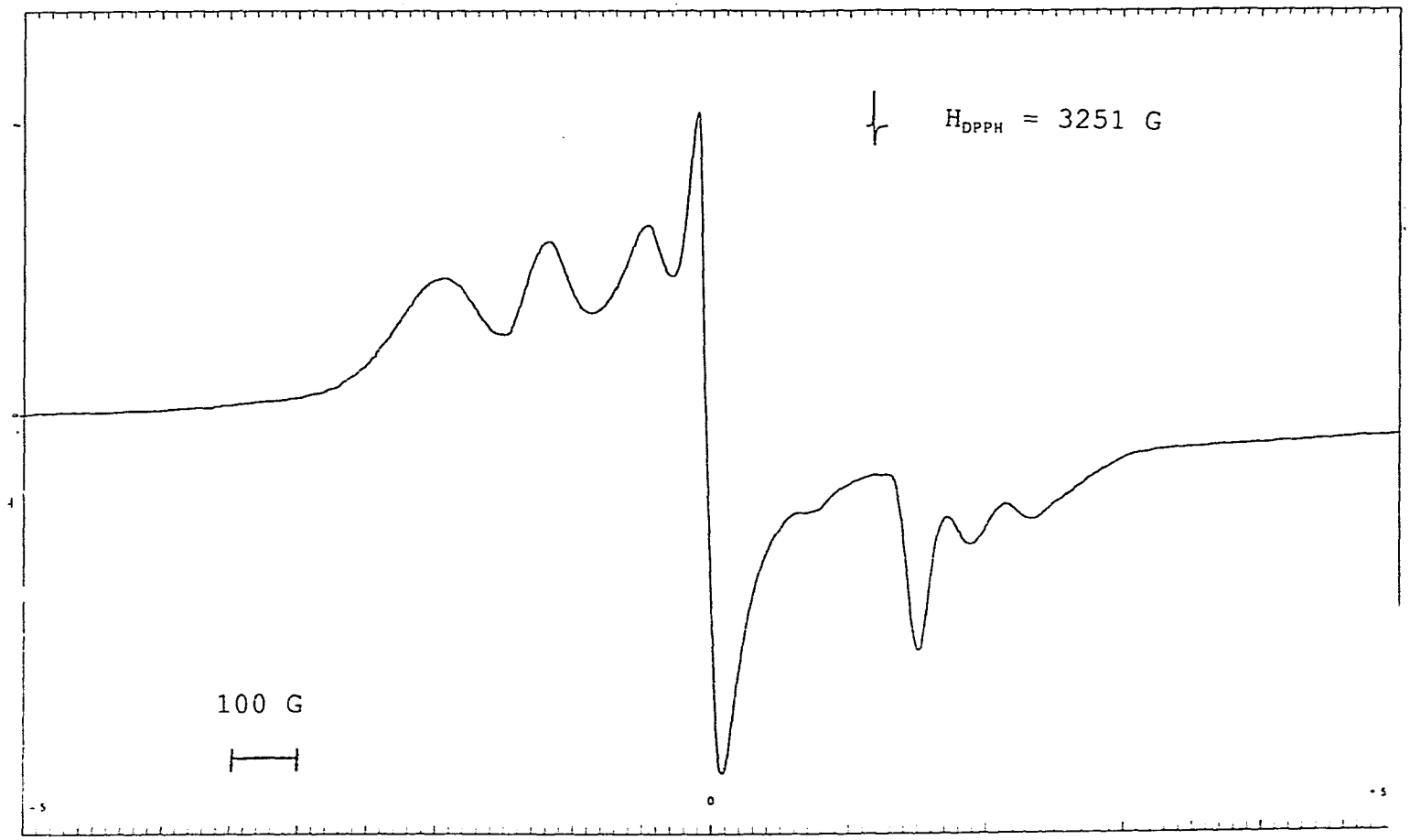

Fig. 6.22a. ESR spectrum of $[Fe([10]\text{-}aneS_3)_2]^{3+}$ ion in 60% $HClO_4$.

Fig. 6.23. EPR spectrum of $[Fe([9]\text{-}aneS_3)_2]^{3+}$ ion in CH_3CN.

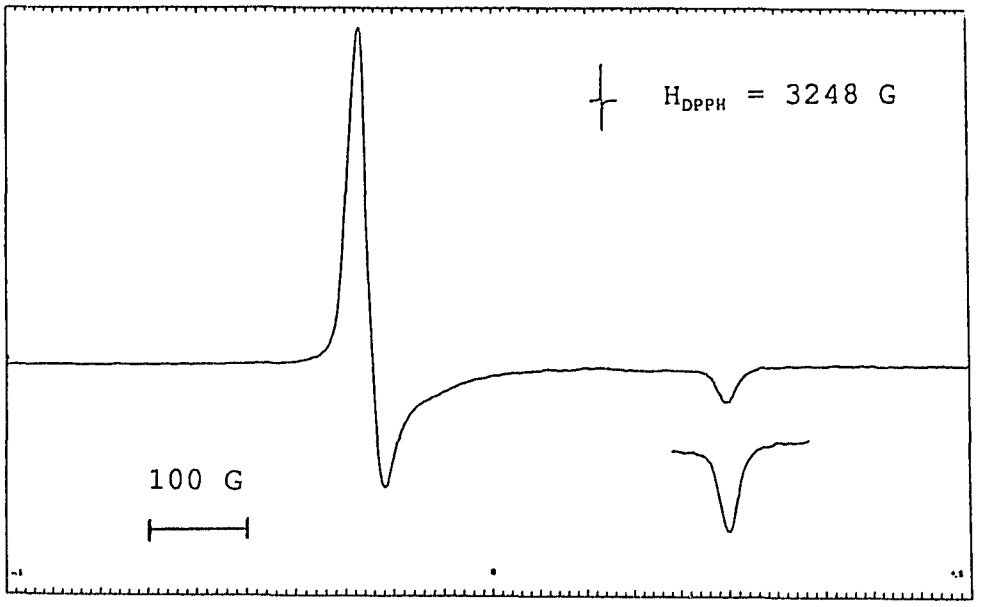

field distortion parameters were determined from eqn. 6.14.; $R/\lambda = 0$, and $\Delta/\lambda = -5.074$; and $E/\lambda = -3.490$ Using a value of $\mu_{eff} = 2.46$,[161] an appropriate value for the spin-orbit coupling constant, λ, was obtained from a plot of μ_{eff} *vs* kT/λ,[163] for $\Delta/\lambda = -5.074$ yielding $\lambda = -391$ cm^{-1} and $\Delta = 1984$ cm^{-1}. An energy separation of $\Delta \geq 700$ cm^{-1} was suggested by Küppers *et al*[161] based on Mössbauer studies of the $[Fe([9]\text{-}aneS_3)_2](PF_6)_3$ complex. Thus the energy pattern of the ground state was obtained for the $Fe([9]\text{-}aneS_3)_2^{3+}$ ion:

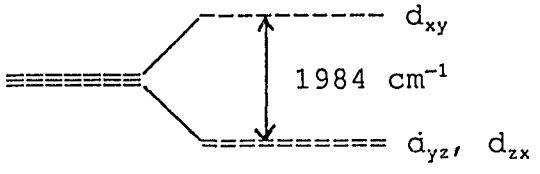

6.7.2. EPR spectrum of $[Co([10]\text{-}aneS_3)_2](ClO_4)_2$:

The e.s.r. spectrum of $Co([10]\text{-}aneS_3)_2^{2+}$, **53**, in CH_3CN at 77 K is shown in Fig. 6.24. The spectrum is characteristic of low spin d^7 ion in a distorted octahedral geometry. The ground state of low spin Co(II) is ^2E_g which is unstable towards Jahn-Teller distortions. Axial compression would cause the unpaired electron to be in the $d_{x^2-y^2}$ orbital and axial elongation, in the d_{z^2} orbital. The symmetry may be further lowered due to the asymmetry of the ten-membered ring. The crystal structure of ion **53** shows three unequal Co-S bond lengths: 2.257(3), 2.320(3) and 2.395(3) Å. The unique bond length of 2.395(3) Å (greater than the calculated sum of

---

Fig. 6.24. EPR spectrum of $[Co([10]\text{-}aneS_3)_2](ClO_4)_2$ in CH_3CN at 77 K.

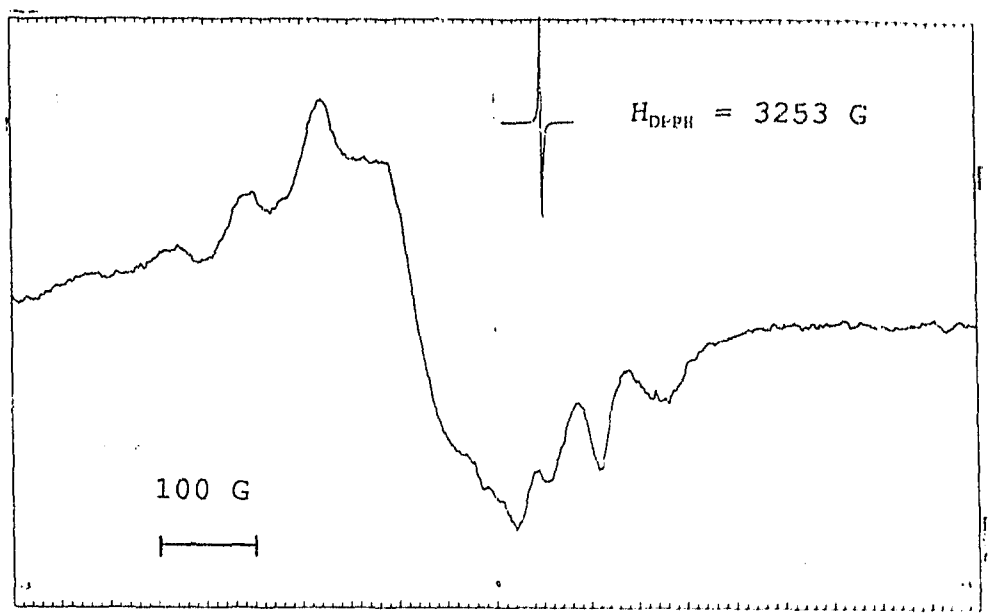

covalent radii of 2.360 Å) suggests that the complex is essentially axially elongated and equatorially compressed. However, the equatorial bond lengths are unequal giving rise to an overall rhombic distortion in the complex. Due to the intense hyperfine structure (^{59}Co, I = 7/2) the g- anisotropy in the $g_\perp$ feature of the esr spectrum of the frozen sample, (Fig. 6.24) was not discernible. Thus, $g_\parallel$ = 2.001 and $g_\perp$ = 2.086. The Co([18]-aneS_6)$^{2+}$ complex cation is axially elongated with an axial Co-S bond lengths of 2.251(1) and 2.292(1) Å.[157] The esr spectrum is axial with $g_\parallel$ ~ 2 and $g_\perp$ = 2.09.[157] The variable EPR solution and powder spectra of the [Co(**64**)$_2$](ClO$_4$)$_2$ are characteristic of a low spin d_z^2 ground state,[168,176] with an axially elongated spectrum at 4.2 K. As the temperature is raised, one of the $g_\perp$ components and the $g_\parallel$ signal approach each other. The Co-S bond lengths participate in a dynamically averaged process at higher temperatures. The crystal structure of the [Co(**64**)$_2$](BF$_4$)$_2$.2CH$_3$NO$_2$ is axially compressed with an axial Co-S bond length of 2.240(7) Å. The axially elongated solution spectrum and the axially compressed solid state structure is, therefore, indicative of a "planar dynamic" effect.[168] The room temperature esr spectrum of the Co(II) complex ion **53**, (Fig. 6.25.), in the present study, shows eight lines due to hyperfine interaction with ^{59}Co nucleus I = 7/2, A = 40 gauss and g_{av} = 2.083.

Fig. 6.25. ESR spectrum of $[Co(\mathbf{53})_2]^{2+}$ ion at room temperature.

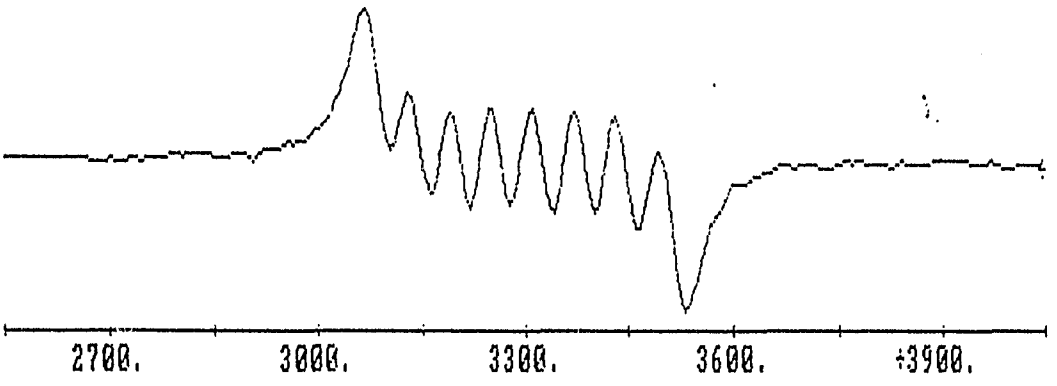

Specifics: CO10S3CL04
: CH3CN
:

Operator: CS
Npts: 1024.
Centerfield: 3300.00
Gain: 5.00E4
Mod.amp.(G): .50
Mod.frq.(kHz): 100.00

Date: 05/08/90
Nscans: 3.
Sweepwidth: 1500.00
Tcon(msec): 1000.00
Mwv.frq.(GHz): 9.6209
Mwv.pwr.(mW): 150.00

Scan time(sec): 200.
Temp.(K) 298.00
Phase(deg): 10.50
ymin: .75
ymax: 76.95

6.8. Redox studies:

6.8.1. Chemical oxidation:

Oxidation of $Ni([10]\text{-}aneS_3)_2^{2+}$ cation, **55**, in CH_3CN using NO^+ gives a yellow-orange Ni(III) species, frozen solutions of which show an esr spectrum (Fig. 6.26.) with g_{xx} = 2.089, g_{yy} = 2.040, and g_{zz} = 2.021, characteristic of a low spin Ni(III) d^7 ion in a distorted octahedral environment. Similar spectra are obtained in $HClO_4$ using PbO_2 (Fig. 6.27.), $Co(H_2O)_6^{3+}$ (Fig. 6.28.) or $Fe([9]\text{-}aneS_3)_2^{3+}$ as an oxidant. The sequence g_{xx}, g_{yy} > g_{zz} > g_e suggests that the unpaired electron is in the d_z^2 orbital ($^2A_{1g}$ ground state). The esr spectrum is characteristic of a rhombic distortion in the Ni(III) complex, consistent with the Jahn-Teller splitting of the ^2E_g state and the asymmetry of the ten- membered ring.

The e.s.r. spectrum of $[Ni([9]\text{-}aneS_3)_2]^{3+}$ ion obtained by the oxidation of the corresponding Ni(II) complex using NO^+ in CH_3CN or Co^{3+} in aqueous solutions is anisotropic with g_{xx} = 2.074, g_{yy} = 2.053 and g_{zz} = 2.015, Fig. 6.29. From the g values, it can be deduced that the oxidation is metal centered and the unpaired electron is in the d_z^2 orbital similar to that in $[Ni([10]\text{-}aneS_3)_2]^{3+}$ ion. Similar e.s.r. spectra have been reported for $[Ni(\mathbf{22})_2]^{3+}$ ion.[152]

The yellow-orange $[Ni([10]\text{-}aneS_3)_2]^{3+}$ ion is stable in 1 M $HClO_4$ for ~3 mins, in concentrated (60%) $HClO_4$ at room temperature for ~20 mins, and at lower temperatures (5 °C) for about 18h. The uv-visible spectrum (Table 6.13.) shows three

Figs. 6.26. ESR spectrum of the oxidation product of $[Ni(\mathbf{23})_2]^{2+}$ ion with NO^+ in CH_3CN at 77 K.

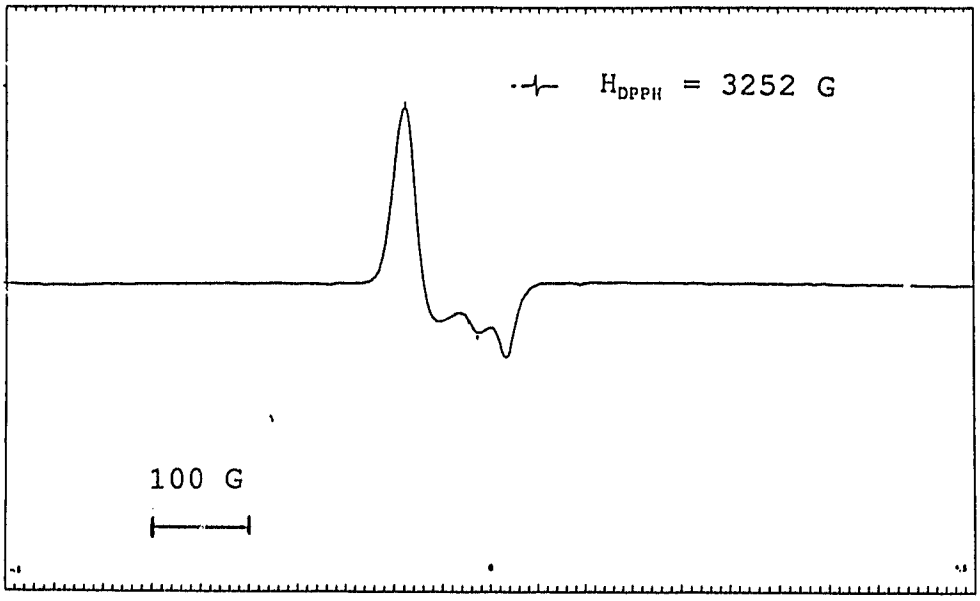

Fig. 6.27. ESR spectrum of the oxidation product of $[Ni(\mathbf{23})_2]^{2+}$ ion with PbO_2 in $HClO_4$ at 77 K.

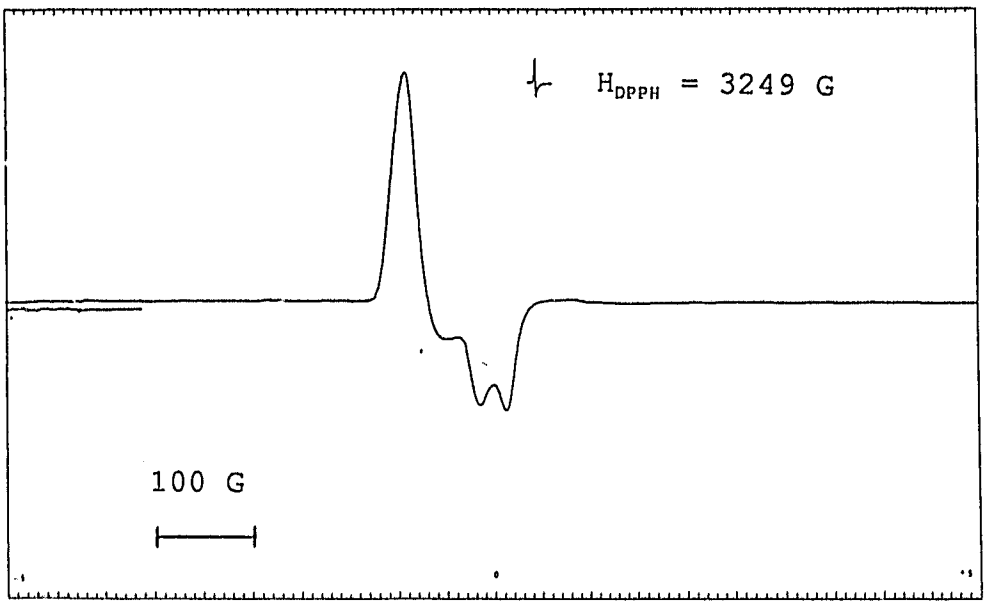

Fig. 6.28. ESR spectrum of the oxidation product of $[Ni(\mathbf{23})_2]^{2+}$ ion with $[Co(H_2O)_6]^{3+}$ ion at 77 K.

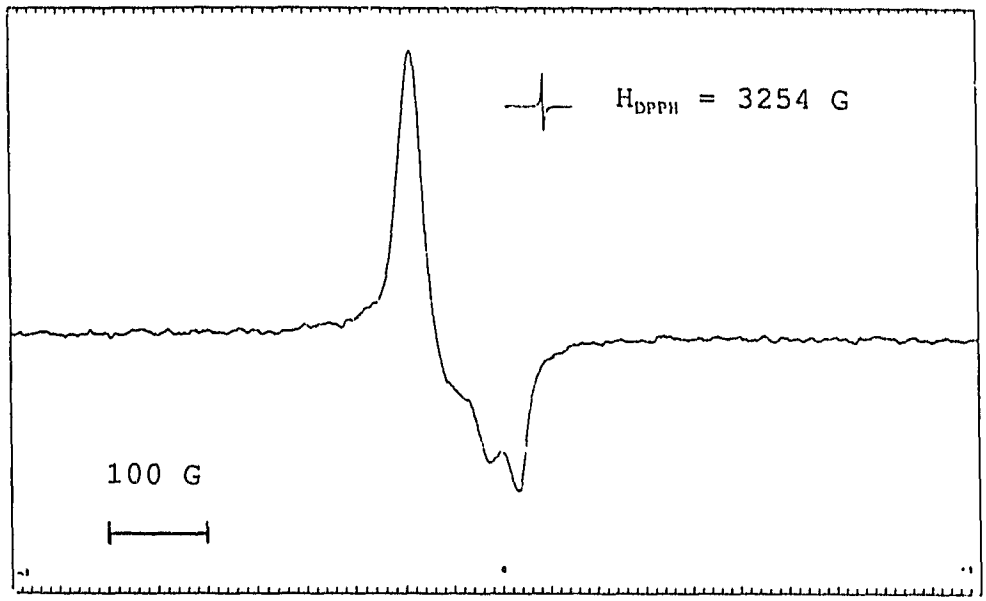

Fig. 6.29. ESR spectrum of the oxidation product of $[Ni(\mathbf{64})_2]^{2+}$ ion with NO^+ in CH_3CN at 77 K.

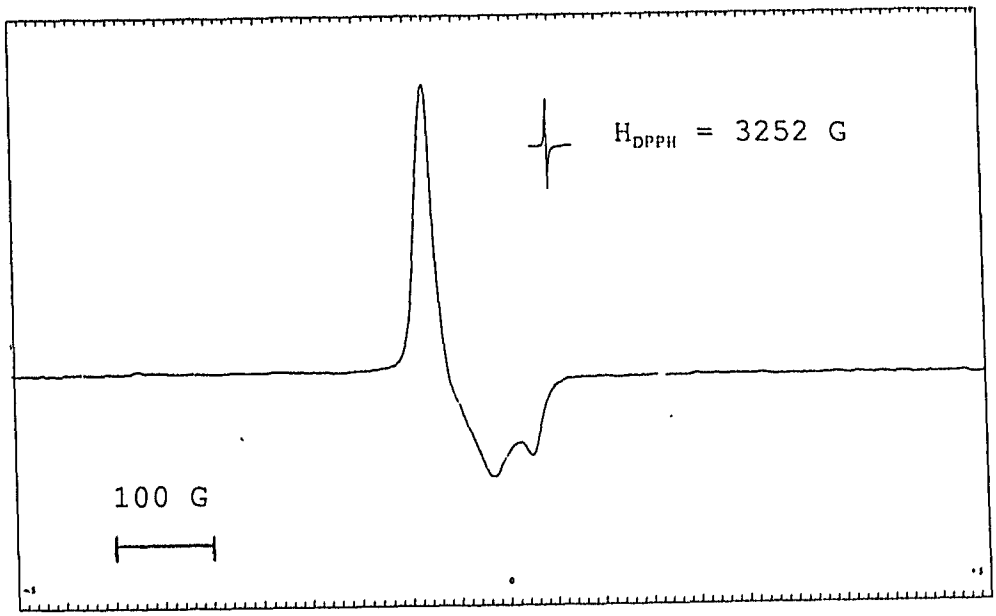

bands at 567 nm, 411 nm, 346 nm and 306 nm and are tentatively assigned to the transitions $^2{}_aT_{1g} \leftarrow {}^2A_{1g}$, $^2{}_aT_{2g} \leftarrow {}^2A_{1g}$, $^2{}_bT_{1g} \leftarrow {}^2A_{1g}$ and $^2{}_bT_{2g} \leftarrow {}^2A_{1g}$ respectively. The 10Dq value was found to be 17921 cm^{-1} by comparison with similar complexes.[134,167]

$Fe([10]aneS_3)_2^{3+}$ cation is stable indefinitely in 60% $HClO_4$ at room temperature and is stable for about 2 h in 1 M $HClO_4$. Use of concentrated $HClO_4$ in stabilising higher oxidation states is well documented. Recently,[124] the structure of $Fe([9]\text{-}aneS_3)_2^{3+}$ cation has been obtained and it was found to be stable only in solutions of $HClO_4$.

The esr spectrum of frozen solutions (77 K) of the $Pd([10]\text{-}aneS_3)_2^{3+}$ cation (obtained by oxidation of compound **56** with NO^+ in CH_3CN) is characteristic of a tetragonally elongated octahedral complex, $g_\parallel = 2.005$ and $g_\perp = 2.042$, (Fig. 6.30.). The $g_\parallel$ feature shows nuclear hyperfine interaction due to 33% abundant ^{105}Pd nuclei (I = 5/2). The hyperfine interaction in the $g_\perp$ feature is just discernible ($A_\perp$ = 20 G, $A_\parallel$ ~5 G). The orange Pd^{3+} cation can also be generated in $HClO_4$ solutions, frozen solutions of which show similar ESR characteristics. These g values compare well with those obtained for the corresponding $Pd([9]\text{-}aneS_3)_2^{3+}$ and $Pd([9]\text{-}aneN_3)_2^{3+}$ species.[92,96] The axial S atoms in the $Pd([10]\text{-}aneS_3)_2^{2+}$ are suitably disposed to allow octahedral stereochemistry around the d^7 metal ion upon oxidation. The unpaired electron occupies the d_{z^2} orbital. This is consistent with the EPR spectra of other Pd(III) species.[136,177]

Fig. 6.30. ESR spectra of $[Pd([10]\text{-}aneS_3)_2]^{3+}$ cation obtained by oxidation of the corresponding Pd(II) complex cation with NO^+ in CH_3CN at 77 K.

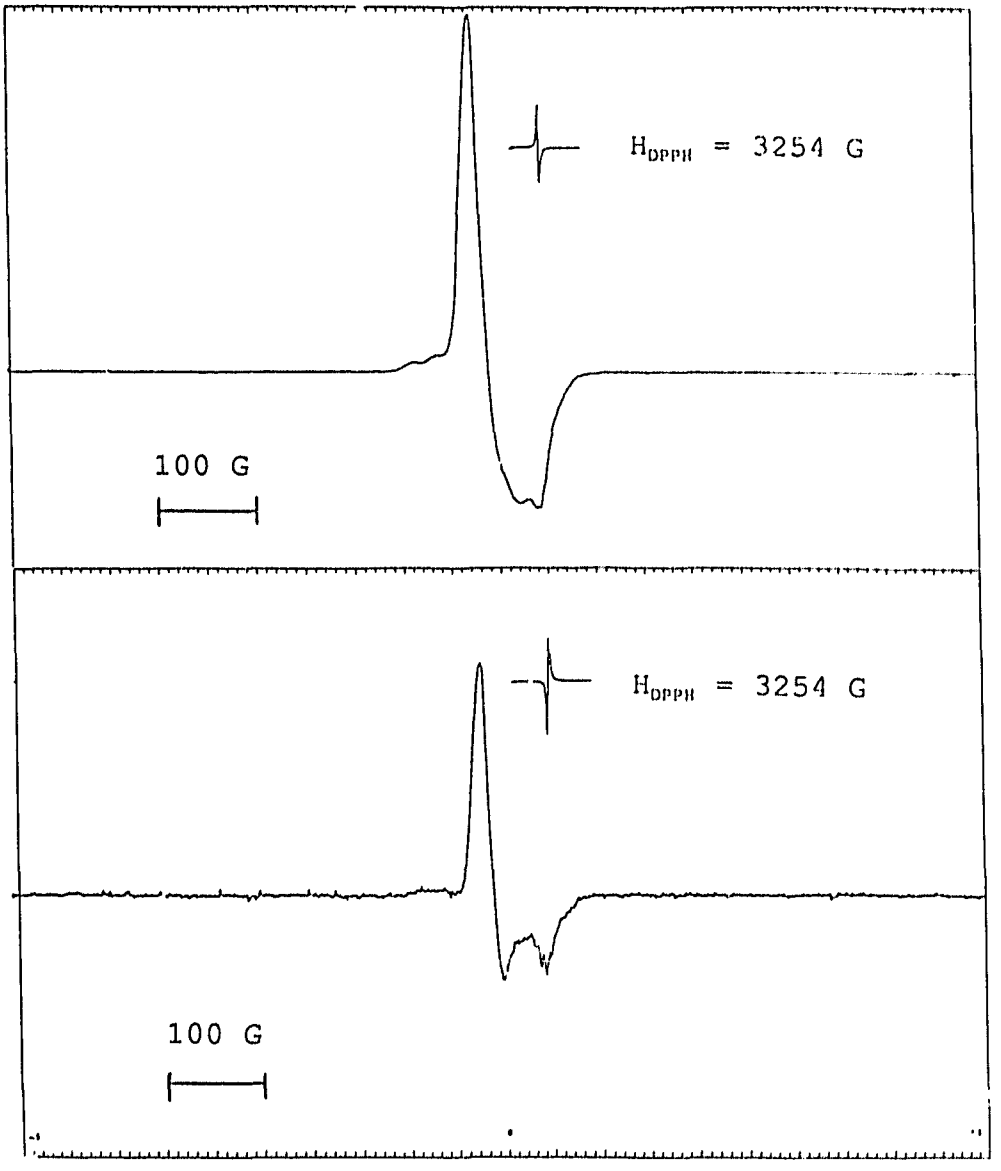

6.8.2. Chemical reduction:

Reduction of $Ni([9]\text{-}aneS_3)_2(ClO_4)_2$ electrochemically or chemically using $NaBH_4$ in acetonitrile under an inert atmosphere yielded a pale yellow Ni(I) species. Frozen solutions (77 K) of this species yielded an esr spectrum (Fig. 6.31.), with a near isotropic g value of 2.133, since the $g_\parallel$ and $g_\perp$ features are not fully resolved. Hyperfine interaction with one N atom (I = 1, 3 lines) from the CH_3CN is seen on the low field component ($g_\parallel$ = 2.198), with a coupling constant of ~40 G.

Mixed coordination environments have been known to stabilize Ni(I) species against disproportionation and monomeric Ni(I) species have been isolated.[105,178] Addition of

---

Fig. 6.31. ESR spectrum of Ni(I) complex cation obtained by reduction of $[Ni(\mathbf{64})_2]^{2+}$ with $NaBH_4$ in CH_3CN at 77 K.

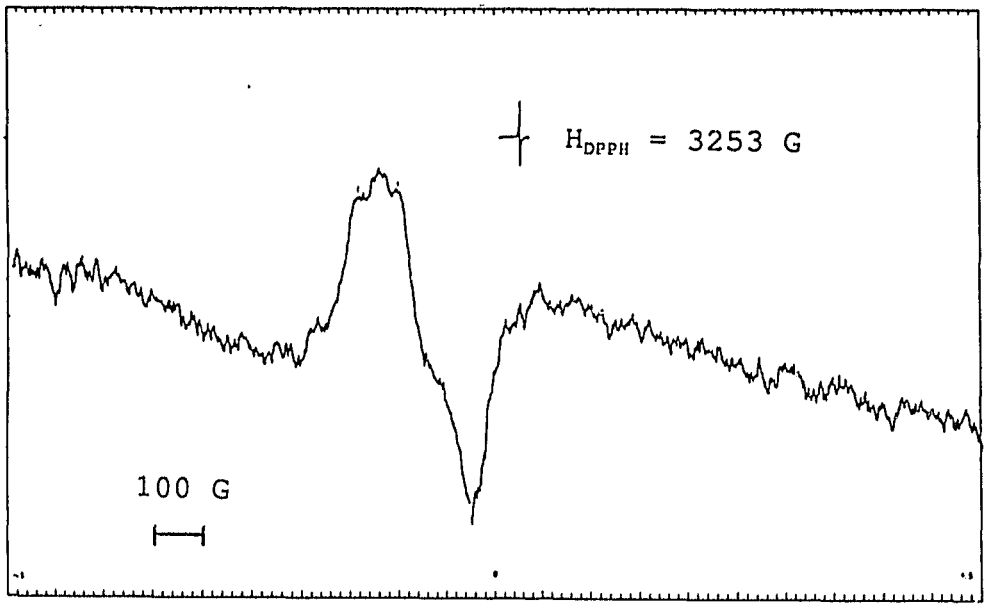

PPh_3 produced a deep yellow species which is also esr active with a different g value of 2.162 (Fig. 6.32.). Hyperfine interaction is now seen on the high field component (g = 2.030) and four lines are discernible due to the coupling of one N atom (I = 1) from the CH_3CN solvent and one P atom (I = 1/2) from the PPh_3 molecule. The coupling constants were found to be ~40 G and ~60 G respectively. The triplet due to N atom (I = 1) is further split by the P atom (I = 1/2). Although a six-line pattern is expected, because of possible overlap due to the similarity of the coupling constants of N and P atoms a four-line pattern is exhibited, Fig. 6.32. The tetrahedral preference of the Ni(I) ion and the octahedral preference of the two trithia ligands may result in the displacement of the S atom from the metal. It is possible that PPh_3 may be substituted on to the Ni(I) centre alongwith one N atom from the solvent together with resulting in a tetrahedral geometry.

Reduction of $[Ni([10]\text{-ane}S_3)_2]^{2+}$ in CH_3OH or CH_3CN with $NaBH_4$ yields an esr active Ni(I) species. The esr spectrum in CH_3OH is anisotropic with g_{xx} = 2.015, g_{yy} = 2.116, and g_{zz} = 2.206, Fig. 6.33., and is characteristic of a Ni(I) d^9 complex ion. The Ni(I) species so formed is stable in the absence of oxygen. The geometry around the Ni(I) ion may be an elongated octahedron with the unpaired electron in the $d_{x^2-y^2}$ orbital. The spectrum is consistent with the presence of $[Ni(23)_2]^+$ in solution. In the presence of air the pale yellow solution is

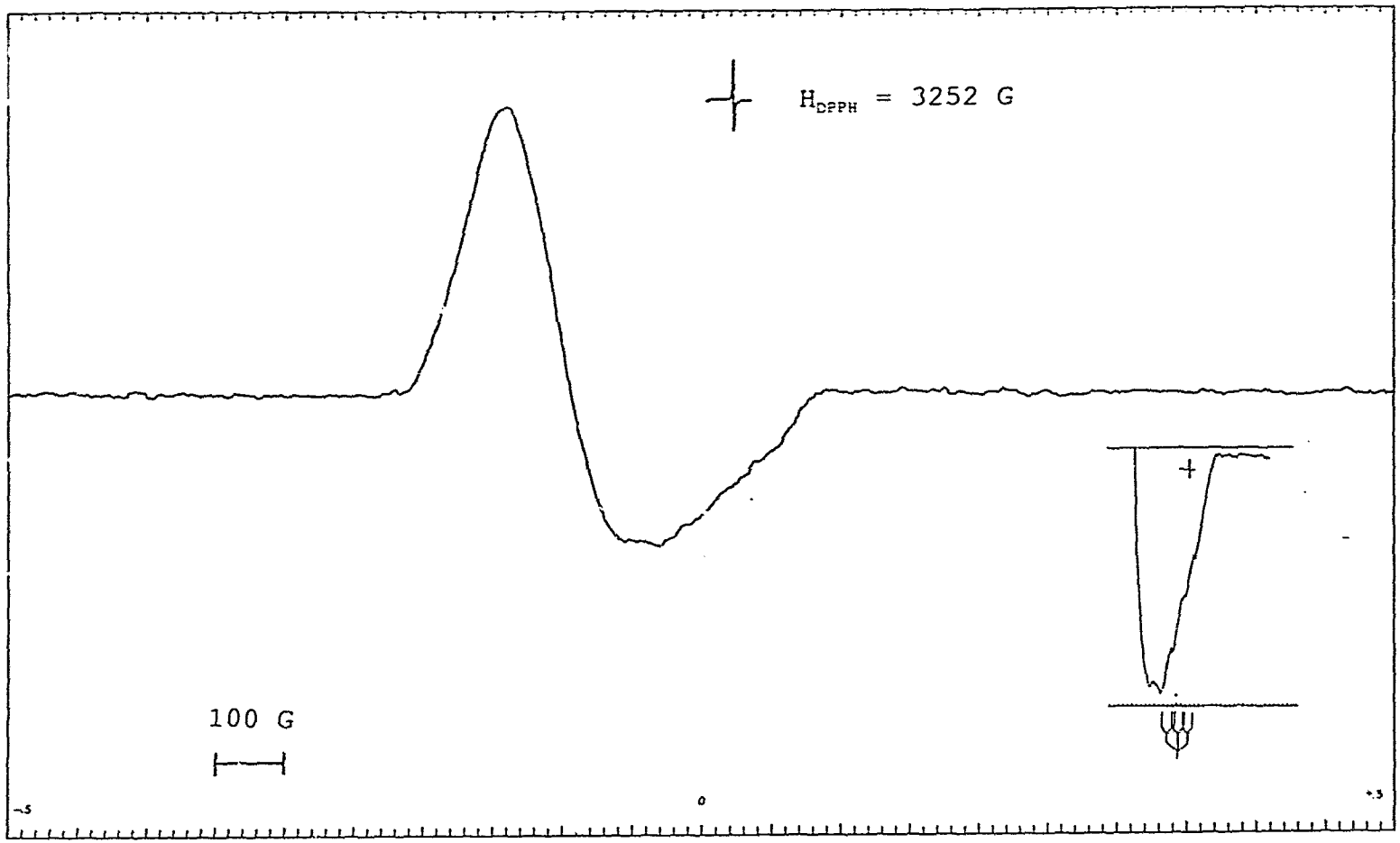

Fig. 6.32. ESR spectrum of Ni(I) complex cation of 64 containing PPh_3 at 77 K.

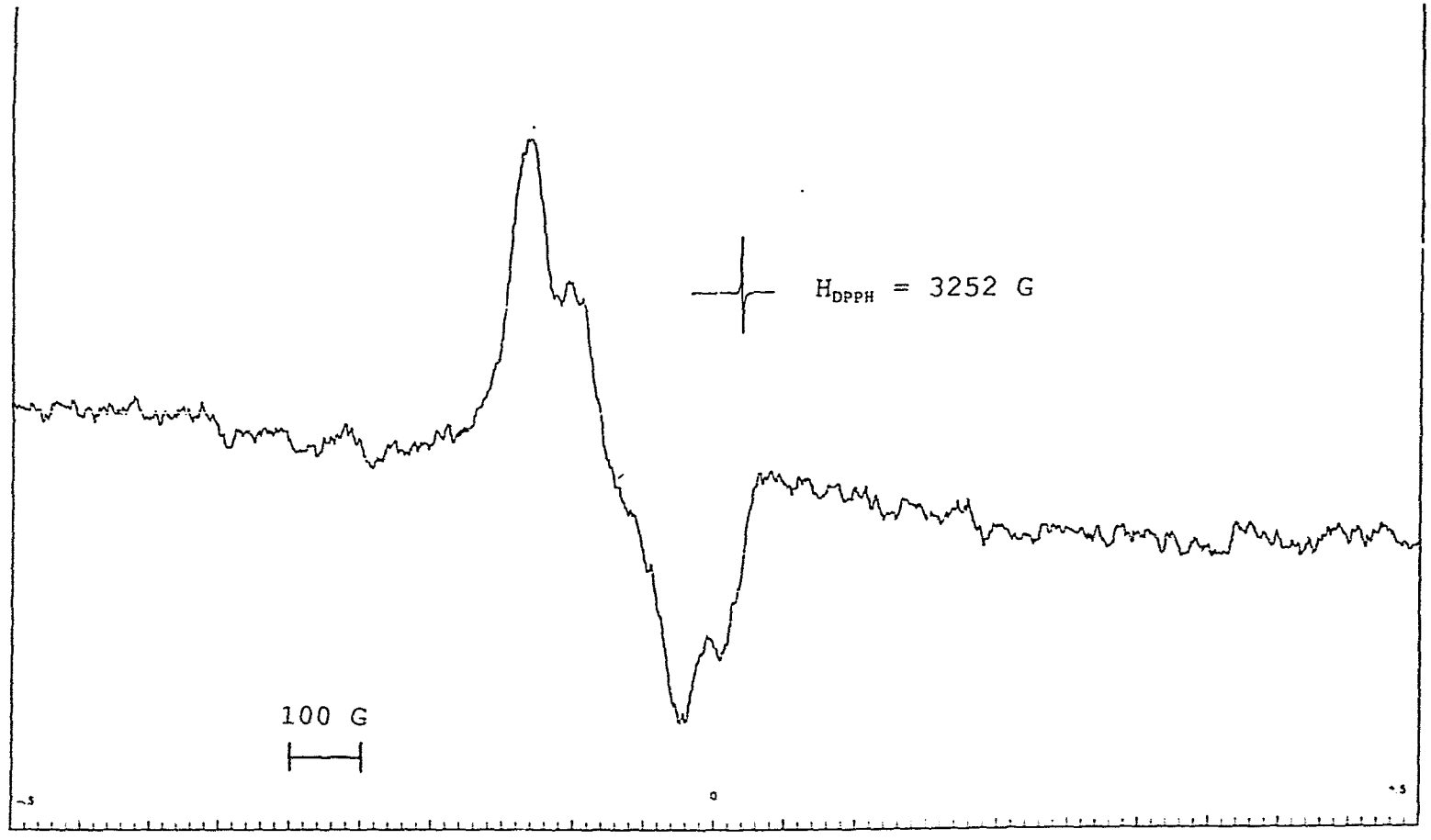

Fig. 6.33. ESR spectrum of Ni(I) complex cation obtained by reduction of $[Ni(\mathbf{23})_2]^{2+}$ with $NaBH_4$ in CH_3OH at 77 K.

decolorised and upon reduction with $NaBH_4$ only a very small amount of the Ni(I) complex ion is formed again. Addition of PPh_3 to CH_3CN solutions of the Ni(II) complex of **23**, containing $NaBH_4$, yielded a deep yellow solution which was esr active, Fig. 6.34., but had a different spectrum. The spectrum was intense and broad and near isotropic with a g value of 2.155. Four hyperfine lines were seen in the high field component (g = 2.008) analogous to the Ni(I) species containing **64**, Fig. 6.32. The triplet arising from the N atom (I = 1) of the solvent molecule (CH_3CN) is further split by the P atom (I = 1/2) in the PPh_3 molecule exhibiting a four-line pattern for reasons cited earlier. The similarity of the esr spectrum, Fig. 6.34. with that of Fig. 6.32. (comparable g values), suggests that the ligating atoms and the geometry of the Ni(I) species is the same in both the cases. This is consistent with a tetrahedral Ni(I) species stabilised with one S atom from each of the ligand [10]-aneS_3, one P atom from the PPh_3 molecule and one N atom from the solvent.

The formation of a detectable Ni(I) complex ion reflects the ability of the soft S atoms in stabilizing the soft Ni(I) ion in Pearson's sense.[20] Presence of a mixed coordination environment containing softer P atoms also helps in stabilizing the Ni(I) ion. The S donor atoms in thioether ligands can thus act as π- acceptors using empty d- orbitals on the S atoms thereby stabilizing low oxidation states as is confirmed by the formation of the esr active Ni(I) complexes.

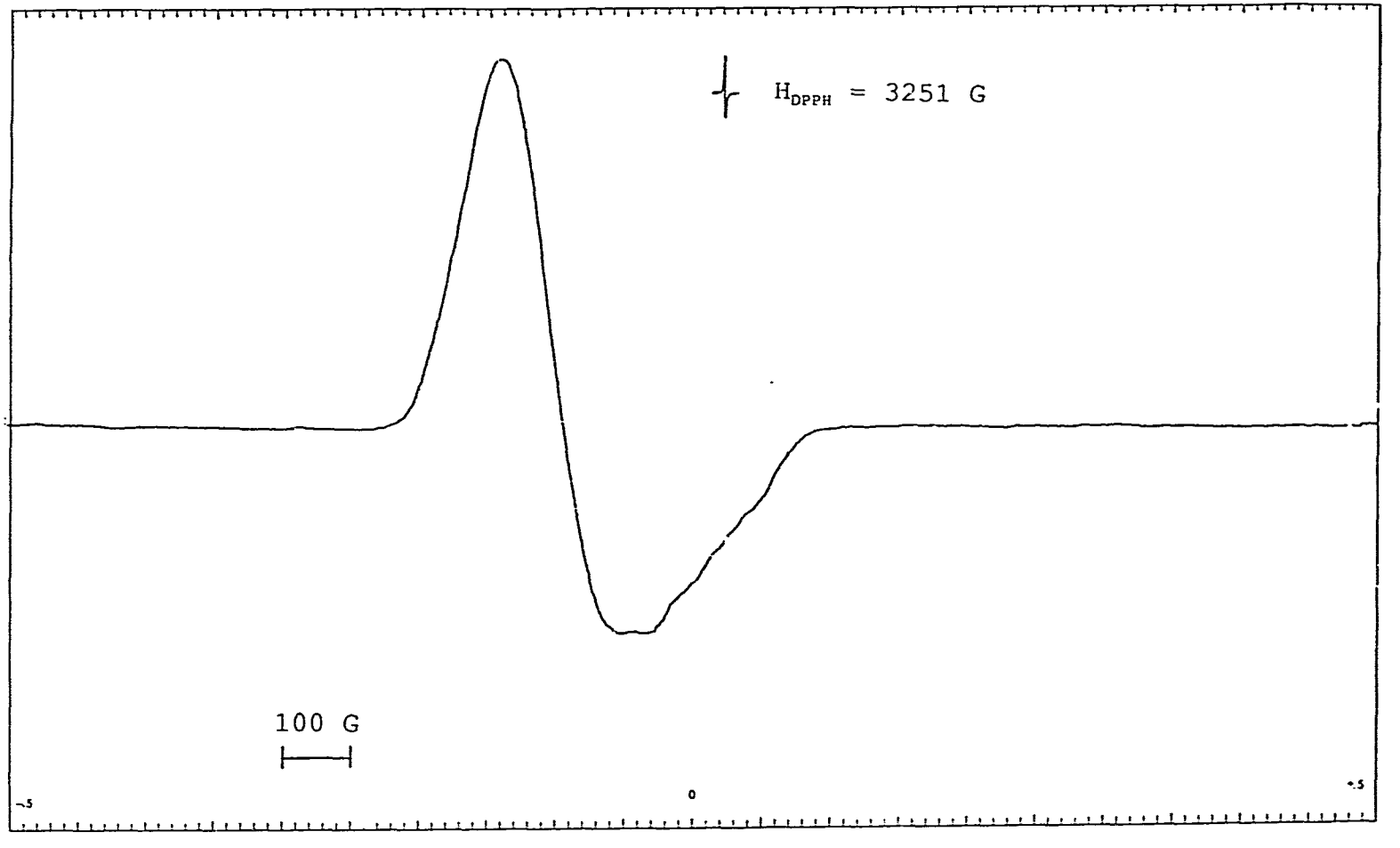

Fig. 6.34. ESR spectrum of Ni(I) cation of **23** in CH_3CN with PPh_3 at 77 K.

6.8.3. Electrochemistry:

Electrochemical data of Fe(II), Co(II), Ni(II) and Pd(II) bis complexes of **23**, together with related crown thioether complexes are summarised in Table 6.15. In non-aqueous solutions, Pt wires were used as working electrodes and a Ag wire was used as a reference electrode. Ferrocene was used as an external standard and the $E_{1/2}$ value for the Fc^+/Fc couple *vs* the Ag wire was found to be between 0.30 and 0.40 V. The external standard was run before and after each sample. All potentials are reported against the Fc^+/Fc standard couple ($E_{1/2}$ of Fc^+/Fc *vs* NHE = 0.40 V) and were found to be internally consistent. A solution of 0.1 M NEt_4BF_4 was used as the supporting electrolyte. The $E_{1/2}$ values were cross checked in some cases using a Ag^+/Ag (0.1 M $AgNO_3$) couple as the reference electrode.

In aqueous solutions a saturated calomel electrode, SCE, ($E_{1/2}$ = 0.242 V *vs* NHE) or a Ag/AgCl electrode ($E_{1/2}$ = 0.20 V *vs* NHE) were used. A solution of 1.0 M $NaNO_3$ or 1 M CF_3SO_3H was used as the supporting electrolyte.

The cyclic voltammogram of $[Fe(\mathbf{23})_2]^{2+}$ complex ion in CH_3CN shows a reversible wave at 0.92 V *vs* Fc^+/Fc corresponding to the $[Fe(\mathbf{23})_2]^{3+/2+}$ couple, (metal-centred oxidation), Fig. 6.35a. In 1 M CF_3SO_3H the $E_{1/2}$ value was found to be 1.1 V *vs* SCE. This oxidation can be carried out chemically in 1 M $HClO_4$ or 1 M CF_3SO_3H using PbO_2 as an oxidant or in CH_3CN using $NOBF_4$ as an oxidant to yield a green Fe^{3+} complex cation. If

sodium persulfate is used as an oxidant an orange product is obtained. From analogy with the Fe complexes of [9]-aneS_3,[161]

Table 6.15.

Redox potentials of the complexes.

Complex	$E_{1/2}$ (*vs* Fc^+/Fc) (V)	ΔE (mV)	$E_{1/2}$ (*vs* NHE) (V)
$[Fe(\mathbf{23})_2]^{3+/2+}$	0.92	71	1.32
$[Fe(\mathbf{23})_2]^{3+/2+}$	1.10[a]	83	1.34
$[Co(\mathbf{23})_2]^{3+/2+}$	0.01	94	0.41
$[Co(\mathbf{23})_2]^{2+/+}$	-0.85	58	-0.45
$[Co(\mathbf{23})_2]^{3+/2+}$	0.23[b]	112	0.43
$[Co(\mathbf{64})_2]^{3+/2+}$	-	-	0.42[d]
$[Co(\mathbf{22})_2]^{3+/2+}$	-	-	-0.41[e]
$[Co(\mathbf{23})_2]^{2+/+}$	-0.65[b]	118	-0.45
$[Co(\mathbf{64})_2]^{2+/+}$	-	-	-0.48
$[Ni(\mathbf{23})_2]^{3+/2+}$	0.90	78	1.30
$[Ni(\mathbf{23})_2]^{2+/+}$	-1.00	170	-0.60
$[Ni(\mathbf{23})_2]^{2+/+}$	-0.95[c]	171	-0.55
$[Pd(\mathbf{23})_2]^{3+/2+}$	0.55	104	0.95
$[Pd(\mathbf{64})_2]^{3+/2+}$	0.61[f]	84	-
$[Pd(\mathbf{23})_2]^{2+/+}$	-0.83	-	-0.43

[a]in 1 M CF_3SO_3H, $E_{1/2}$ *vs* Ag/AgCl.
[b]in 1 M $NaNO_3$, $E_{1/2}$ *vs* saturated calomel electrode (SCE).
[c]Ag^+/Ag (0.1 M $AgNO_3$) reference electrode, $E_{1/2}$ *vs* Fc^+/Fc.
[d](ref.95) [e](ref.76) [f](ref.92)

Fig. 6.35a. Cyclic voltammogram for the $[Fe(\mathbf{23})_2]^{3+/2+}$ couple in CH_3CN containing 0.1 M NEt_4BF_4.

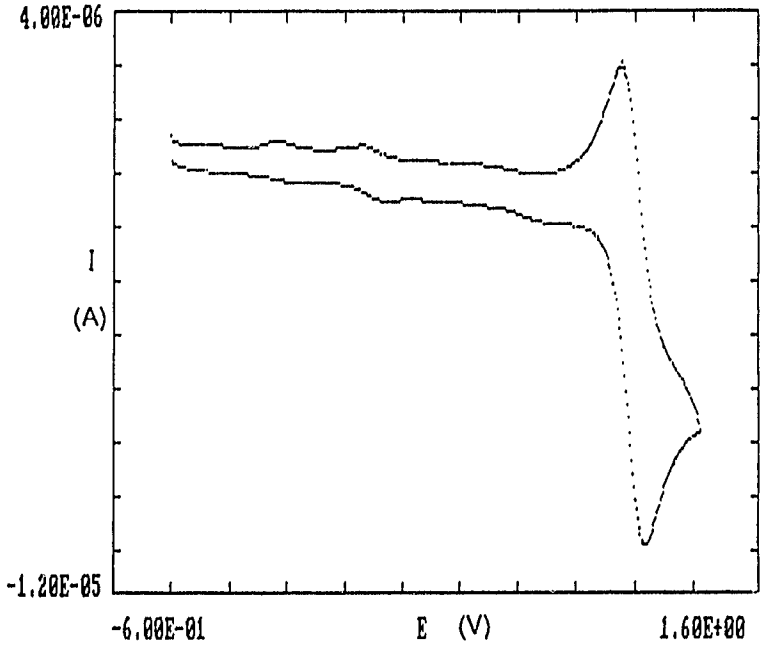

Fig. 6.35b. Cyclic voltammogram for the $[Fe(\mathbf{23})_2]^{3+/2+}$ couple in 1 M CF_3SO_3H.

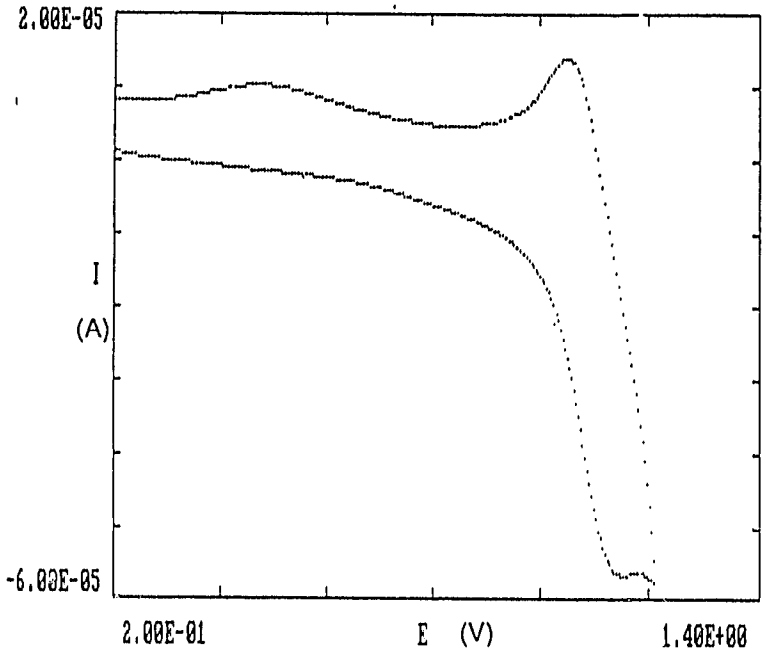

64, this orange species is indicative of ligand oxidation and not the formation of the Fe(III) complex cation.[87,161]

Electrochemical studies on $Co(\mathbf{23})_2^{2+}$ in CH_3CN showed two redox waves with $E_{1/2}$ = 0.41 V (*vs* NHE) attributed to the $Co(\mathbf{23})_2^{3+/2+}$ couple and -0.45 V (*vs* NHE) due to the $Co(\mathbf{23})_2^{2+/+}$ couple, Fig. 6.36. The $Co(\mathbf{23})_2^{2+/+}$ couple is reversible with a peak to peak separation of 58 mV. In aqueous solutions two quasi-reversible waves were obtained at 0.43 V and -0.45 V for the two one electron redox couples $Co(\mathbf{23})_2^{3+/2+}$ and $Co(\mathbf{23})_2^{2+/+}$ respectively, Fig. 6.37. The $E_{1/2}$ values are similar to those obtained for the $Co(\mathbf{64})_2^{3+/2+}$ and $Co(\mathbf{64})_2^{2+/+}$ couples, (Table 6.15.). The redox potential of the $[Co(\mathbf{23})_2]^{2+/+}$ couple moves slightly to more positive values relative to the $Co(\mathbf{64})^{2+/+}$ couple based on the nine- membered ligand **64**, and is also reversible in CH_3CN solutions. The larger trithia ligand **23** thus stabilizes the soft Co(I) ion. In comparison with the Co complexes of triaza ligands the redox potentials of the $Co^{3+/2+}$ couple based on trithia ligands are much more positive. The difference between the $E_{1/2}$ values of the $[Co(\mathbf{23})_2]^{3+/2+}$ couple and the $[Co(\mathbf{22})_2]^{3+/2+}$ couple[76] is 840 mV. This again reflects the ability of the softer S atoms in stabilizing the Co(II) ion, whereas, the N ligands stabilize the Co(III) state.

Electrochemical studies on the $Ni([\mathbf{23}])_2^{2+}$ complex ion in CH_3CN (using a Ag wire as the reference electrode and ferrocene as the external standard) showed two quasi-reversible redox couples, one at 0.90 V (*vs* Fc^+/Fc, ΔE = 78

Fig. 6.36. Cyclic voltammogram of $[Co(\mathbf{23})_2](ClO_4)_2$ in CH_3CN containing 0.1 M NEt_4BF_4.

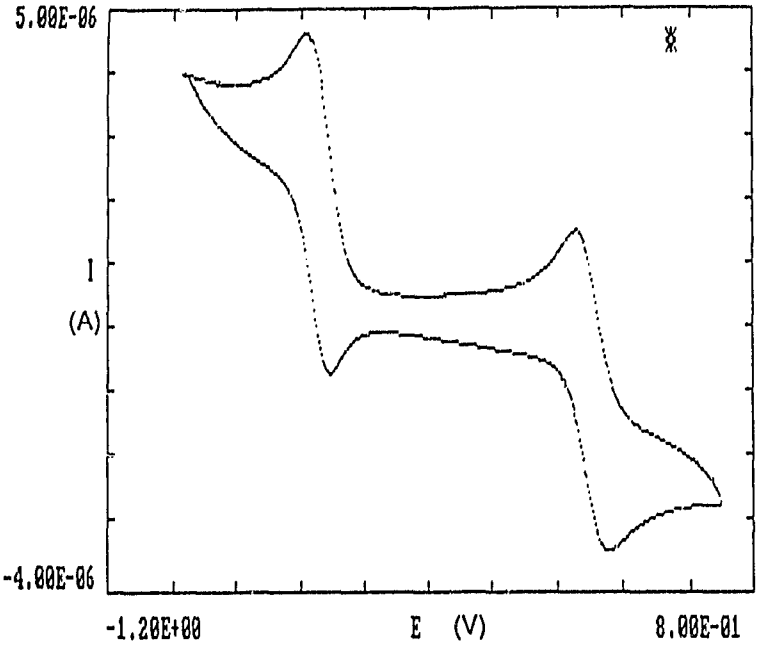

Fig. 6.37. Cyclic voltammogram of $[Co(\mathbf{23})_2](ClO_4)_2$ in 1 M $NaNO_3$.

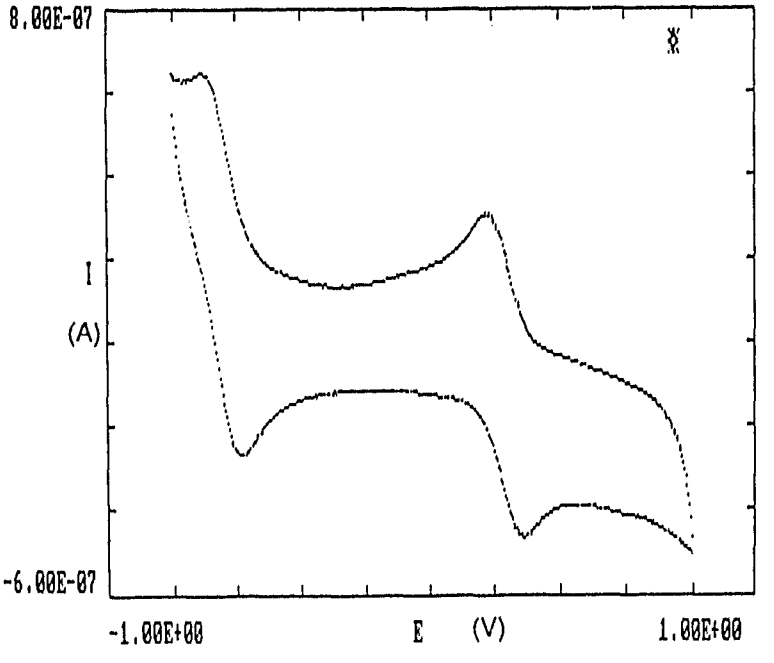

reversible redox couples, one at 0.90 V (*vs* Fc^+/Fc, ΔE = 78 mV), due to $[Ni(\mathbf{23})_2]^{3+/2+}$ couple and another at -1.00 V (*vs* Fc^+/Fc, ΔE = 170 mV), due to $[Ni(\mathbf{23})_2]^{2+/+}$ couple, Fig. 6.38. In a different experiment, when $Ag/AgNO_3$ (0.1 M) was used as a reference electrode in CH_3CN, a quasi-reversible redox wave was obtained at -0.95 V *vs* Fc^+/Fc (ΔE = 171 mV) due to $Ni(\mathbf{23})_2^{2+/+}$ and another irreversible wave was seen at 0.0 V *vs* Fc^+/Fc, Fig. 6.39. Upon adding PPh_3, the oxidation peak at 0.0 V disappeared and a more reversible wave at -1.08 V (*vs* Fc^+/Fc) ΔE = 70 mV, was obtained, Fig. 6.40. This suggests a stabilisation of the Ni(I) complex which may be a distorted octahedral species or a tetrahedral species containing sulfur atoms from trithia ligands and phosphorus atom of the PPh_3 molecule.

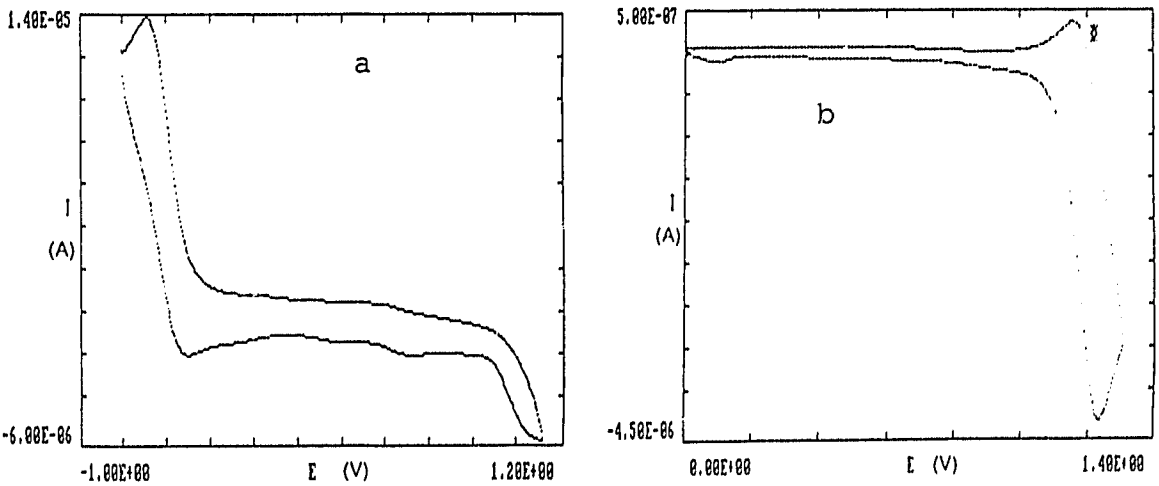

Fig. 6.38. Cyclic voltammogram for a) $[Ni(\mathbf{23})_2]^{2+/+}$ b) $[Ni(\mathbf{23})_2]^{3+/2+}$ couples in CH_3CN containing 0.1 M NEt_4BF_4, Ag wire as reference electrode.

Fig. 6.39. Cyclic voltammogram for the $[Ni(23)_2]^{2+/+}$ couple in CH_3CN containing 0.1 M NEt_4BF_4, $Ag/AgNO_3$ (0.1 M) as reference electrode.

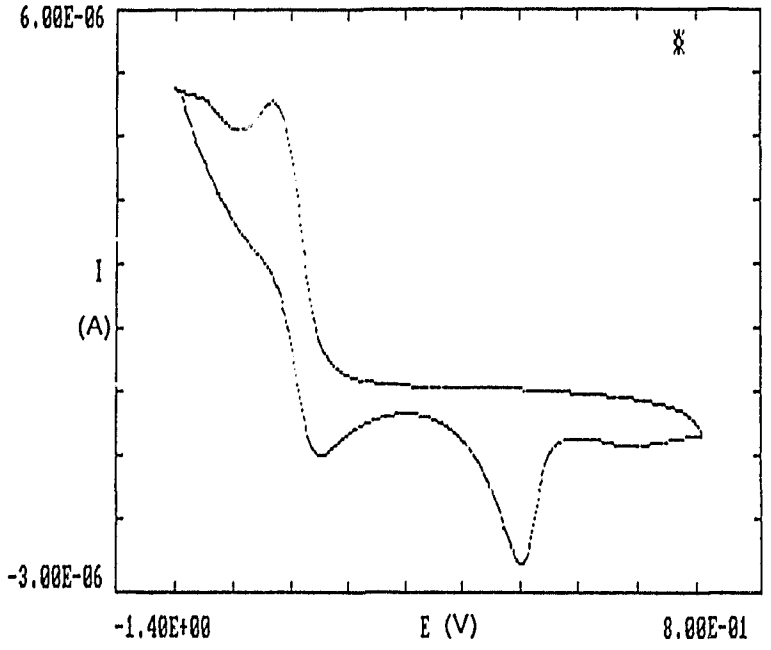

Fig. 6.40. Cyclic voltammogram of the Ni(I) species in the presence of PPh_3.

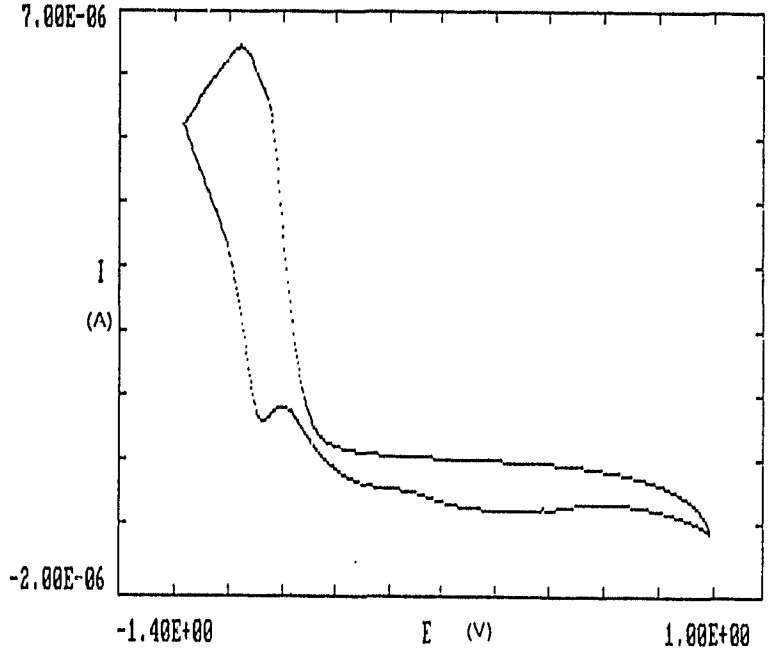

Unusual electronic structures have been noted in the past in crown thioether complexes. The Cu complex $Cu([9]\text{-}aneS_3)_2^{2+}$ is octahedral with the axial Cu-S distance (2.459 Å) comparable to the equatorial Cu-S bonds (2.419, 2.426 Å)[86] with relatively little tetragonal distortion as expected in Cu(II) complexes. Ag(I) complexes of **64** are octahedral as opposed to the expected tetrahedral structure.[93] Low spin Co(II) complexes of **64** are octahedral.[86] EPR data on Rh complexes of **64** are also consistent with a quasi-octahedral geometry around Rh(II) ion rather than the square planar geometry usually observed in Rh(II) complexes.[90] The esr data (see Section 6.8.2.) confirms the stabilization of a Ni(I) species. In light of the electrochemical and esr evidence this Ni(I) complex may be in a distorted octahedral environment due to the geometrical constraints imposed by the tridentate ligand. In a mixed coordination environment with PPh_3 a Ni(I) tetrahedral species is stabilized.

Cyclic voltammetry of $[Pd([10]\text{-}aneS_3)_2](PF_6)_2$ in CH_3CN showed a quasi-reversible redox wave at $E_{1/2}$ = 0.55 V *vs* Fc^+/Fc (ΔE = 104 mV), attributed to the $[Pd(\mathbf{23})_2]^{3+/2+}$ couple, Fig. 6.41. The cation $[Pd([10]\text{-}aneS_3)_2]^{3+}$ can be generated chemically with NO^+ in CH_3CN solutions and Co^{3+} or $HClO_4$ in aqueous solutions. The redox wave at -0.83 V is attributed to the $Pd^{2+/+}$ couple and is irreversible, Fig. 6.41. Pd(I) complexes of related crown thioethers have been generated electrochemically.[179] For example, a reversible redox wave has

been obtained for the $[Pd(\mathbf{82})]^{2+/+}$ couple in CH_3CN, $E_{1/2}$ = -0.74 V *vs* Fc^+/Fc, ΔE = 72 mV.[179]

Fig. 6.41. Cyclic voltammogram of $[Pd(\mathbf{23})_2](PF_6)_2$ in CH_3CN containing 0.1 M NEt_4BF_4.

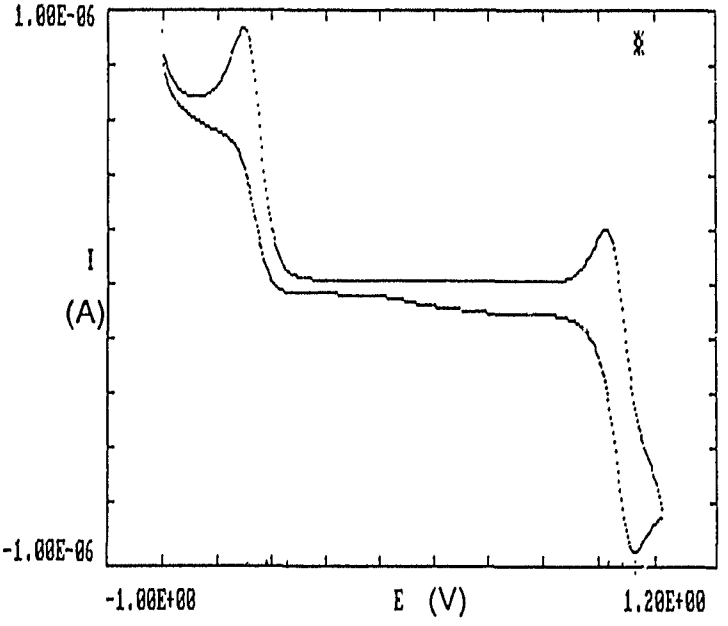

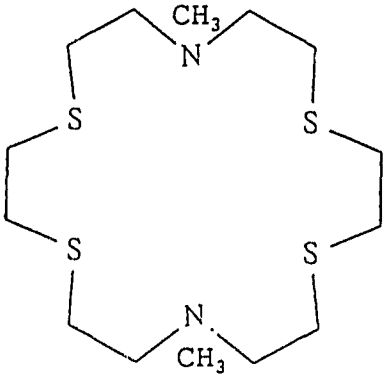

82

Irreversible reduction waves have been obtained for the Pd(II) complexes of the hexathia ligand, [18]-aneS_6, and the trithia ligand, **64** at E_p = -0.73 V to -0.88 V *vs* Fc'/Fc in CH_3CN.[179] At lower temperatures, quasi-reversible waves were obtained for the $Pd^{2+/+}$ couple based on **64**. In the case under study, it is, therefore, reasonable to assign the reduction wave at $E_{1/2}$ = -0.83 V to the Pd(I) complex ion. The Pd(I) reduction wave occurs at more anodic potentials compared to ligands containing harder N atoms, *e.g.*, the $E_{1/2}$ for the $Pd(\mathbf{83})_2^{2+/+}$ couple occurs at -1.53 V *vs* Fc'/Fc.[180,181] Incorporation of softer S atoms in the ligand framework moves the half-wave potentials to more positive values as is obtained for the $[Pd(\mathbf{24})_2]^+$ ion at -1.18 V *vs* Fc'/Fc (see Chapter 4). Thus the π- acid nature of the thioether donor atoms help stabilize the soft Pd(I) ion relative to the aza ligand systems.

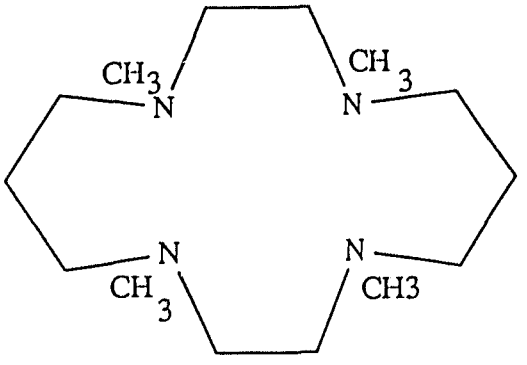

6.9. Electron transfer reactions:

Electron transfer reactions of transition metal complexes can be studied in several ways (see Chapter 1). In the present study, the nmr line broadening technique has been used to measure directly the electron transfer rates of the transition metal complexes. Fe(II), Co(II, III), Ni(II) and Pd(II) bis- complexes of the ligand [10]-aneS_3, **23**, are all stable in both aqueous and non-aqueous solutions towards ligand dissociation. The Fe(II)/(III) pair and the Co(II)/Co(III) pair have been successfully synthesised and characterised. The $[Fe(\mathbf{23})_2](PF_6)_3$ salt is stable in the solid state when stored under vacuum or in an inert atmosphere for about a week. The Fe(III) solutioms are stable for about two hours both in 1 M $HClO_4$ and in dry, degassed CH_3CN. The Fe complexes of **23** are low spin in both oxidation states. In other words, the oxidation of $[Fe(\mathbf{23})_2]^{2+}$ to $[Fe(\mathbf{23})_2]^{3+}$ involves the electronic configurational change of [core]$(t_{2g})^6$ → [core]$(t_{2g})^5$, *i.e.*, removal of a non-bonding electron. As a result, the effective reorganization energy involved in the electron transfer is very small. The oxidation of the corresponding $[Co(\mathbf{23})_2]^{2+}$ involves the electronic configurational change of [core]$(t_{2g}^6 e_g^*)$ → [core](t_{2g}^6), *i.e.*, removal of an electron from an antibonding e_g orbital. Since the electron transfer occurs between low spin Co(II) and low spin Co(III) complex ions, there is no contribution from the barrier due to the spin change as is often the case in Co

complexes with aza ligands. For example, the oxidation of $[Co(\mathbf{22})_2]^{2+}$ involves change from high spin Co(II) to low spin Co(III) complex ion. All these factors make the $[FeS_6]^{3+/2+}$ and the $[CoS_6]^{3+/2+}$ ideal systems for the study of electron transfer reactions.

The electron transfer barriers in $[Co([9]\text{-}aneN_3)_2]^{3+/2+}$ and $[Co([9]\text{-}aneS_3)_2]^{3+/2+}$ have been measured and analysed in the frame of the Marcus-Sutin model.[47,153] The kinetics of the outer-sphere one-electron reduction of $[Co(\mathbf{22})_2]^{3+}$ by $[Cr(OH_2)_6]^{2+}$ and $[V(OH_2)_6]^{2+}$ and the one-electron reduction of $[Co(\mathbf{64})_2]^{3+}$ by $[Co(phen)_3]^{2+}$ have been measured by stopped-flow spectrophotometry.[95] From the measured rate constant for the cross reaction, the self-exchange rate constants for the $[Co(\mathbf{23})_2]^{3+/2+}$ and $[Co(\mathbf{64})_2]^{3+/2+}$ have been estimated using the Marcus cross-correlation (eqn. 1.27., Chapter 1). The Marcus analysis depends on the availability of self-exchange rate data for the reagents used in these studies. Instead, a direct method of determining the self-exchange rate can be used in certain cases.

Recently,[160,182] the self-exchange rate constant for the $[Co(\mathbf{64})_2]^{3+/2+}$ couple was determined using ^1H nmr line-broadening techniques. The ^1H nmr of the corresponding $[Co(\mathbf{23})_2]^{3+}$ ion is dense and complicated due to the asymmetry of the ten-membered ring. As a result, the ^1H nmr line broadened spectra are poorly resolved making line-width measurements difficult. On the other hand, the simplicity and the sensitivity of the ^{59}Co

nmr spectrum renders it apt to be used as a probe for the study of outer-sphere electron transfer reactions. The rate constant of the self exchange reaction

$$[Co^{*}(\mathbf{23})_2]^{3+} + [Co(\mathbf{23})_2]^{2+} \rightleftharpoons [Co(\mathbf{23})_2]^{3+} + [Co^{*}(\mathbf{23})_2]^{2+} \quad \text{-- 6.21.}$$

in CH_3CN was determined using the ^{59}Co nmr line broadening technique. The ^{59}Co nmr spectrum of $[Co(\mathbf{23})_2]^{3+}$ ion showed one intense line at δ 2336 (*cis* isomer) and another relatively broad and weak line at δ 2268 (*trans* isomer). Addition of paramagnetic $[Co(\mathbf{23})_2](ClO_4)_2$ complex to CH_3CN solutions of the diamagnetic $[Co(\mathbf{23})_2]^{3+}$ ion at ambient temperatures resulted in additional broadening of the Co(III) resonance line, Fig. 6.42., Table 6.16. The line-width of the ^{59}Co nmr resonance at δ 2336 is plotted against the concentration of the paramagnetic species in Fig. 6.43. From the slope of the plot the self-exchange rate constant k_{11} for the reaction 6.21. was determined as follows: In the slow exchange region,

$$k_{11} = \frac{\pi\{\text{FWHM (Hz)}\}}{[\text{Co(II)}]\ (\text{M})} = \pi(\text{slope})\ (M^{-1}s^{-1}). \quad \text{--- 6.22.}$$

$$= 4.3 \times 10^5\ M^{-1}s^{-1}.$$

(FWHM = Full width at half maximum)

Although the temperature dependence of the line broadening was not monitored, the line broadening was assumed to be in the

Fig. 6.42. Variation of line-width of ^{59}Co nmr spectra of $[Co(\mathbf{23})_2]^{3+}$ ion with the concentration of the paramagnetic $[Co(\mathbf{23})_2]^{2+}$ ion (see also Table 6.16.).

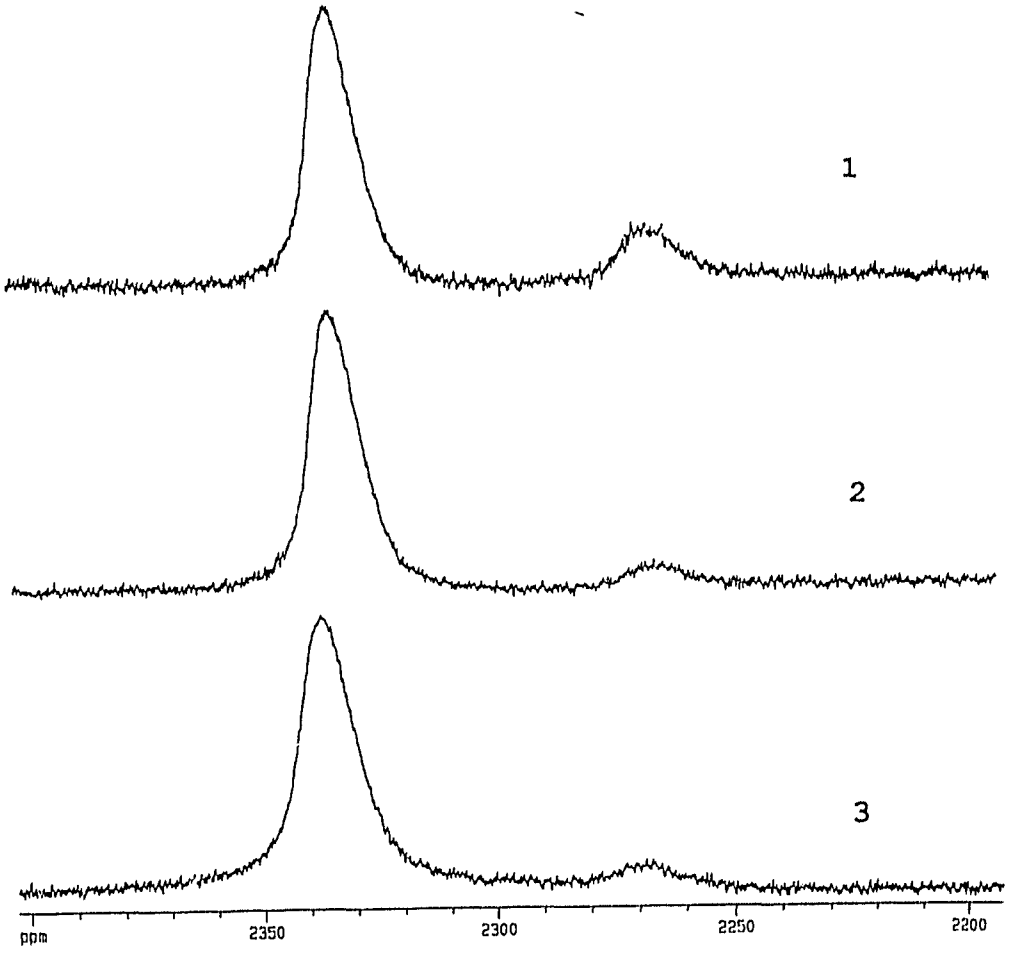

Fig. 6.42. (contd.)

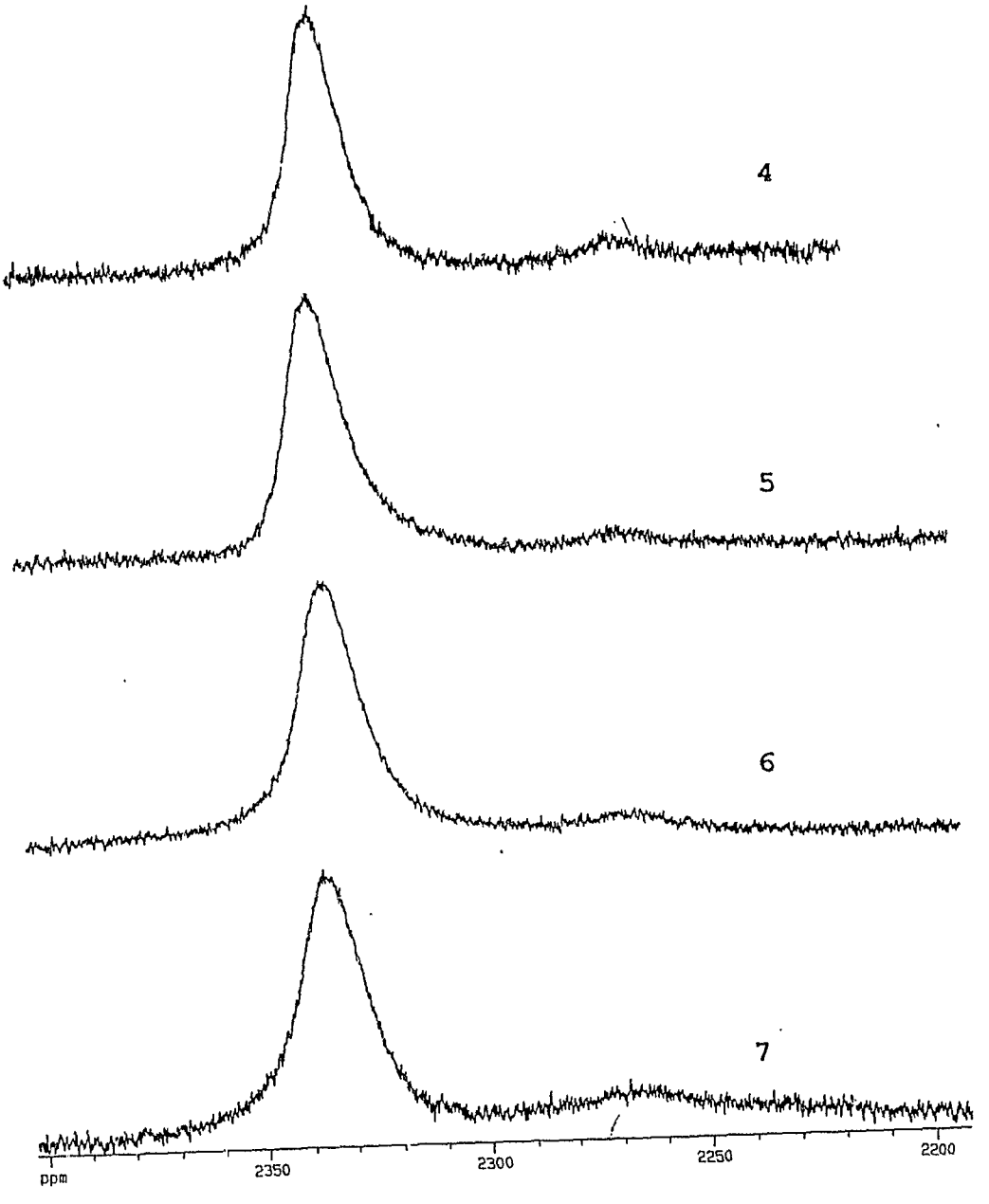

Table 6.16. Dependence of the spectral line-width of $[Co(\mathbf{23})_2]^{3+}$ ion on the concentration of the paramagnetic $[Co(\mathbf{23})_2]^{2+}$ ion.*

Spectrum #	[Co(II)], (mM)	Line-width, (Hz)
1	0.00	996
2	0.70	1033
3	1.40	1173
4	1.84	1191
5	2.49	1317
6	3.16	1428
7	3.78	1478

* 1.5 mM [Co(III)]; I = 0.2 M $\{N(C_2H_5)_4BF_4\}$; 75% CH_3CN, 25% CD_3CN; T = 303 K.

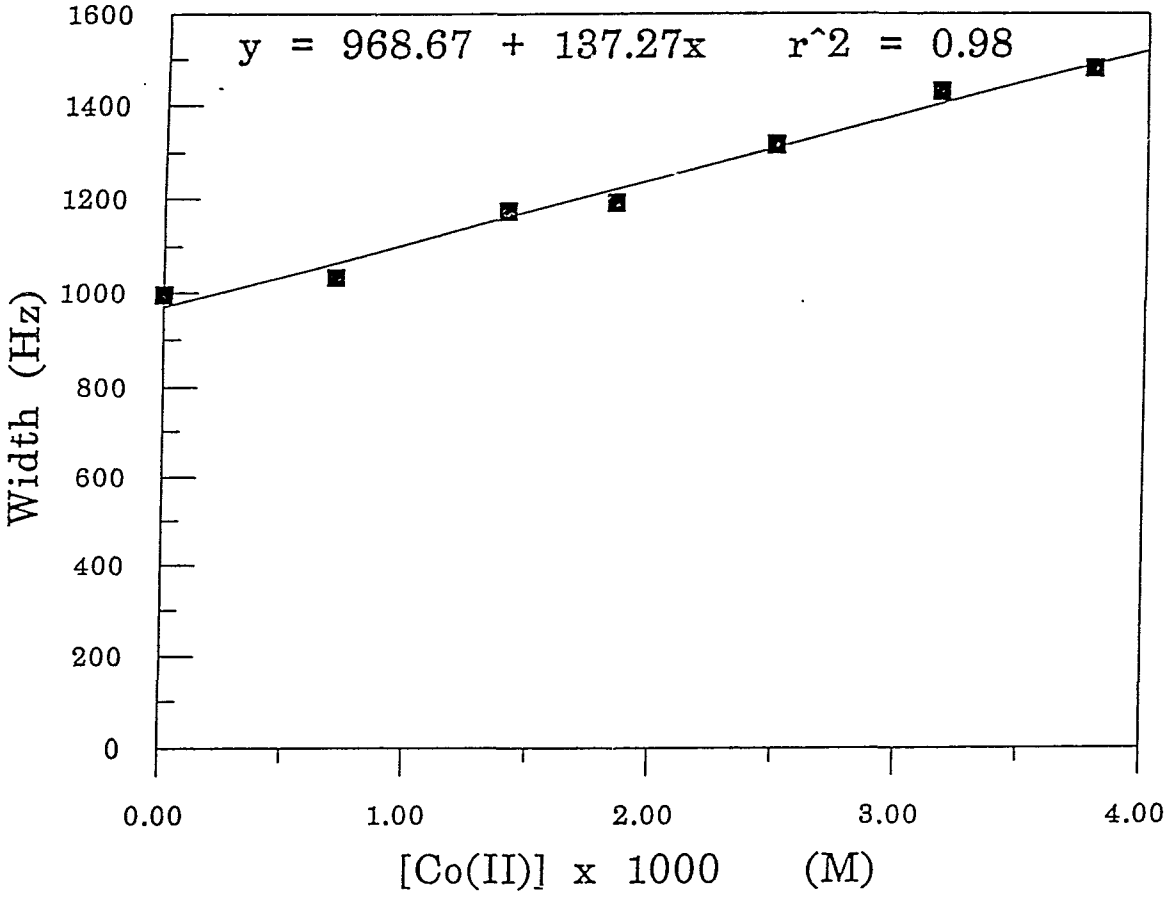

Fig. 6.43. Plot of ^{59}Co nmr line-width of the $[Co(23)_2]^{2+}$ ion *vs* the concentration of the paramagnetic $[Co(23)_2]^{2+}$ ion.

slow-exchange regime. The assumption is reasonable considering the fact that the line broadening was found to be independent of the concentration of the diamagnetic species. The value of 4.3 x 10^5 $M^{-1}s^{-1}$ for k_{11} is about six orders of magnitude higher than that obtained for the $Co-N_6$ systems, *e.g.*, $[Co(\mathbf{22})_2]^{3+/2+}$, (8 x 10^{-2} $M^{-1}s^{-1}$).[95] The electron transfer in the amine system, $[Co(\mathbf{22})_2]^{3+/2+}$ involves change from the high spin Co^{2+} to the low spin Co^{3+} ion. As a result the Co-N bond distances in both the reduced and the oxidised forms are very different.[95] In the thia systems, *e.g.*, $[Co(\mathbf{23})_2]^{3+/2+}$ both the Co(III) and the Co(II) ions are in the low spin state resulting in a very small change in the Co-S bond distances in the two oxidation states. The smaller inner-sphere reorganization energy leads to a larger self exchange rate constant for the CoS_6 systems. Similar observations have been made by Dubs *et al*[154] in their study of electron transfer reactions between a low spin Co(II) and Co(III) S_3N_3 complex, where the electron transfer self exchange rate was also measured by the ^1H nmr line broadening technique and was found to be 4.5 x 10^3 $M^{-1}s^{-1}$, significantly larger (four orders of magnitude) than the corresponding CoN_6 systems.

The self-exchange rate constant for the reaction,

$$[Co^*(\mathbf{64})_2]^{3+} + [Co(\mathbf{64})_2]^{2+} \rightleftharpoons [Co(\mathbf{64})_2]^{3+} + [Co^*(\mathbf{64})_2]^{2+} \quad -- \ 6.23.$$

was also determined using the ^{59}Co nmr line broadening

technique. The ^{59}Co nmr spectrum of diamagnetic $[Co(\mathbf{64})_2]^{3+}$ ion in D_2O showed a single peak at δ 1511. Addition of paramagnetic $[Co(\mathbf{64})_2]^{2+}$ ion resulted in an increase of the diamagnetic line-width, Fig. 6.44., Table 6.17. From the plot of the line-width *vs* the paramagnetic Co(II) concentration, Fig. 6.45., the self exchange rate constant for the reaction 6.23. was found to be 1.3 x 10^5 $M^{-1}s^{-1}$. This value compares well with the rate constant obtained from the ^1H nmr line broadening measurements, 1 x 10^5 $M^{-1}s^{-1}$.[182] This value is higher than that obtained indirectly from the Marcus cross-correlation, 1.3 x 10^4 $M^{-1}s^{-1}$.[95] Based on the force constants for the Co-S bonds in the reaction 6.23., the self exchange rate constant was calculated using the Marcus-Sutin model and was found to be 1 x 10^6 $M^{-1}s^{-1}$.[95] The self exchange rate constant obtained for the $[Co(\mathbf{64})_2]^{3+/2+}$ couple in the present study agrees reasonably well with the predicted value. The similarity of the self exchange rate constant for $[Co(\mathbf{23})_2]^{3+/2+}$ couple in CH_3CN and the $[Co(\mathbf{64})_2]^{3+/2+}$ couple in water suggests that the contribution to the outer-sphere reorganization barrier due to solvation effects is small.

Thus the knowledge of the self exchange rate constant for the $Co^{3+/2+}$ redox couple based on the trithia ligand **23** would now permit the complex to be used as an one-electron outer-sphere reagent in electron transfer reactions in non-aqueous solutions.

Fig. 6.44. Variation of line-width of ^{59}Co nmr spectra of $[Co(\mathbf{64})_2]^{3+}$ ion with the concentration of the paramagnetic $[Co(\mathbf{64})_2]^{2+}$ ion (see also Table 6.17).

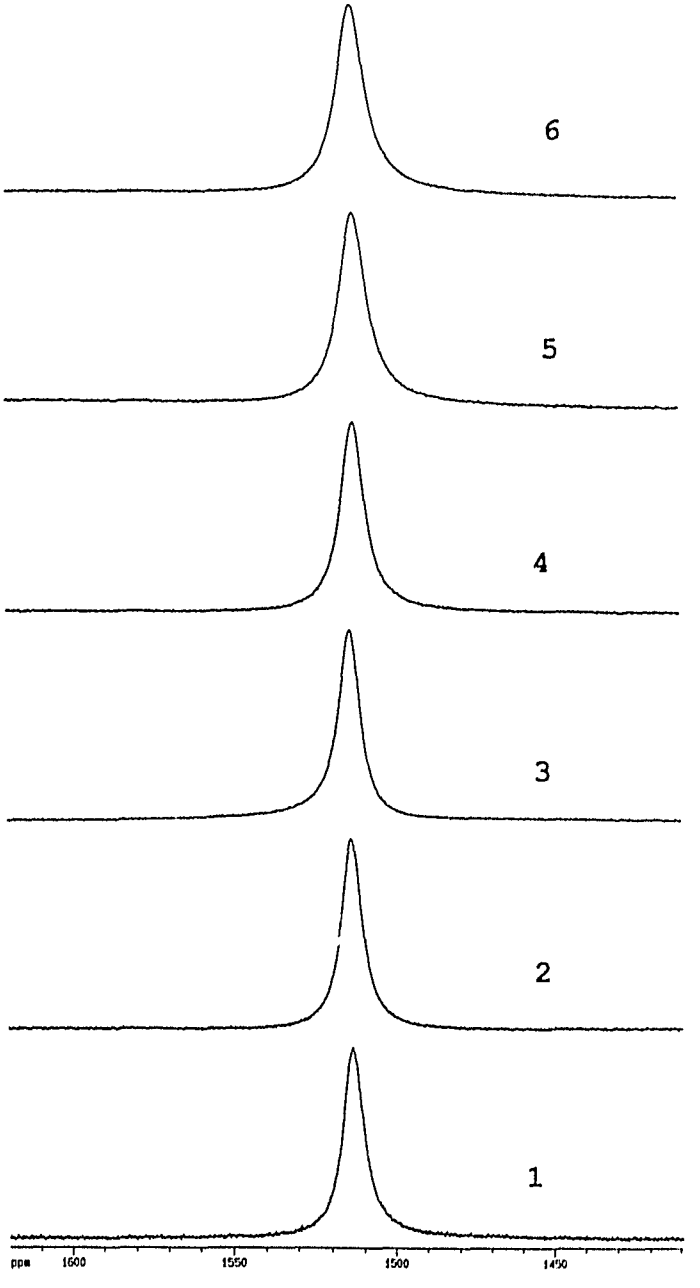

Table 6.17. Dependence of the spectral line-width of $[Co(\mathbf{64})_2]^{3+}$ ion on the concentration of the paramagnetic $[Co(\mathbf{64})_2]^{2+}$ ion.*

Spectrum #	[Co(II)], (mM)	Line-width, (Hz)
1	1.04	611
2	1.93	644
3	3.20	679
4	4.54	752
5	7.32	870
6	8.21	913

* 1.3 mM [Co(III)]; I = 0.1 M ($NaNO_3$); D_2O; T = 303 K.

Fig. 6.45. Plot of ^{59}Co nmr line-width of the $[Co(\mathbf{64})_2]^{3+}$ ion *vs* the concentration of the paramagnetic $[Co(\mathbf{64})_2]^{2+}$ ion.

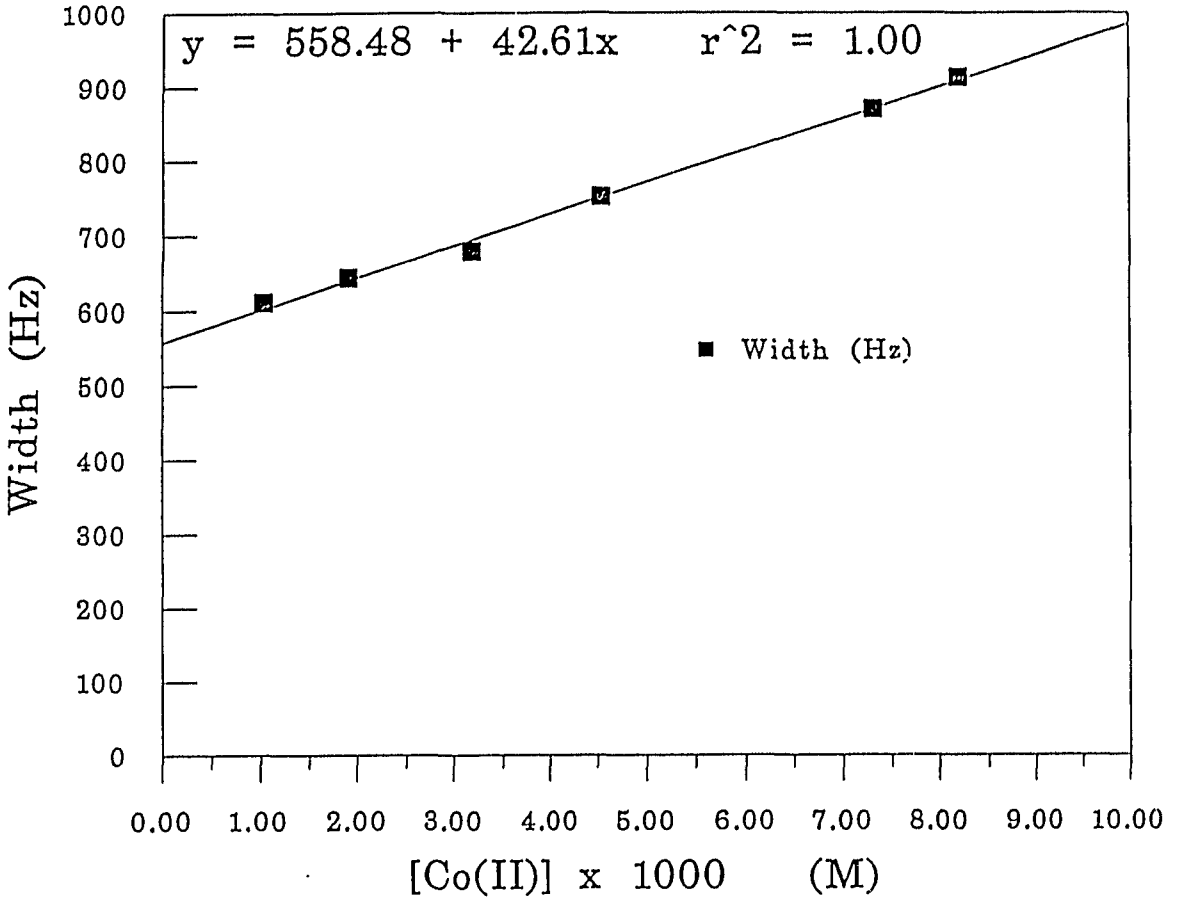

For the self exchange reaction,

$$[Fe^{*}(\mathbf{23})_2]^{3+} + [Fe(\mathbf{23})_2]^{2+} \rightleftharpoons [Fe(\mathbf{23})_2]^{3+} + [Fe^{*}(\mathbf{23})_2]^{2+} \quad -- \ 6.24.$$

the rate constant was determined by the ^1H nmr line broadening measurement. The experiment was carried out in 0.5 M D_2SO_4. The multiplet centered at δ 2.52 in the ^1H nmr spectra of diamagnetic $[Fe(\mathbf{23})_2]^{2+}$ ion (Fig. 6.46., Table 6.18.) was monitored. The line-width of this multiplet was then plotted as a function of the concentration of the paramagnetic Fe(III) complex ion, Fig. 6.47. From the slope of the plot the self exchange rate constant was determined using equation 6.22. and found to be 8×10^5 $M^{-1}s^{-1}$. This rate constant is greater than the self-exchange rate constant obtained for the corresponding $[Co(\mathbf{23})_2]^{3+/2+}$ couple (4×10^5 $M^{-1}s^{-1}$). The electron transfer for the FeS_6 system involves removal of a t_{2g} non-bonding electron, $t_{2g}^6 \rightarrow t_{2g}^5$, whereas, in the CoS_6 system oxidation of the Co(II) complex ion involves removal of an electron from the anti-bonding e_g orbital, $t_{2g}^6 e_g^{*} \rightarrow t_{2g}^6$. Therefore, the reorganization barrier for the FeS_6 system is smaller than that for the CoS_6 system.

In a similar manner, from the ^1H nmr line broadening of the diamagnetic Fe(II) bis- complex of **64**, Table 6.19.,Fig. 6.48., the self exchange rate constant for the reaction,

$$[Fe^{*}(\mathbf{64})_2]^{3+} + [Fe(\mathbf{64})_2]^{2+} \rightleftharpoons [Fe(\mathbf{64})_2]^{3+} + [Fe^{*}(\mathbf{64})_2]^{2+} \quad -- \ 6.25.$$

Fig. 6.46. Variation of line-width of ^1H nmr spectra of $[Fe(\mathbf{23})_2]^{2+}$ ion with the concentration of the paramagnetic $[Fe(\mathbf{23})_2]^{3+}$ ion.

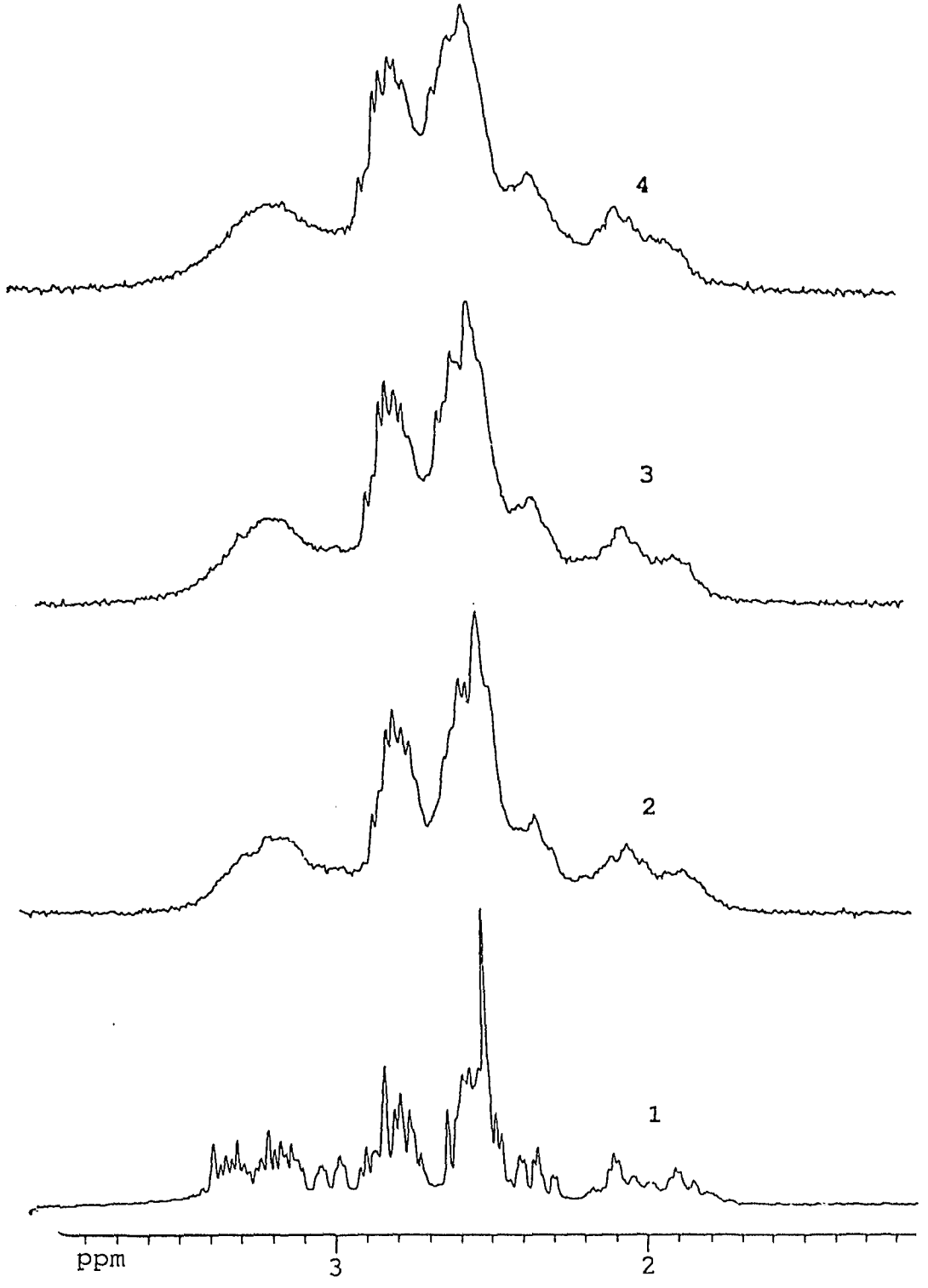

Fig. 6.46. (contd.)

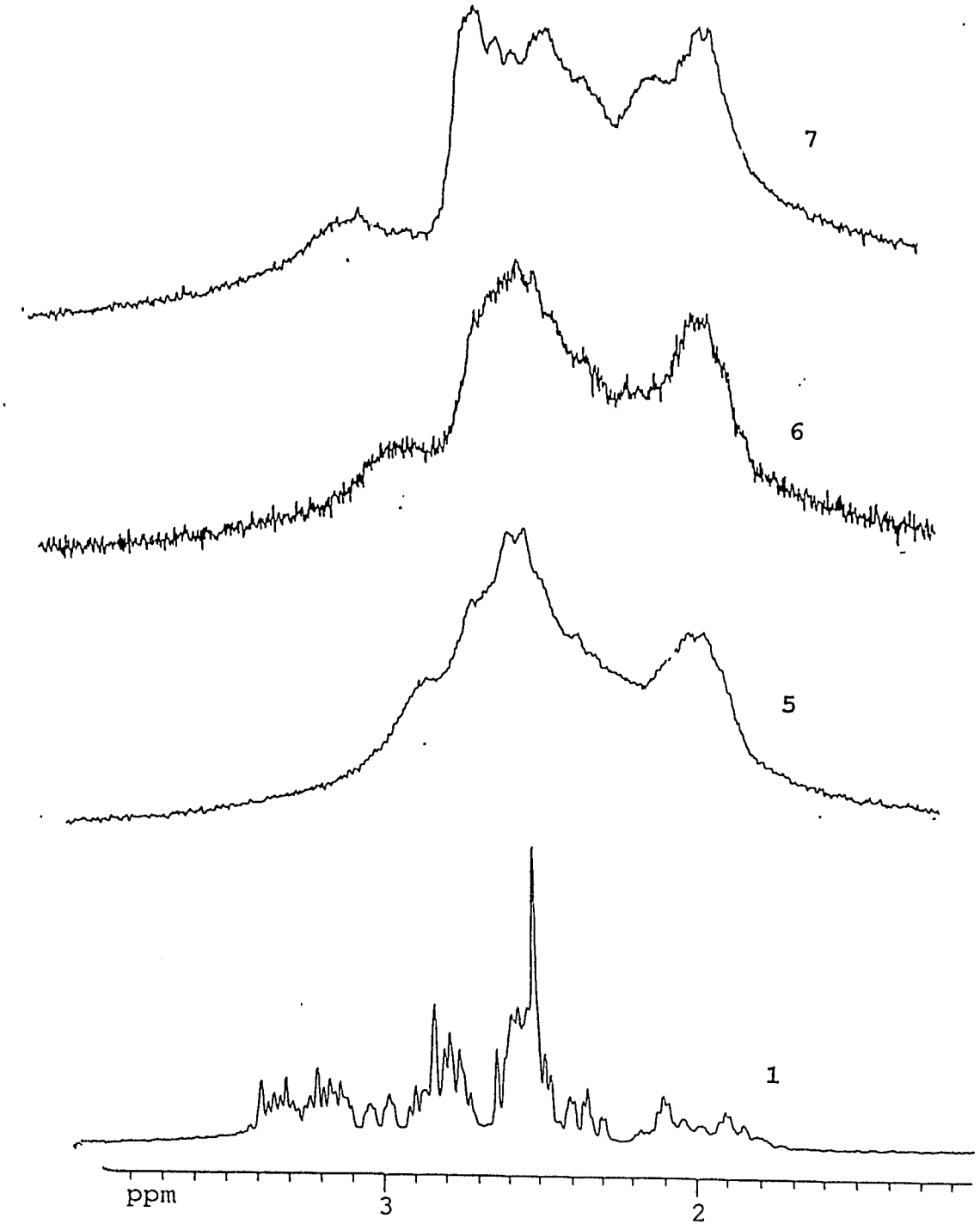

Table 6.18. Dependence of the spectral line-width of $[Fe(\mathbf{23})_2]^{2+}$ ion on the concentration of the paramagnetic $[Fe(\mathbf{23})_2]^{3+}$ ion.*

Spectrum #	[Fe(III)], (mM)	Line-width, (Hz)
1	0.000	32
2	0.043	44
3	0.068	48
4	0.103	60
5	0.205	92
6	0.274	104
7	0.324	120

* 0.014 M [Fe(II)]; I = 1.0 M (0.5 M D_2SO_4); T = 303 K.

Fig. 6.47. Plot of ^{1}H nmr line-width of the $[Fe(\mathbf{23})_2]^{2+}$ ion *vs* the concentration of the paramagnetic $[Fe(\mathbf{23})_2]^{3+}$ ion.

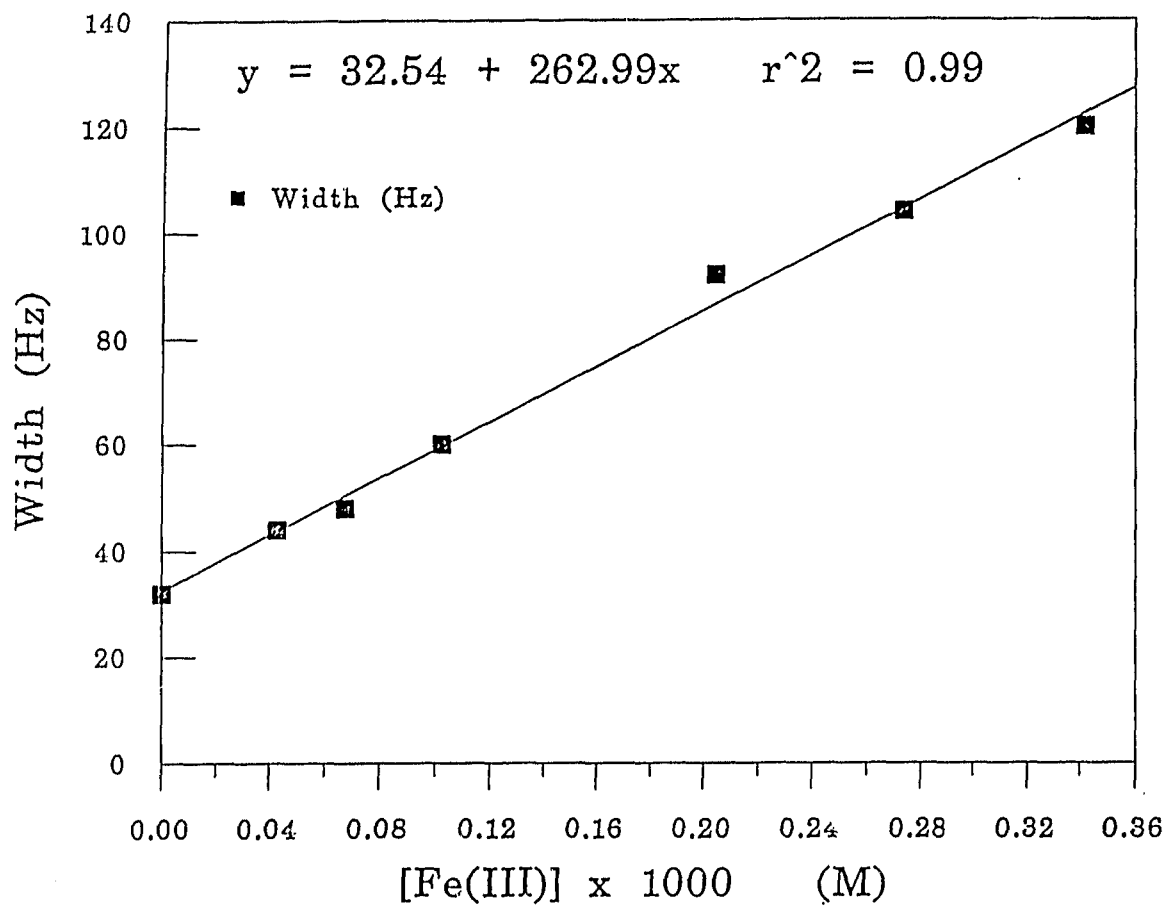

Table 6.19. Dependence of the spectral line-width of $[Fe(\mathbf{64})_2]^{2+}$ ion on the concentration of the paramagnetic $[Fe(\mathbf{64})_2]^{3+}$ ion.*

Spectrum #	[Fe(III)], (mM)	Line-width, (Hz)
1	0.000	46
2	0.046	50
3	0.069	56
4	0.092	64
5	0.160	78

* 0.009 M [Fe(II)]; I = M (0.5 M D_2SO_4); T = 303 K.

Fig. 6.48. Variation of line-width of ^1H nmr spectra of $[Fe(\mathbf{64})_2]^{2+}$ ion with the concentration of the paramagnetic $[Fe(\mathbf{64})_2]^{3+}$ ion (see also Table 6.19.).

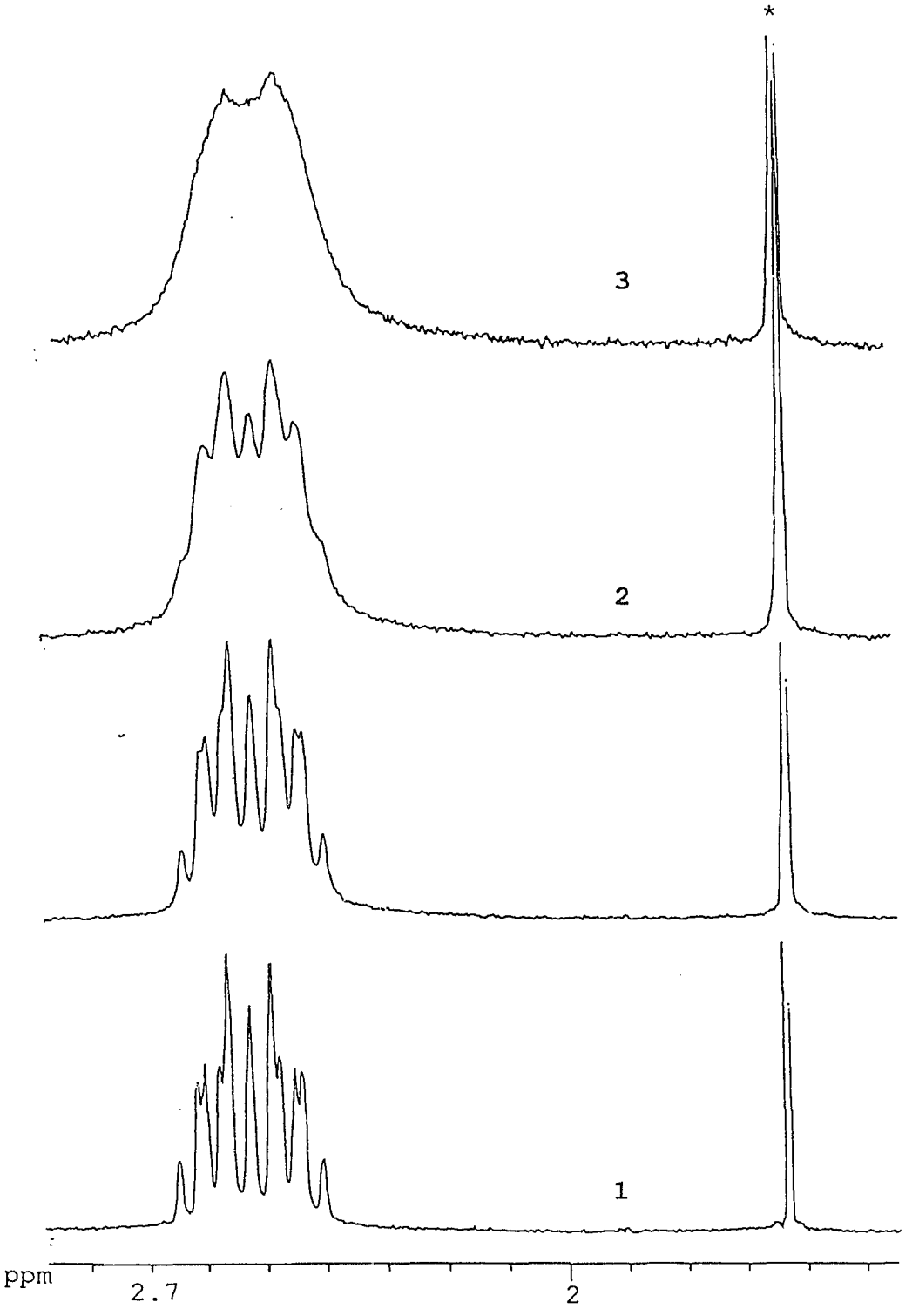

Fig. 6.48. (contd.)

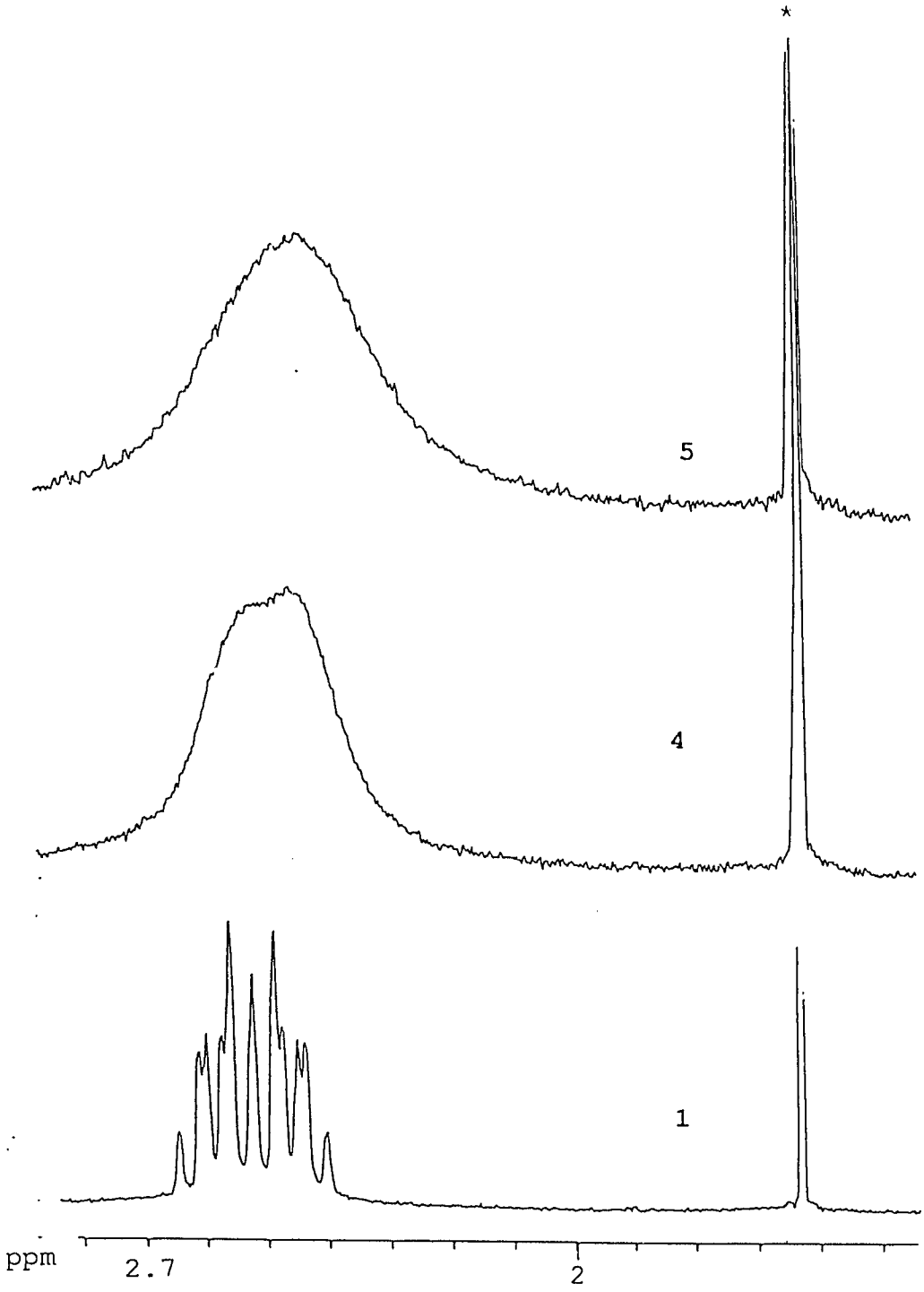

Fig. 6.49. Plot of ^{1}H nmr line-width of the $[Fe(\mathbf{64})_2]^{2+}$ ion *vs* the concentration of the paramagnetic $[Fe(\mathbf{64})_2]^{3+}$ ion.

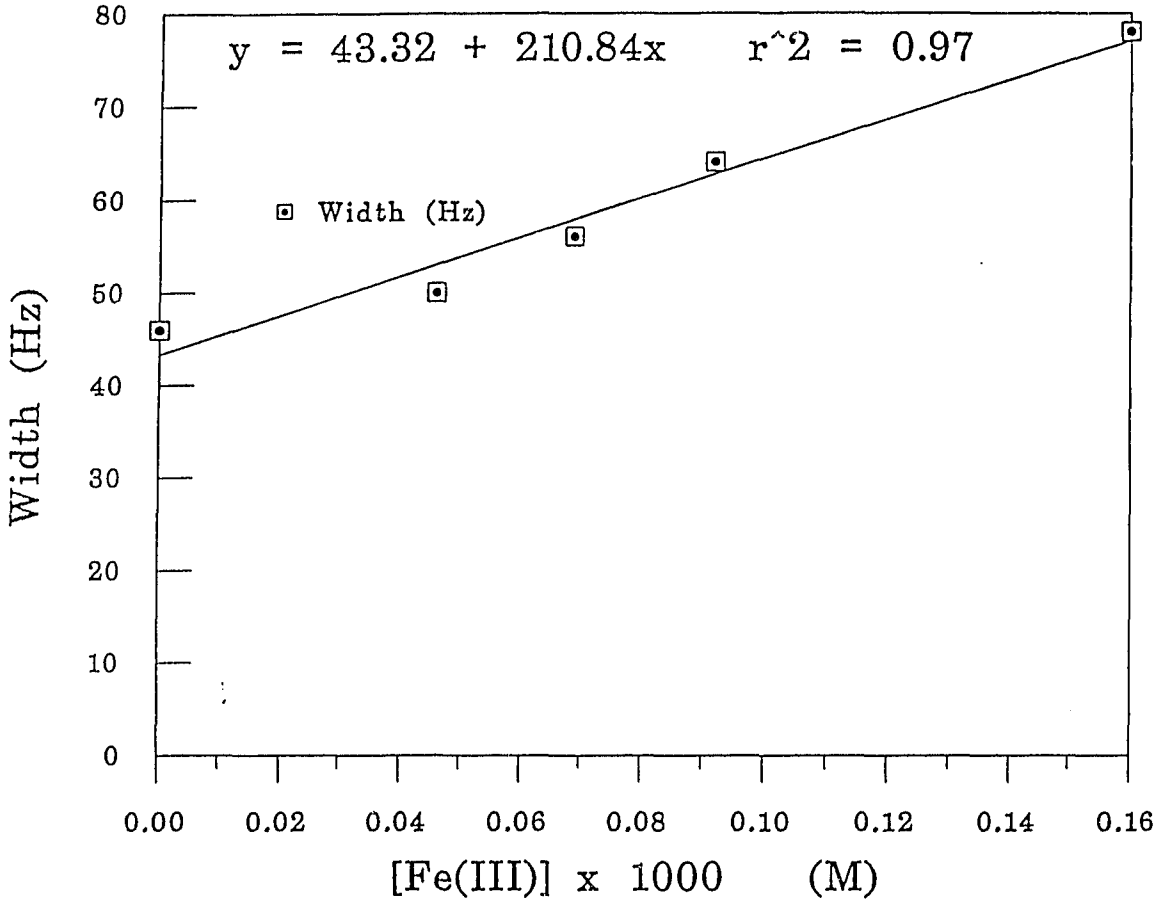

was determined from the plot of line-width *vs* the concentration of the paramagnetic Fe(III) complex ion (Fig. 6.49.). A value of 7 ± 2 x 10^5 $M^{-1}s^{-1}$ was obtained for the self exchange rate constant. This value is in agreement with that obtained by Macartney[182] (6 ± 2 x 10^5 $M^{-1}s^{-1}$) for the same reaction 6.25., and serves to confirm the correctness of the order of magnitude of the previously reported rate constant.

6.10. Conclusions:

The transition metal complexes, Fe(II/III), Co(II/III), Ni(II) and Pd(II), with [10]-aneS_3, **23**, were successfully synthesised and characterised by x-ray crystallography, uv-visible, nmr and esr spectroscopies. Stable octahedral complexes with two trithia ligands were formed as a result of the endodentate conformation of the ligand in these complexes. Detailed ligand field analyses of Fe(II/III), Co(II/III) and Ni(II/III) complexes were made and ligand field distortion parameters for the Fe complexes were calculated from the esr spectra and thereby the energy level pattern for the ground state was obtained. The ligand field parameters and the redox properties of the complexes based on the trithia ligand were compared with those of the triaza analogs. The lower values of the nephelauxetic ratios for the bis- complexes of the trithia ligands reflect the higher degree of covalency of the metal-sulfur bond relative to the metal-nitrogen bond in the triaza analogs. Transition metal ions in low oxidation states

[Ni(I), Fe(II), Co(II)] were stabilized by the soft S atoms. Due to the π- acid properties of the S atoms, a low spin state for the Co^{2+} complex ion was obtained.

Evidence for fluxionality at the Pd(II) centre in the bis- trithia complex has been provided in the ^{13}C nmr spectra. Moreover, the axial S atoms in the Pd(II) complex adopted a *syn* conformation. The fluxional process thus serves as a compromise between the square planar preference of the d^8 metal centre and the octahedral preference of the trithia ligand. The self exchange rate constant for the electron transfer reactions of the $[Co(\mathbf{23})_2]^{3+/2+}$ couple has been obtained directly for the first time using ^{59}Co nmr spectroscopy. Knowledge of the self exchange rates for the $[Fe(\mathbf{23})_2]^{3+/2+}$ and $[Co(\mathbf{23})_2]^{3+/2+}$ couples by direct methods enable these complexes to serve as one-electron outer sphere reagents for use in Marcus cross reactions.

CHAPTER 7

Synthesis and reactivity of Ni(II) complex of 4,8-diaza-1-thiacyclodecane.

7.1. Introduction:

The importance of the use of ten- membered macrocycles in the formation of octahedral complexes has been amply demonstrated in the previous chapters. The geometrical constraints imposed by the tridentate ligand on the metal ion upon complexation renders it stable toward ligand dissociation in the octahedral complexes. The trithia ligand [10]-aneS_3, **23**, has been used to form complexes with Fe(II/III), Co(II/III), Ni(II) and Pd(II) ions. Metal ions in low oxidation states *viz.*, Ni(I), Co(II), Fe(II) have been stabilized due to the the π- acid properties of the S donor atoms. These complexes serve as one-electron outer sphere reagents in electron transfer reactions (Chapter 6).

Incorporation of the harder N atoms allows for stabilization of both lower and higher oxidation states. The ligand [10]-aneS_2NH, **24** (Chapter 4), exhibits intermediate properties between the triaza ligand [10]-aneN_3, **66**, and the trithia ligand, **23**. An elongated octahedral complex was obtained for the Ni(III) bis- complex of the trithia ligand. In contrast the Ni(III) complex of the mixed donor ligand **24** exhibited a compressed octahedral coordination as evidenced by esr in both the cases. The possible occurrence of a mixed donor environment in methanogenic bacteria has been reported recently.[103] Hence it is of interest to investigate the ligating abilities of the mixed donor ligand [10]-aneSN_2, **25**, and compare them with other members of the series.

7.2. Synthesis:

The acid chloride method to synthesise the ligand **25** was attempted as outlined in Scheme 2.3. (Chapter 2). Separation of the cyclised amide **43** from the hydrochloride salt of the amine **42** proved difficult. Ligand **25** was obtained in about 30% yield but contained small quantities of the open chain amine **42**. This method of synthesis was discontinued, since the parallel synthesis of ligand **25** as outlined in Scheme 2.2. (Chapter 2) yielded the pure ligand.

The synthesis outlined in Scheme 2.2. is based on the Richman-Atkins[31] method of cyclization which involves the condensation of bis-sulfonamide sodium salts and compounds having sulfonate esters as leaving groups, to facilitate ring closure. The cyclised tosylate **38** was obtained in 70% yield. Detosylation of the cyclised tosylate was carried out using 30% HBr in acetic acid solutions. The ligand hydrobromide salt was obtained in 46% yield (for details of preparation see Section 2.1.5.). The advantages of this method are that the intermediate compounds in the synthesis can be isolated in analytically pure forms and can be stored indefinitely. The Ni bis- complex of **25** was synthesised as outlined in Section 2.1.6. Recrystallization of the Ni complex **44** from ethanol/water mixture afforded purple crystals suitable for X-ray diffraction studies.

7.3. Crystal structure of [Ni([10]-aneSN$_2$)$_2$]Br$_2$.2H$_2$O, 44:

Pink crystals of the Ni complex of bis [10]-aneSN$_2$, **25**, were obtained by slow evaporation of solutions of the complex in aqueous ethanol (95 : 5 v/v). The crystal was mounted in a Lindemann's tube directed along the *c* axis. The crystal dimensions were 0.62 × 0.12 × 0.16 mm^3. The experimental work was carried out at 20 °C. Both Weissenberg and precession photography methods were used to establish the symmetry and unit cell dimensions. The crystallographic data are given in Table 7.1. After photography, the crystal was transferred to a *Picker* four-circle diffractometer automated with a PDP11/10 computer. The final lattice parameters were obtained from a least-squares refinement of 24 accurately centered, high angle reflections. Intensity measurements were carried out with Zr-filtered Mo radiation, λ = 0.71069 Å.

The scanning was carried out in the $\theta/2\theta$ mode using 200 steps of 0.01° in 2θ and counting for 0.25 s per step. Background counting was done for 25 s at each end of the scan. A set of three standard reflections preceded each batch of 50 measurements. A total of 1943 reflections were measured out of which 1559 ($I > 3\sigma(I)$) were used in the final data set.

After correction for absorption effects, Ni and Br atoms were located by MULTAN.[56] The atomic scattering factors together with the Ni *f* curves were taken from ref. 57. Completion and refinement of the structure was achieved by difference electron density maps and by least squares

Table 7.1. Experimental crystallographic data for $[Ni([10]\text{-aneSN}_2)_2]Br_2.2H_2O$, **44**.

Compound	**44**
Formula	$Ni_1S_2N_4C_{14}H_{36}O_2Br_2$
MW	575.1
Crystal color	pink
Crystal system	monoclinic
Space group	$P2_1/n$ (No. 14)
Cell dimensions	
a (Å)	11.419(3)
b (Å)	9.439(2)
c (Å)	10.288(3)
α (°)	90
β (°)	96.66(3)
γ (°)	90
V (Å^3)	1101.46
Z	2
D_{calc} (g/cm^3)	1.734
D_{meas} (g/cm^3)	1.727
Crystal dimensions (mm^3)	0.62×0.12×0.16
Diffractometer	Picker
Radiation (λ, Å)	Mo-K_α (0.71069)
Filter	Zirconium
Measurement	2θ (2 - 50°)
Octants collected	±h,k,l
std. reflections	3:040,004,600
no. refln. collected	1943
no. refln. I > nσ(I)	1559 (n = 3)
no. parameters	115
Linear abs coeff. (cm^{-1})	49.56
Solution method	MULTAN
R^a	0.0411
R_w^b	0.0472

[a] $R = \Sigma\| F_o| - |F_c\| / \Sigma |F_o|$

[b] $R_w = [\Sigma w(|F_o| - |F_c|)^2 / \Sigma w(|F_o|)^2]^{1/2}$ where $w = 1.41/(\sigma^2 F + 0.001F^2)$

minimizing. The asymmetric unit consisted of half a molecule of the complex cation, one bromide ion and one molecule of water of crystallization. Hydrogen atoms were not included in the calculations. All non-hydrogen atoms were refined anisotropically. The refinement converged to $R = 0.0411$ and $R_w = 0.0472$, with a maximum shift/esd of 0.009 on the final cycle. A final difference map had a maximum peak of 0.77 eÅ^{-3}.

The structure of the Ni complex is shown in Fig. 7.1. The fractional atomic coordinates are given in Table 7.2. The bond lengths and the bond angles are listed in Table 7.3. The complex is centrosymmetric and the molecule has an inversion symmetry with the Ni atom occupying a special position. The Ni atom is coordinated by two N atoms and one S atom from each ligand in a facial manner, to form a distorted octahedral complex. Two geometrical isomers are possible for the $\{Ni([10]\text{-aneSN}_2)\}^{2+}$ ion, the *cis* isomer and *trans* isomer based on ring conformation. In the present case both the S atoms and the trimethylene linkages are *trans* to one another.

The average five-membered intra-ligand angle, S-Ni-N is 85.5(1)° (mean of 2) and is slightly larger than those found in $[Ni([9]\text{-aneSN}_2)_2]^{2+}$, 85.1(3)°,[122] ([9]-aneSN$_2$ = **84**). In the open chain complex, Ni(**85**)$_2^{2+}$,[183] the average S-Ni-N angle is 85.0°. As a result of the relief of strain, the six-membered intra-ligand angle is comparable to the corresponding N-Ni-N angle in the $[Ni([10]\text{-aneN}_3)_2]^{2+}$ complex, (86.6(6)°).[152]

Fig. 7.1. ORTEP diagram of **44** with 25% thermal ellipsoids.

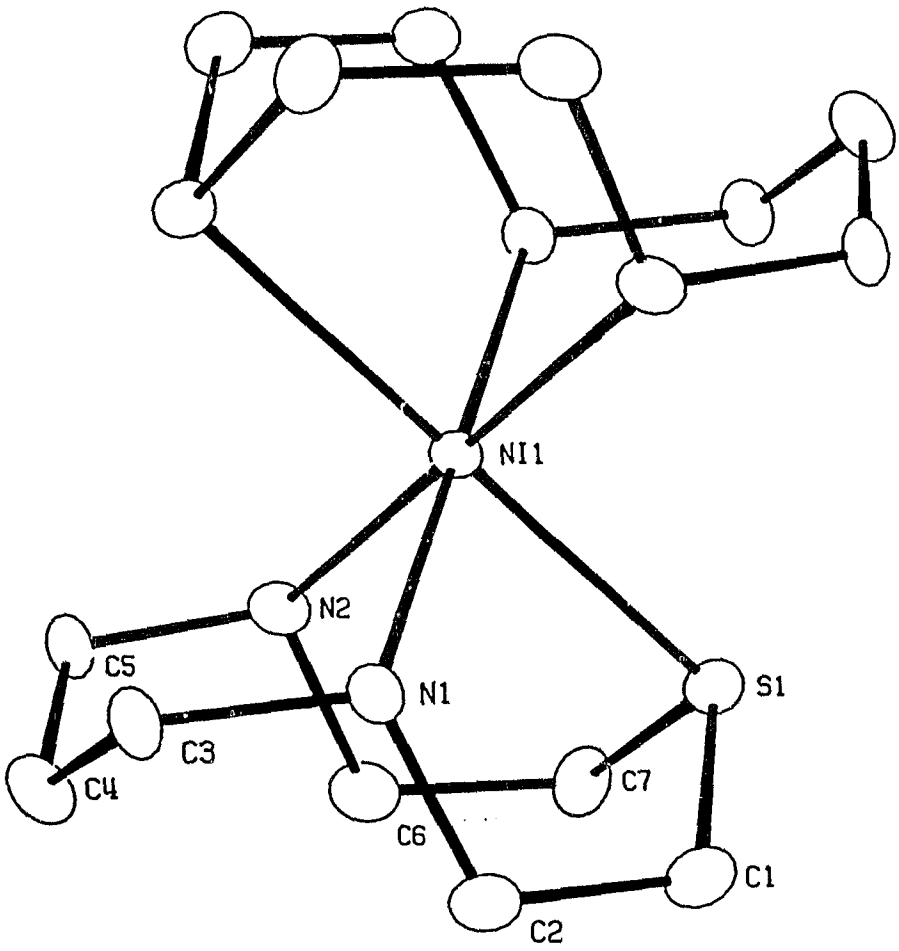

Table 7.2.

Fractional atomic coordinates and temperature parameters.

Atom	x/a	y/b	z/c	Ueq
Br(1)	47518(6)	23928(7)	87721(7)	448(3)
Ni(1)	50000(0)	50000(0)	50000(0)	213(3)
S(1)	68833(12)	60867(15)	55821(15)	312(4)
O(1)	1640(6)	-5(7)	4605(7)	84(3)
N(1)	5818(4)	3104(5)	5805(4)	29(1)
N(2)	5665(4)	4452(5)	3202(4)	30(1)
C(1)	7570(5)	4658(7)	6555(6)	39(2)
C(2)	7130(5)	3190(7)	6133(6)	36(2)
C(3)	5482(5)	1797(6)	5029(6)	36(2)
C(4)	5836(6)	1801(7)	3632(6)	41(2)
C(5)	5350(5)	2993(7)	2729(6)	36(2)
C(6)	6960(5)	4684(7)	3184(6)	37(2)
C(7)	7423(5)	5985(7)	3992(6)	38(2)

Estimated standard deviations are given in parentheses.

Coordinates × 10^n where n = 5,5,5,4,4,4 for Br,Ni,S,O,N,C.

Temperature parameters × 10^n where n = 4,4,4,3,3,3 for Br,Ni,S,O,N,C.

U_{eq} = the equivalent isotropic temperature parameter.

$U_{eq} = 1/3 \sum_i \sum_j U_{ij}' * a_j * (a_i . a_j)$

Primed values indicate that U_{iso} is given

$T = \exp-(8\pi^2 U_{iso} \sin^2\theta/\lambda^2)$

Table 7.3.

Interatomic distances (Å)

Atoms		Distance
S(1)	-Ni(1)	2.395(1)
N(1)	-Ni(1)	2.141(5)
N(2)	-Ni(1)	2.143(4)
C(1)	-S(1)	1.803(6)
C(7)	-S(1)	1.816(6)
C(2)	-N(1)	1.499(7)
C(3)	-N(1)	1.494(8)
C(5)	-N(2)	1.491(8)
C(6)	-N(2)	1.498(7)
C(2)	-C(1)	1.521(9)
C(4)	-C(3)	1.538(9)
C(5)	-C(4)	1.523(9)
C(7)	-C(6)	1.542(9)

Estimated standard deviations are given in parentheses.

Table 7.3. (contd.)

Bond angles (°)

Atoms			Angle
N(1)	-Ni(1)	-S(1)	85.5(1)
N(2)	-Ni(1)	-S(1)	85.5(1)
N(2)	-Ni(1)	-N(1)	87.1(2)
C(1)	-S(1)	-Ni(1)	98.0(2)
C(7)	-S(1)	-Ni(1)	98.1(2)
C(7)	-S(1)	-C(1)	106.8(3)
C(2)	-N(1)	-Ni(1)	114.9(4)
C(3)	-N(1)	-Ni(1)	114.2(4)
C(3)	-N(1)	-C(2)	110.7(5)
C(5)	-N(2)	-Ni(1)	114.1(3)
C(6)	-N(2)	-Ni(1)	115.1(4)
C(6)	-N(2)	-C(5)	109.4(4)
C(2)	-C(1)	-S(1)	114.5(4)
C(1)	-C(2)	-N(1)	113.8(5)
C(4)	-C(3)	-N(1)	114.7(5)
C(5)	-C(4)	-C(3)	117.1(5)
C(4)	-C(5)	-N(2)	115.3(5)
C(7)	-C(6)	-N(2)	112.8(5)
C(6)	-C(7)	-S(1)	113.4(4)

Estimated standard deviations are given in parentheses.

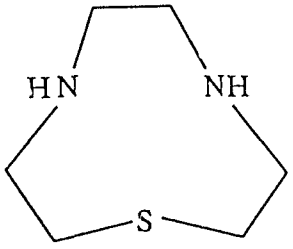

84

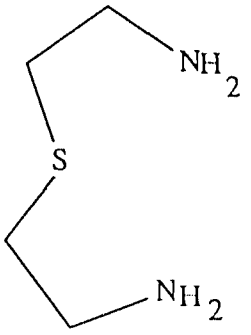

85

The average Ni-N bond length is 2.142(5) Å and is comparable to the average Ni-N bond length of 2.134(30) Å, in the $[Ni([10]\text{-}aneN_3)_2]^{2+}$ complex cation, which also contains the propyl linkage. However, the Ni-N bond length (2.142(5) Å) is longer than those in the open chain complex, $Ni(\mathbf{85})_2^{2+}$ (2.11 Å)[183] and the $[Ni([9]\text{-}aneSN_2)_2]^{2+}$, (2.115(7) Å).[122] The Ni-S bond length (2.395(1) Å) is shorter than that in the $Ni(\mathbf{85})_2^{2+}$ ion, (2.455 Å) and the $[Ni([9]\text{-}aneSN_2)_2]^{2+}$ ion, (2.418(1) Å). This may reflect the ability of the ten-membered ring to expand and for the S atom to reach over and encapsulate the Ni atom better than the nine-membered ring.

The trigonal twist angle ϕ, Fig. 3.2., page 85, is 58°, similar to that of the $[Ni([10]\text{-}aneN_3)_2]^{2+}$ ion,[152] deviating only two degrees from the octahedral value of 60°, Fig. 7.2. Molecular mechanics conformational analysis of **23** have been carried out recently,[155] and the most stable conformation was found to be [1333]. However, facial tridentate complexation requires a conformation in which all of the ligating atoms are

Fig. 7.2. Projection of the NiS_2N_4 core on to the plane perpendicular to the pseudo-3-fold axis of the molecule.

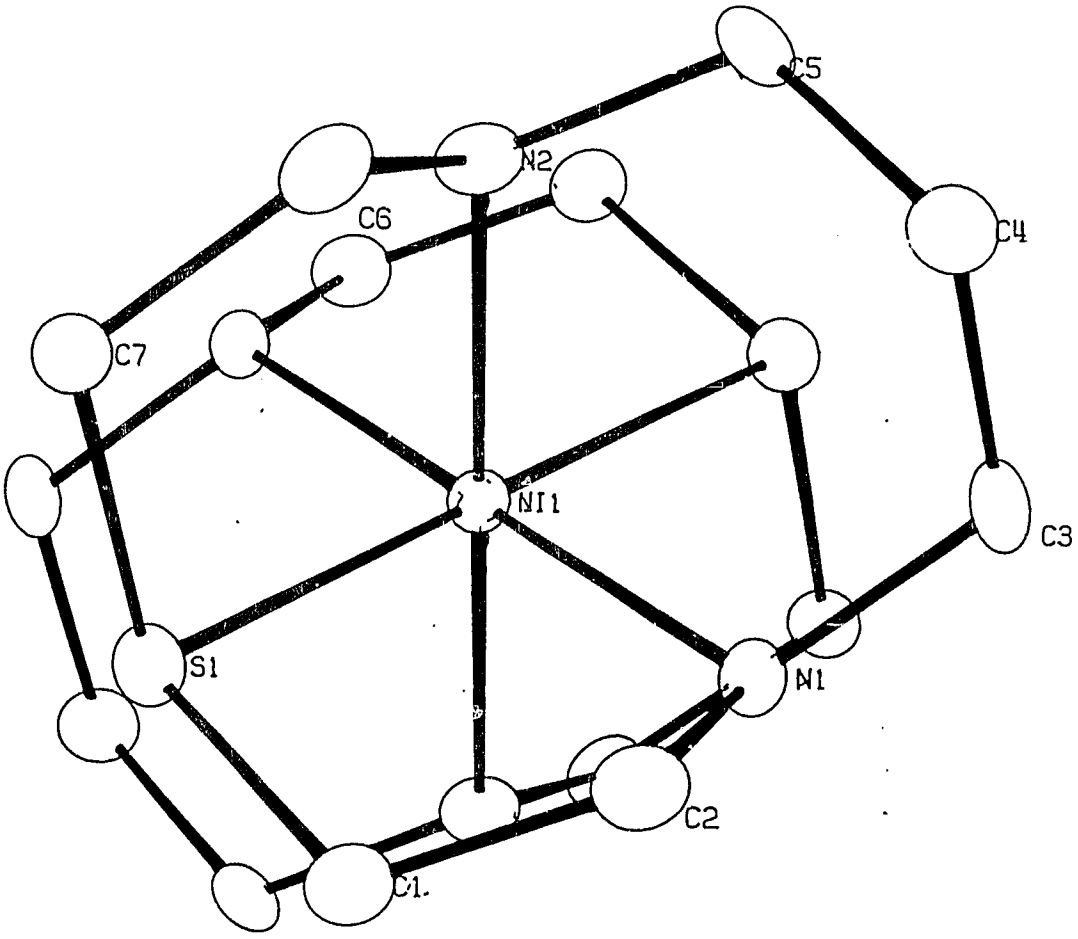

syn endodentate. The conformations that meet this requirement are [2323], [2233], [1333] and [1324], Fig. 7.3.

Fig. 7.3. Possible conformations of [10]-aneSN_2 suitable for complexation.

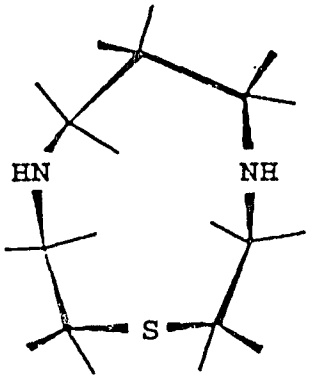

[1324]

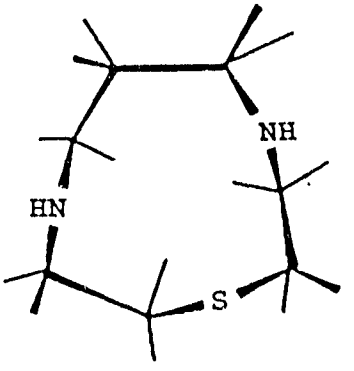

[1333]

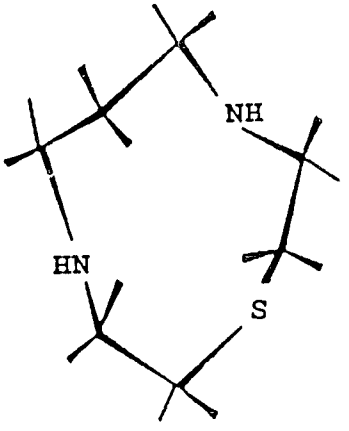

[2233]

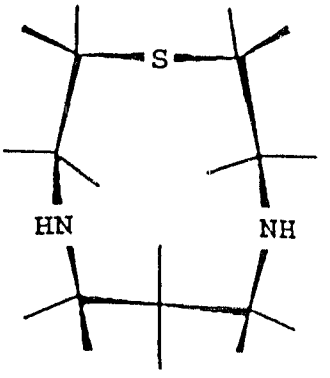

[2323]

In comparison, the conformation of the ten- membered ring, **25**, in the Ni(II) complex under study was found to be [2323], Fig. 7.2. Presumably, a conformational change has occurred in the ligand to facilitate complexation to the Ni(II) ion. The conformation of the nine- membered ring, **84**, in the Ni(II) complex is [333],[184] where the ligand is considered to be a triangle with three sides each comprised of three bonds.

7.4. Spectroscopic studies and electrochemistry:

The electronic spectra of $Ni([10]aneSN_2)_2(ClO_4)_2$, **44**, shows transitions due to $^1E_g \leftarrow {}^3A_{2g}$ at 880 nm (11364 cm^{-1}, ε = 13 M^{-1} cm^{-1}), $^3T_{2g} \leftarrow {}^3A_{2g}$ at 818 nm (12225 cm^{-1}, ε = 14 $M^{-1}cm^{-1}$) and $^3T_{1g}(F) \leftarrow {}^3A_{2g}$ at 529 nm (18904 cm^{-1}, 14 $M^{-1}cm^{-1}$), ν_2 and $^3T_{1g}(P) \leftarrow {}^3A_{2g}$ at 343 nm (29155 cm^{-1}, ε = 27 $M^{-1}cm^{-1}$), ν_3. Since the transitions to the spin forbidden and spin allowed ^1E_g and $^3T_{2g}$ states approach each other in energy, the energies of these bands cannot be used directly to calculate ligand field parameters in the usual manner.[121] Hart *et al*[183] have used a modified equation to calculate ligand field parameters for Ni(II) complexes of mixed donor ligands.

$$\nu_1 = \nu_m + 1.142\ \delta_m\ (\varepsilon_1/\varepsilon_2 - 1), \qquad -7.1.$$

where, ν_1 is the line position of the $^3T_{2g} \leftarrow {}^3A_{2g}$ band and ν_m is the mid-point in energy of the two bands, δ_m is the separation in energy of the transitions to $^1E_g \leftarrow {}^3T_{2g}$ as observed, ε_1 and ε_2 are the extinction coefficients of the higher and lower energy bands and the factor 1.142 is derived from an analysis

of Ni(II) spectra with first row donors. Applying this equation, ν_1 has been calculated to be equal to 11844 cm_{-1}. The ligand field strength Dq equals 1184 cm^{-1}. The Racah parameter B_{35} (see Chapter 6 for notation) was calculated from:[121]

$$B_{35} = \frac{(\nu_2 + \nu_3 - 3\nu_1)}{15} \qquad -7.2.$$

B for free ion = 1038 cm^{-1} and nephelauxetic ratio (β_{35}) for the complex has been found to be 0.80. From the energy ratio ν_3/ν_1 = 2.46 the value for Dq/B was read from the relevant Tanabe-Sugano plot[121] to be 1.3. The ν_2 band was predicted to be 18689 cm^{-1} which compares well with the experimentally obtained value of 18904 cm^{-1}. The ligand field parameters for the ten- membered series are given in Table 7.4. for comparison.

Table 7.4.

Ligand field parameters for Ni(II) complexes of ten- membered macrocycles.

Ligand	10Dq (cm^{-1})	B_{35} (cm^{-1})	β_{35}	B_{33} (cm^{-1})	β_{33}
[10]-aneN_3	12500	937	0.90	719	0.69
[10]-aneSN_2	11844	835	0.90	710	0.68
[10]-aneS_2N	12376	778	0.75	-	-
[10]-aneS_3	12500	717	0.69	735	0.71

Using equations 6.3. and 6.6. the parameters *f* and *h* were found to be 1.33 and 1.67 respectively, [$g(Ni^{2+})$ = 8.9, $k(Ni^{2+})$ = 0.12][163].

Oxidation of the Ni(II) complex, **44**, in aqueous solutions with Co^{3+} yielded a Ni(III) complex cation. The esr spectrum of frozen solutions of this Ni(III) species at 77 K was anisotropic with $g_{\parallel}$ = 2.046 and $g_{\perp}$ = 2.236, and is due to the presence of a Jahn-Teller distorted low spin octahedral complex, Fig. 7.4. The sequence $g_{\perp} > g_{\parallel} > g_e$ is consistent with the presence of a low spin d^7 ion. No hyperfine structure was noticed in the $g_{\parallel}$ feature. Thus, for the Ni(III) species the four N atoms occupy the equatorial plane with the two S atoms in the apical positions. The corresponding Ni(III) complex of **24** showed an inverted spectrum characteristic of a compressed octahedral complex (see Chapter 4). Thus, by changing the nature of the ligating atoms axial compression or elongation can be achieved as observed in the present study.

Cyclic voltammetry of the Ni complex, **44**, in aqueous solutions containing 1 M $NaNO_3$ showed a quasi-reversible wave with $E_{1/2}$ = +0.97 V *vs* saturated calomel electrode, Fig. 7.5., (1.21 V *vs* NHE, ΔE = 150 mV). This wave is attributed to the $[Ni(\mathbf{25})_2]^{3+/2+}$ couple. The $E_{1/2}$ values for the $Ni^{3+/2+}$ couple based on the ten- membered macrocycle is given in Table 7.5. The redox potentials increase as the harder N atoms are substituted by the softer S atoms. This is consistent with

Fig. 7.4. ESR spectrum of **44** + Co^{3+} in aqueous solutions.

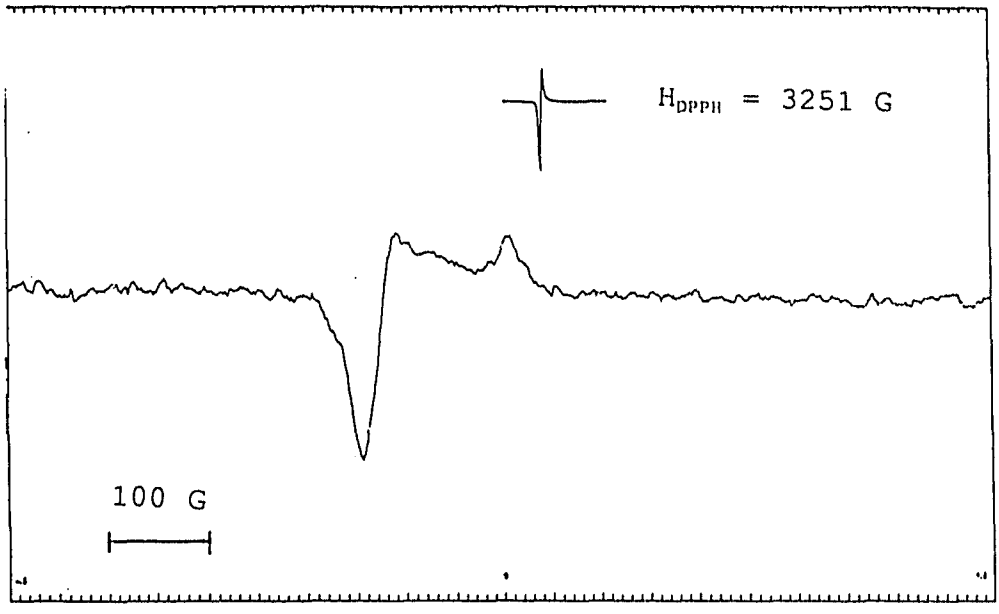

Fig. 7.5. Cyclc Voltammogram of **44** in H_2O containing 1 M $NaNO_3$.

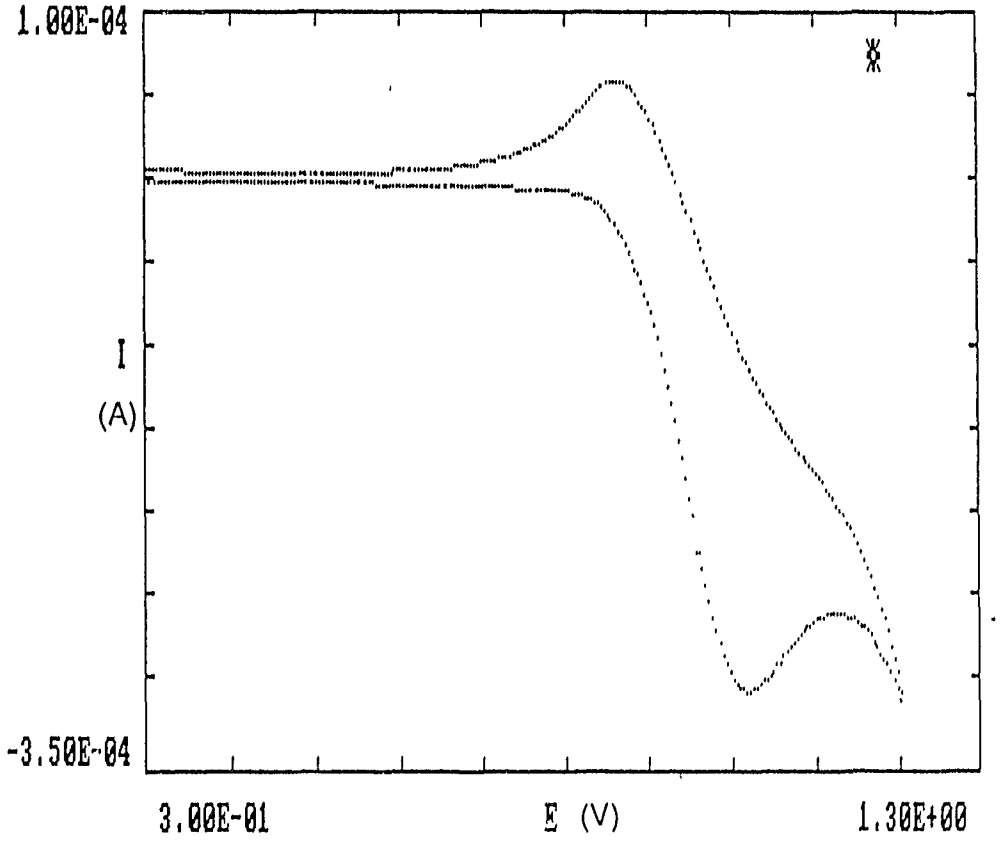

the ability of the trithia ligand to stabilize Ni(II) relative to Ni(III) and the triaza ligand to relatively stabilize the Ni(III) complex cation.

Table 7.5.

Redox potentials for the $Ni^{3+/2+}$ couple based on the ten membered macrocycles.

Ligand	#	$E_{1/2}$ (V) *vs* NHE	ΔE (mV)	Ref.
[10]-aneN_3	**66**	0.997	78	152
[10]-aneSN_2	**25**	1.20	150	PW
[10]-aneS_2N	**24**	1.26	114	PW
[10]-aneS_3	**23**	1.30	78	PW
macrobicycle	**26**	1.30	90	PW

PW = present work.

7.5. Conclusions :

The mixed donor macrocycle and its Ni(II) complex was synthesised and structurally characterised. The ligand field parameters were deduced from the electronic spectra and compared with other ten- membered macrocycles containing N and S donor atoms. The incorporation of the soft S atom in the macrocycle resulted in a small increase in the redox potential relative to the triaza ligand. The Ni(III) complex ion based

on **25** is in an elongated octahedral coordination as opposed to the compressed octahedral coordination seen in the complex ion based on the ligand [10]-aneS_2N, **24**. The nature of the ligating atoms, conformational effects and the constraints imposed by the macrocyclic ligand are, therefore, important in determining its complexation properties.

REFERENCES

1. Douglas, B. E., McDaniel, D. H., and Alexander, J. J.; "Concepts and Models of Inorganic Chemistry", 2nd ed., John Wiley & Sons, Inc., p. 254-256 (1983).

2. Porterfield, W. W.; "Inorganic Chemistry - A Unified Approach", Ch. 10, p. 465-505, Addison-Wesley Publishing Company, Inc., (1984).

3. Kauffman, G. B.; *J. Chem. Educ.*, 36, 521 (1959).

4. Sidgwick, N. V.; "The Electronic Theory of Valency", Clarendon Press, Oxford, (1927).

5. Pauling, L.; "The Nature of the Chemical Bond", Cornell University Press, Ithaca, N.Y., (1940).

6. Bethe, M.; *Ann. Physik.*, 3, 133 (1929).

7. Penney, W., and Schlapp, R.; *Phys. Rev.*, 41, 194 (1932).

8. Van Vleck, J. M.; *Phys. Rev.*, 41, 708 (1932).

9. Mulliken, R. S.; *Phys. Rev.*,40, 55 (1932).

10. Orgel, L. E.; "Introduction to Transition Metal Chemistry, Ligand Field Theory", John Wiley & Sons, Inc., N.Y., (1963).

11. Tanabe, Y., and Sugano, S.; *J. Phys. Soc. Japan.*, 12, 556 (1957).

12. Ballhausen, C. J.; "Introduction to Ligand Field Theory", McGraw-Hill, N.Y., (1962).

13. Griffith, J. S.; "The Theory of Transition Metal Ions", Cambridge University Press, N.Y., (1961).

14. Cotton, F. A.; "Chemical Applications of Group Theory", John Wiley & Sons, Inc., N.Y., (1963).

15. Melson, G. A.; "Coordination Chemistry of Macrocyclic Compounds", p.2, ed., Melson, G.A., Plenum Press, N.Y., (1979).

16. Lindoy, L. F.; "The Chemistry of Macrocyclic Ligand Complexes", Cambridge University Press,

17. McAuley, A., Subramanian, S., and Whitcombe, T.; *J. Chem. Soc., Chem. Commun.*, 539 (1985).

18. Cotton, F. A., and Wilkinson, G.; "Advanced Inorganic Chemistry", 5th ed., p. 52, John Wiley & Sons, Inc., N.Y., (1988).

19. Ahrland, S., Chatt, J., and Davies, N.; *Quart. Revs.*, 12, 265 (1958).

20. Pearson, R. G.; *J. Am. Chem. Soc.*, 85, 3533 (1963).

21. Haines, R. I., and McAuley, A.; *Coord. Chem. Revs.*, 39, 77 (1981).

22. Chaudhuri, P., and Wieghardt, K.; *Prog. Inorg. Chem.*, 25, 329 (1987).

23. Hancock, R. D., and Martell, A. E.; *Comments. Inorg. Chem.*, 6, 237 (1988).

24. Schwarzenbach, G.; *Helv. Chim. Acta.*, 35, 2344 (1952).

25. Cabbiness, D. K., and Margerum, D. W.; *J. Am. Chem. Soc.*, 91, 6540 (1969).

26. Busch, D. H., Farmery, K., Goedken, V., Katovik, V., Melnyk, A. C., Sperati, C. R., and Tokel, N.; *Adv. Chem. Ser.*, 100, 44 (1971).

27. Baker, A. D., Armen, G. H., and Funaro, S., *J. Chem. Soc., Dalton Trans.*, 2519 (1983).

28. Curtis, N. F.; *J. Chem. Soc.*, 4409 (1960).

29. Lindoy, L. F., and Busch, D. H.; "Preparative Inorganic Reactions", vol. 6, ed., Jolly, W., Interscience, N.Y., p. 1 (1971).

30. Bosnich, B., Poon, C. K., and Tobe, M. L.; *Inorg. Chem.*, 4, 1102 (1965).

31. Richman, J. E., and Atkins, T. J.; *J. Am. Chem. Soc.*, 96, 2268 (1974).

32. Rossa, L., and Vögtle, F.; "Topics in Current Chemistry", ed., Vögtle, F., Springer-Verlag, Berlin, 113, 1 (1983).

33. Buter, J., and Kellogg, M.; *Org. Synth.*, 65, 150 (1987).

34. Buter, J., and Kellogg, M.; *J. Chem. Soc., Chem. Comm.*, 466 (1980).

35. Olson, D. C., and Vasilevskis, J.; *Inorg. Chem.*, 10, 1228 (1971).

36. Hay, R. W.; "Bio-Inorganic Chemistry", Ch. 6, Ellis Horwood Ltd., West Sussex, England, (1984).

37. Lappin, A. G., and McAuley, A.; Advances in Inorganic Chemistry, vol. 32, Ed. Sykes, A.G., Academic Press, Inc., (1988).

38. Busch, D. H.; *Acc. Chem. Res.*, 11, 392 (1978).

39. Wilkins, R. G.; "The Study of Kinetics and Mechanisms of Reactions of Transition Metal Complexes", Allyn and Bacon, p 129 (1974).

40. Wilkins, R. G.; "The Study of Kinetics and Mechanisms of Reactions of Transition Metal Complexes", Allyn and Bacon, p 141 (1974).

41. Swift, T. J., and Connick, R. E.; *J. Chem. Phys.*, 37, 307 (1962).

42. Johnston, E. R., and Grant, D. M.; *J. Mag. Res.*, 47, 282 (1982).

43. Smolenaers, P. J., and Beattie, J. K.; *Inorg. Chem.*, 25, 2259 (1986).

44. Beattie, J. K., and Smolenaers, P. J.; *J. Phys. Chem.*, 90, 3684 (1986).

45. Jordan, R. B., and Angerman, N. S.; *J. Chem. Phys.*, 48, 3983 (1968).

46. McAuley, A., Macartney, D. H., and Oswald, T.; *J. Chem. Soc., Chem. Comm.*, 274 (1982).

47. Marcus, R. A.; *Ann. Rev. Phys. Chem.*, 15, 155 (1964).

48. Marcus, R. A.; *J. Phys. Chem.*, 67, 853 (1963).

49. McAuley, A, Norman, P. R., and Olubuyide, O,; *Inorg. Chem.*, 23, 1938 (1984).

50. Martin, A. E., Ford, T. M., and Bulkowski, J. E.; *J. Org. Chem.*, 47, 412 (1982).

51. Fortier, D. G.; Ph.D. Dissertation, University of Victoria, Victoria, Canada, (1988).

52. Hope, D. B., and Horncastle, K. C.; *J. Chem. Soc., C*, 1098 (1966).

53. Nelson, E. R., Malenthal, M., and Benderly, A. A.; *J. Am. Chem. Soc.*, 79, 3467 (1957).

54. Searle, G. H., and Geue, R. J.; *Aust. J. Chem.*, 37, 959 (1984).

55. Sheldrick, G. M., SHELX76, Program for Crystal Structure Refinement, University of Cambridge, U.K., (1974).

56. Main, P.; "MULTAN", University of York, York, U.K., (1978).

57. "International Tables for X-ray Crystallography", vol IV, Kynoch Press, Birmingham, U.K., (1974).

58. Brodovich, J. C., Haines, R. I., and McAuley, A., *Can. J. Chem.*, 59, 1610 (1981).

59. Brodovich, J. C., and McAuley, A., *Inorg. Chem.*, 20, 1667 (1981).

60. Zompa, L. J., and Margulis, T. N., *Inorg. Chim. Acta.*, 28, 1157 (1978).

61. Bernhard, P. and Sargeson, A. M., *Inorg. Chem.*, 26, 4122 (1978).

62. Yoshikawa, Y., *Chem. Lett.*, 109 (1978).

63. Royer, D. J., Grant, D. G., Van Derveer, and Castillo, M. J., *Inorg. Chem.*, 21, 1903 (1982).

64. Hay, R. W., and Jeragh, B., *Inorg. Nucl. Chem. Lett.*, 14, 435 (1978).

65. Zompa, L. J., *Inorg. Chem.*, 17, 2531 (1978).

66. Bulkowski, J. E., U.S. Patent 4 545 937, 1985.

67. Bulkowski, J. E., and Summers, W. E., III., "Copper Coordination Chemistry: Biochemical and Inorganic Perspectives"; Eds., Karlin, K. D., and Zubieta, J., Academic Press, New York, p. 445, 1983.

68. Whitcombe, T. W., Ph.D. dissertation, University of Victoria (1988).

69. Pedersen, E., *Acta Chem. Scand.*, 24, (1970).

70. Raymond, K. N., Corfield, P. W. R., and Ibers, J. A., *Inorg. Chem.*, 7, 1362 (1968).

71. Raymond, K. N., and Basolo, F., *Inorg. Chem.*, 5, 949 (1966).

72. Comba, P., Creaser, I. I., Gahan, L. R., Harrowfield, J. MacB., Lawrence, G. A., Martin, L. L., Mau, A. W. H., Sargeson, A. M., Sasse, W. H. F., and Snow, M. R., *J. Am. Chem. Soc.*, 25, 384 (1986).

73. Margulis, T. N., and Zompa, L. J., *J. Chem. Soc., Chem. Comm.*, 430 (1979).

74. Searle, G. H., and Dwyer, M., *Inorg. Chem. Acta*, 52, 251 (1981).

75. Zompa, L. J., and Margulis, T. N., *Inorg. Chim. Acta.*, 45, L263 (1980).

76. Wieghardt, K., Schmidt, W., Herrmann, W., and Küppers, H-J., *Inorg. Chem.*, 22, 2953 (1983).

77. Miyoshi, K., Tanaka, H., Kimura, E., Tsuboyama, S., Murata, S., Shimizu, H., and Ishizu, K., *Inorg. Chim. Acta*, 78, 23 (1983).

78. Beveridge, A. D., Lavery, A. J., Walkinshaw, M. D., and Schröder, M., *J. Chem Soc., Dalton Trans.*, 373 (1987).

79. Boeyens, J. C. A., Forbes, A. G. S., Hancock, R. D., and Wieghardt, K., *Inorg. Chem.*, 24, 2926 (1985).

80. Nadler, S. D., Dick, J. G., and Langford, C. H., *Can. J. Chem.*, 63, 2732 (1985).

81. Atkinson, N., Blake, A. J., Drew, M. G. B., Forsyth, G., Lavery, A. J., Reid, G., and Schröder, M., *J. Chem. Soc., Chem. Commun.*, 984 (1989).

82. Nicholson, R. S., *Anal. Chem.*, 38, 1406 (1966).

83. Bossu, F. P., Chellappa, K. L., and Margerum, D. W., *J. Am. Chem Soc.*, 99, 2195 (1979).

84. Bhula, R., Osvath, P., and Weatherburn, D. C., *Coord. Chem. Rev.*, (1988).

85. Ray, P. C., *J. Chem. Soc.*, 1090 (1920).

86. Setzer, W. N., Ogle, C. A., Wilson, G. S., and Glass, R. S., *Inorg. Chem.*, 22, 266 (1983).

87. Wieghardt, K., Küppers, H-J, and Weiss, H. Z., *Inorg. Chem.*, 24, 3067 (1985).

88. Rawle, S. C., Sewell, T. J., and Cooper, S. R., *Inorg. Chem.*, 26, 3769 (1987).

89. Bell, M. N., Blake, A. J., Gould, R. O., Holder, A. J., Hyde, T. I., Lavery, A. J., Reid, G., and Schröder, M., *J. Incl. Phen.*, 5, 169, (1987).

90. Rawle, S. C., Yagbasan, R., Prout, K., and Cooper, S. R., *J. Am. Chem. Soc.*, 109, 6181 (1987).

91. Wieghardt, K., Küppers, H-J, Raabe, E., and Krüger, C., *Angew. Chem. Int. Ed. Engl.*, 25, 1101 (1986).

92. Blake, A. J., Holder, A. J., Hyde, T. I., Roberts, Y. V., Lavery, A. J., and Schröder, M., *J. Organomet. Chem.*, 323, 261 (1987).

93. Blower, P. J., Clarkson, J. A., Rawle, S. C., Hartman, JA. R., Wolf, Jr., R. E., Yagbasan, R., Bott, S. G., and Cooper, S. R., *Inorg. Chem.*, 28, 4040 (1989).

94. Blake, A. J., Gould, R. O., Holder, A. J., Hyde, T. I., Lavery, A. J., Odulate, M. O., and Schröder, M., *J. Chem. Soc., Chem. Commun.*, 118 (1987).

95. Küppers, H-J, Neves, A., Pomp, C., Wieghardt, K., Nuber, B., and Weiss, J., *Inorg. Chem.*, 25, 2400 (1986).

96. Hunter, G., McAuley, A., and Whitcombe, T. W., *Inorg. Chem.*, 27, 2634 (1988).

97. Bernhard, P., and Sargeson, A. M., *Inorg. Chem.*, 27, 2582 (1988).

98. Wieghardt, K., Köppen, M., Swirdoff, W., Weiss, J., *J. Chem. Soc., Dalton Trans.*, 1869 (1983).

99. McAuley, A., and Whitcombe, T. W., *Inorg. Chem.*, 27, 3090 (1988).

100. Blake, A. J., Holder, A. J., Hyde, T. I., and Schröder, M., *J. Chem. Soc., Chem. Commun.*, 987 (1987).

101. DeSimone, R. E., and Glick, M. D., *J. Am. Chem. Soc.*, 97, 942 (1975).

102. Cragel, J., Petts, V. B., Glick, M. D., and DeSimone, R. E., *Inorg. Chem.*, 17, 2885 (1978).

103. Cammack, R., "Nickel in Metalloproteins", Advances in Inorganic Chemistry, vol. 32, Ed. Sykes, A. G., Academic Press, Inc., (1988).

104. Reid, G., Blake, A. J., Hyde, T. I., and Schröder, M., *J. Chem. Soc., Chem. Commun.*, 1397 (1988).

105. McAuley, A., and Subramanian, S., *Inorg. Chem.*, 29, 2830 (1990).

106. Ji, S., Gortler, L. B., Waring, A., Battisti, A., Bank, S., Closson, W. D., and Wriede, P., *J. Am. Chem. Soc.*, 89, 5371 (1967).

107. Searles, S., and Nukina, S., *Chem. Rev.*, 59, 1077 (1959).

108. Snyder H. R., and Heckert, R. E., *J. Am. Chem. Soc.*, 74, 2006 (1952).

109. Haskell, B. E., and Bowlus, S. B., *J. Org. Chem.*, 41, 159 (1976).

110. Hancock, R. D., Dobson, S. M., and Boeyens, J. C. A., *Inorg. Chim. Acta*, 133, 221 (1987).

111. Grant, G. J., Carpenter, J. P., Setzer, W. N., VanDerveer, D. G., *Inorg. Chem.*, 28, 4128 (1989).

112. Setzer, W. N., Cacioppo, E. L., Guo, Q., Grant, G. J., Kim, D. D., Hubbard, J. L., and VanDerveer, D. G., *Inorg. Chem.*, 29, 2672 (1990); and references therein.

113. Headly, O. St. C., Nyholm, R. S., McAuliffe, C. A., Sindellari, L., Tobe, M. L., and Venazi, L. M., *Inorg. Chim. Acta*, 4, 93 (1970).

114. Tarantelli, T., Furlani, C., *J. Chem. Soc. A.*, 1717 (1970).

115. Wieghardt, K., Schöffman, E., Nuber, B., and Weiss, J., *Inorg. Chem.*, 23, 4877 (1986).

116. Taira, Z., Yamazaki, S., *Bull. Chem. Soc. Jpn.*, 59, 649 (1986).

117. Wernberg, O., and Hazell, A., *J. Chem. Soc., Dalton Trans.*, 973 (1980).

118. Browning, J., Beveridge, K. A., Bushnell, G. W., and Dixon, K. R., *Inorg. Chem.*, 25, 1987 (1986).

119. Yamazaki, S., *Polyhedron*, 4, 1915 (1985).

120. Canty, A. J., Minchin, N. J., Engelhardt, L. M., Skelton, B. W., and White, A. H., *J. Chem. Soc., Dalton Trans.*, 645 (1986).

121. Lever, A. B. P., "Inorganic electronic spectroscopy", Elsevier Publishing company, New York, (1968).

122. Hart, S. M., Boeyens, J. C. A., Michael, J. P., and Hancock, R. D., *J. Chem. Soc., Dalton Trans.*, 1601 (1983).

123. Cooper, S. R., Rawle, S. C., Hartman, JA. R., Hintsa, E. J., and Adams, G. A., *Inorg. Chem.*, 27, 1209 (1988).

124. Blake, A. J., Holder, A. J., Hyde, T. I., and Schröder, M., *J. Chem. Soc., Chem. Commun.*, 1433 (1989).

125. Gahan, L. R., Lawrance, G. A., Sargeson, A. M., *Aust. J. Chem.*, 35, 1119 (1982).

126. Fortier, D. G., and McAuley, A., *J. Am. Chem. Soc.*, 112, 2640 (1990).

127. Barefield, E. K., Freeman, G. M., amd Van Derveer, D. G., *Inorg. Chem.*, 25, 552 (1986).

128. Handyside, T. M., Lockhart, J. C., McDonnell, M. B., and Rao, P. V. S., *J. Chem. Soc., Dalton Trans.*, 2331 (1982).

129. Wieghardt, K., Tolksdorf, I., and Herrmann, W., *Inorg. Chem.*, 24, 1230 (1985).

130. Geilenkirchen, A., Wieghardt, K., Nuber, B., and Weiss, J., *Z. Naturforsch.*, 44B, 1333 (1989).

131. Curtis, N. F., in "Coordination Chemistry of Macrocyclic compounds", ed. Melson, p 228, G. A., Plenum Press, New York (1979).

132. Taylor, S. G., Snow, M. R., and Hambley, T. W., *Aust. J. Chem.*, 36, 2359 (1983).

133. Bencini, A., Fabbrizzi, L., and Poggi, A., *Inorg. Chem.*, 20, 2544 (1981).

134. Wieghardt, K., Walz, W., Nuber, B., Weiss, J., Ozarowski, A., Stratemeier, H., and Reinen, D., *Inorg. Chem.*, 25, 1650 (1986).

135. Lacroix, R., Hoechli, V., and Müller, K. A., *Helv. Phys. Acta*, 37, 627 (1964).

136. Sastry, M. D., *J. Chem. Phys.*, 64, 3957 (1976).

137. Corfield, P. W. R., Ceccarelli, C., Glick, M. D., Moy, I. W-Y., Ochrymowycz, L. A., and Rorabacher, D. B., *J. Am.*

Chem. Soc., 107, 2399 (1985).

138. Rawle, S. C., and Cooper, S. R., *J. Chem. Soc., Chem. Commun.*, 308 (1987).

139. Blake, A. J., Gould, R. O., Holder, A. J., Hyde, T. I., and Schröder, M., *J. Chem. Soc., Dalton Trans.*, 1861 (1988).

140. Blake, A. J., Holder, A. J., Hyde, T. I., and Schröder, M., *J. Chem. Soc., Chem. Commun.*, 1433 (1989).

141. de Groot, B., and Loeb, S. H., *Inorg. Chem.*, 29, 4084 (1990).

142. Cooper, S. R., *Acc. Chem. Res.*, 21, 141 (1988).

143. Gerber, D., Chongsawangvirod, P., leung, A. K., and Ochrymowycz, L. A., *J. Org. Chem.*, 42, 2644 (1977).

144. Buter, J., and Kellogg, R. M., *J. Org. Chem.*, 46, 4481 (1981).

145. Blower, P. J., and Cooper, S. R., *Inorg. Chem.*, 26, 2009 (1987).

146. Clarkson, J., Yagbasan, R., Blower, P. J., Rawle, S. C., and Cooper, S. R., *J. Chem. Soc., Chem. Commun.*, 950 (1987).

147. Dalley, N. K., Smith, J. S., Larson, S. B., Matheson, K. L., Christensen, J. J., and Izatt, R. M., *J. Chem. Soc., Chem. Commun.*, 84 (1975).

148. DeSimone, R. E., and Glick, M. D., *J. Am. Chem. Soc.*, 98, 762 (1976).

149. Rawle, S. C., Adams, G. A., and Cooper, S. R., *J. Chem. Soc., Dalton Trans.*, 93 (1988).

150. Glass, R. S., Wilson, G. S., and Setzer, W. N., *J. Am. Chem. Soc.*, 102, 5068 (1980).

151. Chandrasekhar, S., and McAuley, A., *72nd Canadian Chemical Conference and Exhibition*, June, 1989.

152. Fairbank, M. G., McAuley, A., Norman, P. R., and Olubuyide, O., *Can. J. Chem.*, 63, 2983 (1985).

153. Sutin N., *Prog. Inorg. Chem.*, 30, 441 (1983).

154. Dubbs, R. V., Gahan, L. R., and Sargeson, A. M., *Inorg. Chem.*, 22, 2523 (1983).

155. Setzer, W. N., Cacioppo, E. L., Guo, Q., Grant, G. J., Kim, D. D., Hubbard, J. L., and VanDerveer, D. G., *Inorg. Chem.*, 29, 2672 (1990).

156. Huheey, J. E., "Inorganic Chemistry -- Principles of structure and reactivity" 3rd ed., Harper and Row, New York, p 73, 1983.

157. Hartman, JA. R., Hintsa, E. J., and Cooper, S. R., *J. Chem. Soc., Chem. Commun.*, 386 (1984).

158. Searle, G. H., and Angely, M. E., *Inorg. Chim. Acta*, 49, 185 (1981).

159. Laszlo, P., "NMR of newly accessible nuclei", vol. 2, ed., Laszlo, P., Academic Press Inc., 1983.

160. Wieghardt, K., Küppers, H. -J., Steenken, S., Nuber, B., and Weiss, J., *Z. Anorg. Allg. Chem.*, 573, 43 (1989).

161. Küppers, H. -J., Wieghardt, K., Nuber, B., Weiss., J., Bill., E., and Trautwein, A. X., *Inorg. Chem.*, 26, 3762 (1987).

162. Jørgensen, C. K., "Absorption Spactra and Chemical Bonding in Complexes", Pergamon Press, New York, 1962.

163. Figgis, B. N., "Introduction to Ligand Fields", Interscience Publishers, New York, 1966.

164. Alexander, J. J., and Gray, H. B., *J. Am. Chem. Soc.*, 90, 4260 (1968).

165. Gale, R., and McCaffery, A. J., *J. Chem. Soc., Dalton Trans.*, 1344 (1973).

166. Backers, G., and Reinen, D., *Z. Anorg. Allg. Chem.*, 418, 217 (1975).

167. Kremer, S., Henke, W., and Reinen, D., *Inorg. Chem.*, 21, 3013 (1982).

168. Reinen, D., Ozarowski, A., Jakob, B., Pebler, J., Stratemeier, H., Wieghardt, K., and Tolksdorf, I., *Inorg. Chem.*, 26, 4010 (1987).

169. Jørgensen, C. K., "Modern Aspects of Ligand Field Theory", North-Holland Publishing Co., New York, 1971.

170. Freeman, R., Murray, G. R., and Richardson, R. E., *Proc. R. Soc., London Ser. A*, 242, 455 (1957).

171. Ramsey, N. F., *Phys. Rev.*, 77, 567 (1950).

172. Juranić, N., *Inorg. Chem.*, 22, 521 (1983).

173. Bramley, R., Brorson, M., Sargeson, A. M., Schäffer, C. E., *J. Am. Chem. Soc.*, 107, 2780 (1985).

174. Bohan, T. L., *J. Mag. Res.*, 26, 109 (1977).

175. Bencini, A., and Gatteschi, D., "Transition Metal Chemistry", eds. Melson, G. A., and Figgis, B. N., vol. 8, Marcel Dekker Inc., New York, 1982.

176. Wilson, G. S., Swanson, D. D., and Glass, R. S., *Inorg. Chem.*, 25, 3827 (1986).

177. Graves, R. E., and Eachus, R. S., *J. Chem. Phys.*, 65, 5445 (1976).

178. Bontempelli, G., Magno, F., Corain, B., and Schiavon, G., *Inorg. Chem.*, 99, 19 (1981).

179. Reid, G., Blake, A. J., Hyde, T. I., and Schröder, M., *J. Chem. Soc., Chem. Commun.*, 1397 (1988).

180. Blake, A. J., Gould, R. O., Hyde, T. I., and Schröder, M., *J. Chem. Soc., Chem. Commun.*, 431 (1987).

181. Blake, A. J., Gould, A. J., Hyde, T. I., and Schröder, M., *J. Chem. Soc., Chem. Commun.*, 1730 (1987).

182. Macartney, D. H., *72nd Canadian Chemical Conference and Exhibition*, June, 1989.

183. Hart, S. M., Boeyens, J. C. A., and Hancock, R. D., *Inorg. Chem.*, 22, 982 (1983).

184. Hancock, R. D., Dobson, S. M., and Boeyens, J. C. A., *Inorg. Chim. Acta*, 133, 221 (1987).